Predicting the fatigue life and introducing structural health monitoring in cord reinforced rubber composites

Yinping Tao

A thesis submitted for the degree of Doctor of Philosophy

School of Engineering and Materials Science

Queen Mary University of London

September 2018

Abstract

Fatigue behaviour of cord-rubber composites is of great interest as components based on these materials are often subjected to cyclic loading during in-service conditions. Unfortunately, there appears a lack of scientific literature addressing this topic compared to that of fibre reinforced plastics (FRPs).

First conventional wedged grips were evaluated as a means to measure the tensile fatigue behaviour of single carbon cord reinforced hydrogenated nitrile butadiene rubber (CC-HNBR) composite samples. However, in these tests, failure was dominated by shear induced interfacial failure mechanisms (debonding), rather than cord fracture. Consequently, an alternative fatigue test for measuring the cord-dominated failure of cord-rubber composites was developed using bollards to introduce the load without creating premature failure near the gripping area.

Later, frequency effect and *R* ratio dependence were investigated based on a comprehensive characterisation of non-relaxing tensile fatigue of the CC-HNBR composites. Frequency has negligible effects on the fatigue life within testing regimes (2, 5, 10 and 20 Hz) due to a very limited self-heating of the rubber matrix as detected using the thermal imaging. Higher *R* ratios tend to increase the fatigue life due to possible crack tip blunting as a consequence of strain induced crystallisation (SIC) of the HNBR matrix. Life predictions of those model composites were made by various constant life diagram (CLD) models. Attempts were further made by modifying Harris's CLD and their applicability were examined. It showed that predictions made by the modified Harris's CLD and piecewise linear CLD were in a good agreement with experimental data at different *R* ratios.

A novel experimental set-up was described that replicated in a simplified way the real-pulley situation encountered under typical service conditions was used to investigate the effect of the bending curvature, frequency and *R* ratio effects on the life-time of the CC-HNBR composite subject to coupled tension and bending conditions. Cord-dominated fracture occurred close to the point where the specimen just left the pulley as detected using thermal imaging due to the combined effects of bending and maximum tension at this site. There was a reduction in fatigue life as a result of a tighter bending radius of the pulley which created a higher level of bending strain whilst similar effects of *R* ratio and frequency were observed to those in tensile fatigue.

Finally, efforts were made to develop smart self-sensing glass cord rubber composites with integrated damage detection capabilities. A simple swelling and infusion method was developed to incorporate carbon nanotubes (CNTs) into the existing elastomeric adhesive coating of glass cords. Conductive CNT-infused glass cords with good self-sensing functions were achieved without affecting the bonding provided by the coating with rubber matrix. The effectiveness of using these smart cords as interfacial damage sensors in cord-rubber composites was demonstrated under static and cyclic loading. It showed the possibility to identify both reversible deformation and irreversible interfacial damage. The simplicity of the proposed swelling and infusion methodology provides great potential for large-scale industrial production or modification of CNT functionalised elastomeric products such as cord-rubber composite.

Declaration

I, Yinping Tao, confirm that the research included within this thesis is my own work or that where it has been carried out in collaboration with, or supported by others, that this is duly acknowledged below and my contribution indicated. Previously published material is also acknowledged below.

I attest that I have exercised reasonable care to ensure that the work is original, and does not to the best of my knowledge break any UK law, infringe any third party's copyright or other Intellectual Property Right, or contain any confidential material.

I accept that the College has the right to use plagiarism detection software to check the electronic version of the thesis.

I confirm that this thesis has not been previously submitted for the award of a degree by this or any other university.

Signature:

Date:

Details of collaborations:

- Numerical modelling in Chapter 4 was carried out in collaboration with Dr. Richard Winslow from Queen Mary University of London, UK.
- Stress distribution within the cord in Chapter 6 was carried out in collaboration with Mr. R. Tashiro, Mr. S. Yonezawa from NSG Technical Research Laboratory, Itami, Japan and Dr. Christopher Stevens from NGF Europe Limited, St Helens, UK.

Details of Accepted Journal Publications:

- Y. Tao, Y. Liu, H. Zhang, C.A. Stevens, E. Bilotti, T. Peijs, J.J.C. Busfield, Smart cord-rubber composites with integrated sensing capabilities by localised carbon nanotubes using a simple swelling and infusion method, Composites Science and Technology, 167 (2018) 24-31.
- Y. Tao, R. Windslow, C.A. Stevens, E. Bilotti, T. Peijs, J.J.C. Busfield, Development of a novel fatigue test method for cord-rubber composites, Polymer Testing, 71 (2018) 238-247.

Details of Journal Paper in Preparation:

- Fatigue of carbon cord-rubber composites: Effect of frequency, *R* ratio and lifetime prediction using constant life models. To be submitted to International Journal of Fatigue in March 2019.

Details of oral conference presentations:

- Manchester Polymer Group Rubber Seminar, May 2018, Manchester, UK.
- International Rubber Conference. October 2017, Cleveland, USA.
- 10th European Conference on Constitutive Models for Rubber (ECCMR X), August 2017, Munich, Germany.
- Innovations in Rubber Design, December, 2016, London, UK.
- International Rubber Conference, October 2016, Kitakyushu, Japan.
- North European PhD seminar, May 2016, the Hanover, Germany.
- 9th European Conference on Constitutive Models for Rubber (ECCMR IX), September 2015, Prague, Czech Republic (Poster).

Awards: SEMS poster winner 2017

Acknowledgements

I would like to express my deepest gratitude to my supervisors Professor James Busfield and Dr Emiliano Bilotti. Their erudition, kindness and a sense of humour always drive me go ahead throughout my PhD. I would like to thank Professor James Busfield for allowing me to attend various international conferences to meet experts around world and have a chance to talk with them. Without these, I could not have been so confident to present in public. In addition, I would like to express my deepest gratitude to Professor Ton Peijs for joining project discussions. The conversations with him are always instrumental and critical. I also would like to thank Dr Han Zhang for all the discussions and guidance involved in my PhD. I am extremely lucky to have such incredible and nice persons to support my PhD research.

I would like to thank NGF Limited (UK) and China Scholarship Council (CSC) for sponsoring my PhD. Especially, I am most grateful to Dr Christopher Stevens being my industrial adviser, allowing me to access the company lab at the start of my PhD and all the useful discussions. I would like to express my gratitude to all technicians particularly Mr. Vince Ford, Dr Thomas Baumard, Mr. Dennis Ife, Mr. Douge Thomsonfor trainings and manufacturing testing rigs.

I also would like to thank all the current and former members in the Soft Matter Group. In particular, I would like to thank Dr Richard Winslow, Miss Francesca Carlo, Mr. Barnabas Shaw for discussions and accompany, creating great memory for every conference I have attended. In addition, I appreciated the discussions with Dr Thomas Baumard, Dr Lewis Tunnicliffe, Dr Menglong Huang, Dr Guangchang Wu and Dr David Stratford Devalba, Miss Yi Liu and Mr Leihao Chen. I also would like to thank all my friends particularly Renjie Liu, Shiping He, Danyang Li, Huihui Xia, Qiang Sheng and Ye Shi for encouragement and emotional support.

Finally, I would like to express my sincere gratitude to my parents and my brother for their support and encouragement. I am so grateful to them for giving me freedom to pursue my dreams. Without them, I would have never be so persistent for my goals and be able to be myself. I love them so much.

For my parents

Table of Contents

List of Abbreviations

ACN	Acrylonitrile
BD	Butadiene
BR	Butadiene rubber
C-C	Compression-compression
CC-HNBR	Carbon cord reinforced hydrogenated nitrile butadiene rubber
CF	Carbon fibre
CFRP	Carbon fibre reinforced plastic
CLD	Constant life diagram
CNTs	Carbon nanotubes
CPCs	Conductive polymer composites
CSM	Chlorosulphonated polyethylene
CV	Conventional vulcanisation
CVD	Chemical vapour deposition
DCP	Dicumyl peroxide
DMA	Dynamic mechanical analysis
DMF	Dimethylformamide
DSC	Differential scanning calorimetry
EPD	Electrophoretic deposition
EV	Efficient vulcanisation
FCG	Fatigue crack growth
FEA	Finite element analysis

FMEP	Friction mean effective pressure
FRPs	Fibre reinforced plastics
GF	Glass fibre
HNBR	Hydrogenated Nitrile Butadiene Rubber
HMPE	High performance polyethylene
HSPs	Hansen solubility parameters
ICE	Internal combustion engine
IFSS	Interfacial shear strength
ILSS	Interlaminar shear strength
MWCNTs	Multiwall carbon nanotubes
NBR	Nitrile butadiene rubber
NMP	N-methylpyrrolidone
NR	Natural rubber
ODR	Oscillating disc rheometer
PE	Polyethylene
PET	Polyethylene terephthalate
PP	Polypropylene
PPS	Polyphenylene sulphide
RFL	Resorcinol formaldehyde latex
RoM	Rule of Mixtures
RT	Room temperature
SBR	Styrene butadiene rubber

SBS	Short-beam shear
SEM	Scanning electron microscopy
SEF	Strain energy function
SEV	Semi-efficient vulcanisation
SHM	Structural health monitoring
SIC	Strain induced crystallisation
T-C	Tension-compression
TGA	Thermogravimetric analysis
T-T	Tension-tension
TPU/CNT	Thermoplastic polyurethane/carbon nanotube
UCS	Ultimate compressive strength
UTS	Ultimate tensile strength
WAXD	X-ray diffraction
WLF	Williams, Landel and Ferry

List of Symbols

A	The function of N_f in Harris's CLD
a	Normalised alternating stress
$\alpha_T, \beta_T, \alpha_C, \beta_C$	The scale and shape parameters for a two parameter Weibulldistribution of the UTS and UCS of the examined material.
β	The shape parameter for the carbon cord strength distribution
C_1, C_2	Material constants for Mooney SEF
C_{10}, C_{20}, C_{30}	Material constants for Yeoh SEF
c	Normalised compressive strength
d_f	The fibre diameter
d	The cord diameter
D	The damage function
D_1	The pulley diameter
ΔD_i	The damage accumulated at stress level r_i
E	Young's modulus
E_f	The fibre modulus
F	Elastic force
F_{max}	The peak pull-out force
$F(X)$	The cumulative failure probability
f	Frequency

$f^{'}$	The fibre volume fraction
f_H	The function of N_f in Harris's CLD
G	Shear modulus
G'	In-phase modulus
G''	Out-phase modulus
I_1, I_2	Strain invariants
k	Boltzmann constant
l	Length
L	The fibre embedded length
L_c	The critical fibre lengh
M_c	Average chain molecular weight between crosslinks
m	Normalised mean stress
N	Number of crosslinks
N_f	The number of cycles to failure
N_{fb}	Bending fatigue life
$n^{'}$	The dimensionless constant
n	The number of applied cycles
p	The failure probability in each cycle
p_H	The function of N_f in Harris's CLD
R	Stress ratio

R_0	Initial electrical resistance
$\Delta R / R_0$	The electrical resistance change
R_{gas}	Gas constant
r	The fibre radius
r_i	Applied stress level
S	Entropy
ΔS	The change in entropy
s	The fibre aspect ratio
T	Absolute temperature
T_g	Glass transition temperature
T_1, T_2	Two forces on a string in contact with the capstan
t	Time
t'	Thickness
U	Internal energy
u	The function of N_f in Harris's CLD
V_0	Initial volume
v	The function of N_f in Harris's CLD
W	The work of deformation
χ	Critical *R* ratio
λ	Extension ratio

λ_i	Principal extension ratios
ρ	Density
ε	Strain
ε_{bmax}	The maximum bending strain
ε_t	The tensile breaking strain of the carbon cord
σ	Stress
σ_a	Alternating stress
σ_m	Mean stress
σ_{min}	Minimum cyclic stress
σ_{max}	Maximum cyclic stress
$\sigma_a^\chi, \sigma_m^\chi, \sigma_{max}^\chi\ \sigma_m^\chi$	The cyclic stress amplitude, the mean stress and the maximum stress for a given value of life at χ
σ_B	Reference strength
σ_f	The tensile stress along the fibre
σ_f^*	The fibre strength
γ	Shear strain
γ_0	Maximum amplitude of shear strain
ω	Angular frequency
δ	Phase angle between stress and strain

δ_D, δ_P, δ_H	Hansen solubility parameter components from dispersion cohesion, polar cohesion and hydrogen bonding cohesion
β	The shape parameter for carbon cord strength distribution
μ	Friction coefficient
θ	The scale parameter for carbon cord strength distribution
V	Volume
ν_m	The Poisson's ratio
ν	Crosslinking density
τ	Interfacial shear strength
τ_0	The maximum amplitude of shear stress
τ_i	The interfacial shear stress
ϕ	The sweeping angle

List of Equations

List of Tables

List of Figures

Chapter 1 : Aim of the study

Cord reinforced rubber composites can be found in everyday applications, from vehicle tires, escalator handrails to folding bellows connecting carriages on trains. In addition to these visible components others are hidden from view, such as the timing belt found inside many modern combustion engines, which is used to synchronise the motion of the crankshaft and the camshaft for the purpose of torque transmission. The structure of a typical timing belt consists of (unidirectional evenly spaced) reinforcing cords, teeth, the backing rubber and facing fabric, as shown in Figure 1-1.

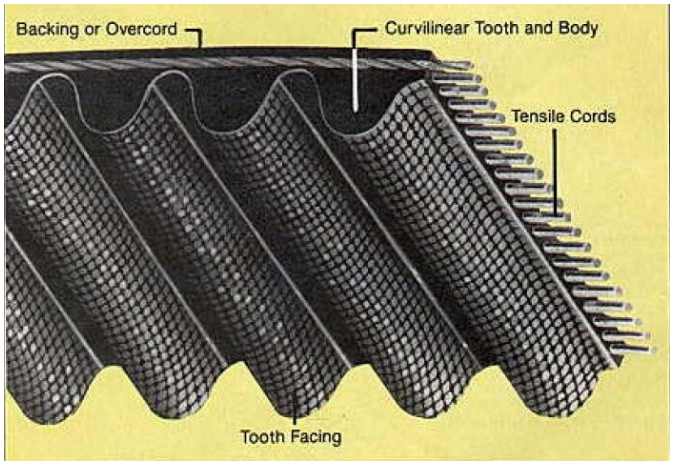

Figure 1-1. The structure of a timing belt. Taken from Miller et al [1].

Compared to traditional metal timing chains, it has the advantage of light weight and less friction thus improved fuel efficiency, as shown in Figure 1-2. To achieve better power transmission, a good meshing between the teeth and the pulley grooves is essential, which requires the reinforcing cords to have a high modulus, low breaking strain (elastic contribution) and minimal creep deformation induced by long-term stress (viscous contribution). Glass cords are the most commonly encountered cords used in the timing belt sector. The structure of glass cord used in this study is created by a primary twisting of the strands with each strand containing typically 600 glass

fibre (GF) filaments, followed by secondary twisting of 13 strands in the opposite twisting direction to make a helical cord approximately 1.1 mm in diameter, as shown in Figure 1-3.

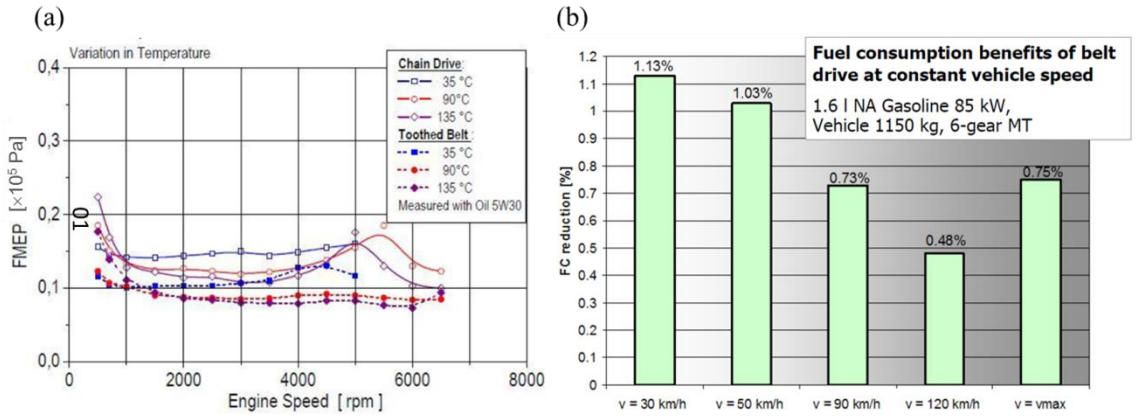

Figure 1-2. (a) The friction mean effective pressure (FMEP) of an internal combustion engine (ICE) as a function of engine speed, showing lower friction induced by timing belts compared with timing chain at 35 °C, 90 °C and 135 °C, (b) fuel consumption reduction of timing belt drive compared to timing chain drive at various speed. Taken from Tiemann et al [2].

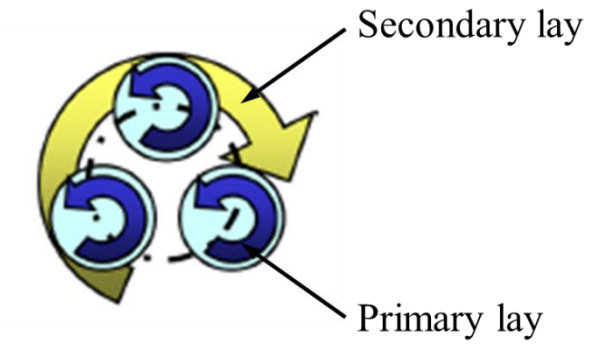

Figure 1-3. Schematic illustration of twisting directions for strand and cord twistings.

As the cost premium of the carbon fibre (CF)relative to the GF is reducing over time, there is a trend to replace at least some of the glass cords with stiffer carbon cords as

the reinforcing elements in timing belts due to much higher tensile modulus of the CF (3~4 times higher than that of GF [3]) so as to improve the dimensional stability and to potentially reduce the weight. The structure of the carbon cord used in this study is simpler, which consists of 6000 carbon fibre filaments twisted together with absence of secondary twisting.

How will such carbon cord reinforced rubber composite perform under tensile fatigue? Furthermore, considering the breaking strain of the CF is approximately 2 % while that of GF is roughly 4 %[3], will the carbon cord reinforced rubber composites also be good at bending situations regardless of the extra stiffness provided by the carbon cord ? These questions related to this topic are of great interest especially for belt manufacturers before its full commercialisation to be used in the next-generation of car engines.

However, there is only a limited amount of scientific work into cord reinforced rubber composites available in the literature examining the fatigue failure modes of components such as cord reinforced belts. In addition, there are very few life prediction studies of such components compared to huge number of studies concerning fibre reinforced plastics (FRPs). Moreover, the structure health monitoring of such composites is also of great interest since the catastrophic failure of the timing belt can lead to serious engine damage. The aim of this study is to investigate the fatigue failure of a model belt incorporating a single carbon cord used to reinforce a hydrogenated nitrile butadiene rubber (CC-HNBR) in an accelerated laboratory testing environment and to introduce structural health monitoring (SHM) into the cord reinforced rubber composites.

Chapter 2 gives a basic overview of the rubber materials studied in this work including their vulcanisation, their key elastic and viscoelastic properties. One of the

issues that arises in elastomer materials when studying their fatigue behaviour or their fatigue behaviour in cord-rubber composites is that the hysteresis heating might have an influence on the their fatigue performance.

Chapter 3 gives a basic overview of composite damage mechanisms described in the past together with underlying micromechanics. A detailed review is undertaken to consider the effects of various factors that might influence the fatigue life. Different life prediction methodologies are evaluated with a particular focus on constant life diagram (CLD) models. Additionally, techniques that might be used to measure the bending fatigue life of the cord or cord-rubber composites that have previously been reported in the literature are explored. Finally, recent works on structural health monitoring (SHM) of fibre reinforced composites are also presented.

Chapter 4 exploresthe various difficulties that are encountered when fatigue testing of a single carbon cord reinforced hydrogenated nitrile butadiene rubber (CC-HNBR) model composite using conventional wedge grips. This work highlights that a bollard test method should be adopted for this type of fatigue testing of soft rubber based matrix composites to avoid the interfacial debonding that results from the shear stress concentrations induced by the wedge grips. A comparison of fatigue data obtained using both types of set-up highlighted that bollard-based testing more closely reflected the intrinsic fatigue behaviour of cord-rubber composites which is dominated by cord-fracture.

Chapter 5 studies the influence of testing frequency and R ratio on the tensile fatigue behaviour of the CC-HNBR model composite using the bollard fatigue test set-up. Furthermore, a modified Harris's CLD was seen to give the most reliable life prediction of cord-rubber composites. The applicability of four other widely adopted CLD models were also examined.

Chapter 6 presented the fatigue behaviour of cord-rubber composites under coupled bending and tensile conditions. It shows a reduction in bending fatigue life with the decrease in the pulley diameter as a result of extra bending strain introduced by the pulley. Similar effects of the frequency and R ratio were observed as it is in the tensile fatigue. Compared to the tensile fatigue, the stress fields under coupled tension and bending were far more complicated.

Chapter 7 demonstratesa simple strategy to introduce and localise conductive nanofillers such as carbon nanotubes (CNTs) into existing elastomeric coatings surrounding the reinforcing cords. These CNTs form a percolating network which can be used for interfacial damage detection in real cord-rubber composites.

Chapter 8 concludes all the key findings in this current work and highlights a series of further beneficial investigations that can be done to advance this investigation further.

Chapter 2 : General knowledge of rubber materials

2.1 Brief historical review for rubber

The term ‘rubber’ was originally introduced by English scientist Joseph Priestley when he observed that dried natural rubber (NR) latex was able to rub out pencil marks. Today the word rubber is used not only for NR but also for any material that possesses rubber-like mechanical properties, that is, large deformation up to 500% - 1000% at relatively low stress [4]. Another word ‘elastomer’ is widely used almost interchangeably with ‘rubber’. Although according to ISO1382:2012 [5] an elastomer is any macromolecular material which returns rapidly approximately to its initial dimensions and shape after substantial deformation by a weak stress and release of the stress. Whereas a rubber is an elastomer which can be, or already is, modified to a state in which it is essentially insoluble (but can swell) in boiling solvent.

NR produced from *Hevea brasiliensis* trees was the primary source of rubber before synthetic rubbers were first manufactured in Germany in the 1930s [6]. The use of NR for industrial application took off following the discovery by Charles Goodyear in 1839 in the United States and Thomas Hancock in the United Kingdom that the NR became stronger and was less susceptible with the temperature change by heating it with sulphur which caused the formation of crosslinks into the polymer network. This process was known as vulcanisation (From ‘Vulcan’, the god of the fire). During the Second World War, the interruption of the supply of NR from plantations mainly located in Southeast Asia and Latin American hastened the development in the United States of methods for the bulk production of synthetic rubbers, including general purpose styrene butadiene rubber (SBR). Over the years, various synthetic rubbers

have been introduced into modern life with a significant proportion being used in transport engineering, healthcare, mineral extraction or the oil and gas industries.

2.2 Types of rubber

2.2.1 Natural rubber (NR)

NR is composed of primarily *cis*-1,4-polyisoprene with a glass transition temperature T_g of around -70 °C [7]. The molecular configuration is shown in Figure 2-1. Because of its stereo-regular structure, NR can crystallise either at low temperature, reaching the maximum crystallisation rate at about -25 °C or at a stretched state with a level of strain at around 400 % at 25 °C [8-10]. This crystallisation behaviour creates a self-reinforcing mechanism, and as a consequence NR exhibits outstanding tensile strength properties and good crack growth resistance when compared to materials that cannot crystallise such as SBR. However, NR is vulnerable to degradation from chemicals, ozone, ultraviolet and high temperature exposure due to the unsaturated double bonds.

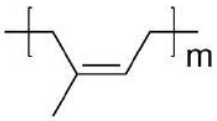

Figure 2-1: The chemical structure of NR.

2.2.2 Styrene butadiene rubber (SBR)

SBR is the most widely used synthetic rubber, mainly used for tyres as a result of its excellent abrasion resistance [11]. SBR is a random copolymer of styrene and butadiene, containing about 23% styrene with a T_g of around -50 °C [12]. The

molecular configuration is shown in Figure 2-2. SBR does not exhibit strain induced crystallisation (SIC) behaviour due to the random copolymer arrangement found in its molecular structure. Compared to NR, an unfilled SBR has much worse mechanical properties. Therefore, reinforcing fillers such as carbon black have to be incorporated into SBR to achieve good mechanical properties for engineering applications.

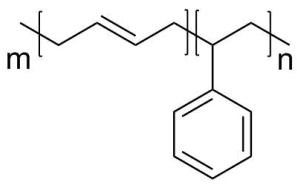

Figure 2-2: Chemical structure of SBR.

2.2.3 Butadiene rubber (BR)

BR is another synthetic rubber. It consists of 1,4-polybutadiene in *cis*- or *trans*-conformation as well as 1,2-polybutadiene. The chemical structure is shown in Figure 2-3 .The glass transition temperature for low-vinyl BR is around -100 °C, among the lowest of all rubbers while that of high-vinyl BR is around 0 °C [12]. BR is used for partial replacement of NR for manufacturing tire tread material due to its high resilience [6].

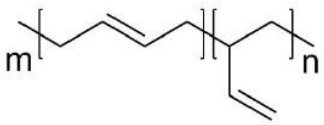

Figure 2-3: Chemical structure of butadiene rubber.

2.2.4 Nitrile butadiene rubber (NBR) and hydrogenated nitrile butadiene rubber (HNBR)

First introduced by Konrad and Tshunkur in 1930 using free radical emulsion polymerisation [13], NBR is widely used in engineering applications such as hoses and seals. NBR, also known as nitrile rubber, is a copolymer of acrylonitrile and 1,3-butadiene. The acrylonitrile (ACN) content can vary from 18% to 50%. The higher amount of ACN in the elastomer gives rise to excellent fuel oil resistance, reduction in resilience, decreased gas permeability and an increase ofT_g. However, NBR is still susceptible to heat and chemical degradation due to the unsaturation in the butadiene portion. To make up for this deficiency, hydrogenation of NBR is employed, as shown in Figure 2-4, and the final product is known as hydrogenated nitrile butadiene rubber (HNBR) with enhanced chemical and heat resistance. These materials are widely used in the oil and gas exploration and extraction industries as well as in automotive engines and oil seals. The comparison in properties between NBR and HNBR is shown in Figure 2-5.

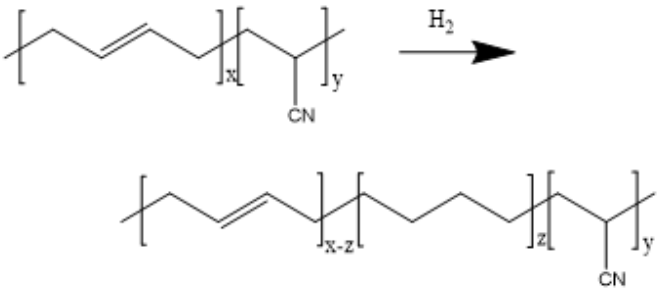

Figure 2-4. The hydrogenation process from NBR to HNBR.

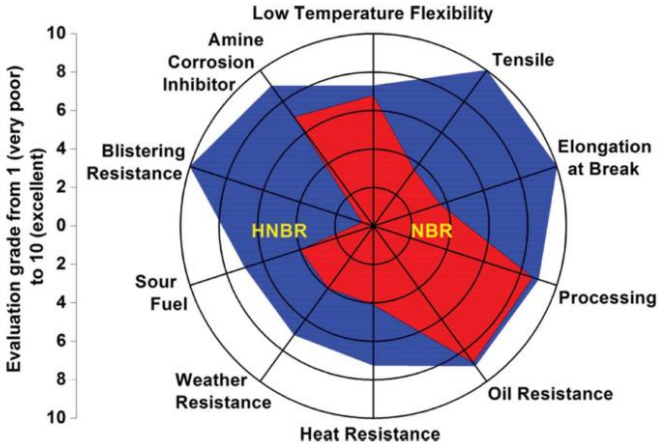

Figure 2-5. The properties comparison between NBR and HNBR. Taken from Wang et al [14].

2.3 Vulcanisation

Vulcanisation which is also known as curing or crosslinking is an essential final step during rubber processing. Essentially, this process transforms linear rubber polymer chains into a three dimensional molecular network. The curing characteristics of a rubber compound are usually measured using an oscillating disc rheometer (ODR). The torque required to oscillate the die, which correlates the degree of vulcanisation is recorded as a function of vulcanisation time at a given temperature, as shown in Figure 2-6. *ts2, Delta torque* and*t90* are three important parameters. *ts2* is used to evaluate the processing window known as the scorch safety of the compound. *Delta torque* provides the assessment of the cross-link density of a crosslinked rubber. *t90* is the time required to reach 90% of *Delta torque*, with a lower *t90* value representing a faster overall cure rate [15].

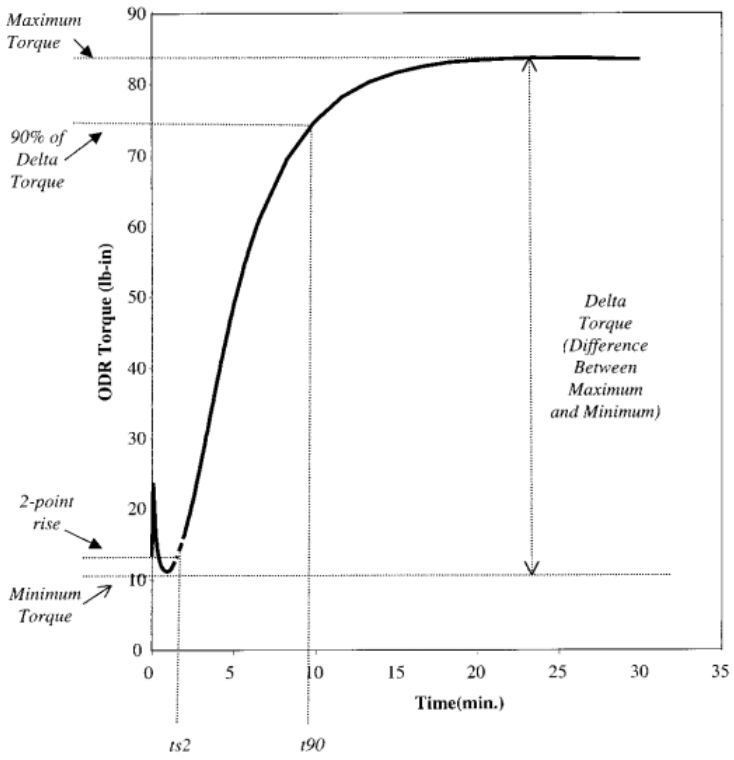

Figure 2-6: The response of the rubber compound in ODR. Taken from Dluzneski et al [15].

There are two types of vulcanisation systems widely used in the rubber industry: sulphur curing systems and peroxide curing systems. The sulphur curing system can be utilised for a number of elastomers with double bonds (unsaturation). Three broad types of sulphur curing systems have been developed over the years: efficient vulcanisation (EV) systems, semi-efficient vulcanisation (SEV) systems and conventional vulcanisation (CV) systems. The detailed curing behaviour is determined by the amount and the ratio of the accelerator to sulphur in the curing system. Different curing systems will result in different bonds connecting the hydrocarbon chains, as shown in Table 2-1[11]. Since the stability of sulphur bond decreases as the number of sulphur atoms per crosslink increases, as shown in Figure 2-7, the susceptibility of CV systems to chemical or thermal ageing is higher. Conversely, the elasticity and

fatigue properties of the CV cured rubbers are usually better due to the flexibility of the polysulphidic links and their labile ability to yield and recombine under strain [15, 16].

Table 2-1: Comparison between CV, SEV and EV.

Type	Sulphur (S, phr)	Accelerator (A, phr)	A/S ratio	Predominant crosslinks/ bonds
CV	2.0-3.0	0.5-1	0.1-0.5	-C-[-S-]$_n$-C-
SEV	1.0-1.7	2.4-1.2	0.7-2.5	-C-[-S-]$_n$-C-, C-S-C
EV	0.3-0.8	2.0-5.0	2.5-16	C-S-C

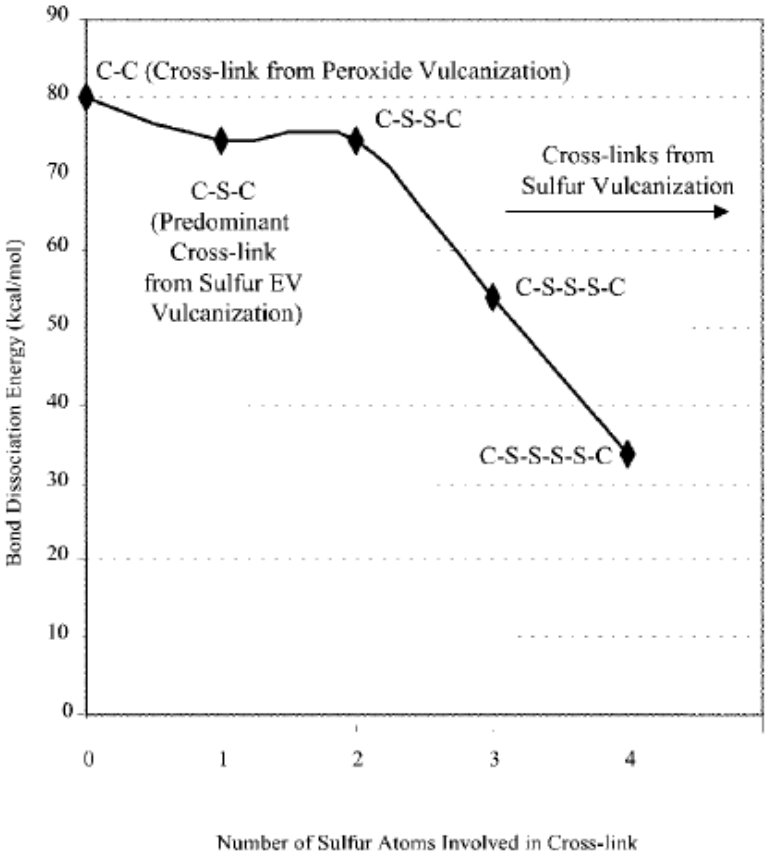

Figure 2-7: Relationship of the number of sulphur atoms in cross-links and bond strength. Taken from Dluzneskiet al [15].

Peroxide curing systems can be utilised for both unsaturated and saturated polymers, as summarised in the Table 2-2. Figure 2-8 shows basic reactions consisting of three steps: homolytic cleavage, hydrogen abstraction and radical coupling. In peroxide cured polymer networks the hydrocarbon chains are connected with stronger C-C bonds instead of less stable -C-[-S-]$_n$-C bond. Therefore, these rubber compounds offer better heat and chemical ageing resistance. In addition, peroxide curing systems can be created with shorter curing times.

Table 2-2: Table of polymers that are susceptible for peroxide curing. Taken from Dluzneskiet al [15].

Polymers that can be effectively cross-linked with peroxides	Polymers that cannot be effectively cross-linked with peroxides
Natural rubber	Polyisobutylene rubber
Styrene–Butadiene rubber	Butyl rubber
Polybutadiene rubber	Halobutyl rubber
Polyisoprene rubber	Polyepichlorohydrin
Nitrile rubber	Polypropylene
Hydrogenated nitrile rubber	Polypropylene oxide
Ethylene–Propylene rubber	
EPDM	
Ethylene–Vinyl acetate	
Acrylonitrile–Butadiene–Styrene	
Silicones	
Fluorocarbon elastomers	
Acrylic elastomers	
Polyurethanes	
Polyethylene	
Chlorinated polyethylene	
Poly(vinyl chloride)	
Chlorosulfonated polyethylene	

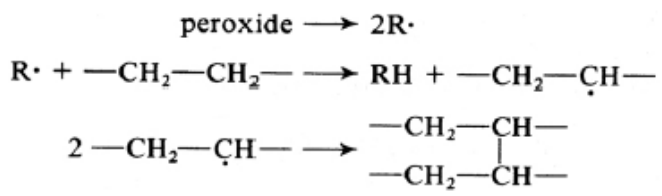

Figure 2-8: Basic reaction scheme of peroxide curing.

2.4 Rubber Elasticity

2.4.1 Thermodynamics of elastomer

Gough [17] first observed the typical thermoelastic phenomena of the rubber in 1805. He noted that:

(1) A rubber retracts reversibly upon heating under a constant load;

(2) A rubber heats up once stretching and cools down when it is retracted.

These effects were later confirmed by Joule [18]. Therefore, these two effects are also known as Gough-Joule effects.

A statistical thermodynamic analysis has been developed to explain thermoelastic effects of rubbery polymers [4], based initially on the first and second law of thermodynamics. The tension can be expressed as Equation 2-1, which is a combination of the contribution from the internal energy change and the entropy change.

$$F = \left(\frac{\partial U}{\partial l}\right)_{T,V} - T\left(\frac{\partial S}{\partial l}\right)_{T,V} \qquad \text{Equation 2-1}$$

The entropy change per unit length can be derived experimentally from the variation of the force with the temperature at a constant length as expressed as Equation 2-2.

$$\left(\frac{\partial S}{\partial l}\right)_{T,V} = -\left(\frac{\partial F}{\partial T}\right)_{l,V} \qquad \text{Equation 2-2}$$

Combining Equation 2-1 and Equation 2-2, we obtain

$$\left(\frac{\partial U}{\partial l}\right)_{T,V} = F - T\left(\frac{\partial F}{\partial T}\right)_{l,V} \qquad \text{Equation 2-3}$$

This provides a fundamental method to determine the thermodynamic quantities from experimental measurements. Correction of Equation 2-3 by using force-

temperature relationship at constant extension ratio λ instead of at constant length l eliminates the influence of thermal expansivity of the unstrained rubber. Figure 2-9 shows that the force is clearly derived from the entropy term at least up to 300% strain.

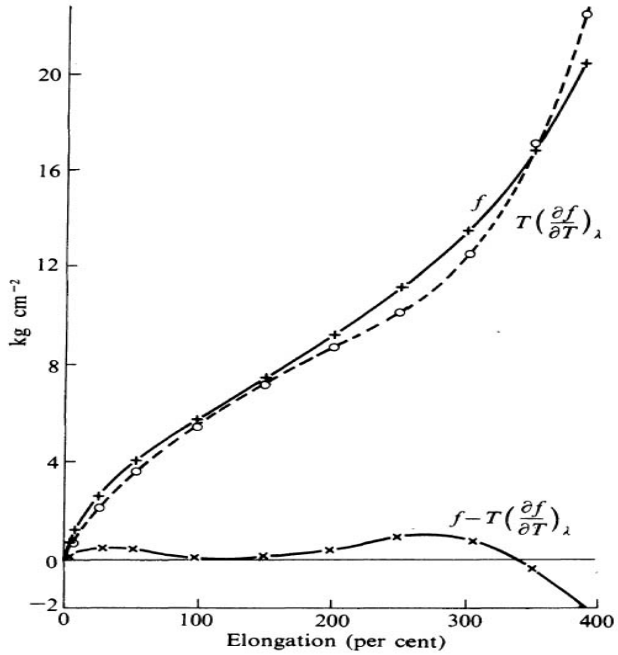

Figure 2-9. Application of stress-temperature data to Equation 2-3. Taken from Anthony et al [19].

2.4.2 Statistical network theory

The rubber elasticity is considerably different from other kinds of solids like glasses or metal. It depends on the number of conformations accessible to a specified condition [4]. The statistic theory was introduced to deal with the elasticity of the long chain molecular network based on several assumptions, that is, no volume change, an affine deformation of the network and the entropy of the whole network equals to the sum of entropies of every individual chain (the chains are 'Gaussian'). The change in entropy after deformation of a molecular network is given by [4]

$$\Delta S = -\frac{1}{2} Nk(\lambda_1^2 + \lambda_2^2 + \lambda_3^2 - 3) \qquad \text{Equation 2-4}$$

Since there is approximately no change in internal energy during deformation, thus it can be stated that

$$W = -T\Delta S \qquad \text{Equation 2-5}$$

Substituting Equation 2-4 into Equation 2-5 gives

$$W = \frac{1}{2}G(\lambda_1^2 + \lambda_2^2 + \lambda_3^2 - 3) \qquad \text{Equation 2-6}$$

$$G = NkT = \rho R_{gas}T / M_c \qquad \text{Equation 2-7}$$

where W is the work of deformation or the elastically stored energy per unit volume orthe elastic stored energy function (SEF), N is the number of chains per unit volume in the rubber network, k is the Boltzmann constant, T is the absolute temperature, λ_1, λ_2, λ_3 are the three principal extension ratios, G is the shear modulus, ρ is the density, R_{gas} is the gas constant, and M_c is the average chain molecular weight between two crosslinks.

It should be noted that the Gaussian treatment is only valid up to moderate extensions. For the higher extensions, a non-Gaussian treatment is preferred.

2.4.3 Phenomenological theory

In addition to the two theories mentioned above which interpret the rubber elasticity in physical or molecular sense, phenomenological theory is another approach to derive a strain energy function W to describe the general properties of rubber materials by employing mathematical reasoning. Rivlin (1948) further developed Mooney's theory (1940) based on the assumption that the materials is incompressible and is isotropic in the unstrained state, the strain energy function is given by

$$W = \sum_{i=0,\, j=0}^{\infty} C_{ij} \left(I_1 - 3\right)^i \left(I_2 - 3\right)^j \qquad \text{Equation 2-8}$$

where C_{ij} is elastic constant, I_1 and I_2 are strain invariants defined as

$$I_1 = \lambda_1^2 + \lambda_2^2 + \lambda_3^2 \qquad \text{Equation 2-9}$$

$$I_2 = \lambda_1^2\lambda_2^2 + \lambda_1^2\lambda_3^2 + \lambda_2^2\lambda_3^2 = \lambda_1^{-2} + \lambda_2^{-2} + \lambda_3^{-2} \qquad \text{Equation 2-10}$$

By putting $i = 1$ and $j = 0$, Equation 2-8 transforms into Equation 2-6, which representing the SEF derived from Gaussian treatment, also known as Neo-Hookean SEF. By addition of the first two terms ($i = 1$ and $j = 0$, $i = 0$ and $j = 1$), the Mooney SEF can be obtained, given by

$$W = C_1\left(I_1 - 3\right) + C_2\left(I_2 - 3\right) \qquad \text{Equation 2-11}$$

where C_1 and C_2 are elastic constants for Mooney SEF.

Later, Yeoh proposed his own SEF for filled rubbers due to the difficulties to fit the experimental data using the Rivlin SEF arising from the imperfect elasticity which will be discussed in the next section. Yeoh SEF is given by

$$W = C_{10}\left(I_1 - 3\right) + C_{20}\left(I_1 - 3\right)^2 + C_{30}\left(I_1 - 3\right)^3 \qquad \text{Equation 2-12}$$

The Yeoh model has the capability to capture shear behaviour reliably despite only using uniaxial tensile test data and therefore is selected for use in Chapter 4 to simulate the behaviour of matrix rubber [20].

2.5 Viscoelasticity

The theories mentioned above assume rubber materials are perfectly elastic. However, in reality, the rubber is a viscoelastic material, that is, the material behaviour also has a time dependence.

2.5.1 Creep and stress relaxation

Creep is a time-dependant increase in displacement under static constant loading while stress relaxation is a time-dependant decrease in tension under a fixed displacement, as shown in Figure 2-10. Creep and stress relaxation can be expressed mathematically under certain specific conditions by models such as the Voigt Model or Maxwell Model. The essential reason why these time dependent effects arise is a consequence of the frictional force between the molecules leading to the time delay when elastomer molecules slide over each other under strain or stress[12].

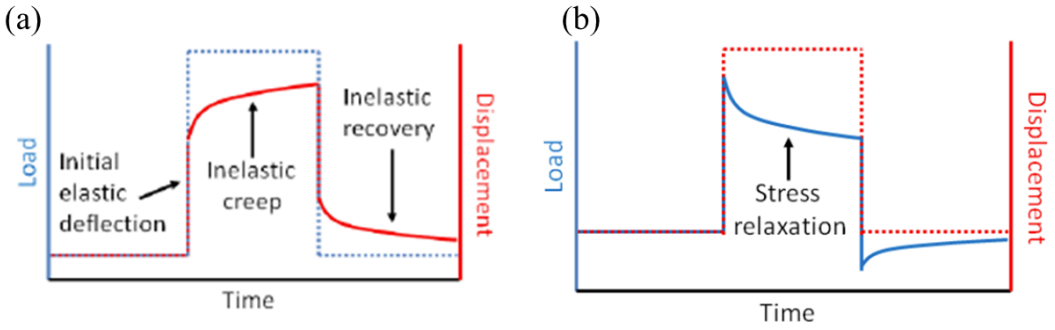

Figure 2-10. (a) Creep and (b) stress relaxation in rubber materials. Taken from Tunnicliffe et al [21].

2.5.2 Cyclic stress softening and Mullins effect

Cyclic stress softening and a specific case known as the Mullins effect are widely observed in all elastomers and are particularly obvious in filled rubbers and unfilled strain-crystallising rubbers such as NR and NBR [22, 23], as shown in Figure 2-11. It can be seen that majority of the softening happens after the first loading for the same amount of applied strain [24]. The Mullins effect also states that the stress strain response returns to the initial first cycle monotonic uniaxial tension path when the strain exceeds the maximum strain previously applied. The detailed underlying physical origins for this behaviour are still under debate. The main explanations today

involves either rubber-filler particle linkage ruptures [25], molecular slippage around the fillers or against each other[26], the breakdown of filler-filler clusters especially at high strain rates [27], breakdown and reformation of cross links or simply to chain disentanglement [28].

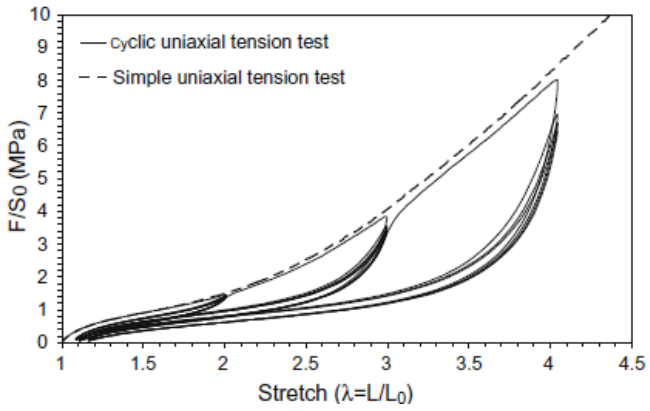

Figure 2-11. Stress strain behaviour of a filled SBR with 50 phr carbon black for simple and cyclic uniaxial tension tests with increasing maximum stretch every 5 cycles. Taken from Diani et al [29].

2.5.3 Hysteresis

The hysteresis is a measurement of the energy loss occurring duringthe loading and unloading process of each cycle, which can be obtained by calculating the area between the stretching and relaxing curve in a force-displacement plot. Some hysteresis is often desired, for example to provide damping in anti-vibration engineering applications.

2.5.4 Dynamic mechanical analysis (DMA)

The viscoelasticity nature of rubber materials becomes more significant when a rubber component is cyclically loaded. When a sinusoidal strain is applied onto the material in the form of

$$\gamma = \gamma_0 \sin \omega t \qquad \text{Equation 2-13}$$

The stress response is given by

$$\tau = \tau_0 \sin\left(\omega t + \delta\right) \qquad \text{Equation 2-14}$$

where δ is the phase angle between stress and strain, $0 < \delta < 90°$ for viscoelastic materials, γ_0 and τ_0 are the maximum amplitude of strain and stress, respectively.

Equation 2-14 can be rewritten according to trigonometric relationship as

$$\tau = (\tau_0 \cos\delta)\sin\left(\omega t\right) + (\tau_0 \sin\delta)\cos(\omega t) \qquad \text{Equation 2-15}$$

Defining the in phase contribution and out of phase contribution as storage modulus G' and loss modulus G'' respectively, we obtain

$$G' = \left(\tau_0 / \gamma_0\right)\cos\delta \qquad \text{Equation 2-16}$$

and

$$G'' = \left(\tau_0 / \gamma_0\right)\sin\delta \qquad \text{Equation 2-17}$$

The loss tangent, tan δ, is defined as the ratio of storage modulus G' and loss modulus G'',

$$\tan\delta = \frac{G''}{G'} \qquad \text{Equation 2-18}$$

In addition, Williams, Landel and Ferry (WLF) [30] demonstrated the equivalent effect of time and temperature on properties of polymeric materials. The resulting WLF function can therefore compensate a relatively limited test frequencies range of a DMA test machine by measuring the response of the rubber over a wide range of temperatures to map out a much wider spectrum of test frequencies.

2.6 Summary

A brief introduction is given in this chapter of the rubber materials used in this thesis. This includes a description of vulcanisation behaviour as well as the essential elastic and viscoelastic properties. When it comes to studying the fatigue behaviour of cord-rubber composites, it is worth commenting on the significant differences in the matrix behaviour compared with fibre reinforced plastics (FRPs). For example, the hysteresis heating effect in cord-rubber composites might well play a significant role during high frequency fatigue tests. A literature review about the fatigue of composites follows in the next chapter with a focus on the fatigue of cord-rubber composites.

Chapter 3 : Literature review

This chapter introduces an introductory review of composite damage mechanisms and their relationship to the underlying micromechanics. This is extended by examining from the literature how different variables affect the fatigue life of cord-rubber composites and how these effects can be modelled. A range of different bending fatigue test configurations are discussed and compared. Finally a review of different damage sensing systems that exploit nanofiller-modified smart textiles for the purpose of the structural health monitoring of cord-rubber system is also undertaken.

3.1 Composite damage mechanisms

A good understanding of mechanisms of damage inception and growth in composite materials is necessary prior to life predictions or design of more damage-tolerant structures. Compared to isotropic materials such as metals, similar crack initiation and crack growth [31, 32] were also found in composites. However, the damage mechanisms in composites are far more complex in terms of failure modes, depending on the loading mode (e.g. tensile, compressive, shear loading) and on whether the loading is parallel to the fibre direction. In this section, attention was paid to the mechanisms of damages in matrix, fibre and interface of unidirectional ductile (polymer) matrix composites under tensile loading. It should be noted that different failure modes often coexist during loading.

3.1.1 Matrix cracking

Dispersed matrix failure mode and localised matrix failure mode are two main types of damage modes in matrix, depending on the level of applied stress / strain on the composites [33]. Cracks initiate from the bulk of matrix and propagate until they strike

an interface, whereupon they might be confined in matrix alone, with increase only in crack density, if the stress at the crack tip is not sufficient to break the fibre as a consequence of low level of applied stress / strain during fatigue process (Figure 3-1 (a)). On the contrary, the fibre at the crack tip will break if the applied stress / strain is sufficiently high, allowing further growth of the crack. If a crack becomes long enough, the shear stress at its tip may cause an interfacial debonding, leading to crack diversion along the fibre direction, as illustrated in Figure 3-1 (b).

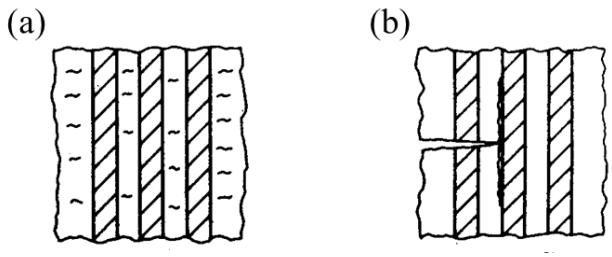

Figure 3-1. (a) Dispersed matrix failure mode with cracks confined in the matrix alone, (b) localized matrix failure mode, showing cracks grow by breaking reinforcing fibres, leading to interfacial failure at a later stage. Taken from Talreja et al[33].

3.1.3 Interfacial debonding

Interfacial debonding occurs when the local stress at the crack tip is higher than interfacial shear strength (IFSS) but still lower than the strength of the reinforcing fibre, as previously described in Figure 3-1 (b). Fibre pull-out in fractography of the composites is indicative of the interfacial damage. For composites having high IFSS, the crack growth may be circumscribed to a single plane normal to the fibre direction, leading to a flat and smooth fracture surface(Figure 3-2(a)) whilst a broom-like fracture surface (Figure 3-2(b)) may result from composite with relatively moderate IFSS. Caution should be taken to avoid the usage of either too high or too low IFSS in the design of damage tolerant composite structures, as the former causes the absence

of fibrepull-out and sliding which are capable of absorbing energy, thus contributing to improved toughness, while the latter makes fibres ineffective as they act in a similar way as a dry bundle in the air.

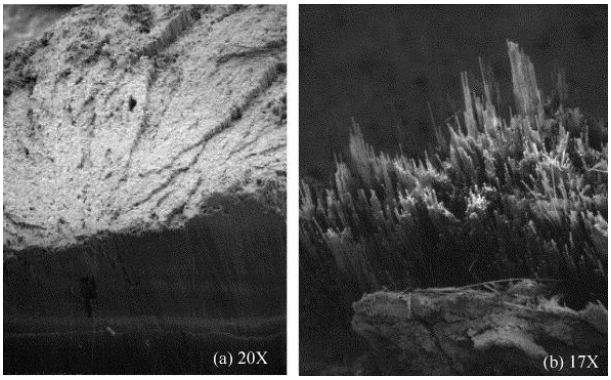

Figure 3-2. (a) A smooth and planar fracture surface of a glass fibre reinforced resin, (b) an irregular fracture surface with broom-like structures, showing fibres were pulled out from the resin matrix. Taken from Myers et al[34].

3.1.2 Fibre fracture

Fibre breakage often occurs in the later stage of fatigue. The fatigue damage can be seen as multiple fibre breakages with the loss of the stiffness and strength of the materials. Fibres manufactured inevitably have intrinsic flaws and have a statistical nature of the strength. On the initial application of the cyclic stress, fibres either having lower strength or at a local stress concentration site (for example, the tip of matrix crack as mentioned before) will fail first. The failure sites are randomly distributed throughout the composite. Upon repeated loading, more and more fibre fractures take place especially those adjacent to previously broken fibres as a result of a significant stress concentration in its neighbouring fibres. It eventually leads to clustering of fibre breaks at cross-sections of the composites and thus catastrophic fracture. The cumulative fibre breakage process during fatigue in composites is illustrated in Figure 3-3.

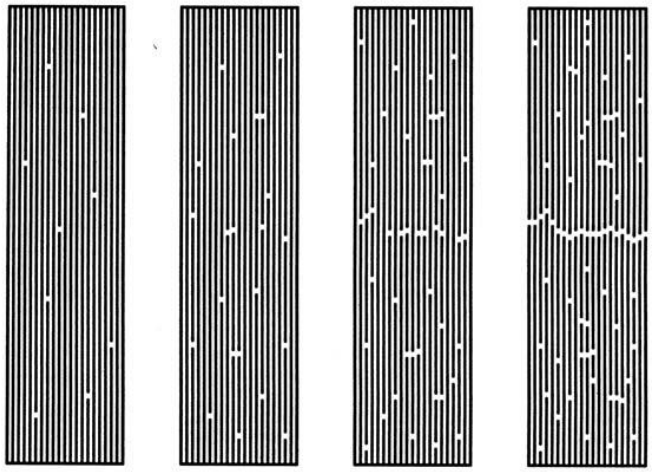

Figure 3-3. Cumulative fibre breakage process during fatigue in composites.

3.2 Composite micromechanics

The previous section considered the damage mechanisms in fibre reinforced composites. Since the fibres are the main load-bearing constituents, there is thus an interest in understanding the stress distribution in those composites. A brief introduction of composite micromechanics is given in this section.

3.2.1 Shear lag model

Several models such as shear sliding model [35], shear lag model [36, 37] and Eshelby [38, 39] model have been proposed to understand the stress fields in the reinforcing fibre and interface upon loading parallel to the fibre direction. The most widely used model is the shear lag model which was originally established by Cox [36] with the assumption that the load transfer only happens at interface through interfacial shear stress. The main differences within different models are the variations in matrix constitutive behaviours and interface conditions [40]. The schematic for calculations of tensile stress and interfacial shear stress along the fibre is shown in Figure 3-4.

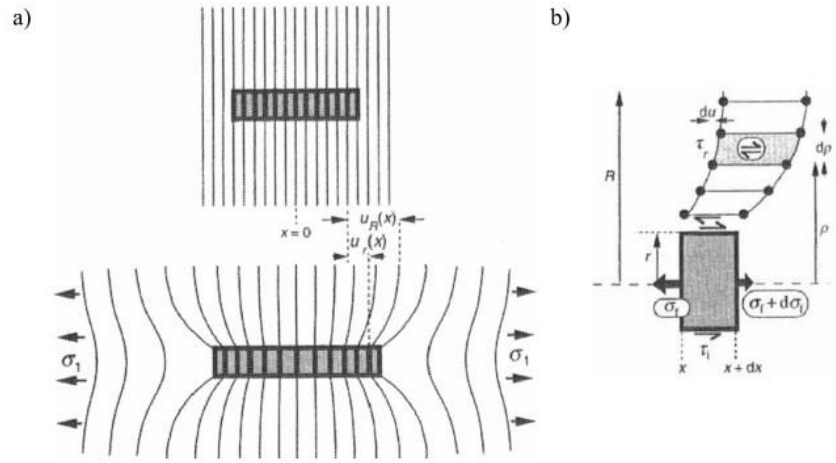

Figure 3-4. Schematic illustration of basis of the shear lag model: (a) Unstressed system and an axial displacement *u* introduced upon applying axial tension along the fibre direction, (b) variation in the shear strain and stress in the matrix with the radical location. Taken from Hull et al [3].

The analysis of the shear lag model gives

$$\sigma_f = E_f \varepsilon_f \left[1 - \cosh(nx/r)\sec h(ns)\right] \qquad \text{Equation 3-1}$$

$$\tau_i = \frac{n\varepsilon_1}{2} E_f \sinh(\frac{nx}{r})\sec h(ns) \qquad \text{Equation 3-2}$$

where σ_f is the tensile stress along the fibre, τ_i is the interfacial shear stress, E_f is the fibre modulus, ε_f is the fibre strain, ε_1 is the overall composite strain, x is the distance from the fibre mid-point, r is the fibre radius, s is the fibre aspect ratio given by L/r, n' is a dimensionless constant given by

$$n' = \left[\frac{2E_m}{E_f(1+\nu_m)In(1/f')}\right]^{1/2} \qquad \text{Equation 3-3}$$

where ν_m is the Poisson's ratio and f' is the fibre volume fraction.

Based on the calculations by Equation 3-1 and Equation 3-2, Figure 3-5 shows both the axial tensile stress and the interfacial shear stress distribution along the fibre in a

unidirectional glass fibre reinforced polyester composites subjected to an axial tensile strain of 0.1 %. It can be seen that the tensile stress is zero at the fibre ends and a maximum is at the centre. The interfacial shear stress is maximum at the ends and zero at the centre. If the fibre is long enough compared to its radius (large aspect ratio), it gives rise to the formation of the plateau region where the fibre has strain equal to that of the matrix and at this time the interfacial shear stress is equal to zero.

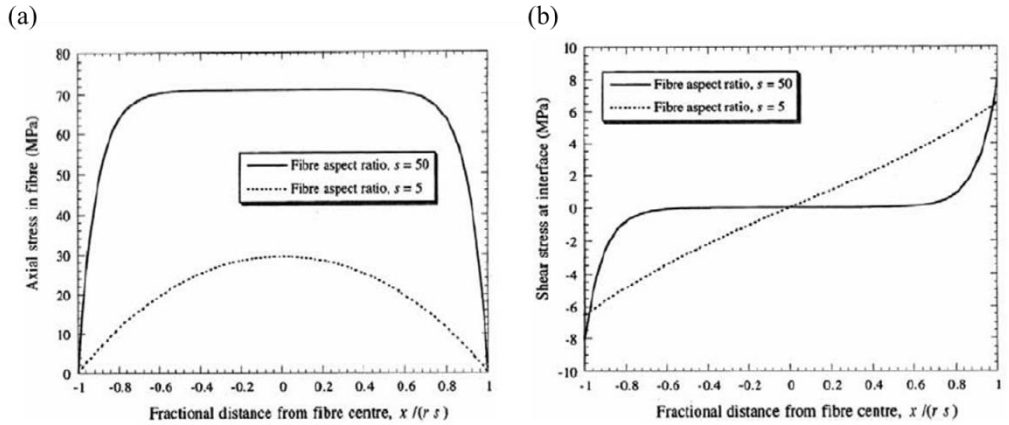

Figure 3-5. Predictions made by Equation 3-1and Equation 3-2, the variations in (a) the tensile stress, and (b) the interfacial shear stress along the fibre in a glass fibre / polyester composite subjected to an axial tensile strain of 0.1 % for two fibre aspect ratios. Taken from Hull et al [3].

3.2.2 Physical meaning of critical fibre length

Critical fibre length is an essential concept in fibre reinforced composite materials. In this section, the physical meaning of critical fibre length will be discussed.

In contrast to shear lag model, Kelly-Tyson model assumes a constant interfacial shear stress at fibre / matrix interface [41]. The tensile stress along the fibre and the interfacial shear stress profile can thus be simplified, as shown in Figure 3-6.

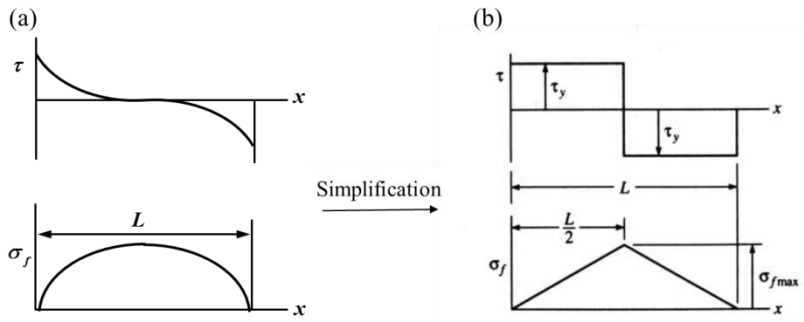

Figure 3-6. The tensile stress along the fibre and the interfacial shear stress profile in (a) shear lag model and (b) Kelly-Tyson model.

As discussed earlier, there are regions close to the fibre ends which are less heavily stressed than the central plateau region. This phenomenon leads to the definition of stress transfer length (also termed as ineffective length) and effective length, as illustrated in Figure 3-7 (a). When the level of external load is increased ((i) => (ii) => (iii)), the tensile stress in the fibre increased proportionally until the stress in fibre reaches fibre strength σ_f^*, leading to fibre breakage and stress redistribution, as shown in Figure 3-7(b).

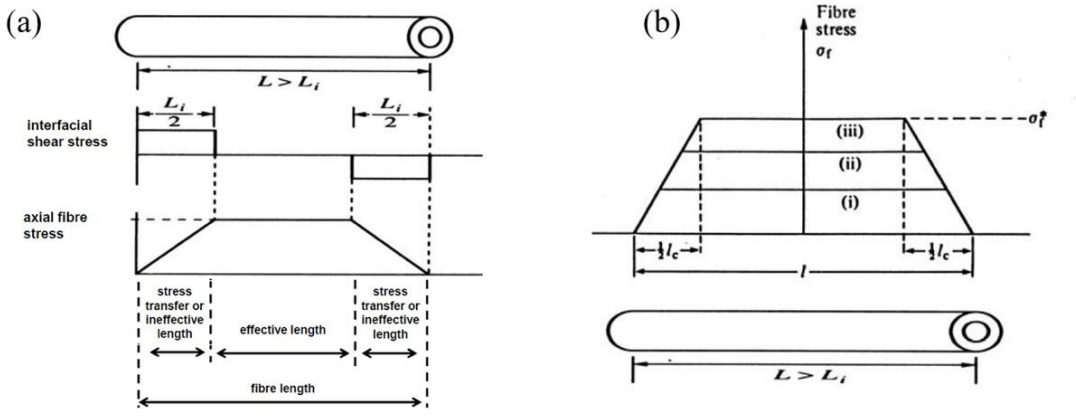

Figure 3-7. Schematic illustrations: (a) definition of stress transfer length (also termed as ineffective length) and effective length, (b) change in stress distribution along fibre as load on composite is increased ((i) => (ii) => (iii)).

The adhesion between the fibre and matrix has a significant influence on the tensile stress along the fibre. The value of the IFSS determines how fast the tensile stress is introduced into the fibre, reflected from the slope of the initial uprising linear part of the axial fibre stress against fibre length plot. The effects of a strong and a weak interface are illustrated in Figure 3-8 (a)-(c). If the interface is very weak, the tensile stress in the fibre cannot reach the strength of the fibre when the external load is increased. In this extreme situation, the fibre won't break in such system. Instead, interfacial debonding and matrix cracking will be the main failure mechanisms.

The reinforcing efficiency is defined as the ratio of the effective length over the whole length of the fibre, which increases as the fibre length increases. And when the fibre in the matrix is ten times the length of the critical length, it has very similar reinforcing effect as the long fibre reinforced composites theoretically when the load is applied parallel to the fibre.

There are two major ways to improve the reinforcing efficiency: (a) increase fibre length or (b) improve the adhesion so as to reach the tensile stress plateau. In either method, there is a critical point where the tensile stress in the mid-point just reaches the fibre strength σ_f^*, as shown in Figure 3-8 (d). The length of fibre in this condition is defined as the critical length L_c, depending on the fibre strength σ_f^*, average IFSS τ and the diameter of the fibre d_f, given by

$$L_c = \frac{\sigma_f^* d_f}{2\tau} \qquad \text{Equation 3-4}$$

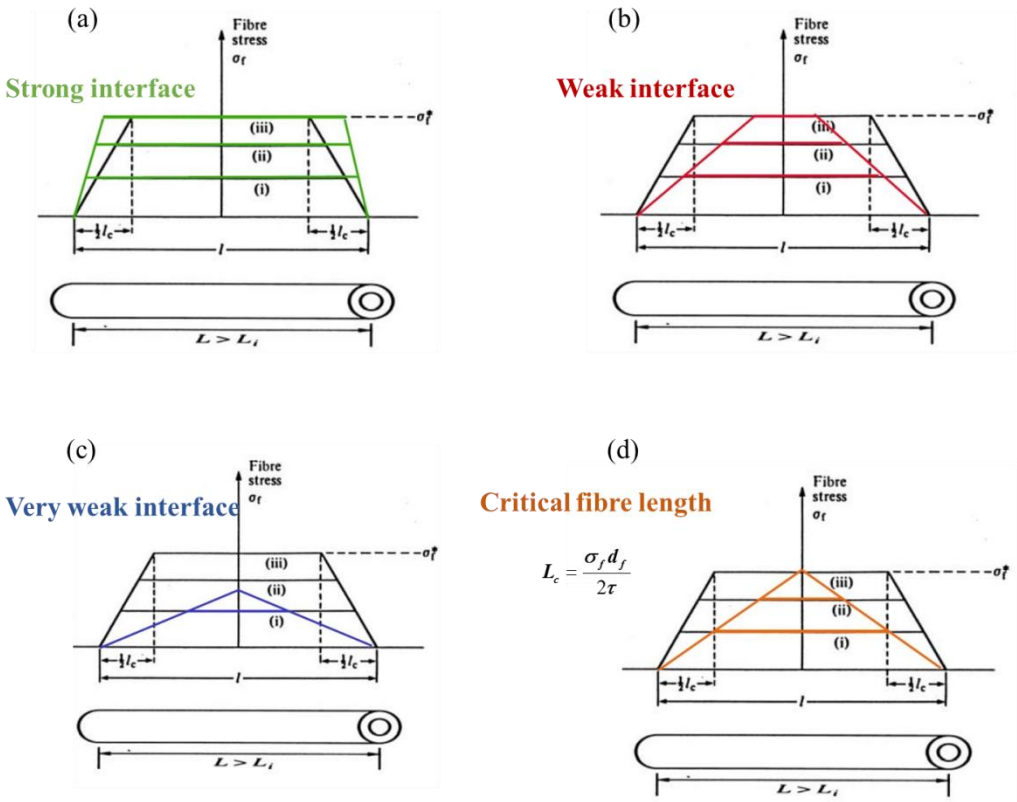

Figure 3-8. The schematics of stress along the fibre: (a) a strong interface, (b) a weak interface, (c) a very weak interface and (d) at a critical fibre length. The physical meaning of the IFSS determines how fast the tensile stress is introduced into the fibre.

3.3 Interfacial bonding

Assumptions that the interfacial bonding is 'perfect' is made in a number of theories, for example, shear lag model. In practice, however, many important events such as debonding, cracking and fibre sliding will occur in the interfacial region. These processes will promote the plastic deformation of the matrix and also influence the onset and the nature of failure. Therefore, it is necessary to characterise the interface and understand its behaviour prior to study the fatigue behaviour of the cord-rubber composites.

Molecular entanglement, electrostatic attraction, cationic–anionic attraction, chemical bonding and mechanical interlocking are five main types of interfacial

bonding mechanisms in fibre reinforced composites, as shown in Figure 3-9. In this section, experimental measurements of bond strength reported in the literature were briefly reviewed. This is followed by the introduction of treatment of cord / yarn / textiles for enhanced adhesion with rubber and the effects of dynamic loading on adhesion evolution.

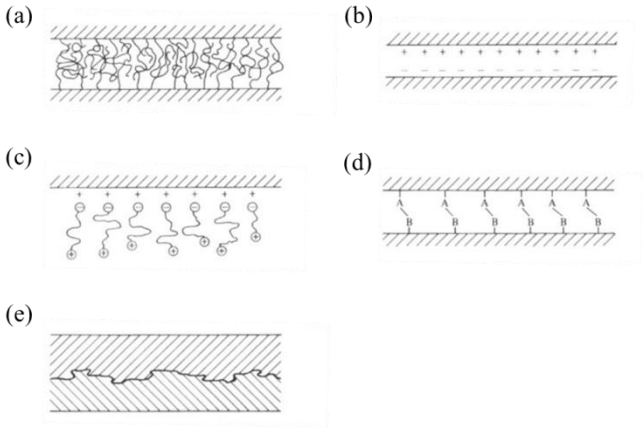

Figure 3-9. Interfacial bonding mechanisms: (a) molecular entanglement, (b) electrostatic attraction, (c) attraction of cationic groups at the end of molecules to an anionic surface, i.e. silanes, (d) A-B (covalent, ionic or metallic) bonds formation through localised chemical reactions, (e) mechanical keying.

3.3.1 Experimental measurement of the bond strength

Single-fibre pull-out test

Bowling *et al.* investigated the pull-out behaviour of a nickel ductile wire from an epoxy resin and established a model using the concept of a yielded zone to describe the debonding and the subsequent pull-out [42]. The single-fibre pull-out test was firstly reviewed thoroughly by Di Francia *et al.*[43] and the pull-out process was interpreted mathematically with a complete description of experimental events. In the single fibre pull-out test, the fibre which was partially embedded in a matrix was pulled out by a tensile load. The average IFSS τ at can be calculated by

$\tau = F_{max}/(\pi dL)$ Equation 3-5

where F_{max} is the peak pull-out force, d is the cord diameter and L is the embedded length.

The average IFSS τ can be thus determined by the slope of best-linear fit of the peak pull-out force F_{max} against the embedded area πdL plot. A schematic illustration of the stress distribution is shown in Figure 3-10.

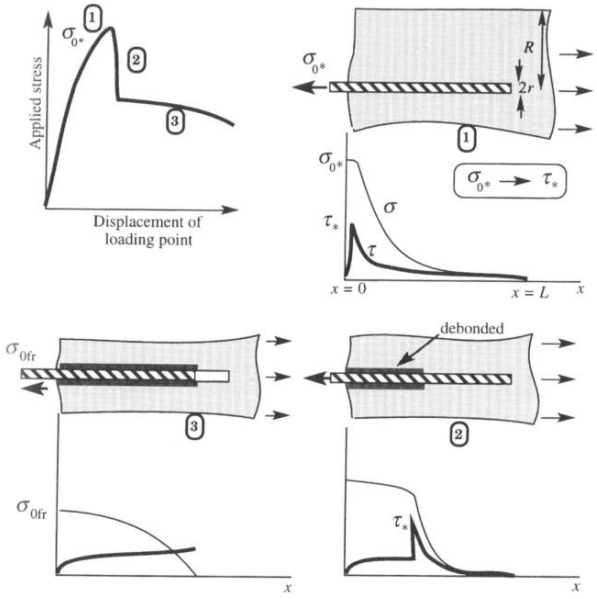

Figure 3-10. Schematic stress distribution and load-displacement plot during the single fibre pull-out test. Taken from Hull et al[3].

Single fibre push-out test

Single fibre push-out test was first introduced by Marshall [44] for interfacial characterisation of ceramic matrix composites. Several studies were carried out to numerically analyse the interfacial stress state for the single fibre push-out test [45, 46]. During the test, either pyramidal or flat end indenter can be employed with application of a progressively increasing compressive axial load to the top surface of

the embedded fibre until the fibre was protruded out from the bottom surface of the sample. Poisson's ratio effect, in this situation, raises the stress level corresponding to the frictional sliding. SEM micrographs of the sample morphology after the test is shown in Figure 3-11.

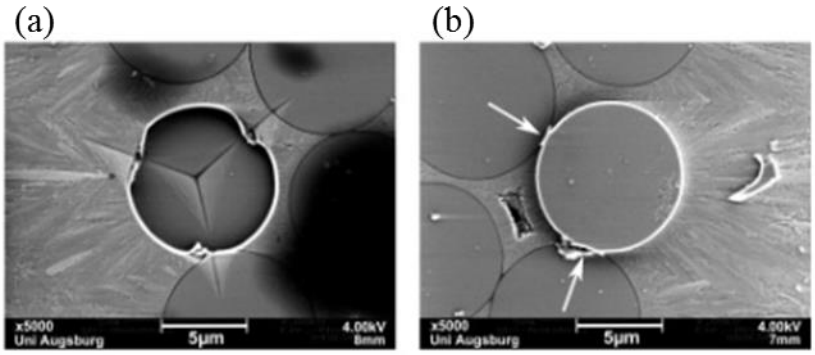

Figure 3-11. SEM images of SiC fibre in SiC matrix composites: (a) sample front side. The dark colour of the fibre indicates the push-out, (b) sample back side, showing the fibre protrudes from the surface. Taken from Mueller et al [47].

Full fragmentation test

In the fragmentation test, either a single fibre or multiple fibres are embedded in a matrix which is subjected to an axial tensile force. The fibres are fractured into small pieces until complete failure of the composite. The fragmentation process of a carbon fibre reinforced epoxy model composite is shown in Figure 3-12. The resulting longest fibre segment is considered as L_c of the examined system, therefore, the IFSS can be deduced from

$$\tau = \frac{\sigma_f^* d_f}{2L_c} \qquad \text{Equation 3-6}$$

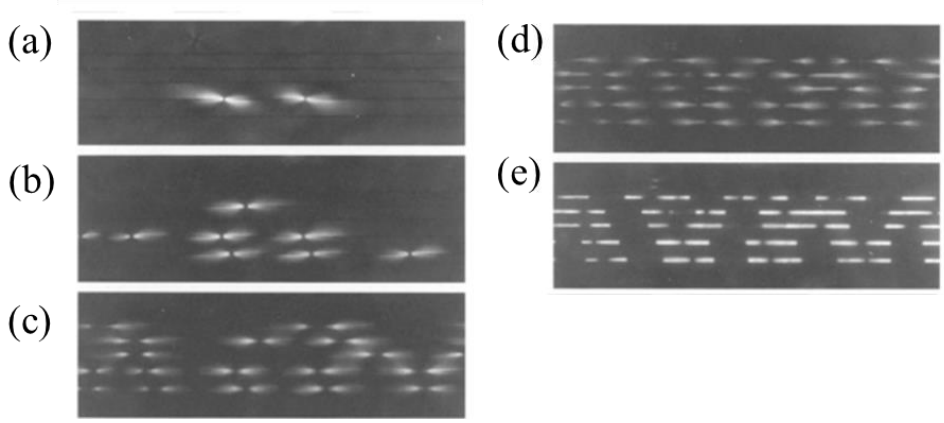

Figure 3-12. Polarized-light micrographs showing the failure process in a multi-fibre model composite containing five commercially surface-treated (100%) carbon fibres embedded in an epoxy matrix at an interfibre spacing of nine fibre diameters. The applied strains are: (a) 1.2%, (b) 1.5%, (c) 2.1%, (d) 2.7% and (e) 4.3% (failure of specimen), respectively. Taken from van den Heuvel et al [48].

Wang *et al*[49] also investigated the fragmentation process in a transparent single carbon fibre (T300) epoxy composites experimentally and numerically by finite element analysis to study the resulting stress redistribution in the fibre, matrix and interface, as shown in Figure 3-13. A good agreement was found between the experimental results and simulation analysis.

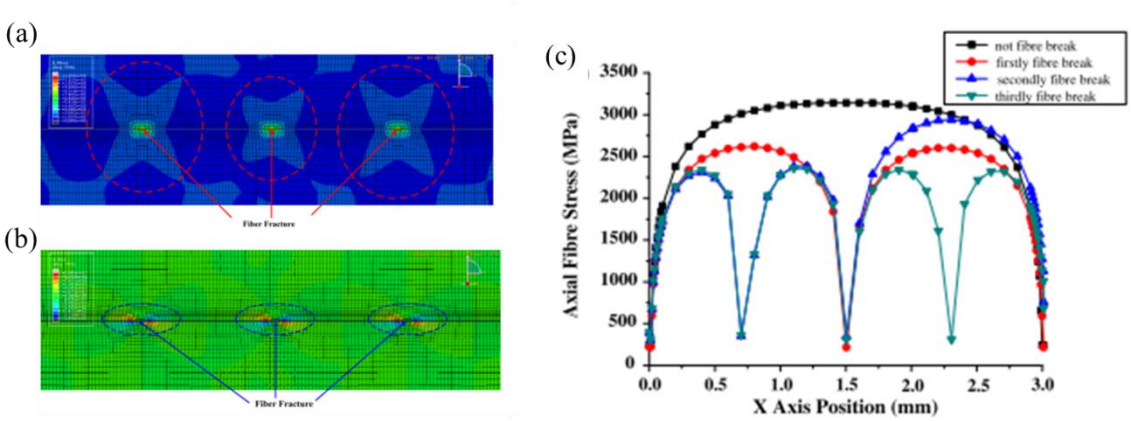

Figure 3-13. The contours of stress redistribution after fibre break: (a) the Von Mises stress in the matrix, (b) the shear at fibre/matrix interfaces, (c) fibre axial stress redistribution after fibre breaks. Taken from Wang et al [49].

Other indirect measurement of adhesion

Interlaminar shear strength (ILSS) measurements can be considered a qualitative evaluation of fibre / matrix adhesion despite of deficiency in relating ILSS to actual IFSS between individual fibre and the matrix. Except that, it implies the relative strength from the fracture morphology (fibre failure, matrix failure and bond failure), as shown in Figure 3-14, since the failure tends to happen at the weakest location.

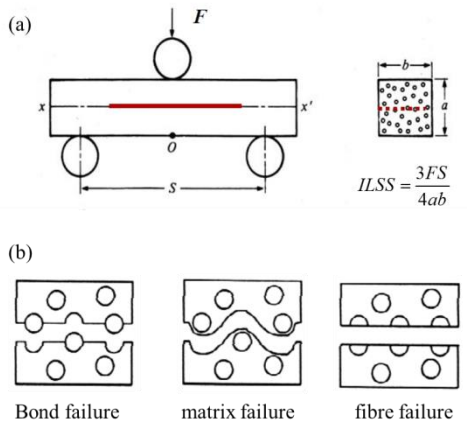

Figure 3-14. (a) Interlaminar shear strength measurement (ILSS), (b) the fracture morphology.

3.3.2 Adhesion of fibre materials to the rubber compounds

Nowadays, different types of cords are used in reinforced rubber products such as glass, aramid, nylon and polyester. For cotton, one of the first fibres used in rubber, the only treatment necessary for achieving a good adhesion is a drying process. Cotton fibres have a surface with filaments sticking out of the surface of the fibre, leading to mechanical anchoring to the rubber matrix. However, the adhesion between synthetic fibres and rubbers is always low due to their smooth surfaces and low chemical reactivity (to rubber polymer molecules) [50]. Resorcinol formaldehyde latex (RFL) standard adhesive treatment method, dating back to 1935 [51], is typically utilised to promote cord-rubber adhesion, where the latex phase is to co-vulcanise with the rubber

matrix whereas the resorcinol formaldehyde resin phase is to bond preferably with textile through hydrogen bond [50, 52, 53], as shown in Figure 3-15.

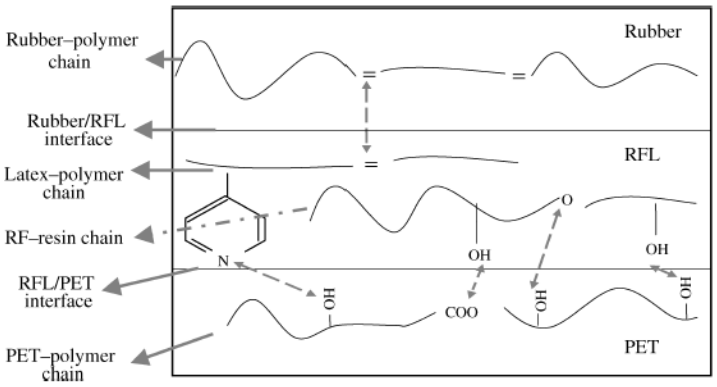

Figure 3-15. Possible interfacial reactions between the functional groups of polyethylene terephthalate (PET) fabrics, RFL and rubber as indicted by double arrows. Taken from Jamshidi et al[51].

W.B. Wennekes [53] investigated the fundamental knowledge of the physical and chemical processes involved in the adhesion between RFL-treated aramid cords and the rubber and how RFL formulations influence the adhesion systematically. Recently, UV-assisted chemical modification of PET fabrics [54] and silane coupling agent treatment [55] prior to RFL dipping process were used to improve the fabric-rubber adhesion.

Schematic representations of preparation of RFL treatments for various fibres and the general layout of the fibre treatment for a two dip system are shown in Figure 3-16 and Figure 3-17 respectively. It should be noticed that a pre-dip treatment made from highly active isocyanates in an organic solvent becomes necessary if the fibre itself lacks polarity or hydrogen groups such as polyester and aramid where the bulk aromatic groups sterically hinder the amide functionalities.

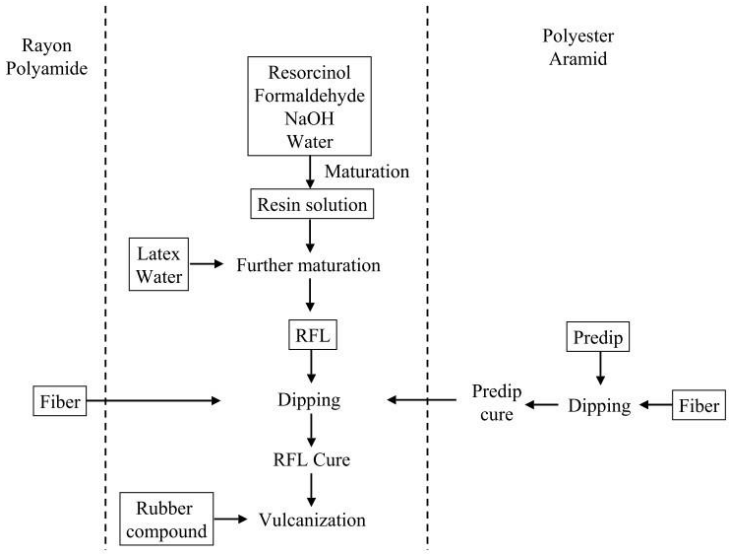

Figure 3-16. Schematic representation of RFL treatments for various fibres. Taken from Wennekes [56].

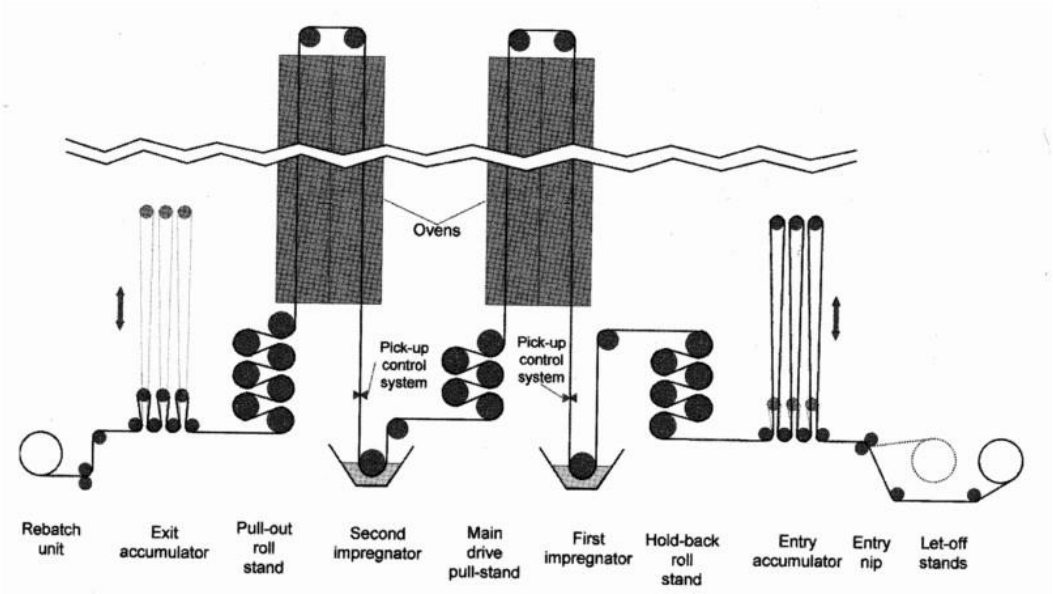

Figure 3-17. General layout of the fibre treatment for a two-dip system. Note: the cord is moving from right to left. Taken from Wootton et al [57].

3.3.3 Interfacial adhesion evolution of cord-rubber composites during dynamic loading

Since the cord-rubber composites such as the tire and synchronous belts are often subjected to the repeated loading in the service conditions, the dynamic effects on the adhesion evolution between the cord and the rubber is more of particular interest than static bonding in terms of prevention from interfacial debonding.

Langevin *et al.*[58] studied the steel cord to rubber adhesion under periodic shear stress on a Firestone Flexometer and examined the influence of rubber properties such as hysteresis as well as heat resistance on the cord-rubber interfacial properties. More recently, Shi *et al.* investigated the adhesion evolution in polyester cord - natural rubber (NR) composites as well as steel cord - NR composites by pull-out tests after cyclically loading those composites at varying testing frequencies, temperatures and pre-defined number of cycles [59]. They also assessed the effect of various adhesion promoters and cyclic testing conditions [60, 61] to reach satisfactory lifetime. Valantin *et al.*[52, 62] studied the effect of fatigue loading on interfacial properties in unidirectional polyamide cord - rubber composites including peeling strength, resorcinol formaldehyde latex (RFL) / textile delamination, RFL / rubber debonding and indentation modulus across the textile / rubber interface after selected fatigue cycles.

3.4 Influences of different variables on the fatigue behaviour of cord-rubber composites

Although a large amount of work has been devoted to understand the fatigue behaviour and life prediction of the fibre reinforced plastics (FRPs) in the form of nano-/micro - particle reinforced [63, 64], short-fibre reinforced [65], unidirectional

long fibre reinforced [66], or laminates [67], rather limited efforts were made on cord-rubber composites. In this section, studies concerning the dependence of fatigue life of cord-rubber composites on different factors are reviewed, aiming to gain a better understanding of the fatigue behaviour of cord-rubber composites.

3.4.1 The effect of specimen size, cord angle, ply lay-up and cord spacing

Lee *et al.* assessed the effect of the specimen size on the tensile fatigue behaviour of a 19 mm wide angle-plied nylon cord elastomer composite laminate $[+38/-38°]_{2s}$ with length-to-width ratios (*L/W*) of 5.3, 4.0, 3.3 and 0.5 in the load-controlled cyclic tests [68]. It showed that the coupons with *L/W*=0.5 failed in the form of fibre fracture whilst the samples of other three different *L/W* ratios failed in delamination due to the geometric restriction. Since the fibres were embedded off-axis (at a cord angle of 38°) under axial tensile loading, matrix dominant failure processes (debonding and matrix cracking lead to delamination) is the main failure mode and fibre fracture will never occur unless most of the fibres were gripped at both ends, where the *L/W* ratio is less than 1.28 (Cotangent (cot) 38°). Furthermore, the specimens having higher *L/W* ratios were found to have a shorter fatigue life, resulting from a larger interply strain in the middle of the longer specimens, as shown in Figure 3-18. However, it should be noted that variations in fatigue life induced by different *L/W* ratios were close to data scatter range.

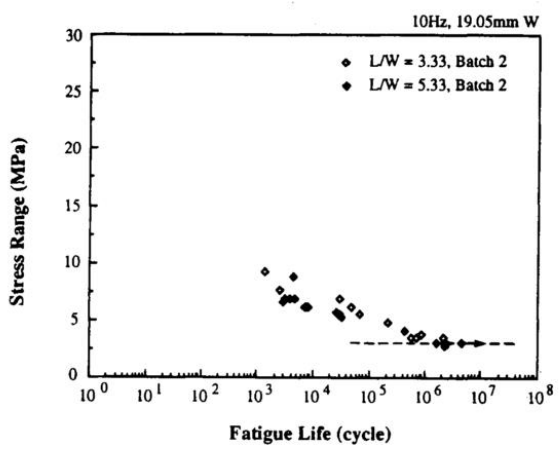

Figure 3-18: Stress range against fatigue life of the nylon cord elastomer matrix laminate $[+38/-38°]_{2s}$, showing slight reduction in fatigue life of specimens with a larger *L/W* ratios. Taken from Lee et al [68].

Song et al. [69] continued to investigate the cord reinforcement effect including the ply lay-up, cord construction and cord angle. Table 3-1 listed the samples employed in their study. 4-ply lay-up was introduced to order to diminish the possible twisting action which happens in the 2-ply lay-up, as shown in Figure 3-19.

Table 3-1. Specimen compositions and static strength data used in the study of Song et al [69].

ID	Cord construction	Compound	End count	Cord angle	Interply insert	Ply	Static strength Kgf/mm width	MPa
C1	3+9+15X.22	MAC2-SVI	45	+19/-19°		2	26.4	61.3
C7	3+9+15X.22	MAC2-SVI	45	+19/-19°	rubber A	2	30.8	59.5
C15	3+9+15X.22	MAC2	45	+19/-19°		2		
C17	3+9+15X.22	MAC2	45	+19/-19°		4		
C3	3+9+15X.22	MAC2-SVI	45	+19/-19°		4	49.5	56.6
C4	3+9+15X.22	MAC2-SVI	45	+25/-25°		4	36.6	42.7
C19	3+9+15X.22	MAC2-SVI	45	+38/-38°		4		
C2	3/6X.35	MAC2-SVI	48	+19/-19°		2	25.8	59.3
C8	3/6X.35	MAC2-SVI	48	+19/-19°	rubber A	2	29.1	56.2
C5	3/6X.35	MAC2-SVI	48	+19/-19°		4	47.3	54.4

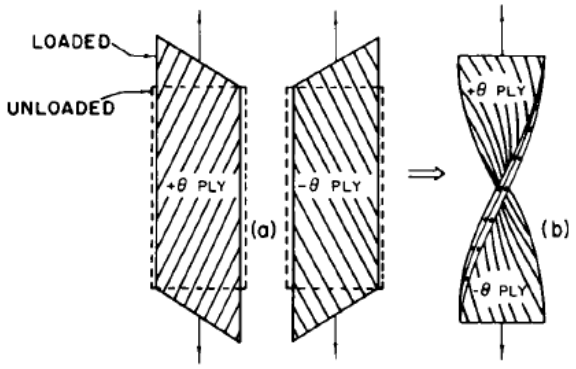

Figure 3-19. Deformation patterns that occur in off-axis loading of (a) individual plies at $+\theta$ and $-\theta$ cord angles, (b) two-ply $\pm\theta$ laminate, taken from Walter et al [70].

It was revealed that 4-ply composite laminates exhibited significantly higher lifetime compared to that of 2-ply composite laminates at a given stress range regardless of the cord construction, as shown in **Error! Reference source not found.**.This was attributed to the higher level of static tensile strength in terms of load per unit length, as shown in Table 3-1. Similarly, the samples with larger cord angles have a shorter fatigue life (Figure 3-21 (a)) due to the reduced virgin strength despite the fact that the $[+19/-19°]_{2s}$ laminate exhibited the largest interply shear strain as depicted in Figure 3-12 (b).

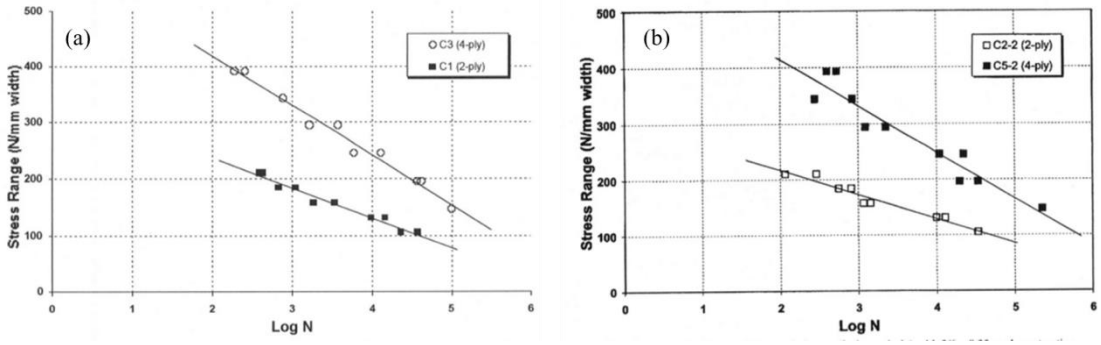

Figure 3-20. S-N data for two different ply lay-ups (2-ply versus 4-ply) with cord construction (a) 3+9+15×0.22 and (b) 3/6×0.35. Taken from Walteret et al [70].

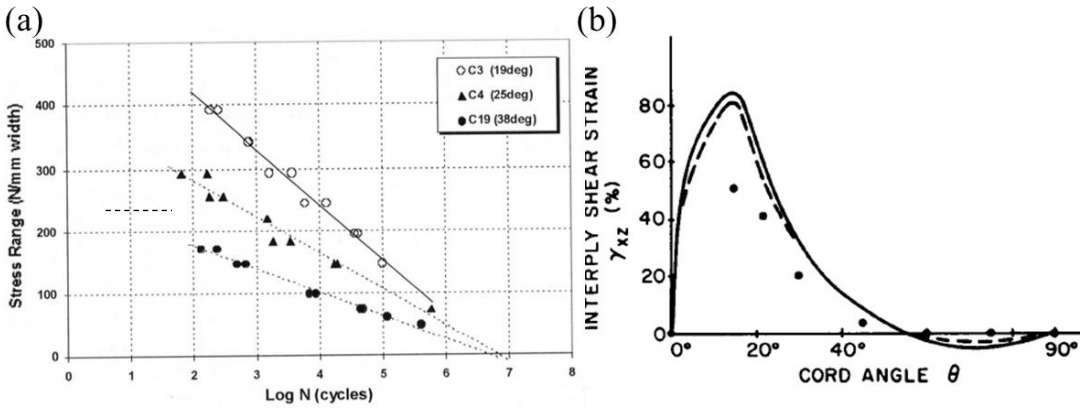

Figure 3-21. (a) S-N data of the nylon cord elastomer matrix laminate for three different cord angles (19°, 25° and 36°), showing samples with larger cord angles have a shorter fatigue life, (b) comparison between theoretical predicted (——， Kelsey; ----, Puppo and Evensen) and experimental measured (●, Lou and Walter) values of interply shear strain as a function of the cord angle θ for 2-ply 110/2 polyester-rubber laminate at 10% axial extension. Taken from Walter et al [70].

Interestingly, the S-N data was merged into one single trend when normalised by the static tensile strength either in different ply layups or different cord angles, as shown in Figure 3-22, indicating the same fatigue failure mechanism.

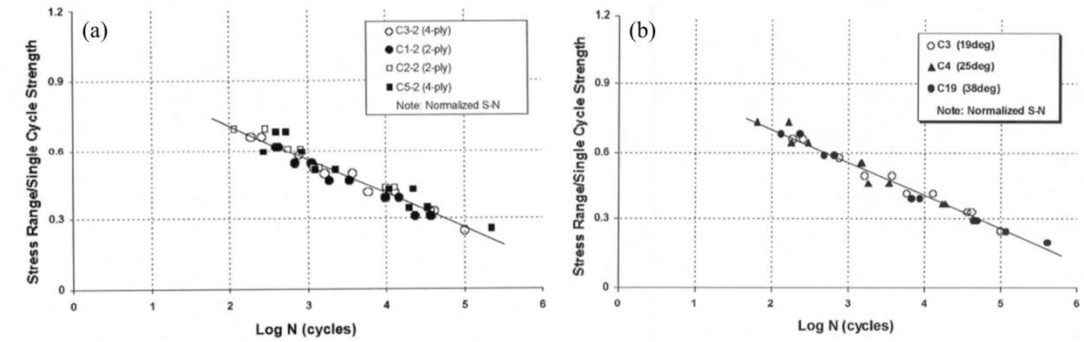

Figure 3-22. Normalised S-N data for different (a) ply lay-ups and (b) cord angles. Taken from Walter et al [70].

Moreover, the crack tended to be highly constrained by the wire reinforcements [71]. The steel wire reinforced NR composites specimens with narrower wire spacing can suppress the crack tip deflection more efficiently at non-relaxed conditions. As a consequence, the crack growth was retarded.

3.4.2 The effect of the frequency

Frequency effect is of particular interest regarding the fatigue behaviour of cord-rubber composites. The self-heating effect, owning to viscoelastic nature of the matrix [67, 72] (the low heat conductivity and high damping factor particularly for rubbery matrix) and frictional heating effect generated from specimen and device [73], give rise to its complexity.

Though studies based on the FRPs shed some light on the frequency influence, the conclusions are not always consistent, depending on the types of materials tested and the loading parameters employed in each study. In general, the cycles to failure increased with frequency up to a certain level and then decreased due to the self-heating [74]. However, Zhou *et al.*[64] reported the fatigue life of the 40 wt % talc-filled polypropylene (PP) increased with frequency up to 2 Hz and then decreased but did not appear to be frequency-sensitive above 5 Hz at 80% and 85% yield strength respectively. Further increasing the frequency to 10 Hz and 20 Hz, the failure mode changed to the thermal failure in a form of thermal softening and necking, as shown in Figure 3-23. In the highest frequency, the heat generated under fatigue loading was large enough to melt the PP matrix.

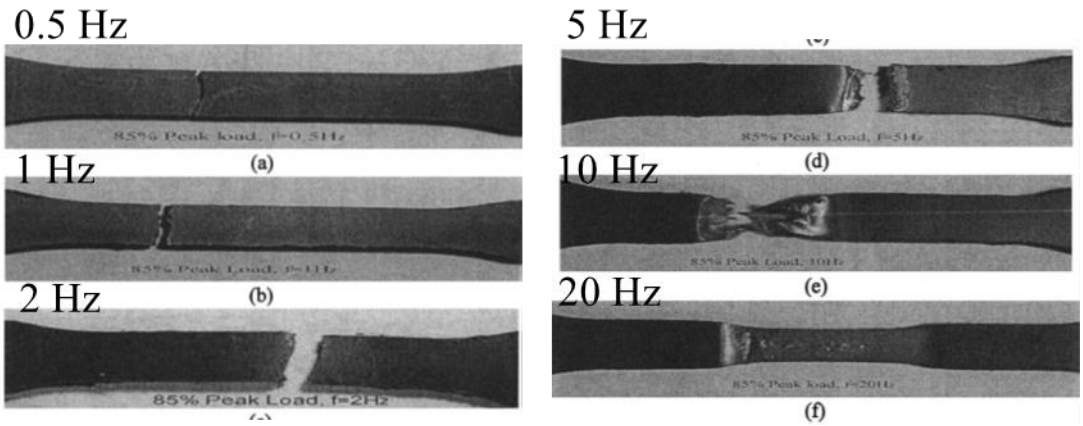

Figure 3-23. Failure images of the 40 wt % talc-filled PP fatigue specimens tested at different cyclic frequencies and at peak cyclic load equivalent to 85% of the yield strength: (a) 0.5 Hz,(b) 1 Hz,(c) 2 Hz, (d) 5Hz,(e) 10 Hz and (f) 20 Hz. Taken from Zhou et al [64].

Kotik *et al.*[67] found the frequency sensitivity was large at small stress amplitude for the short-beam shear (SBS) fatigue behaviour of glass fibre reinforced polyester laminates while the variation in fatigue life was not significant for the frequency range (1, 3, 6 and 10 Hz) used in their study based on the statistical analysis. At the lowest stress amplitude, the mean life was larger at larger frequencies. However, the results at intermediate stress amplitude led to opposite trend, as shown in Figure 3-24. They attributed this contradiction to the limited test data or to a rate-dependent effect.

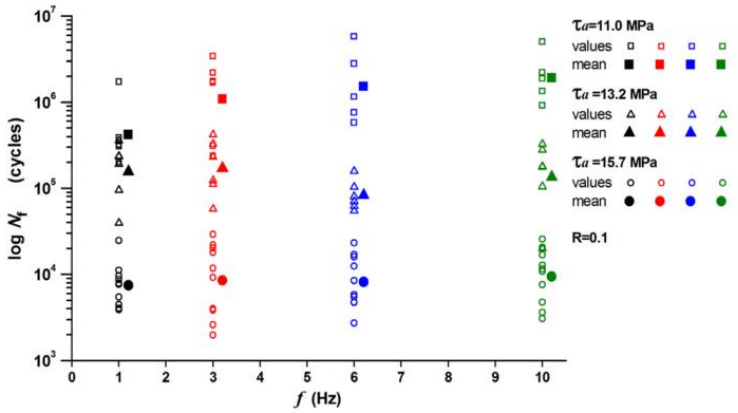

Figure 3-24. SBS fatigue life as a function of loading frequency. Taken from Kotik et al [67].

Lee *et al.*[68] demonstrated that the use of higher frequency led to a reduced fatigue life of nylon fibre reinforced rubber composites life at the same level of stress amplitude in their testing domain (1, 5 and 10Hz) due to hysteresis loss with the specimen temperature rise by up to 90 °C at 10 Hz as well as a higher strength degrading rate reflected from a rise in the slope of the S-N curves.

Figure 3-25 shows the temperature built up at a faster rate at 10Hz than that at 1Hz and reached the plateau at lower stress range even at higher frequency as the heat generated was balanced by the surrounding environment. In addition, the higher frequency appeared to lower the fatigue limit, as illustrated by Figure 3-26. Similar finding was also reported in [75] for a short glass fibre reinforced polyamide 6. It was noted that the frequency had negligible effect on the number of cycles of the onset of the debonding.

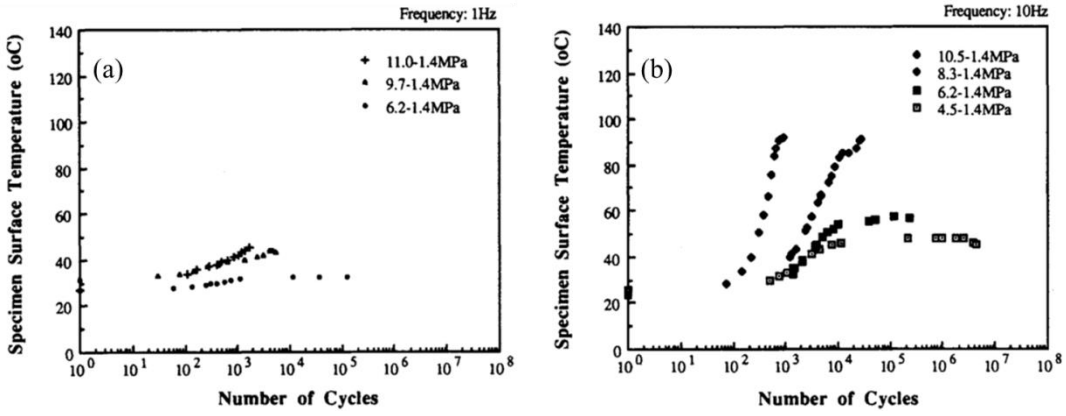

Figure 3-25. Sample surface temperature as a function of the number of cycles for the nylon fibre reinforced elastomer matrix composite at (a) 1Hz and (b) 10Hz. Taken from Lee et al [68].

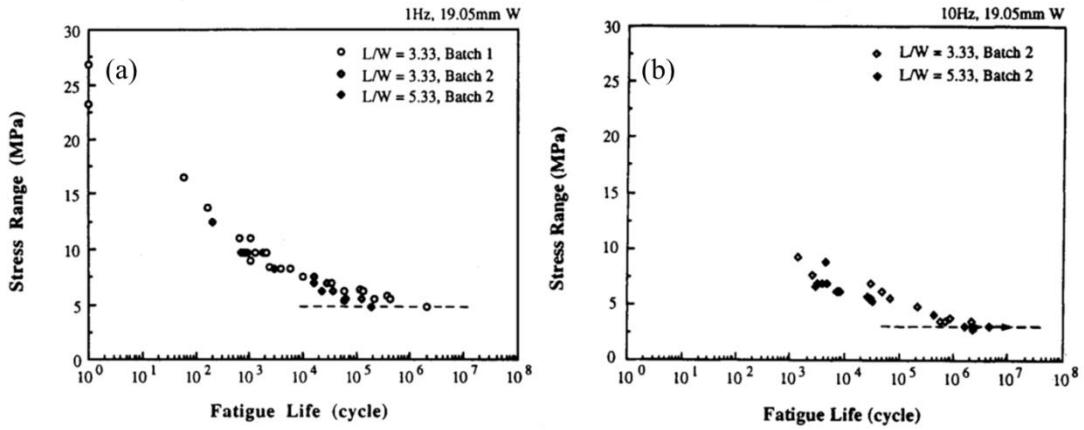

Figure 3-26. The effect of frequency on the fatigue endurance limit: S-N data at (a) 1Hz and (b) 10Hz. Taken from Lee et al [68].

3.4.3 The effect of *R* ratio

R ratio is defined as the ratio of minimum to maximum cyclic stress. Different from metallic materials whose fatigue life decreases with the increasing of *R* ratio due to reduction in crack closure effect at higher *R* ratio [76], the usage of higher *R* ratio often has a beneficial effect on the fatigue resistance of fibre reinforced composites. Kawai *et al.* investigated *R* ratio dependence of three kinds of multidirectional carbon fibre reinforced plastic (CFRP) laminates with $[45/90/-45/0]_{2s}$, $[0/60/-60]_{2s}$ and $[0/90]_{3s}$ lay-ups under tension-tension (T-T), tension-compression (T-C) and compression-compression (C-C) cyclic loading [77]. It was observed that fatigue life increased with increasing *R* ratio at a given maximum cyclic stress in T-T section. There was no obvious *R* ratio dependence in C-C section where the S-N data at R =2 and R = 10 overlapped with each other. The slope of S-N curve at C-T section was the steepest, indicating the highest sensitivity of changes in fatigue strength of those materials when loaded in C-T section. Typical S-N data of CFRP laminates with $[45/90/-45/0]_{2s}$ lay-up under three different loading modes is shown in Figure 3-27.

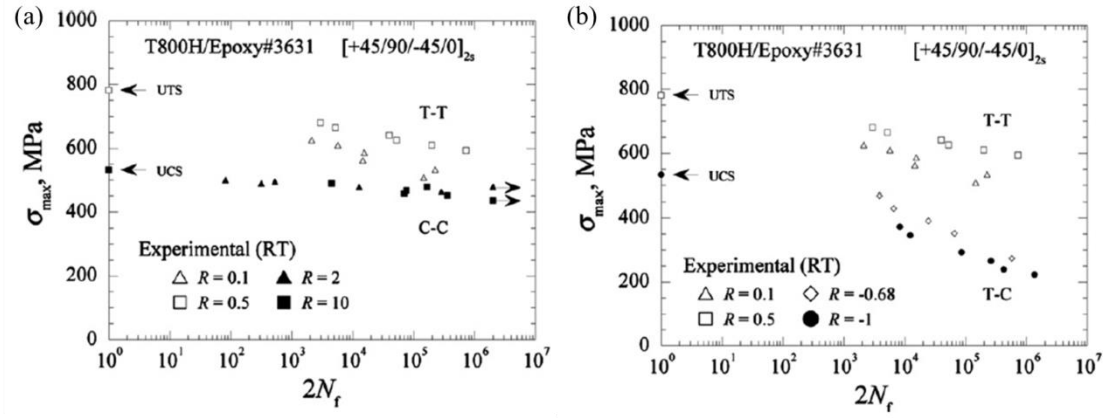

Figure 3-27. S–N relationships for CFRP laminate $[45/90/-45/0]_{2s}$ at room temperature: (a) T–T (R = 0.1 and 0.5) and C–C (R = 2 and 10) fatigue loading, (b) T–T (R = 0.1 and 0.5) and T–C (R = -1 and -0.68) fatigue loading. Taken from Kawai et al [77].

Similar improvement in fatigue life by increasing R ratio was also found in the T-T section by Gathercole *et al*. [78], as shown in Figure 3-28.

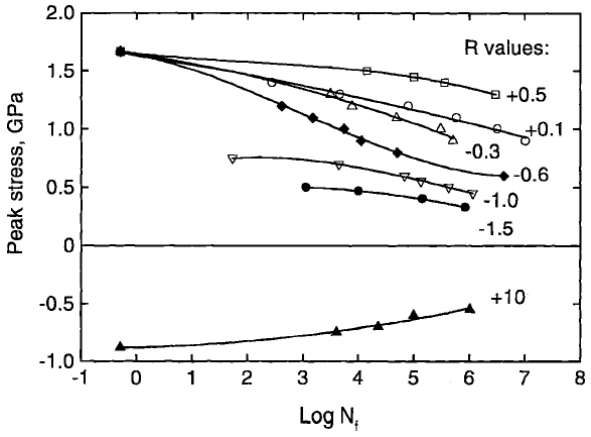

Figure 3-28. S-N curves for a CFRP laminate $[(\pm 45,0_2)_2]_s$ at various R ratios. Taken from Gathercole et al. [78].

In terms of cord-rubber composites, Ku *et al.*[79]studied the effect of minimum stress σ_{min}on the fatigue behaviour of a nylon fibre reinforced elastomer at a given

stress range Δσ. It was noted that there is a positive correlation between σ_{min} and R for a constant amplitude test ($R = 1/(1 + \Delta\sigma/\sigma_{min})$). Their study revealed that the use of minimum stress led to a longer life time up to a critical minimum stress level, beyond which an opposite trend was found, with a shorter fatigue life occurring at a given stress range (Figure 3-29).

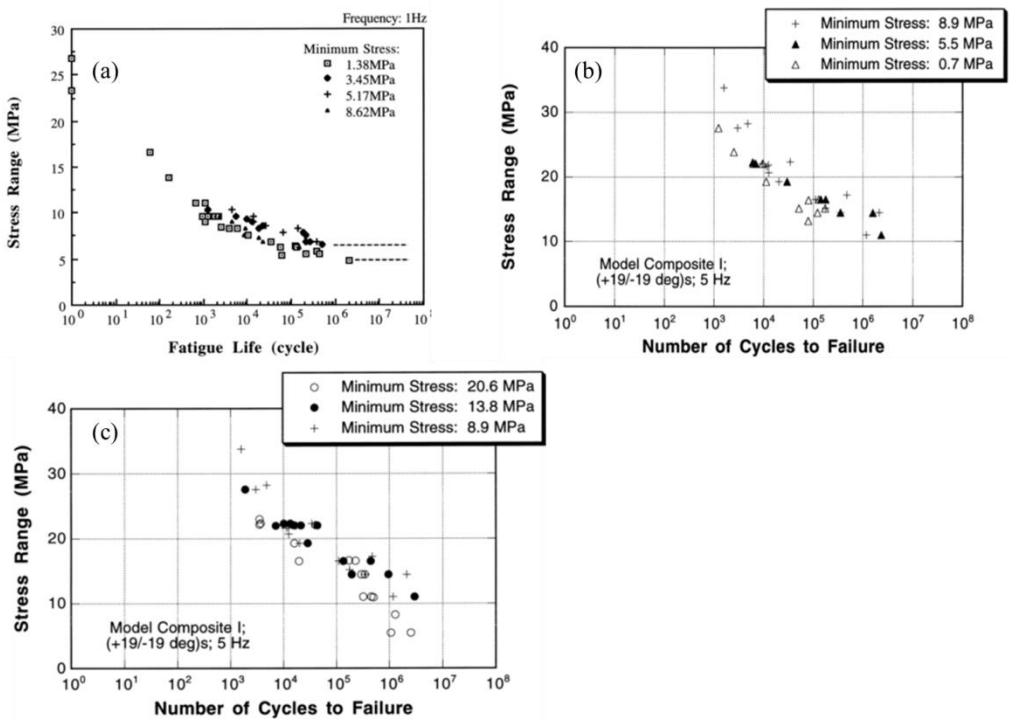

Figure 3-29. Effect of minimum stress on (a) the nylon cord reinforced composite from bias aircraft tire carcass, (b) and (c) model composite reinforced with steel wires. Taken from Ku et al [79].

This minimum stress effect stemmed from the nonlinear stress-strain behaviour of the cord-rubber composites exhibiting strain stiffening. A shorter strain range was experienced at the same applied stress range when the level of the minimum stress was raised, as shown in Figure 3-30 (a). As a result of a shorter strain range, there was less mechanical work or hysteresis thus less chance of damage accumulation in form of cord-rubber debonding. However, with minimum stress exceeding the stress at the

knee point, where the cord-matrix debonding process starts (Figure 3-30 (b)), the cracks were less likely to have complete closure during the unloading portion of each cycle due to higher level of minimum cyclic stress, leading to the increased damage potential. Due to these two contradicting trends, the S-N curve initially shifted to the longer life region roughly up to the knee point and afterwards moved back to the shorter life region when the damage potential became dominant.

It can be implied by Ku's investigation that a consistently shorter fatigue life of such cord-rubber composites could be observed at a given strain range with higher level of applied minimum strain. This is due to the fact that a larger stress range will always be expected (Figure 3-30(c)) and the damage potential keeps increasing at ahigher minimum strain level in a strain-controlled fatigue test.

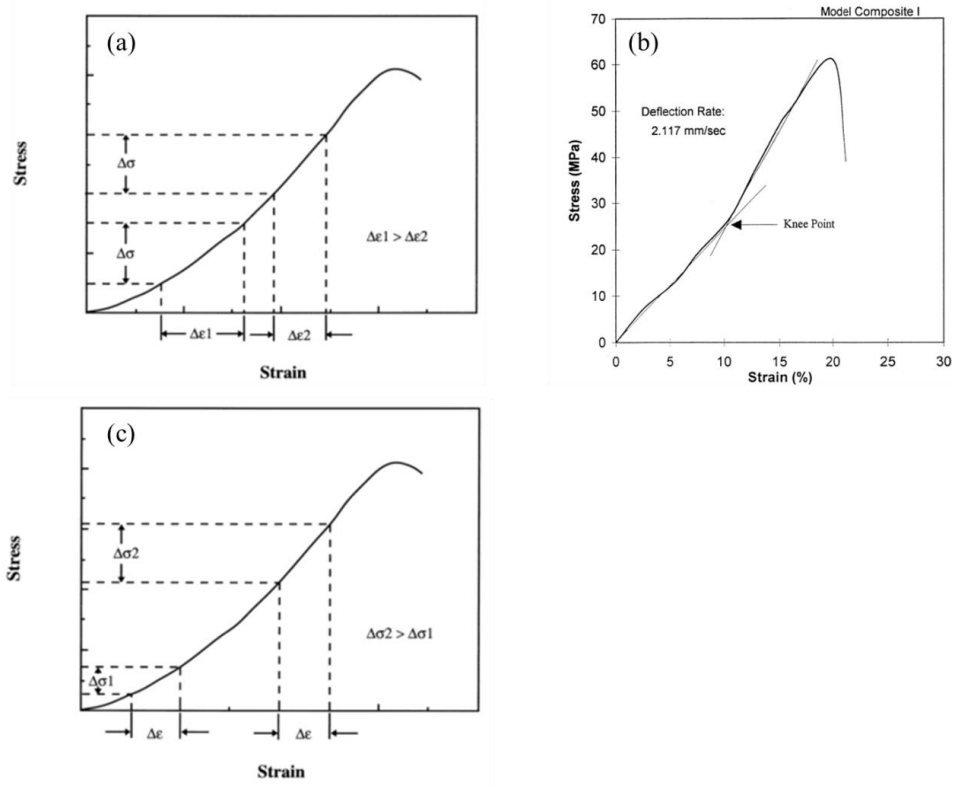

Figure 3-30. Typical tensile stress-strain curve for the cord-rubber composite with (a) strain response at the given stress range $\Delta\sigma$, (b) the definition of knee point in the static tensile stress-strain curve, (c) stress response at the given strain range $\Delta\varepsilon$. Taken from Ku et al [79].

Kawamoto [71] investigated the effect of *R* ratio on the fatigue crack growth (FCG) behaviour of continuous steel wire reinforced NR composites with and without carbon black. It was found that the FCG rate was slower at higher *R* ratio. And further SEM observation of the crack tip showed the increased extent of the surface roughness due to strain induced crystallisation (SIC) of NR and strain induced carbon black orientation. The highly orientated structure crystals exhibited higher crack resistance in the direction perpendicular to its orientated direction whilst less resistance parallel to the orientated structure, leading to the crack deflection.

Seichter *et al.*[80, 81] investigated the FCG behaviours of both rubber blends and textile-rubber composites using pure shear tests. The textile were coated with RFL and one ply of the textile was symmetrically embedded between two rubber layers. The overall geometry was shown in Figure 3-31 with small beads at the top and bottom of the specimen for the purpose of clamping. Table 3-2 listed the strength and nominal elongation at break of the textile–rubber composites, pure rubbers, and textiles used in their study.

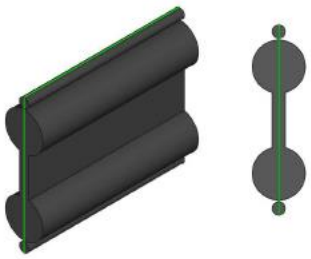

Figure 3-31. Specimen geometry for FCG tests. Taken from Seichter et al [81].

Table 3-2: Strength σ_{max} and nominal elongation at break ε_{break} of textile–rubber composites, pure rubbers (1616, 1620) and textiles (PE270, EP100, EE100). Taken from Seichter et al [81].

	1616_PE270	1616_EP100	1616_EE100	1616
$\varepsilon_{\text{break}}$	63 %	82 %	79 %	276 %
σ_{max} / N/mm^2	17.9	41.8	36.5	8.8
	1620_PE270	1620_EP100	1620_EE100	1620
$\varepsilon_{\text{break}}$	59 %	110 %	88 %	467 %
σ_{max} / N/mm^2	17.7	37.2	33.0	10.1
	PE270	EP100	EE100	
$\varepsilon_{\text{break}}$	29 %	30 %	23 %	
F_{max}/w	62.1 kN/m	153.9 kN/m	154.4 kN/m	

The results showed that the FCG rates of the textile-rubber composites were lower than that of the pure rubber materials at a given tearing energy, owning to stiffening effect of the textile reinforcement which hinders the crack propagation. Additionally, there was no distinctive difference in the FCG rate either in the case of the different textiles-same rubber blends or the different rubber blends-same textiles, as depicted in Figure 3-32. It was noted that the crack developed in a different manner, that is, the crack growth ceased after the first 50000 cycles in the case of rubber-textile composite materials whilst it grew continuously for the case of the pure rubber blends. The initial growth happened in the rubber-textile composites was caused by the less effective crack termination effect entailed by the weakened but not completely dissected cords by introducing an artificial notching before FCG tests. After the complete rupture of those damaged cord, the rest of the intact cords hindered the further propagation of the crack in a more efficient way.

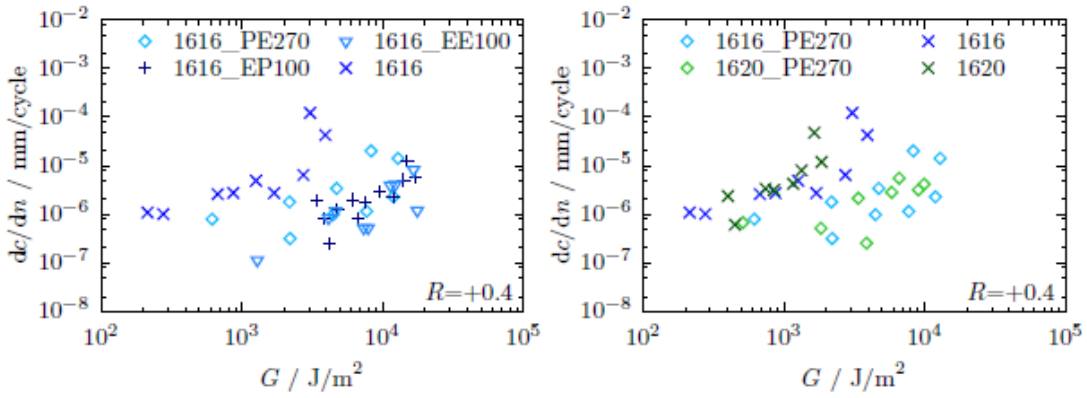

Figure 3-32. FCG tests results for rubber blends and rubber-textile composites.Taken from Seichter et al[81].

Strain induced crystallisation (SIC) of the HNBR

Since the first discovery of strain induced crystallisation (SIC) of NR by Katz in 1925, a large amount of research [8-10, 82, 83] was conducted to study the kinetics of SIC and the corresponding energy dissipation. Real-time wide-angle X-ray diffraction (WAXD) of unfilled vulcanised NR sample was developed to study the structural evolution, as shown in Figure 3-33.

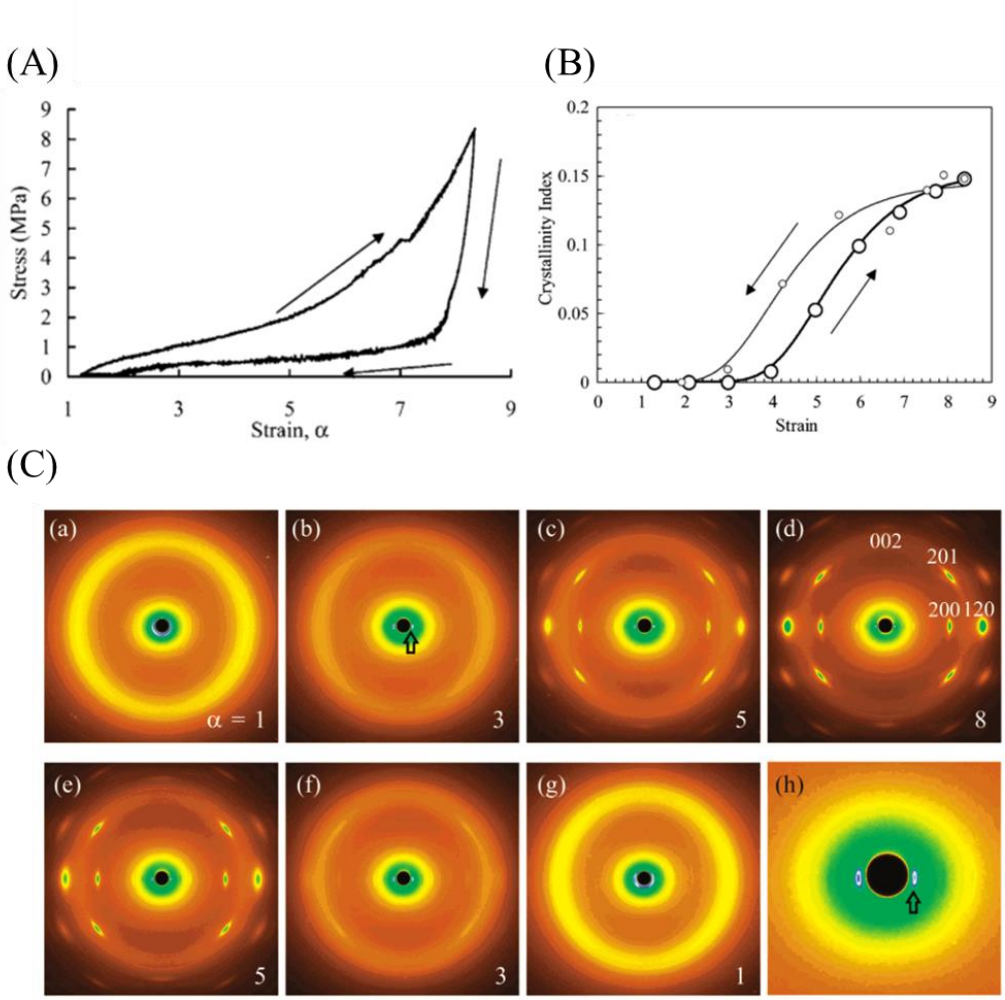

Figure 3-33. (A) Tensile stress-strain curve of unfilled vulcanised NR sample, (B) variation of crystallinity index during loading and unloading, (C) WAXD pattern change of vulcanised NR by synchrotron X-ray diffraction measurements: (a)-(d) represent loading and (d)-(h) represent unloading, with α indicating the elongation of NR sample. Taken from Tosaka et al [9].

In contrast, strain induced crystallisation (SIC) of the HNBR has not received much attention until late 20th century. Braun *et al* [84] reported copolymers with low acrylonitrile (ACN) content (< 30 wt.%) and high ACN content (40-50 wt. %) can crystallise either thermally or upon drawing. Figure 3-34 shows the thermal transition behaviour of HNBR with an ACN content of 18, 27, 34, 38, 43 and 48 wt. %.

Moreover, the crystallisation behaviour of a fairly alternating copolymer HNBR with 48 wt. % ACN content was studied. It was found SIC commenced suddenly at elongation $\lambda \cong 2$ at room temperature. A unit cell with a = 0.5 nm, b = 0.36 nm and c = 0.77 nm was proposed in their study. Crystallinity was developed due to the alternating sequence of hydrogenated butadiene (BD) and ACN at the high content of ACN whilst it was attributed to long sequences of tetramethylene units at low ACN content [14]. Kobatake [85] also reported that at least 5 tetramethylene units were required in order to render crystallinity upon stretching for HNBR containing low ACN content.

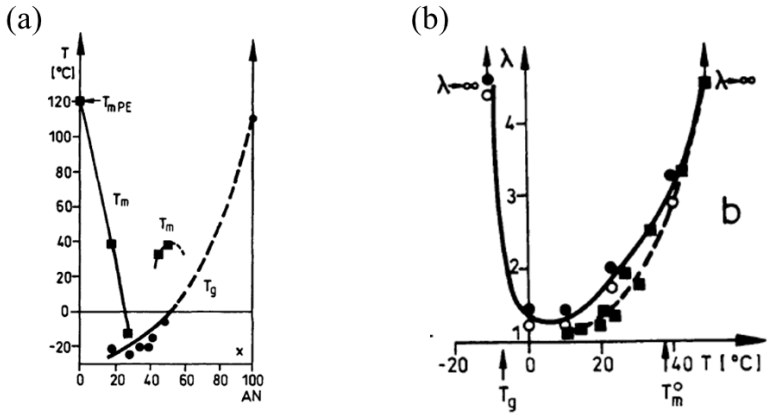

Figure 3-34. (a) Glass transition temperature T_g (●) and melting temperature T_m (■) for HNBR with various ACN contents, polyethylene (PE) and polyacrylonitrile, (b) elongation λ of beginning crystallisation as a function of temperature in HNBR with 48 wt. % ACN. Taken from Braun et al [84].

However, Bielinski *et al.*[86] revealed that dicumyl peroxide (DCP) cured HNBR containing 33.5 wt. % ACN content exhibited a small degree of ordering even before elongation and the crystallinity was further induced upon drawing. The WAXD spectrum indicated two characteristic diffraction angles, 2θ=19° and 23°, as shown in Figure 3-35.

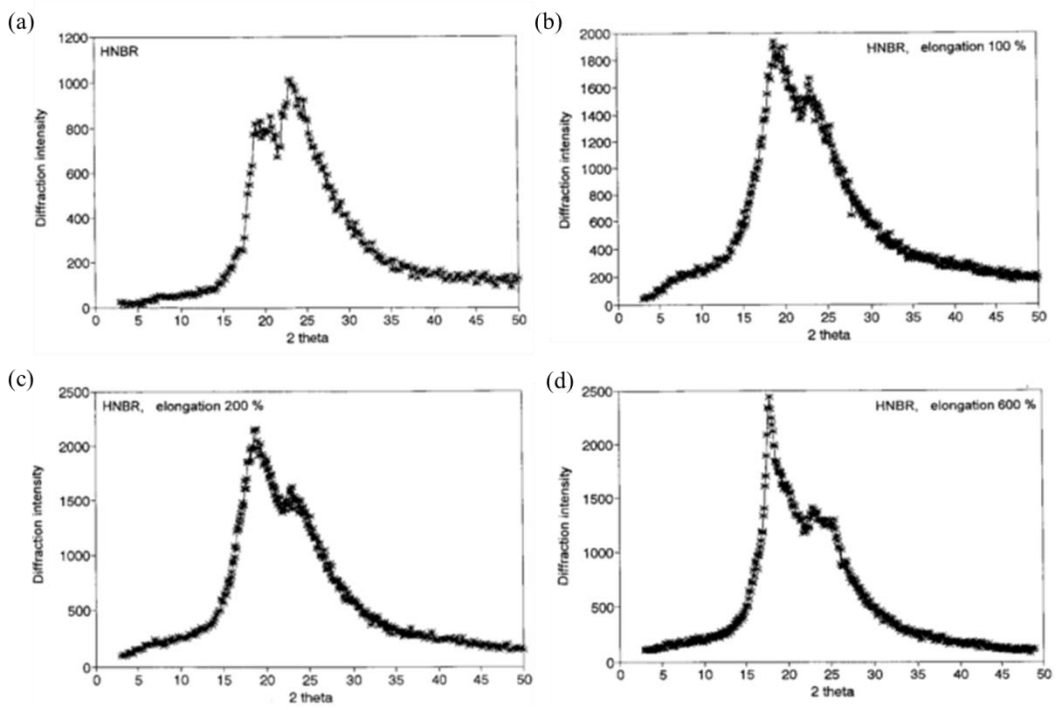

Figure 3-35. WAXD pattern of DCP cured HNBR with 33.5 wt. % ACN: (a) virgin sample, (b) 100 %elongation, (c) 200% elongation and (d) 600% elongation. Taken from Bielinski et al [86].

Severe and White [87] investigated the crystallisation behaviour of HNBR containing varying ACN contents using DSC. It was observed that DSC scan of unstretched sample only revealed a step change T_g without the presence of melting transition. A significant crystallinity, however, can be developed by annealing the HNBR at low temperature for certain period of time (that is at 0 °C for 3 month in their study) even for the case of HNBR with low ACN content, as shown in Figure 3-36. It was later confirmed that HNBR with 49.9 wt. % and 42 % ACN content at a stretching ratio of 600% show sharp spots in WAXD pattern though HNBR with 16.35wt. % ACN showed no sign of crystallisation upon drawing, as shown in Figure 3-37.

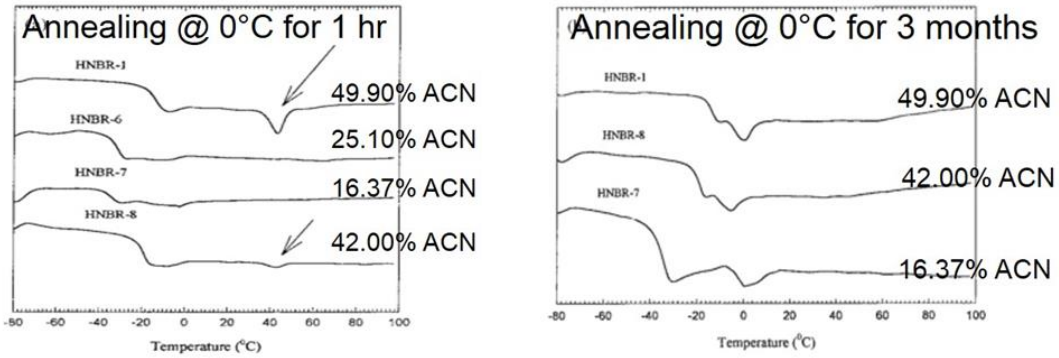

Figure 3-36. DSC curves of HNBR with various ACN content after annealling. Arrow indicates the endotherm melting peak. Taken from Severe and White [87].

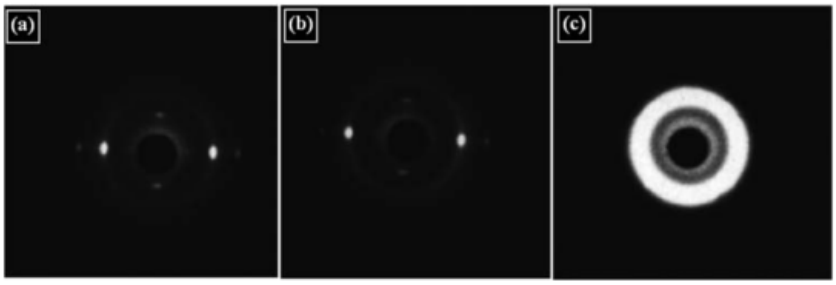

Figure 3-37. WAXS pattern for HNBR stretched at 600% elongation: (a) HNBR-1 (49.9 wt. % ACN), showing diffused halo and sharp spots, (b) HNBR-8 (42 wt. % ACN), showing sharp reflections, (b) HNBR-7 (16.35 wt. % ACN), showing diffused halo with no distinctive spot or arc. Taken from Severe and White[87].

Alcock *et al.*[88] analysed the cold crystallization behaviour of HNBR with 36% ACN content and 96% saturation using DSC. Surprisingly, an increase in crystallinity was found in the cases of exposure to low temperature near or even well below T_g (= -19 °C) for pre-determined periods (up to 48 h), as shown in Figure 3-38.

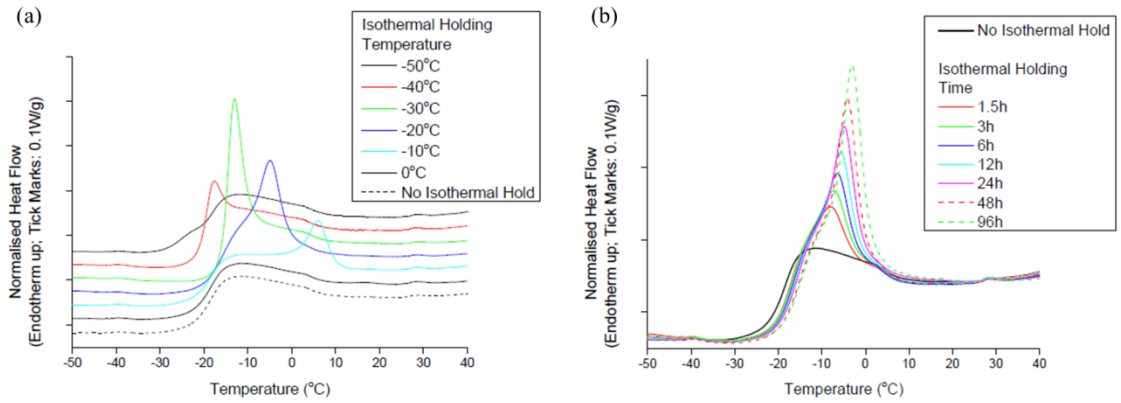

Figure 3-38. DSC traces of HNBR: (a) exposure to various isothermal holding temperatures for 24 hrs, (b) various isothermal holding time at an isothermal holding temperature at -20 °C. Taken from Alcock et al [88].

Unfortunately, very few studies were performed to detect the real time SIC of the HNBR compounds. Very recently, the dependence of crystallinity on the stretch ratio at three temperatures (20 °C, 30 °C and 40 °C) of the HNBR with 44 wt.% ACN (HNBR-44) was first studied *in situ* by Ulu and the coworkers [89]. The specimens were mounted on a dynamic tensile tester accompanying by the simultaneous WAXS measurements. It revealed that the stiffening of the materials was strongly related to the onset of the SIC, which occurred at 250 % strain at 20 °C and 350% strain at 40°C.

In addition, the melting of the crystallites during unloading appeared to take place at a lower stretch ratio than the onset of the SIC, as shown in Figure 3-39.

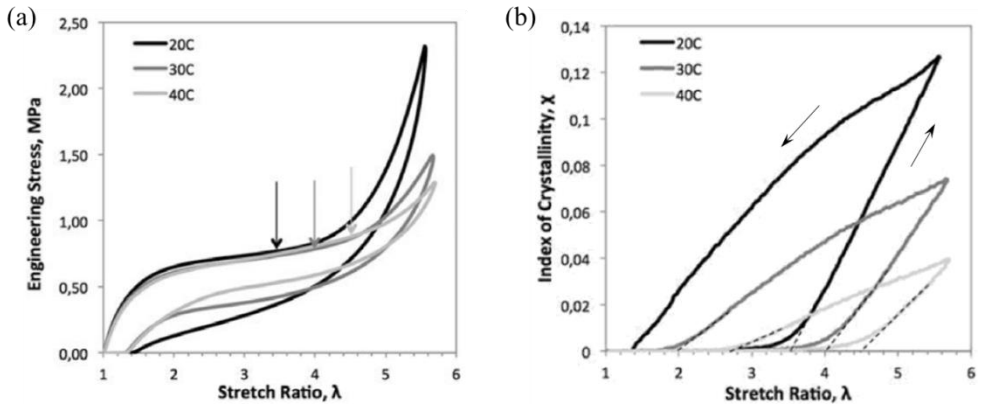

Figure 3-39. (a) Engineering stress versus stretch ratio of HNBR-44, showing the stiffening of the materials, (b) the evolution of crystallisation index against stretch ratio of HNBR 44. Take from Ulu et al [89].

3.5 Life prediction of fibre reinforced composites

In this section, analytical life prediction methodologies for the fibre reinforced composites were reviewed, particularly various constant life diagram (CLD) models. The commonly used parameters encountered in a fatigue test are shown in Figure 3-40. The main parameters used in the CLDs are normalised alternating stress $a = \sigma_a/\text{UTS}$ and normalised mean stress $m = \sigma_m/\text{UTS}$, where UTS is the ultimate tensile strength of the examined material.

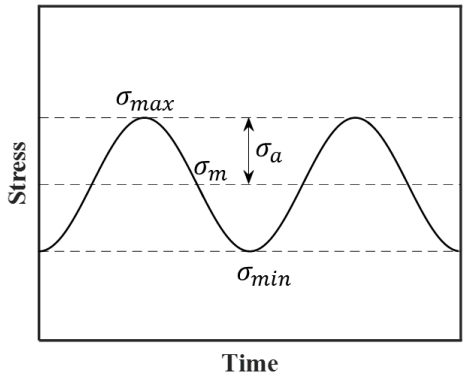

Figure 3-40. Commonly used test parameters during fatigue test.

A number of cumulative damage models were proposed based on the fatigue damage induced by repeated loading which was reviewed by Socie and Morrow [90], Hwang and Han [91] and Post, Case and Lesko [92]. In damage models, the damage function *D* is defined as a function of the number of applied cycles *n*, the applied stress level r_i, frequency *f*, temperature *T*, moisture content *M*, etc. Considering the same loading situation, *D* can be written as

$$D = f(n, r_i) = f(n / N_f) \qquad \text{Equation 3-7}$$

It should satisfy the initial and final boundary conditions.

$D = 0$ when n=0 Equation 3-8

$$D = \sum_{i=1}^{m} \Delta D_i = 1 \text{ when failure occurs} \qquad \text{Equation 3-9}$$

where N_f is the number of cycles to failure, *m* is the number of load sequence, ΔD_i is damage accumulated at stress level r_i.However, such methods require a detailed understanding of the way in which the fatigue damage affects the material's residual properties. In practice, the designer usually needs to assess the service life before this type of information is available. Therefore, another methodology based on the phenomenological modelling of the fatigue data is required. A series of CLD models have been proposed to cope with this deficiency. This approach has no identified physical mechanism of degradation as it is only based on a mathematical analysis of the fatigue data over a wide range of stress ratios. A typical $\sigma_a - \sigma_m$ plane is exemplified in Figure 3-41. Care must be exercised as a singularity occurs from all compressive (C-C) region to tensile-compressive (T-C) regions where *R* jumps from $-\infty$ to $+\infty$. In addition, at *R* = 1 (alternating stress equals zero), this type of loading could be considered as a constant creep load rather than a fatigue load [93]. Both linear

and nonlinear CLDs were presented in detail below and only constant amplitude loading was considered.

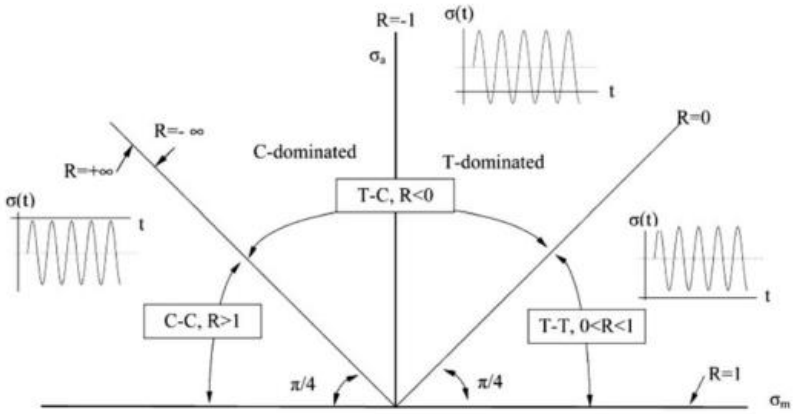

Figure 3-41. Annotation of the $\sigma_a - \sigma_m$ plane. Taken from Philippidis et al [94].

3.5.1 Linear CLD

With the assumption of identical failure mechanism in both tension and compression, the linear CLD is based on a single experimentally derived S-N curve. It offers the simplicity for life prediction, nevertheless, at the cost of compromising the accuracy. It is the most popular CLD especially for metal materials. However, the intrinsically oversimplified assumption limited its application for anisotropic composite materials due to different damage mechanisms under tension (dominated by reinforcing fibre) and compression (governed by the matrix and fibre-matrix interaction).

3.5.2 Piecewise linear CLD [94]

Piecewise linear CLD requires several experimentally-determined S-N curves as well as the static properties including UTS and ultimate compressive strength (UCS) for the construction of the model. Predictions are made by linear interpolation between two adjacent *R* ratios at the $\sigma_a - \sigma_m$ plane.

3.5.3 Harris's CLD

The CLDs mentioned above are characteristic for their linearity. However, it was observed later the constant-life curves plotted as alternating stress against mean stress were asymmetric and shifted slightly to the right of alternating stress axis [78, 95, 96]. Harris *et al.* studied the fatigue responses of carbon/ Kevlar-49/ epoxy hybrid composites [97] and several varieties of carbon fibre reinforced epoxy composites [65]. They made the first attempt to interpret the fatigue data over the whole range of *R* ratios in a systematic way. At the early stage, it was demonstrated that constant-life curves in the $\sigma_a - \sigma_m$ plane followed parabolic curves, as shown in Figure 3-42, in the form of

$$a = f_H(1-m)(c+m) \qquad \text{Equation 3-10}$$

where a is the normalised alternating stress, $a = \sigma_a / \text{UTS}$; m is the normalised mean stress, $m = \sigma_m / \text{UTS}$; c is the normalised compressive strength, $c = \sigma_c / \text{UTS}$; f_H is a function of N_f.

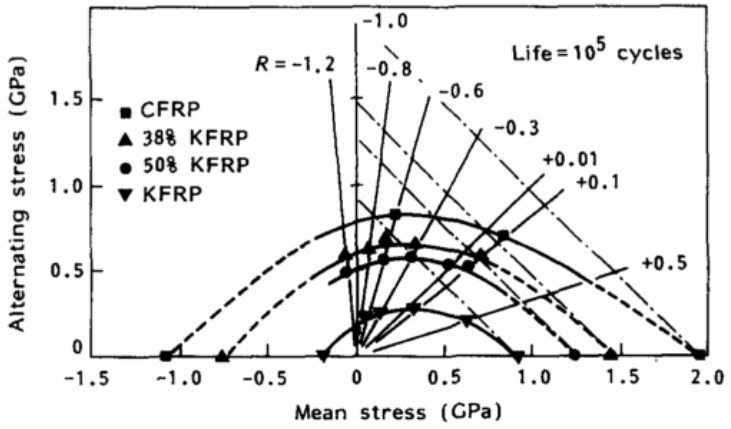

Figure 3-42. Constant life diagram on the fatigue response of unidirectional CFRP/KFRP hybrids. Taken from Adam et al [97].

Later, they proposed a more general nonlinear parametric model based on the analytical modelling of the fatigue data obtained for a wide range of carbon-fibre and glass fibre composites. It was revealed that all the constant-life lines followed similar bell shape [96, 98], as shown in Figure 3-43. The previously-proposed parabolic form was then modified by introduction of two extra parameters u and v, given by

$$a = f_H(1-m)^u(c+m)^v \qquad \text{Equation 3-11}$$

where $f_H = Ac^{-p_H}$, A, p_H, u, v are functions of N_f.

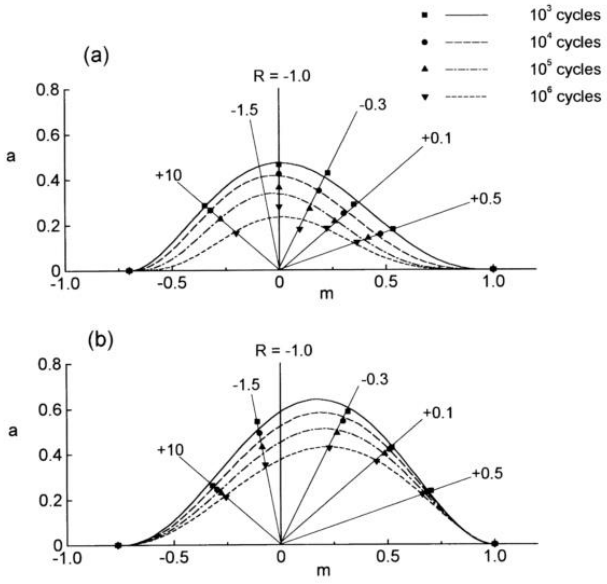

Figure 3-43. Bell shape constant-life diagrams for: (a) E-glass/913 and (b) HTA/982 laminates of $[(\pm 45, 0_2)_2]_S$ lay-up. Taken from Harris et al [98].

3.5.4 Kawai's CLD

Despite of its improved accuracy on life prediction, Harris's model still requires a large number of time- and cost-consuming fatigue characterisations conducted over a wide range of *R* ratios. Moreover, a slightly complex identification of the proper mathematical functions was also involved so as to give the best fit of the fatigue data. For the purpose of efficiency and convenience, Kawai [77] proposed a new model

which only requires the S-N data at the critical *R* ratio χ , defined as the ratio of the UCS to the UTS of the considered material, together with the UCS and UTS of the tested material. The shape of the constant-life curve progressively changes from a straight line at low cycles to a nested parabola at high cycles, as shown in Figure 3-44. The theoretical formulation is defined as follows:

$$-\frac{\sigma_a-\sigma_a^{\chi}}{\sigma_a^{\chi}}=\begin{cases}\left(\frac{\sigma_m-\sigma_m^{\chi}}{UTS-\sigma_m^{\chi}}\right)^{(2-\psi_{\chi})} & \sigma_m^{\chi}\le\sigma_m\le UTS\\ \left(\frac{\sigma_m-\sigma_m^{\chi}}{UCS-\sigma_m^{\chi}}\right)^{(2-\psi_{\chi})} & UCS\le\sigma_m\le\sigma_m^{\chi}\end{cases} \qquad \text{Equation 3-12}$$

where $\psi_{\chi}=\sigma_{max}^{\chi}/\sigma_B$, σ_a^{χ} and σ_m^{χ} represent the cyclic stress amplitude and the mean stress for a given value of life *N* during fatigue loading at the critical stress ratio χ .

The predicted CLD was bounded within the static failure envelope: two solid lines connecting the peak point ($\sigma_m^{peak}=(1/2)(1+\chi)\sigma_B$, $\sigma_a^{peak}=(1/2)(1-\chi)\sigma_B$) with the UTS and UCS on the abscissa. The reference strength σ_B was defined as

$$\sigma_B=\begin{cases}\sigma_T & \sigma_T\ge|\sigma_C|\\ |\sigma_C| & |\sigma_C|\ge\sigma_T\end{cases} \qquad \text{Equation 3-13}$$

If neither of value allows smooth curve fitting, the alternative value of σ_B could be obtained by extrapolation of reference fatigue data to $2N_f=1$ on the *S-N* plot.

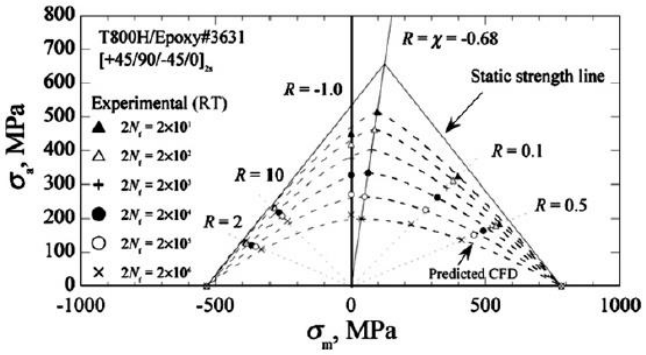

Figure 3-44. Anisomorphic constant-life diagram for $[45/90/-45/0]_{2s}$ CFRP laminate at room temperature. Taken from Kawai et al[77].

It was also demonstrated in Figure 3-45 that the predictions agreed with the experimental results reasonably well regardless of the laminate types. Kawai's model in the form of piecewise nonlinear curves allows the minimum amount of experimental data for the ease of testing while maintaining reasonable accuracy.

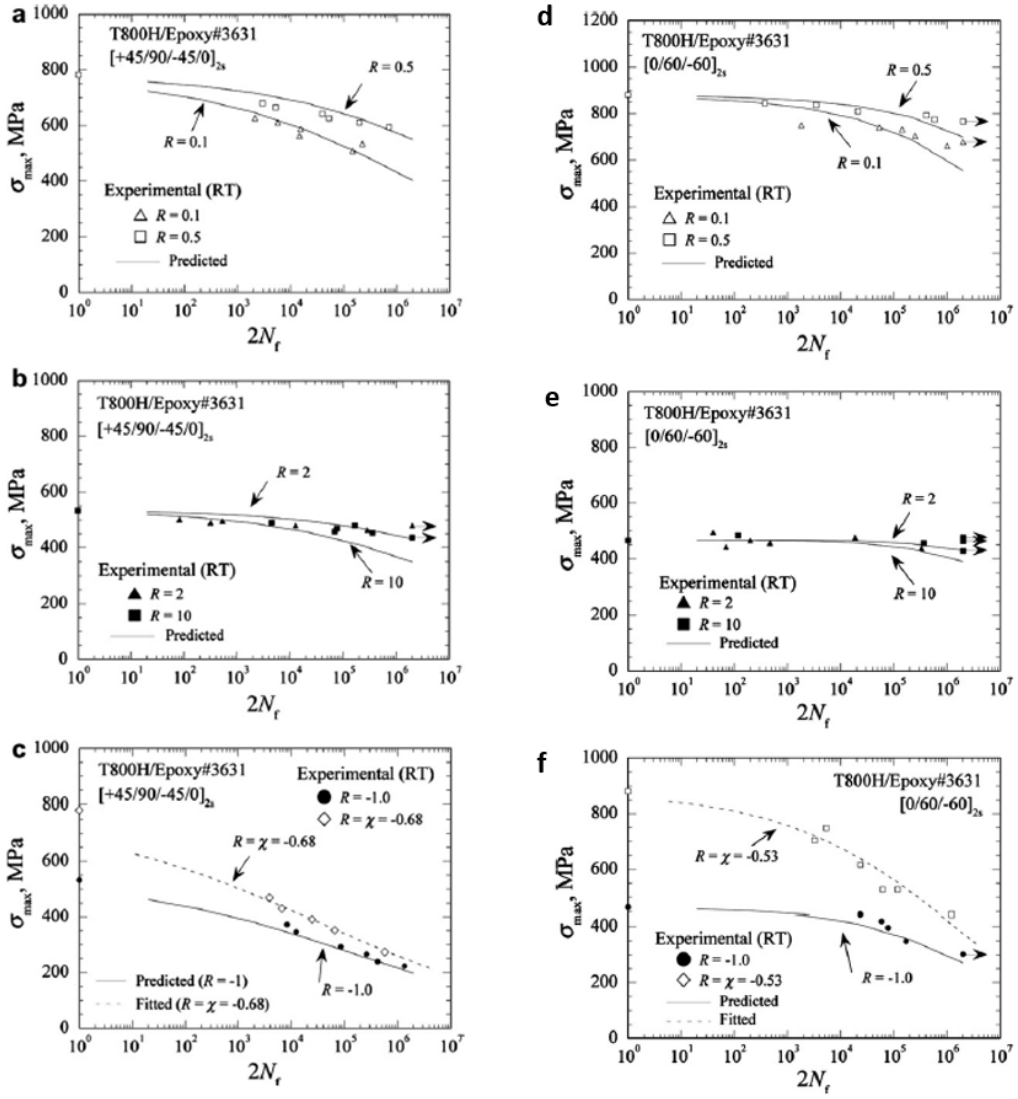

Figure 3-45. Comparison between the predicted S-N curves on the basis of Kawai's CLD model and experimental data for two different laminate lay-ups for T-T, T-C and C-C regions. Taken from Kawai et al [77].

3.5.5 Kassapoglou's CLD

The approaches mentioned above are all involved at least some fundamental fatigue testings, empirically-derived functions and parameters. Kassapoglou [99] purposed a new CLD model by assuming the failure probability in each cycle p is constant and independent of the current state. This approach was shown to produce reasonably

accurate analytical results when applied to the a range of materials under both in-plane [78, 100] and out-of-plane loading [101, 102].

In this model, P_i is defined as the failure probability between the 1st cycle and the i th cycle, given by

$$P_i = p(1-p)^{N-1} \qquad \text{Equation 3-14}$$

The probability P of failure any cycle between the 1st cycle and the N^{th} cycle,

$$P = \sum_{i=1}^{N} P_i = \sum_{i=1}^{N} p(1-p)^{N-1} \qquad \text{Equation 3-15}$$

Since it is postulated that p is independent of cycles,

$$P = Np(1-p)^{N-1} \qquad \text{Equation 3-16}$$

Considering the original definition of P which is the probability of failing between 1st cycle and N^{th} cycle, when the entire structure fails at an arbitrary cycle $N_a < N$, Equation 3-16could become potentially meaningless since the structure has already failed. However it can be circumvented if P is seen as the materials get infinitely close to the critical damage level. Figure 3-46 shows the failure probability P after N cycles as a function of N when $p = 1\times10^{-6}$, where N_c is the most probable cycle to fail. N_c can be solved by differentiating Equation 3-16 with respect to N, given by

$$N_c = -1/\ln(1-p) \qquad \text{Equation 3-17}$$

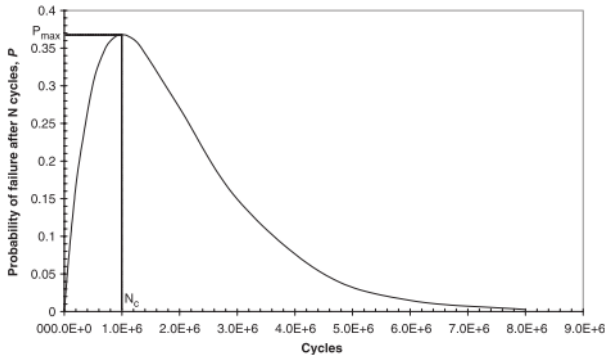

Figure 3-46. Probability of failure P as a function of N when $p = 1\times10^{-6}$. Taken from Kassapoglou et al [99].

For different loading conditions as shown in Figure 3-47, the determination of *p* is demonstrated as follows.

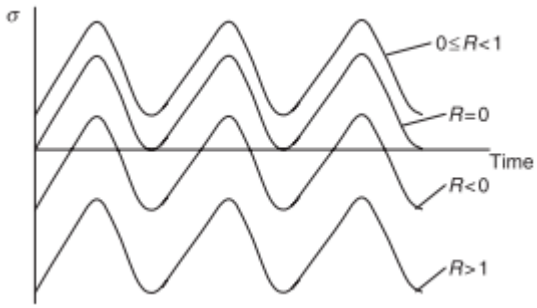

Figure 3-47. Types of cyclic loading as a function of *R*. Taken from Kassapoglou et al [99].

For the case of $R = 0$, failure probability per cycle *p* is actually equal to the failure probability in the static load excursion from 0 to σ_{max}. Therefore, an accurate statistical distribution such as two parameter-Weibull distribution, normal distribution or any other preferred non-normal distribution is necessary to define static strength distribution. For example, *p* can be calculated by Equation 3-18 provided the static strength is normally distributed.

$$p = \int_{-\infty}^{\sigma_{max}} \frac{1}{s\sqrt{2\pi}} \exp\left[\frac{-(x-\sigma_m)^2}{2s^2}\right] dx \qquad \text{Equation 3-18}$$

For the case of $0 \le R < 1$ (T-T section) and $R > 1$ (C-C section), since the material didn't fail from 0 to the starting stress, thus there is no probability to fail in this loading region (from 0 to the starting stress). Therefore it is assumed that the probability density function can be modified by narrowing the distance between the 1st percentile x_1 and the mean strength σ_m by the constant of proportionality *r,* as shown in Figure 3-48 where $r = 1 - R$ for $0 \le R < 1$ and for $r = 1 - 1/R$ for $R > 1$. The modified

probability density function is a Weibull distribution for the case of the original static strength distribution is normal, given by

$$f = \frac{\alpha}{\beta^{\alpha}} x^{\alpha-1} e^{-(x/\beta)^{\alpha}}$$ Equation 3-19

where α and β can be solved iteratively by combination of Equation 3-20 to Equation 3-23.

$$\beta(1-\frac{1}{\alpha})^{1/\alpha} = \sigma_m$$ Equation 3-20

$$e^{-(x_1/\beta)^{\alpha}} - e^{-(x_2/\beta)^{\alpha}} = 0.98$$ Equation 3-21

$$x_1 = \sigma_m - 2.326s$$ Equation 3-22

$$x_2 = \sigma_m + 2.326s$$ Equation 3-23

The probability per cycle p is given by the two parameter Weibull distribution

$$p = 1 - e^{-(\sigma/\beta)^{\alpha}}$$ Equation 3-24

Substituting Equation 3-24 into Equation 3-17 gives

$$\sigma_{\max} = \frac{\beta_T}{(N)^{1/\alpha_T}},\ 0 \le R < 1$$ Equation 3-25

$$\left|\sigma_{min}\right| = \frac{\beta_C}{(N)^{1/\alpha_C}},\ R > 1$$ Equation 3-26

where $\alpha_T, \beta_T, \alpha_C, \beta_C$ are scale and shape parameters for a two parameter Weibull distribution of the UTS and UCS of the examined material.

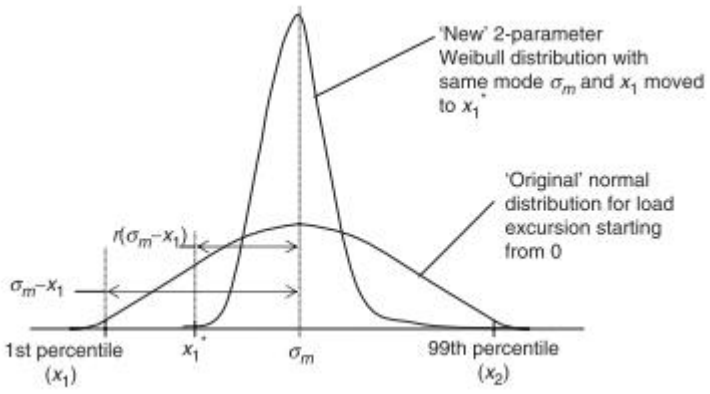

Figure 3-48. Modification of probability density function for load excursions not starting at zero. Taken from Kassapoglou et al [99].

For the case of $R<0$ (T-C section), the failure probability P after N cycles can be worked out by

$$P = N(p_T + p_C - 2p_T p_C)(1-p_T)^{(N-1)}(1-p_C)^{(N-1)} \qquad \text{Equation 3-27}$$

where p_T is the failure probability per cycle from 0 to maximum stress, p_C is the failure probability per cycle from minimum stress to 0.

Again, N_c can be obtained by differentiating Equation 3-27 with the respect of N,

$$N_C = -\frac{1}{\ln(1-p_T)+\ln(1-p_C)} \qquad \text{Equation 3-28}$$

where p_T and p_C can be deduced in the similar way as Equation 3-24, thus the relationship between N and stress can be obtained as follows:

$$N = \frac{1}{(\sigma_{max}/\beta_T)^{\alpha_T} + (|\sigma_{min}|/\beta_C)^{\alpha_C}},\ R<0 \qquad \text{Equation 3-29}$$

Kassapoglou's CLD can be very useful for some preliminary design at initial stage with the benefit of circumventing time-consuming fatigue testing. However, it should be stressed that this model oversimplifies the fatigue damage process by employing a constant failure probability per cycle p. As indicated by Figure 3-49, a good agreement

with experimental results was observed for the case of high maximum stress. On the other hand, the predictions deviated significantly from the test results for the case of low maximum stress. This is attributed to the extra failure modes such as delamination took place during the low-amplitude dynamic loading which is not present during the static loading. As a result, a single constant parameter p is not sufficient for the description of the failure behaviour at low amplitude. It also explains the accurate prediction close to static strength level of the materials as p adequately represents the damage mechanism during high applied load. Therefore, it is advised that p should be modified as a function of the current state of the material and the number of cycles the material has gone through for more rigorous applicability.

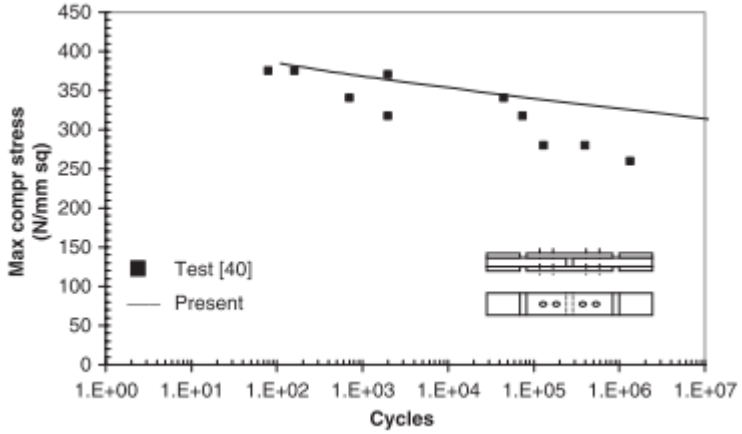

Figure 3-49. Tension-compression (R=-1.66) fatigue of T300/914 bolted joints. Taken from Kassapoglou et al [99].

Table 3-3 summarised the mathematical formulations and remarks for various CLD models mentioned above.

Table 3-3: Mathematical formulations and remarks for various CLD models

Theory of CLD models	Formulations	Parameters	Comments and drawbacks
Linear CLD	$\frac{\sigma_a}{\sigma_o}+\frac{\sigma_m}{\sigma_o}=N^{-1/k}$	k,σ_0	Assuming failure mechanism in tension and compression is the same which is unrealistic.
Piecewise linear CLD	$\sigma_a^{'}=\frac{\mathrm{UTS}}{\frac{\mathrm{UTS}}{\sigma_{a,1TT}}+r^{'}-r_{1TT}}$ for T-T $\sigma_a^{'}=\frac{\sigma_{a,i}(r_i-r_{i+1})}{(r_i-r^{'})\frac{\sigma_{a,i}}{\sigma_{a,i+1}}+(r^{'}-r_{i+1})}$ for T-C $\sigma_a^{'}=\frac{\mathrm{UCS}}{\frac{\mathrm{UCS}}{\sigma_{a,1CC}}+r^{'}-r_{1CC}}$ for C-C	Similar to linear CLD with 2 parameters for each piecewise region	Linear interpolation.

Harris's CLD	$a = f_H (1-m)^u (c+m)^v$ $f = A_1 \log N + B_1$ $u = A_2 \log N + B_2$ $v = A_3 \log N + B_3$ $f = Ac^{-p_H}$	u, v, A, p_H	Produce acceptable results for a wide range of CFRP and GFRP laminates.
Kawai's CLD	$\frac{\sigma_a^\chi - \sigma_a}{\sigma_a^\chi} = (\frac{\sigma_m - \sigma_m^\chi}{UTS - \sigma_m^\chi})^{(2-\psi_\chi)}$ for $UTS \geq \sigma_m \geq \sigma_m^\chi$ $\frac{\sigma_a^\chi - \sigma_a}{\sigma_a^\chi} = (\frac{\sigma_m - \sigma_m^\chi}{UCS - \sigma_m^\chi})^{(2-\psi_\chi)}$ for $UCS \leq \sigma_m \leq \sigma_m^\chi$	$\sigma_a^\chi, \sigma_m^\chi, \psi_\chi$	Asymmetric; Critical R ratio is defined as the ratio of UCS over UTS of the examined material.
Kassapoglou's CLD	$\sigma_{\max} = \frac{\beta_T}{(N)^{1/\alpha_T}}$ for $0 \leq R < 1$ $\lvert\sigma_{min}\rvert = \frac{\beta_C}{(N)^{1/\alpha_C}}$ for	$\alpha_T, \beta_T, \alpha_C, \beta_C$	The basic assumption of the model is that the probability of failure of the material during each cycle is constant and independent of the current state or number of cycles up to this point

	$R > 1$ $N = \frac{1}{(\frac{\sigma_{\max}}{\beta_T})^{\alpha_T} + (\frac{\sigma_{\min}}{\beta_C})^{\alpha_C}}$ for $R < 0$		

3.6 Bending fatigue

In the previous section, attention was paid to tensile fatigue of cord-rubber composites and its life prediction. However, in the real operation conditions, cord-rubber composites found in components such as a pneumatic tyre or a timing belt often undergo a combination of tension and bending deformations rather than simple extension alone. In the literature, a good description of bending fatigue test methods of fibre-reinforced plastics (FRPs) has already been standardised, as shown in Table 3-4.

Table 3-4. Test methods for bending fatigue of FRPs, taken from [103].

Nation	Designation	Title
France	NF T51-120-1-1995	Plastics and composites. Determination of the bending fatigue properties. Part 1: General principles
	NF T51-120-2-1995	Plastics and composites. Determination of the bending fatigue properties. Part 2: Bending test on test pieces gripped at one end
	NF T51-120-3-1995	Plastics and composites. Determination of the bending fatigue properties. Part 3: Three-point bending test on unsecured test pieces
	NF T51-120-4-1995	Plastics and composites. Determination of the bending fatigue properties. Part 4: Four-point bending test on unsecured test pieces
	NF T51-120-5-1995	Plastics and composites. Determination of the bending fatigue properties. Part 5: Alternating plane-bending test
	NF T51-120-6-1995	Plastics and composites. Determination of the bending fatigue properties. Part 6: Buckling bending test
Int.	ISO 13003:2003	Fiber-reinforced plastics: Determination of fatigue properties under cyclic loading conditions
Japan	JIS K 7082-93	Testing method for complete reversed plane bending fatigue of carbon fiber-reinforced plastics
	JIS K 7083-93	Testing method for constant-load amplitude tension—tension fatigue of carbon fiber-reinforced plastics
UK	BS-ISO 13003:2003	Fiber-reinforced plastics: Determination of fatigue properties under cyclic loading conditions
USA	ASTM C394-00 (2008)	Standard test method for shear fatigue of sandwich core materials
	ASTM D3479/D3479M-12	Standard test method for tension—tension fatigue of polymer matrix composite materials
	ASTM D6115-97 (2011)	Standard test method for mode I fatigue delamination growth onset of unidirectional fiber-reinforced polymer matrix composites
	ASTM D6873/D6873M-08	Standard practice for bearing fatigue response of polymer matrix composite laminates
	ASTM D7615/D7615M-11	Standard practice for open-hole fatigue response of polymer matrix composite laminates

Generally, cyclic three-point bending [104] and four-point bending tests [105] were often employed. In contrast, bending fatigue tests for cord-rubber composites were rarely reported. One industrially available way to measure the bending fatigue properties of cord-rubber composite is to make use of the belt dynamometer which simulates the real operating conditions, in this case, for the timing belts, as shown in

Figure 3-50. Here, the bottom pulley is the driving pulley and the upper one is the driven pulley. Before the test, a pretension of 10 N was applied to ensure the match between the belt teeth and the pulley teeth. However, it requires a closed belt sample to perform such kind of tests which tends to be cost-intensive. The manufacturer usually won't start to produce such kind of sample until some primary investigations were finished.

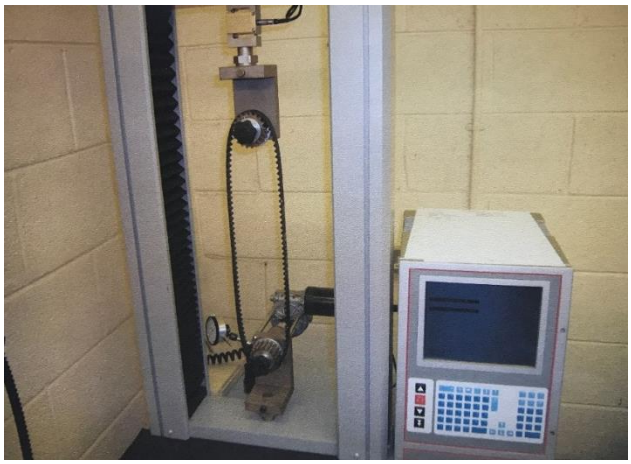

Figure 3-50. Test set-up for bending fatigue tests of a real timing belt. The bottom pulley is the driving pulley and the upper one is the driven pulley. Both pulleys have a diameter of 100 mm. Taken from Hayes [106].

Instead, studies based on flex fatigue properties of the reinforcing cords were often conducted due to its simplicity and lower cost. Several equipment designs and their experimental results are presented below.

Nkiwane *et al.*[107] reported the accelerated flex fatigue behaviour of the raw and RFL-dipped nylon 6,6 tire cords and yarns respectively by flexing the cord and yarn over a pin so as to cause them to follow the curvature of the pin surface. The 35 cm sample was pulled backward and forward at various stress levels at a testing speed of 40 cycles per minute. The fibre section in contact with the pin is 7 cm along where the sample broke. The test set-up and the fatigue life-stress curves were shown in Figure

3-51. A reduction in flex fatigue life in the dipped cords was observed due to the presence of rubbery component dispersed on the surface in the form of particles, leading to earlier crack initiation.

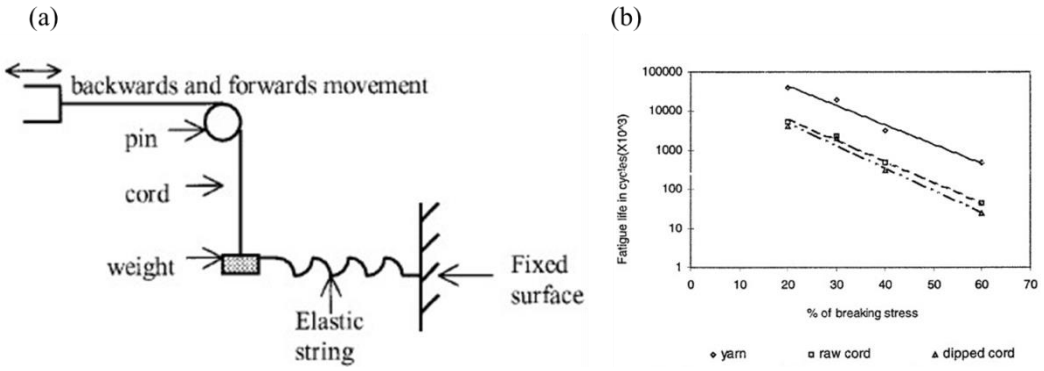

Figure 3-51. (a) Schematic of flex fatigue over a pin, (b) flex fatigue life-stress relationship of nylon 6, 6 yarn, raw cord and dipped cord, showing a worse flex life in dipped cord due to earlier crack initiation as a consequence of the presence of rubbery component. Taken from Nkiwane et al [107].

Additionally, they also classified the bending failure into two categories, that is, fatigue fracture failure and tensile fracture failure depending on the experimental variables such as the stress levels and failure characteristics, as shown in Figure 3-52. At low stress level, axial splitting is a common failure mode for the polymer cords as a result of localised plastic deformation with fibrils oriented along the direction of the applied stress. Kink bands were caused by combined effect of the presence of a compressive stress component, arising from bending deformation and a shear stress component arising from the twist structure. At high stress level, brittle fracture became predominant starting with a sudden failure of a defect, leading to the catastrophic failure of the entire cord.

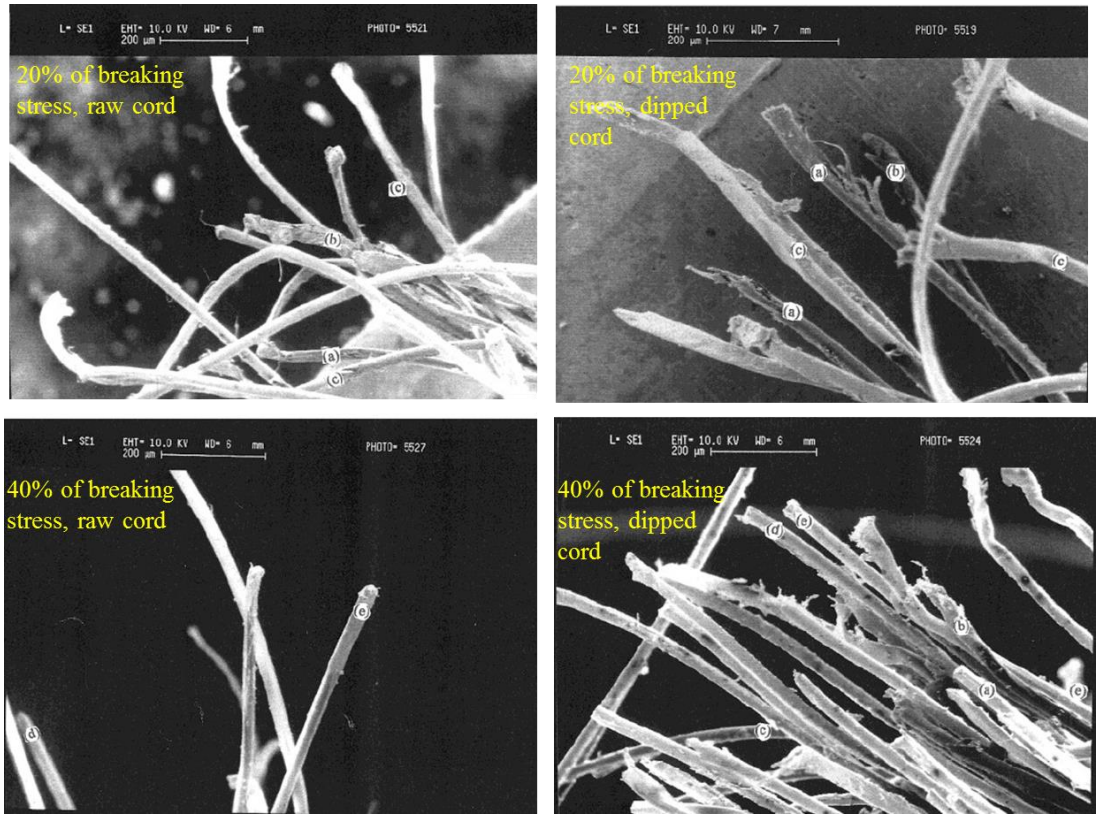

Figure 3-52. SEM observation of raw cord (left) and dipped cord (right) at 20% and 40% of breaking stress respectively, showing (a) axial splitting; (b) abrasion and peeling; (c) kink bands; (d) brittle fracture; (e) high-speed breaks. Taken from Nkiwane et al [107].

Furusawa *et al.* [108] successfully improved bending fatigue properties of cords by hybridising high stiffness carbon fibres with low stiffness glass fibres, namely one core strand made of 6000 carbon fibres and twelve outer strands consisting 600 glass fibers for each strand. The flex fatigue test was performed on the test equipment as shown in Figure 3-53 (a). The hybrid cords of various twisting angles, twisting directions and strand diameters were wound around two 10 mm (diameter) pulleys which rotates at a frequency of 10 Hz and the axial load was 10 N. They found that the failure was often initiated from the inside of the helical cord in the form of debonding along the interfaces between the strands. The fatigue damage was accumulated by the cyclic shearing stress along the interfaces between strands under

bending deformation of the cord, and eventually developed into debonding, shown in Figure 3-53 (b). Moreover, a simplified mechanical model was proposed to explain the dependence of flex fatigue performance on the cord geometrical factors so as to propose optimum cord construction for high bending fatigue durability in design.

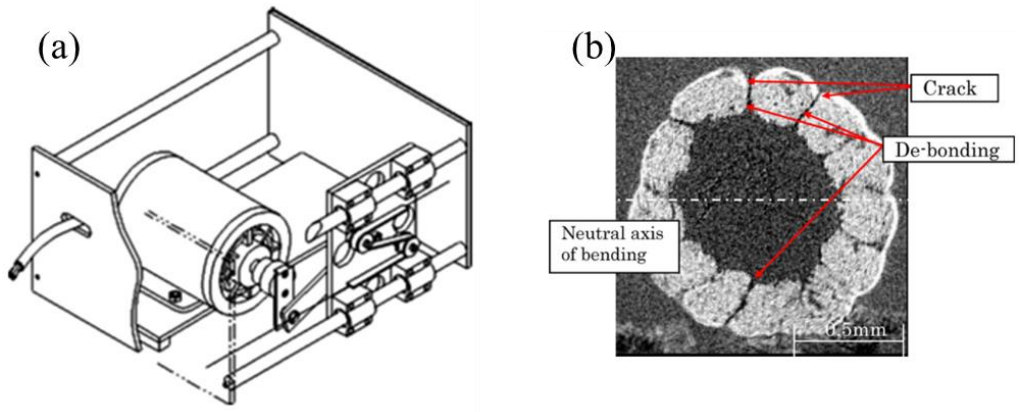

Figure 3-53. (a) Helical hybrid cord bending fatigue test equipment, (b) sample failure morphology using CT-scanner, showing debonding along the interfaces between the strands, taken from Furusawa et al [108].

The aforementioned bending fatigue test methods has its limits of flexing over a fixed pin or pulley and not capable to study the influence of environmental conditions on flex properties. Recently Cai *et al.* investigated the influence of bending angle, temperature and pretension on the bending fatigue of Nomex fibre (a kind of aramid fibre) [109] and high performance polyethylene (HMPE) [110] by making use of a self-designed bending testing apparatus which is based on fixed point bending introduced by pins coupled with a Xenon lamp irradiation system and a temperature control system. Figure 3-54 shows the active images of the fibre during bending fatigue.

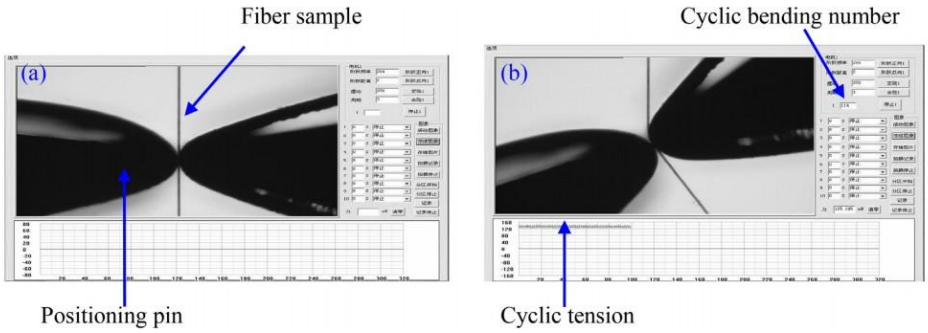

Figure 3-54. The active images of fibre during bending fatigue process: (a) fibre before bending, (b) fibre during bending at a bending angle of 45 °. Taken from Cai et al [109].

It was found that the bending fatigue life of fibres decrease with increasing bending angle and pretension, as shown in Figure 3-55. The observation of the fatigue fracture morphologies of HMPE fibres at different temperatures using CCD camera showed more fibre fibrillations occurred at higher temperatures and a bent hook-like end was formed attributed to the melting of some fibrils at temperatures higher than 80 °C, as shown in Figure 3-56.

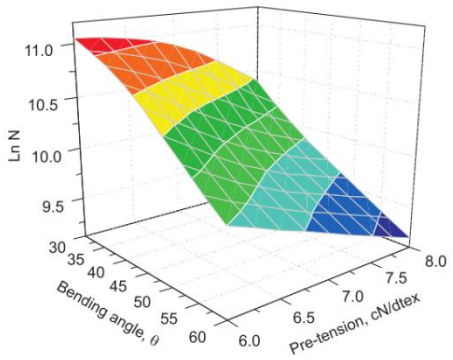

Figure 3-55. Relationship between bending fatigue life of HPPE fibre and the pre-tension as well as bending angle, showing a reduction in cycles to failure with increasing pre-tension and bending angle. Taken from Cai et al [110].

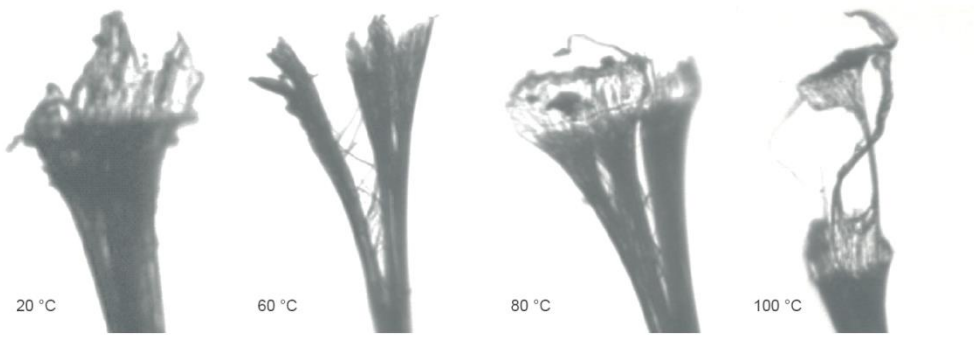

Figure 3-56. Fracture morphologies of HPPE fibres at different temperatures, showing more fibre fibrillations at higher temperature and a hook-like feature due to the melting of fibrils. Taken from Cai et al [110].

Liu *et al.* [111] studied the bending fatigue behaviour of a single Kevlar fibre by using the fixed point bending instrument and simulated the single fibre bending procedure by finite element modelling, which was found to be consistent with the experimental results.

Bending over sheave test is another effective laboratory experiment to evaluate the cyclic bending fatigue properties of wires [112, 113], ropes [114] and cord-rubber composites [115].

Ridge *et al.* [116] assessed the influence of manually introduced damages such as internal and external wire breaks, corrosion, abrasive wear and plastic wear on the fatigue endurance of two different types of wire structures using the bending over sheave machine as shown in Figure 3-57. In contrast to the tension fatigue of the wires where manually introduced damages led to a significant reduction of the lifetime, it was observed that the bending fatigue endurances of the wires had little to do with the previously introduced impairment but were largely dependent on the ratio of the diameter of the driving pulley to the diameter of the rope (D/d) and the wire structure. These two factors are directly related to the wire bending strain under repeated bending conditions.

Sloan *et al.* [117] investigated the effect of D/d, a polyurethane coating and the rope structure on the bending fatigue life of high-modulus polyethylene (HMPE) ropes by using bending over sheave techniques. The results indicated that a more tightly fitted groove and the introduction of the coating material outside the rope enhanced the lifetime substantially, which conflicted with the findings reported by Nkiwane *et al* [107]. This might be due to the difference in coating nature and its dispersion state on the surface of the cords. Moreover, the heat build-up generated by back-and-forth movement of the rope could be reduced by blending with Vectran® fibres noted for high temperature thermal stability.

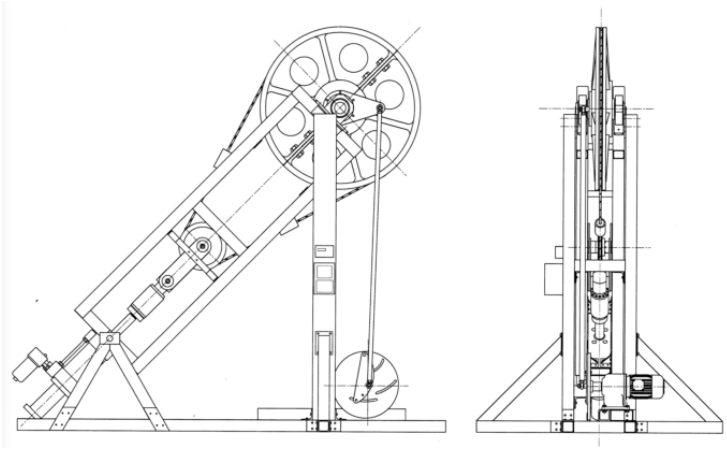

Figure 3-57. Bending over sheave fatigue test rig. Taken from Ridge et al [116].

The common characteristic of the flex fatigue test methods reported in literature is that almost all make use of a cylindrical pulley structure to introduce certain level of bending strain into the studied material. This design principle can be employed in our study for bending fatigue investigation of the cord-rubber composite.

3.7 Structure health monitoring (SHM) of fibre reinforced composites

Since its first application in engineering composites [118], structural health monitoring (SHM) based on real-time resistivity measurements has evolved rapidly during the last few years, ranging from various conductive polymer composites (CPCs) to nano-engineered carbon or glass fibre reinforced composites [119-121]. Conductive networks based on carbon nanotubes (CNTs) or graphene have been employed to detect various failure modes particularly in electrically insulating composites. For instance, Chou *et al.*[122, 123] successfully demonstrated the possibility to identify ply delamination, transverse micro-cracking and fibre breakage in glass fibre reinforced epoxy laminates under both tensile and flexural conditions by resistivity measurements with CNTs dispersed in the epoxy matrix. By this top-down method, a resistivity change has been successfully correlated to deformation of the entire percolated CNT network throughout the bulk matrix whereas damage at the fibre-matrix interfacial region associated with stress transfer has been disregarded [124]. Moreover, nanofiller loading needs to be carefully controlled to avoid excessive increase in resin viscosity and nanoparticle filtration effects during the composite manufacturing process [125].

Self-sensing smart yarns were developed as a bottom-up method to address some of the aforementioned issues by locally modifying the surface of non-conductive fibres with CNTs or graphene for interfacial strain and damage sensing [126-128]. Mäder *et al.*[124, 128] first reported an approach based on the incorporation of CNT-filled sizing on glass fibre (GF) surfaces via a solution-based process and demonstrated its potential usage as interfacial sensors upon both static and dynamic tensile loading, as shown in Figure 3-58.

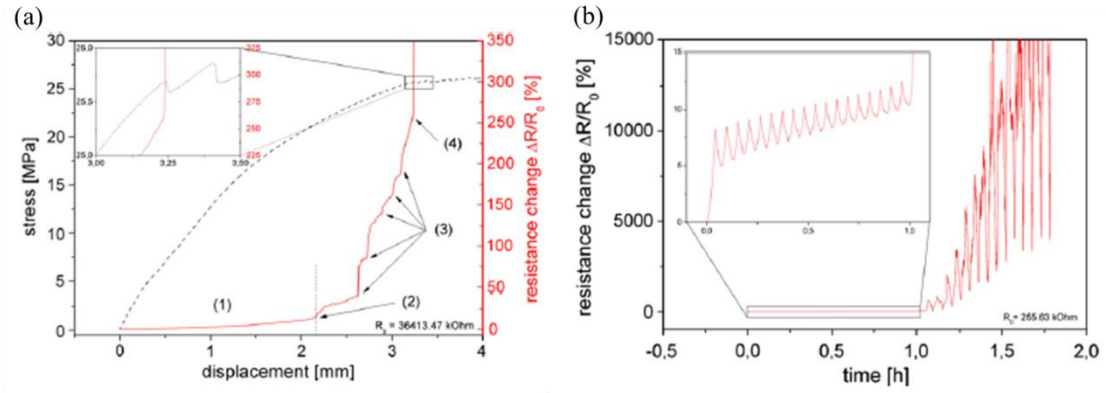

Figure 3-58. (a) Quasi-static tensile loading of CNT coated GF embedded in polypropylene with simultaneous resistance change measurement. The step-wise increase of resistance change corresponds to the evolution of interphase failures. (b) stress controlled cyclic loading between 0 and 22 MPa. The amplitude of resistance changes significantly after the occurrence of severe interphase damage.

Bilotti *et al.*[129] fabricated a conductive thermoplastic polyurethane/carbon nanotube (TPU/CNT) fibre via a continuous extrusion process with good strain sensing ability. Furthermore, they demonstrated the possibility to obtain self-sensing yarns by coating a commercially available Spandex yarn with a TPU/CNT conductive polymer composite coating [126, 130], as shown in Figure 3-59.

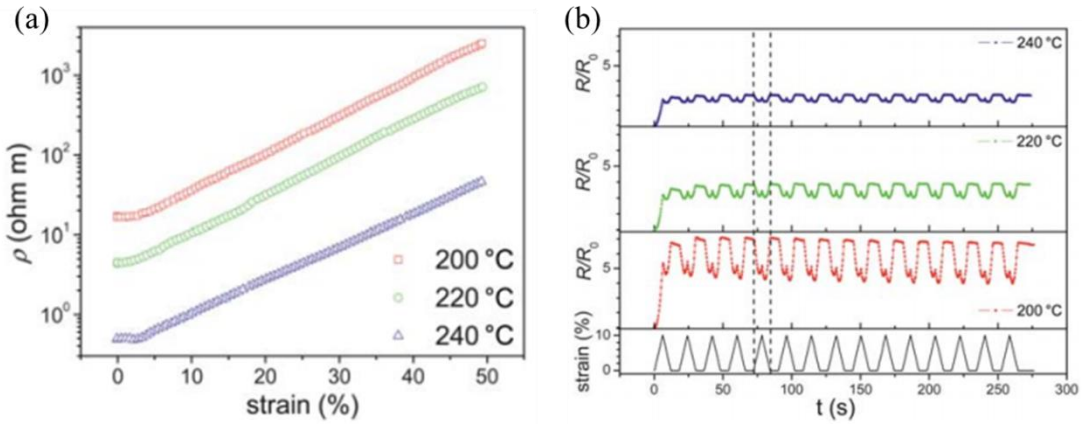

Figure 3-59. (a) Resistance -strain dependence of a Spandex yarn coated with TPU/3% CNT, showing resistance increases with increasing strain, (b) strain- controlled cyclic

loading of the same conductive yarn, showing the strain sensing behaviour and partially recoverable resistance at different temperatures.

Other techniques used to develop CNT-coated smart textile materials include electrophoretic deposition (EPD) [131, 132], chemical vapour deposition (CVD) [133, 134], electrospray [135] and spray coating [136, 137]. For instance, hierarchical CNT-GF with preferred CNT alignment was achieved by CVD and employed for *in-situ* SHM of glass fibre reinforced composites during flexural testing [127]. A novel EPD process was developed for coating CNTs onto glass fibre surfaces and these functional interphases were exploited for damage detection [131]. The effectiveness of CNT deposition onto carbon fibre prepregs by a simple spray coating technique was also reported with a good correlation between crack propagation and electrical resistivity signals during *in-situ* damage sensing tests [136].

However, most of above-mentioned research works on SHM have focused on fibre reinforced plastics (FRPs) while no study has been conducted on real-time damage detection of cord-rubber composites. One of the difficulties in developing health monitoring systems based on CNTs for cord-rubber composites is in achieving an even spatial distribution of CNTs throughout the highly viscous rubber matrix and the complexity of depositing CNTs onto the cord surface using the techniques mentioned previously. The latter is particularly complicated by the presence of an elastomeric adhesive coating on commercially available cords. Different types of cords are used in reinforced rubber products such as glass, aramid, nylon and polyester. These cords are often treated with bespoke coatings to enhance the adhesion with rubber matrix. Adhesion can be improved by varying the resorcinol formaldehyde latex (RFL) impregnation system, or by adding an external adhesive coating which is often based on chlorosulphonated polyethylene (CSM) [50, 52, 138].

Recently, Coleman *et al.* pioneered an interesting novel approach to incorporate graphene into NR-based rubber bands[139], polyethylene film [140] and Kevlar fibre by a simple swelling process Figure 3-60 shows the preparation and applications of graphene filled rubber bands as breath monitors. It opens up a new route to introduce nanofillers into rubber materials without complex manufacturing procedures. This technique could be potentially beneficial for making smart cord-rubber systems.

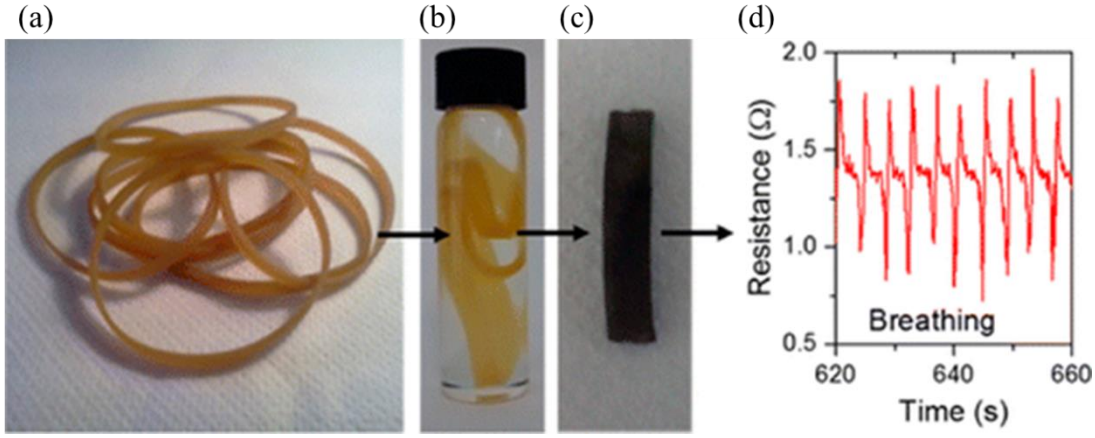

Figure 3-60. (a) As-bought NR-based elastic bands,(b) elastic band while soaking in swelling solvent toluene,(c) a graphene-infused band prepared by swelling in toluene then soaking in an NMP:water:graphene mixture for 4 h followed by washing and drying,(d) applications of G-bands as breath monitors with resistance traces showing slow breathing.

3.8 Conclusion

This review gives a basic knowledge of composite damage mechanisms during fatigue loading and its underlying micromechanics related to various failure modes. The interfacial bonding between the cord and the rubber using resorcinol formaldehyde latex (RFL) was briefly introduced, including the commonly used measuring techniques, the fundamental bonding principles and the influence of dynamic loading on the interfacial adhesion evolution.

Most fatigue studies focused on rigid fibre reinforced plastics (FRPs). Nevertheless, it seems appropriate to treat these studies as a guide for relevant cord-rubber composite studies, albeit these materials show greatly different viscoelastic behaviour of the polymer matrix. Detailed knowledge of how various loading parameters such as the frequency and *R* ratio affect the fatigue performance of carbon cord reinforced rubber composite is desirable before they can be introduced in mass products. In addition, the underlying micro-structural change of the material and self-heating heating effect associated with fatigue loading are key factors for lifetime interpretation.

An accurate life prediction of composite materials has remained a challenging task over the years due to their complex failure modes (fibre fracture, debonding, matrix cracking and delamination). Constant life diagram (CLD) models can be possibly employed as a useful tool for life prediction by making certain modification, with the advantage of no need to identify how fatigue loading influences the residual properties of materials.

Bending fatigue characterisation of cord-rubber composites still remains less explored area despite of the fact that various test equipment are developed to evaluate the flex properties of cords, yarns and wires. It is of importance to learn from those current testing methodologies so as to design a laboratory-feasible, cost-effective experiment set-up to allow more investigation into their fatigue behaviour under coupled tension and bending conditions.

A lot of efforts has been made on the structure health monitoring (SHM) of composites by either modifying resin matrix or fibre surfaces (that is interfacial region in a composite). However, to the best of the author's knowledge, none has been conducted for cord-rubber system. As the wide application in automotive structural components, it is beneficial to create smart hierarchical cord composite materials to

avoid catastrophic failure. Meanwhile, it should bear in mind to keep the simplicity of the proposed methodology to apply for large-scale industrial production of nanocarbon functionalised elastomeric products.

Chapter 4 : Development of a novel fatigue test method for cord-rubber composites

4.1 Introduction

The development of a robust and reliable testing methodology which must include the selection of an appropriate test configuration, with an appropriate specimen geometry and suitable dimensions is essential when determining repeatable and reliable mechanical test data for any examined material. For instance, dumb-bell shaped test pieces such as those specified in ASTM D412 and ISO 37 are routinely used to determine the tensile stress versus strain behaviour of rubber based materials [141, 142]. As a result of their flared specimen ends, the stress in the gripping region is much lower than that in the gauge section, which reduces the probability of failure arising at or near the grips. When it comes to investigating the tensile fatigue behaviour of materials, additional factors need to be accounted for in order to avoid premature failure in the gripping region. For rigid FRPs, technical standards for tension-tension fatigue testing such as ISO 13003:2003 [143] and ASTM 3479 / ASTM 3479-12 [144] have been established, where straight sided specimens with adhesively bonded end tabs are typically employed. Bailey *et al.* [145] evaluated the influence of end tab materials and clamping force on the fatigue test results for glass fibre reinforced epoxy composites and pointed out the significant risk of failure in or near the gripping region. Baere *et al.*[146] numerically assessed the effect of four different end tab geometries on stress concentration factors in the tabbed region for a uniaxial tensile test of carbon fabric reinforced polyphenylene sulphide (PPS) using wedge grips. Portnov *et al.*[147, 148] investigated the stress-strain state in the clamped region of carbon fibre epoxy

Part of this chapter has been published in *Polymer Testing,https://doi.org/10.1016/j.polymertesting.2018.09.001*

composites by both analytical models and finite element analysis. As an alternative to end gripping, Peijs *et al*. [149] used filament-wound rings for fatigue testing of hybrid polyethylene / carbon fibre epoxy composites to avoid shear failure in the clamping region.

In contrast to rigid composites, for the case of flexible rubber composites tension-tension fatigue test standards are less well developed. For cord-rubber composites, it has been reported that fatigue tests could be carried out on angle-ply laminates using conventional wedge grips, however, several studies [69, 150-152] have repeatedly demonstrated that failure is often initiated at the edges of the specimen due to the high levels of interply shear strain, eventually causing delamination. Moreover, it has proven extremely difficult to test unidirectional cord-rubber composites in on-axis fatigue loadings as a consequence of the significantly higher levels of shear stress concentrations arising from the extremely low shear modulus of the elastomeric matrix [153, 154]. Furthermore, chemical inertness and the low shear modulus of rubber matrices limit the potential use of adhesively bonded end tabs as often recommended in the fatigue testing of rigid FRPs [145].Therefore, one of the most important requirement of this investigation was to develop a more robust fatigue test method to improve current fatigue testing procedures for cord-rubber composites.

In this investigation, an initial effort was made to assess the fatigue damage evolution in a single carbon cord reinforced hydrogenated nitrile butadiene rubber (CC-HNBR) model composite tested using wedge grips. This approach is still routinely employed for the fatigue testing of both rigid and flexible composites. Nevertheless, this test configuration initiated failure in the gripping region with cord-rubber interfacial debonding being the main failure mode while ultimate cord fracture was completely absent. Further attempts were made to interpret the observed

interfacial failure mode by classical stress transfer models together with numerical simulations to quantitatively evaluate the damage introduced by conventional wedge grips. Subsequently, inspired by the capstan approach adopted for the mechanical testing of fibrous materials, a novel bollard fatigue test set-up was proposed for fatigue testing of unidirectional cord-rubber composites. This test method has been demonstrated effective in terms of preventing premature failure in the clamped region by minimising shear stress concentrations, leading to more reliable fatigue test data being measured for cord-rubber composites.

4.2 Experimental

4.2.1 Materials

Hydrogenated nitrile butadiene rubber (HNBR) compounds and carbon cords were supplied by NGF Europe Limited (UK). The detailed formulation of the HNBR compound is commercially sensitive and is not disclosed here. The carbon cord consists of 6000 carbon fibre (Toray T700) filaments with a final twist of 82 twists per metre and an average diameter of 0.7 mm. These cords had been dipped through a crosslinkable latex system as well as an external adhesive overcoat to enhance the adhesion with the HNBR compound prior to reception. The same latex as used in the dip was also supplied for characterisation purposes in the form of a dried latex sheet.

4.2.2 Sample preparation

Previously compounded HNBR was re-milled immediately prior to moulding using a two-roll mill for 5 min at room temperature (RT) and was shaped into flat sheets to be used for compression moulding. The milling process also ensured a more even dispersion of additives after initial mixing and storage. The vulcanization behaviour of the HNBR compound was characterised using a moving die rheometer (MDR2000,

Alpha Technology, USA) at 180°C according to ASTM D-3182 to determine vulcanisation time.

A specially designed mould was used to manufacture the model composite samples. The carbon cord was sandwiched between two HNBR sheets of 240 mm × 15 mm × 2 mm with a 5 N preload applied to either end of the cord to ensure they were fully straightened prior to moulding (see Figure 4-1) and then they were moulded using a hydraulic hot press at 180 °C for 20 min.

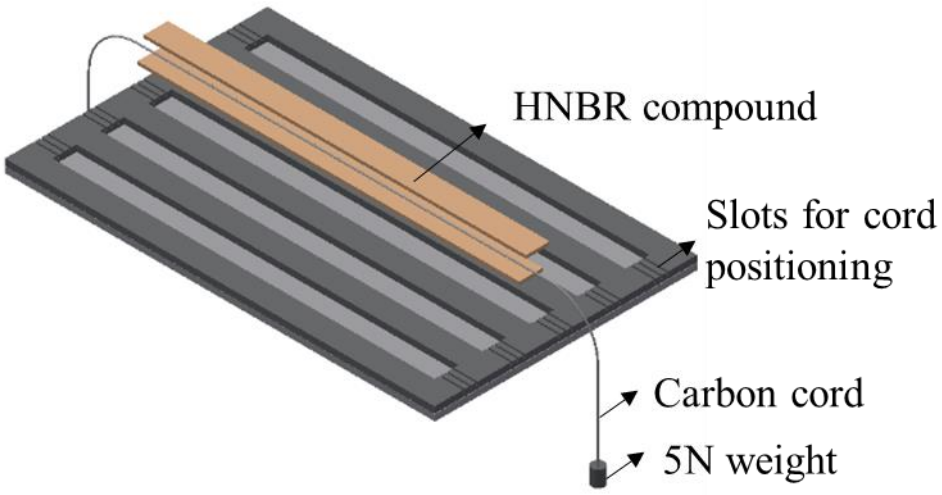

Figure 4-1. A specially designed mould used for making CC-HNBR model composite samples. The carbon cord was positioned in the middle slot.

After moulding, unidirectional single carbon cord reinforced hydrogenated nitrile butadiene rubber (CC-HNBR) model composite test samples were obtained with dimensions of 240 mm × 15 mm × 4 mm, with the carbon cord extending out from either end of the sample for another meter. Specimens for wedge grip fatigue tests and pull-out experiments were cut to size using a scalpel from these moulded composites as required. Specimens for bollard fatigue tests were used as moulded. The dimensions of each type of specimen are illustrated in Figure 4-2.

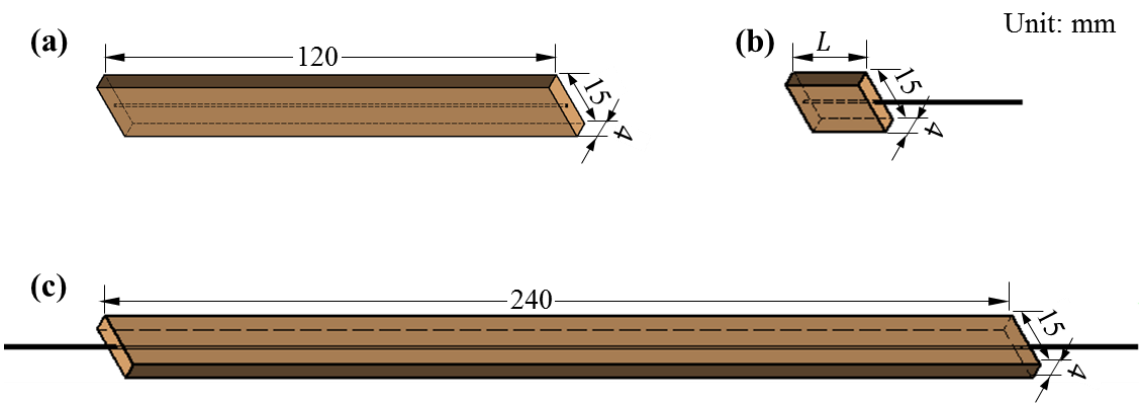

Figure 4-2. The dimensions of CC-HNBR model composite specimens for (a) wedge grip fatigue tests, (b) pull-out experiments, L=5.8, 6.1, 10.3, 19.1, 19.5, 21.1, 24.7, 25.0, 30.9 mm respectively, and (c) bollard fatigue tests.

4.2.3 Characterisations

Wedge grips fatigue tests

Fatigue testing was performed on an Instron E10000 (UK) in a load-controlled test mode, using a 10 kN load cell together with pneumatic wedge grips operating at a pressure of 100 kPa to avoid slippage in the grips. The specimen was subjected to a sinusoidal load. The gauge length of the specimen was 80 mm, leaving 20 mm gripping length at either end. A thermal camera (FLIR A35sc, USA) was used to monitor the damage evolution. A schematic of the test-set up is presented in Figure 4-3 (a).

Static cord pull-out tests

Static cord pull-out tests were performed on an Instron 5967 (UK) universal mechanical tester using a 1 kN load cell at a crosshead speed of 20 mm/min to determine the average interfacial shear strength (IFSS) τ between cord and rubber. The specimen was fixed in the bottom grip without compressing its lateral surfaces. The carbon cord was extracted by a tensile force from the HNBR matrix. A schematic

illustration of the test set up can be seen in Figure 4-3 (b). The average IFSS τ was derived using

$$\tau = F_{max}/(\pi dL) \quad \text{Equation 4-1}$$

where F_{max} is the peak pull-out force, d is the cord diameter and L is the embedded length [133].

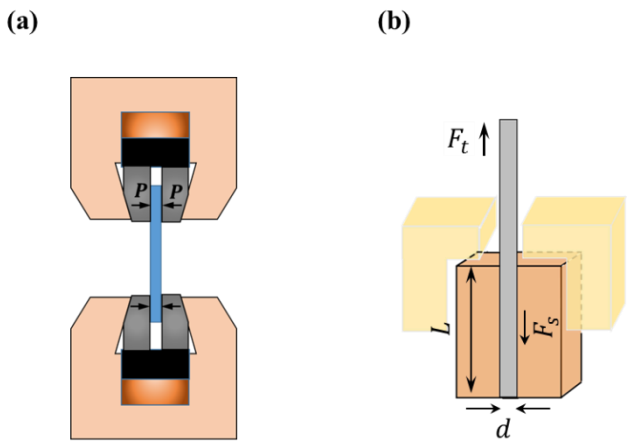

Figure 4-3. Schematic illustration of (a)wedge grip fatigue test set-up, P = 600 kPa, (b) static cord pull-out set-up (not drawn to scale). F_t: pull-out force; F_s: interfacial shear force; d: cord diameter; L: embedded length.

Static cord tensile tests

Static tensile tests of carbon cords were carried out on an Instron 5967 universal mechanical test machine with a 1 kN load cell at a crosshead speed of 250 mm / min. Six repeats were performed for carbon cords with a gauge length of 80 mm. The test set-up is shown in Figure 4-4.

Figure 4-4. Static cord tensile test set-up.

Scanning Electron Microscope (SEM)

The cord-rubber composites were studied before and after failure testing using a FEI Inspect SEM (Netherlands) using sputter gold-coated composite specimens.

Thermogravimetric analysis (TGA) and nitrogen pyrolysis

TGA was performed using a TA Instruments Q500 (USA) to characterise the thermal degradation of the HNBR compound, dried latex and carbon cords under nitrogen atmosphere from 20 °C to 1000 °C at a heating rate of 20 °C/min to help optimise the experimental conditions for nitrogen pyrolysis.

Nitrogen pyrolysis was conducted in a tube furnace (Carbolite STF 16/180, UK). Specimens which had failed during fatigue testing were left in the tube furnace for 1 h at RT with flowing nitrogen. Temperature was then raised to 600 °C with continuous nitrogen flowing and held at 600 °C for 90 min. The specimens were then allowed to cool down overnight to RT under nitrogen. After pyrolysis, the specimens were observed under a digital microscope (Celestron 44302-A, USA). The remaining matrix

rubber with char-like features was either removed with a needle or brushed off with a thin paint brush to reveal the resulting morphology of the embedded carbon cord.

Finite Element Analysis (FEA)

Simulations were built using Abaqus Finite Element Solver (version 6.13, USA) to study the interfacial shear stress distribution between the carbon cord and HNBR matrix in and close to the gripping region. The system was modelled in 3D, utilising natural symmetry such that only half of the system was modelled. It was simulated within the explicit domain, which, whilst not necessarily ideal for modelling elastomers, was required due to the large number of elements (165500 elements) within the system. The simulation was run using dual precision.

The rubber section was modelled as a cuboid of 60 mm length with a cross section of 15 mm × 4 mm. At the centre of this cuboid a 0.7 mm diameter cylindrical cut was extruded to leave space to embed the cord. The carbon cord was modelled as a simple cylindrical cord of 0.7 mm diameter and 65 mm length. The cord was positioned at the centre of the cuboid, with its bottom face flush with the bottom face of the rubber section. The grips were modelled as analytical rigid structures to reduce computational cost. The modelled test system is shown in Figure 4-5 (a).

The carbon cord was modelled with a Young's modulus of 56.7 GPa and a Poisson ratio of 0.3. For the rubber section, its uniaxial tensile test data was fitted to the Yeoh hyperelastic material model where C_{10}= 0.586, C_{20} =0.032, C_{30} =-1.398×10^{-4} (Figure 4-5 (c)) as described in Chapter 2 and a Poisson ratio of 0.495 was used. A tie constraint was applied to bond the rubber section to the cord with the assumption of perfect bonding for simplicity. A penalty friction constraint was assigned between the pneumatic wedge grips and the rubber section. The gripping surfaces of the real test fixture have a textured surface specifically designed to resist specimen slippage,

however, in the FEA model the grips were modelled as analytical rigid with smooth, flat surfaces. Therefore, a higher frictional coefficient μ = 3 was chosen for this interaction to replicate the real gripping surface interaction. Standard C3D8R linear explicit hexahedral elements were used for both the cord and rubber section, while the elements for the rubber section were also assigned to enhanced hourglassing control with additional distortion control. The mesh density was refined in the vicinity of the gripped region and near the core region around the cord, as shown in Figure 4-5 (b).

Two different steps were used to represent the gripping and the straining of the physical specimen. In the gripping step, one of the grips was displaced horizontally into the sample with the other grip being held encastre. The grips were positioned to give a gripping length of 20 mm and to apply a gripping pressure of 600 kPa, which is calculated from the actual pressure applied to close the pneumatic grip and to avoid slippage. In the straining step, both grips were vertically displaced up to 2 mm to apply strain to the specimen. Gripping pressure was maintained at 600 kPa throughout this step.

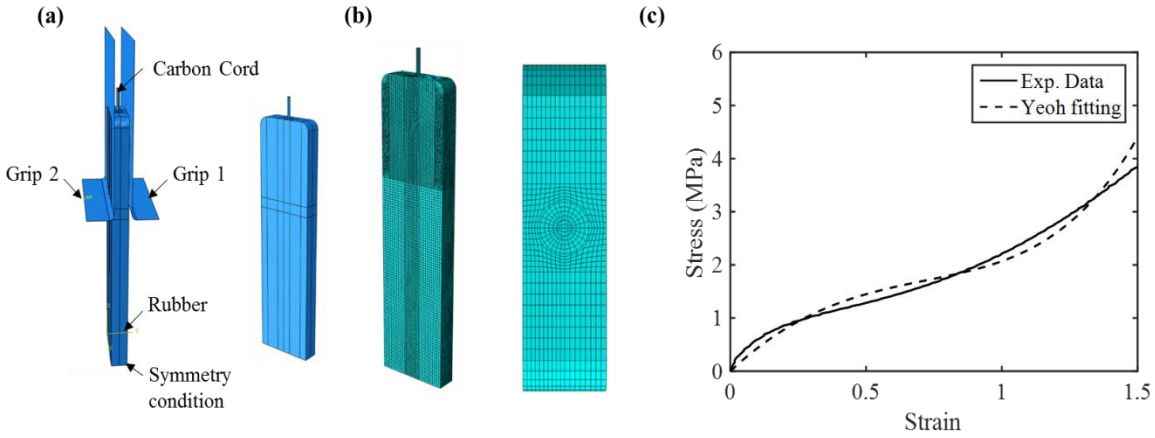

Figure 4-5. (a) Modelled test set-up where only the top half of the system was modelled due to symmetry, (b) meshed assembly, note that the mesh is refined in the vicinity of the gripped region and near the core region around the cord, (c) Yeoh hyperelastic model fitting to the uniaxial tensile data of the HNBR compound at small strains.

Bollard fatigue tests

Figure 4-6 shows the bollard fatigue test set-up which has been designed to characterise the tensile fatigue behaviour of single cord reinforced rubber model composites. Specimen with a total length of 240 mm was used with the cord ends being wrapped around each bollard by 2.5 turns. Moreover, an accurately shaped rubber cushion was applied at the edge of the composite to avoid kinking of the cord.

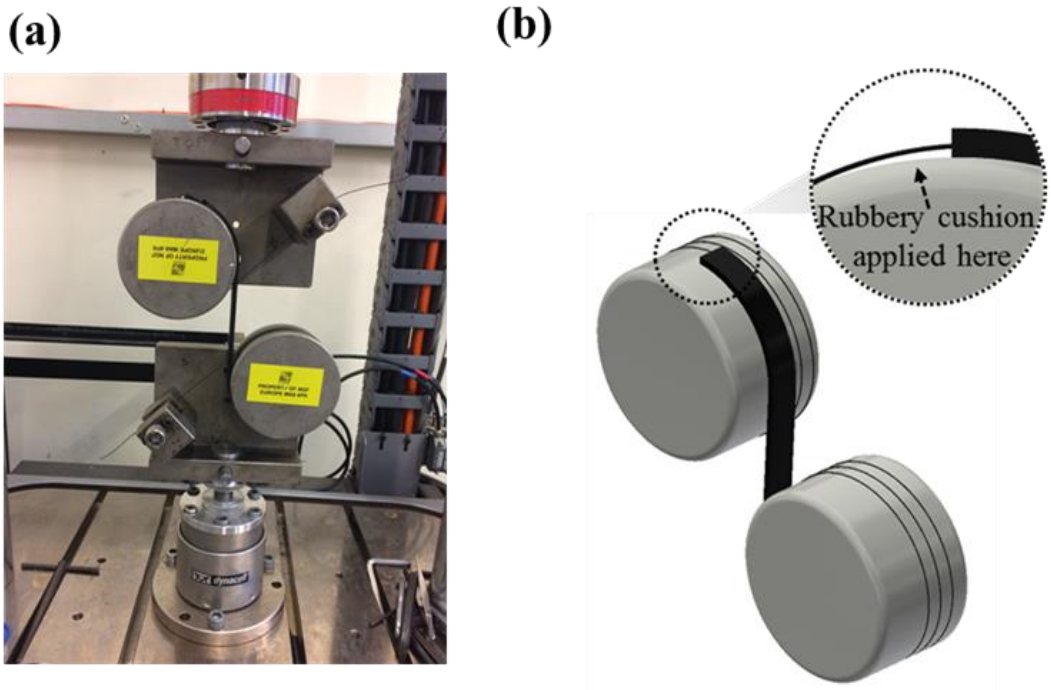

Figure 4-6. (a) Bollard fatigue test set-up, (b) illustration of the bollard test set-up, showing the location of the rubber cushion to avoid kinking of the cord.

4.3 Results and discussions

4.3.1 Damage evolution in cord-rubber composites tested using wedge grips

Figure 4-7 shows the maximum cyclic strain as a function of relative fatigue life N/N_f together with the evolution of interfacial damage in CC-HNBR model

composites as monitored using thermal imaging in the wedge grip based load controlled fatigue tests (Maximum applied stress σ_{max} = 21 % UTS, R = 0.6, f = 2 Hz). Similar maximum cyclic strain profiles were also reported in the work of Lee *et al.*[155] for nylon-rubber composites as well as Shi *et al.*[59] for polyester cord-rubber composites and steel cord-rubber composites [151]. Three stages of deformation were identified during cyclic loading. First, the maximum cyclic strain increased rapidly due to cyclic softening [59]. Then deformation increased progressively at a lower rate until it reached a steady rate, which is the second stage. The slope of this second stage is nearly constant and is defined as the *dynamic creep rate* [155]. In the second stage, damage accumulated through microphenomena such as cord-matrix debonding and matrix cracking with gradual deterioration of bonding between cord and rubber. No obvious temperature rise occurred until $N/N_f = 0.72$. Above this limit, debonding started to develop macroscopically along the cord / rubber interface and this generated larger local strains and thus heat towards the latter stage of dynamic creep (Figure 4-7f and Figure 4-7g). A third stage arose when the rate of increase in maximum cyclic strain surged rapidly, signifying the onset of more substantial amounts of damage. Near the end of the third stage the carbon cord was completely separated from the rubber matrix with circumferential cracks at the interface (Figure 4-7c and Figure 4-7d). The rubber close to the debonded region was highly strained during cyclic loading, leading to a large amount of heat build-up as shown in Figure 4-7h with an approximate 7 °C temperature rise compared to the initial state. However, since the HNBR matrix is not transparent, cord fracture cannot be not easily observed. Further experimental and numerical simulations were carried out to analyse the wedge grip based set-up and to demonstrate this is most likely to lead to shear-dominated interfacial failure only, that is, cord-rubber debonding without cord fracture.

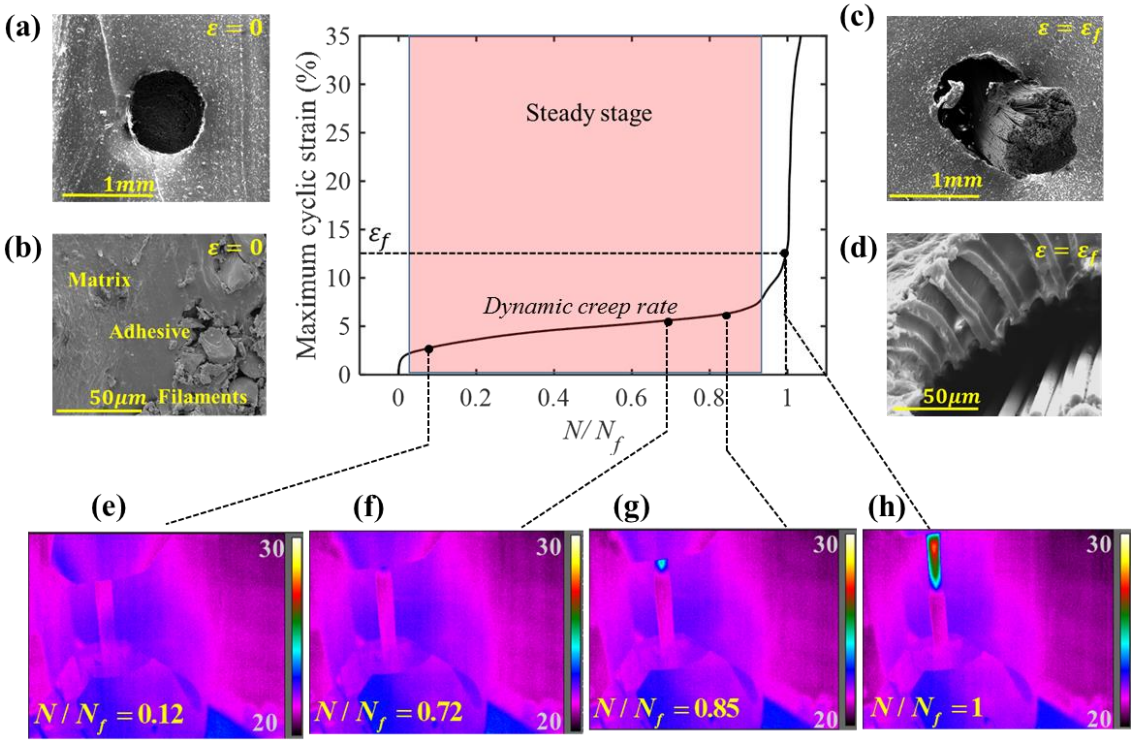

Figure 4-7. Maximum cyclic strain as a function of relative fatigue life N/N_f using thermal imaging in wedge grips load controlled fatigue test (Maximum applied stress σ_{max} = 21 % UTS, R = 0.6, f = 2 Hz) together with interfacial damage evolution in CC-HNBR model composites: (a) sample cross-sectional view in the undeformed state, (b) enlarged view of the interfacial region in (a), showing a well-bonded interface, (c) sample cross-sectional view after fatigue failure, (d) enlarged view of the interfacial region in (c), showing circumferential cracks at the interface; The evolution of debonding during fatigue loading as recorded by thermal imaging: (e) no visible damage, (f) initiation of cord debonding, (g) propagation of debonding, (f) catastrophic failure with cord pull-out.

4.3.2 Fractography of cord-rubber composites tested in wedge grips fatigue set-up

In order to reveal the inner carbon cord, the external HNBR compound was removed using nitrogen pyrolysis. Figure 4-8 (a) presents TGA results of the HNBR compound (rubber matrix used for embedding the carbon cord), dried latex as well as the as-

received carbon cords under nitrogen atmosphere. It can be seen that 20 % weight loss comes from the coatings on the carbon cord. The HNBR compound revealed only one major degradation due to decomposition of polymer chains [156, 157] which started around 300 °C and which was completed at about 500 °C. Unlike the latex, the HNBR compound has a residual mass of 20 wt % at 1000 °C as a result of inorganic additives. Based on TGA data, the temperature for nitrogen pyrolysis was set at 600 °C. It was observed that HNBR matrix formed a very brittle foam char after nitrogen pyrolysis, which could be easily removed. Figure 4-8 (b) shows a representative image of an intact carbon cord after pyrolysis, indicating that all specimens exhibited interfacial failure rather than cord fracture. Therefore, fatigue testing using wedge grips is in fact evaluating only the evolution of interface adhesion and hence is not suitable for assessing the tensile fatigue properties of reinforcing cords embedded in rubber.

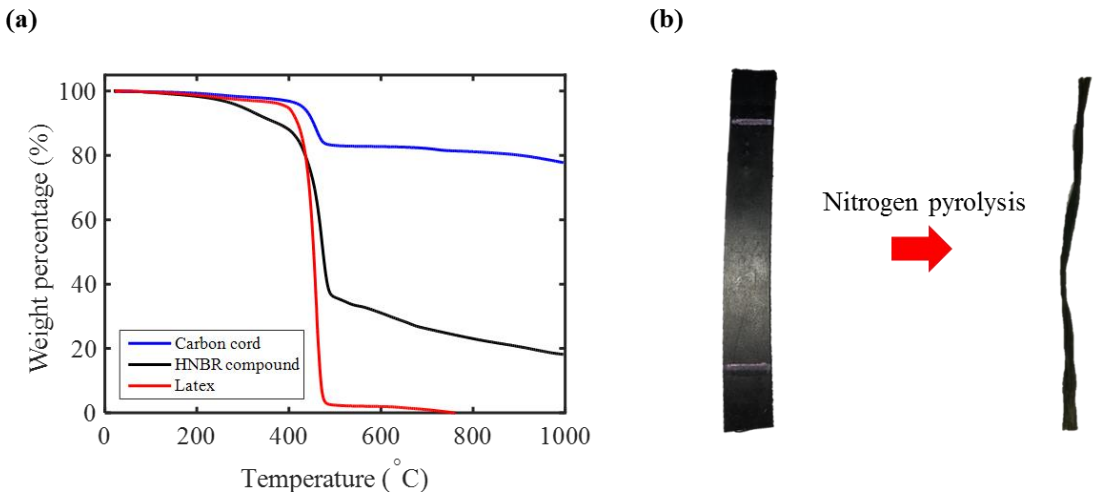

Figure 4-8. (a) TGA results of HNBR compound (rubber matrix), dried latex and as-received carbon cords under nitrogen atmosphere, (b) an intact carbon cord after nitrogen pyrolysis, revealing the absence of cord fracture, with cord-rubber debonding being the main damage mechanism during fatigue testing using wedge grips.

The influence of R ratio (which is the ratio of minimum cyclic load to maximum cyclic load) and test frequency on adhesion fatigue life was investigated using the wedge grips test set-up. The results are shown in Figure 4-9. Similar values of failure strain ε_f (10 - 13 %) were observed in all loading cases regardless of the test frequency or Rratio, supporting the idea that major damage was introduced by the pneumatic wedge grips. The failure strain ε_f is therefore dominated primarily by the clamping geometry and applied pressure. Moreover, the adhesion life had an inverse relationship with the *dynamic creep rate* for all loading cases which was due to the fact that the second stage made up the majority of the specimen's lifetime provided that the failure strain ε_f was similar for all loading cases. In general, however, a change in R ratio and frequency had negligible effect on the interfacial adhesion fatigue life for the values used in this study. This result found for the wedge grip based fatigue tests would be questionable if we generalised it to predict tensile fatigue of cord-rubber composites as the damage reflected more the nature of clamping rather than real experimental parameters.

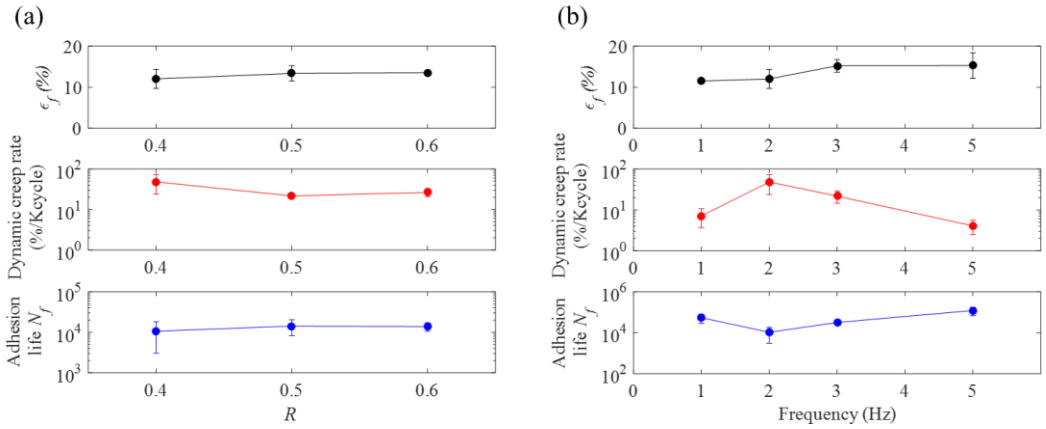

Figure 4-9. (a) Effect of R ratio on the failure strain ε_f, dynamic creep rate and adhesion life at f = 2 Hz andσ_{max}= 370 MPa, (b) effect of frequency at R = 0.4 and σ_{max}= 370 MPa, both showing similar failure strain at different frequencies and an inverse relationship between dynamic creep rate and adhesion life.

4.3.3 Determination of critical length L_c of cord-rubber composites

The underlying mechanism in the absence of cord fracture was interpreted in terms of classical stress transfer model as introduced in Chapter 3 in detail. Shear lag model [36, 37]leads to the concept of critical fibre length L_c, which is the minimum length at which the mid-point of the fibre reaches its failure strength, given by;

$$L_c = \sigma_f d/(2\tau) \qquad \text{Equation 4-2}$$

where $\sigma_f$is the cord strength, τ is the average interfacial shear strength (IFSS) between cord and matrix, and d is the cord diameter. When the embedded cord length is less than L_c, the cord cannot fracture in the rubber matrix as the tensile stress along the cord cannot reach the cord's strength.

As mentioned in Chapter 3, both experimental techniques such as fibre fragmentation tests [3] as well as analytical models and numerical simulations [49, 158-161] allow for the estimation of L_c. In this study, cord pull-out tests and cord static tensile tests were employed in order to measure the average IFSS $\tau$and cord strength $\sigma_f$and through this it allows for the estimation of the critical fibre length L_c for the CC-HNBR system.

Figure 4-10 (a) shows a representative force-extension trace for a carbon cord pull-out experiment from a HNBR matrix with an embedded cord length of 19.1 mm. Three stages occur during the pull-out process [43]: (1) Elastic deformation ending with the initiation of debonding. (2) Propagation of debonding accompanied by small load drops until catastrophic interfacial failure. The small load drops in the curve represent debonding fronts propagating intermittently rather than continuously [42]. (3) Final pull-out of the cord via a frictional sliding mechanism. Figure 4-10 (b) shows the

relationship between peak pull-out force F_{max} and embedded area πdL, with the slope of the best linear fit line being the IFSS τ which is listed in Table 4-1.

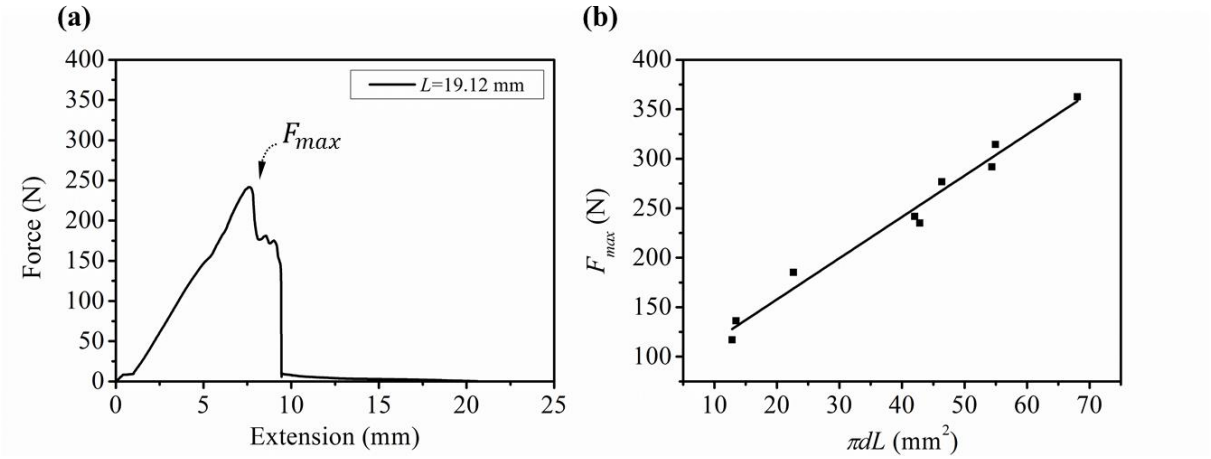

Figure 4-10. (a) Three stages of deformation in the force-extension trace for a cord pull-out experiment with an embedded cord length of 19.1 mm, (b) the relationship between peak pull-out force F_{max} and embedded area πdL. The average interfacial shear strength (IFSS) τ is determined from the slope of the best linear fit.

The strength of the carbon cord was calculated by maximum breaking force recorded by intron machine divided by the cross sectional area of the cord by assuming it is a perfect cylindrical shape with a diameter of 0.7 mm as mentioned in 4.2.1. Its strength distribution was characterised by a two-parameter Weibull distribution [162, 163], given by

$$F(X) = F\{\sigma_f \leq X\} = 1 - \exp[-(X/\theta)^{\beta}] \qquad \text{Equation 4-3}$$

where $F(X)$ is the cumulative failure probability, σ_f is the carbon cord strength, θ, β are the scale parameter and the shape parameter respectively.

Taking the natural log of both sides twice gives;

$$\ln\big(-\ln\big(1 - F(X)\big)\big) = \beta \ln(X) - \beta ln\theta \qquad \text{Equation 4-4}$$

The estimated Weibull parameters θ and β were calculated from the slope and the intercept in a $\ln\left(-\ln\left(1-F(X)\right)\right)$versus$\ln(X)$ plot respectively, as shown in Figure 4-11 (a). The two-parameter Weibull distribution of the carbon cord with a gauge length of 80 mm and its Weibull parameters are shown in Figure 4-11 (b) and Table 4-1, respectively.

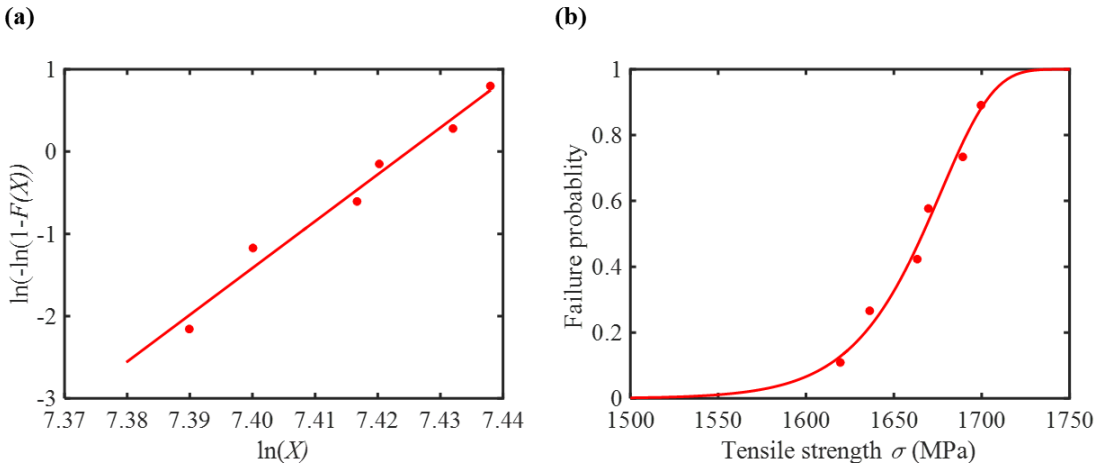

Figure 4-11. (a) $\ln\left(-\ln\left(1-F(X)\right)\right)$ versus $\ln(X)$ plot. Weibull parameters θ and β were taken from the slope and the intercept respectively, (b) the two-parameter Weibull distribution of carbon cords with a gauge length of 80 mm.

Table 4-1. IFSS τ and Weibull parameters of carbon cords.

Properties	Value
τ (MPa)	4.2 ± 0.2
σ (MPa)	1663 ± 33
β	1677
θ	56.9

The strength of carbon cords σ_f together with the IFSS τ gives a value of L_c falling into a range of 130 - 150 mm according to Equation 4-2. In our earlier investigation the gauge length of the composite was 80 mm which is much less than L_c. Therefore, no cord fracture should arise at least in theory. In this case, cord-rubber debonding is expected to be the main failure mode, as has already been observed experimentally.

4.3.4 Numerical simulations of interfacial stress distribution in cord-rubber composites

Simulation were carried out to reveal quantitatively the interfacial damage introduced by clamping using wedge grips. Figure 4-12 shows the shear stress (S_{13}) distribution and maximum principal stress ($S_{\text{max. principle}}$) distribution after lateral gripping and straining steps. After simulated gripping, it can be seen that a dominant shear stress occurs in the clamping region (Figure 4-12a and Figure 4-12c) as a result of a lateral compressive force applied to the surface of the specimen. A peak value of 0.61 MPa was found near the top edge of gripping area. Upon uniaxial loading, the shear stress develops further by the friction between the specimen surfaces and the grip faces [153]. Once a critical displacement has been reached, the gauge length region also begins to deform.

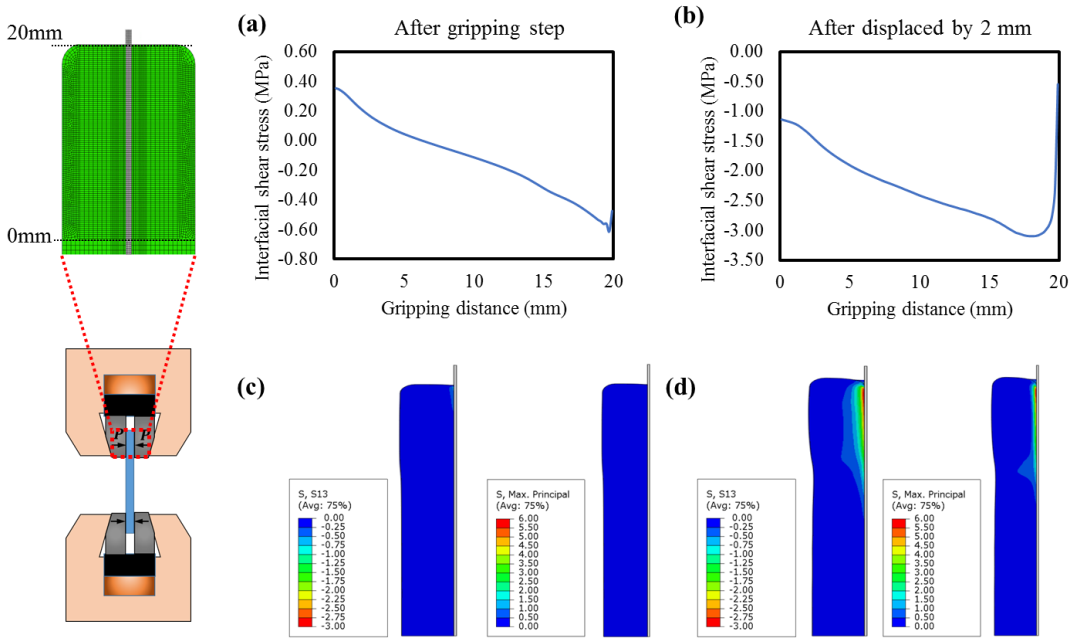

Figure 4-12.(a) Interfacial shear stress in clamping region after wedge gripping action and, (b) after uniaxial straining action, (c) shear stress (S_{13}) distribution and maximum principal stress ($S_{\text{max. principle}}$) distribution in the model after gripping action, and (d) after uniaxial straining action.

Analysing the shear stress field in the model (Figure 4-12b), it can be seen that the shear stress reached a peak value of 3.09 MPa when the grips were displaced by 2 mm, with the shear stress profile circumnavigating the carbon cord, which was affected by the bulging of the rubber originated from the mismatch in elastic properties of the cord and the surrounding HNBR matrix. Since damage tends to initiate in the weakest region in specimens under uniaxial cyclic loading, considering that the measured IFSS from cord pull-out tests was 4.2 MPa and the shear stress concentration at the gripping region with the peak value being approximately three quarter that of the IFSS value, it can be expected from FEA results that debonding is most likely to initiate in the gripping region and propagate along the interface as observed by the thermal imaging. These FEA results further highlight the limitations and the high risk of introducing excessive damage in the interfacial region of unidirectional cord-rubber composites

using wedge grip based test set-up. Therefore, it is clearly necessary to develop an alternative test method to tackle this issue which is especially encountered during fatigue testing. This will be addressed in the following section.

4.3.5 Bollard fatigue testing and comparison with traditional wedge grips testing

For mechanical testing of fibrous materials, the grip design often incorporates a capstan structure to reduce the stress within fibre ends through friction and hence overcomes fibre failure at the jaws faces. The stress reduction is related to the frictional coefficient μ between the contact surface and testing materials as well as the sweeping angle ϕ in radians, known as the capstan effect, given by the Euler-Eytelwein equation [164, 165];

$$T_2 = T_1 e^{\mu\phi} \qquad \text{Equation 4-5}$$

where T_1 and T_2 are two forces in Figure 4-13 (a). Figure 4-13 (b) shows T_2/T_1 as a function of sweeping angle ϕ for difference contact surfaces ($\mu_{rubber-rubber}$=1.16, $\mu_{rubber-stainless\ steel}$=0.64). It can be seen that T_2/T_1 increases exponentially with frictional coefficient μ and the sweeping angle ϕ.

Inspired by this, we propose an alternative design using bollard grips that were specially designed for tensile or fatigue testing of cord-rubber composites. In this scenario T_1 is the tension within the cord end, T_2 is the tension in the cord embedded in the rubber matrix. The value of T_2/T_1 increases significantly by wrapping around each bollard by 2.5 turns and applying circular rubber sleeves onto the bollards (with a resulting conversion from rubber-metal contact to rubber-rubber contact). Since T_2 depends on the applied cyclic load, the tension within the cord end T_1 is dramatically reduced so as to avoid end fracture.

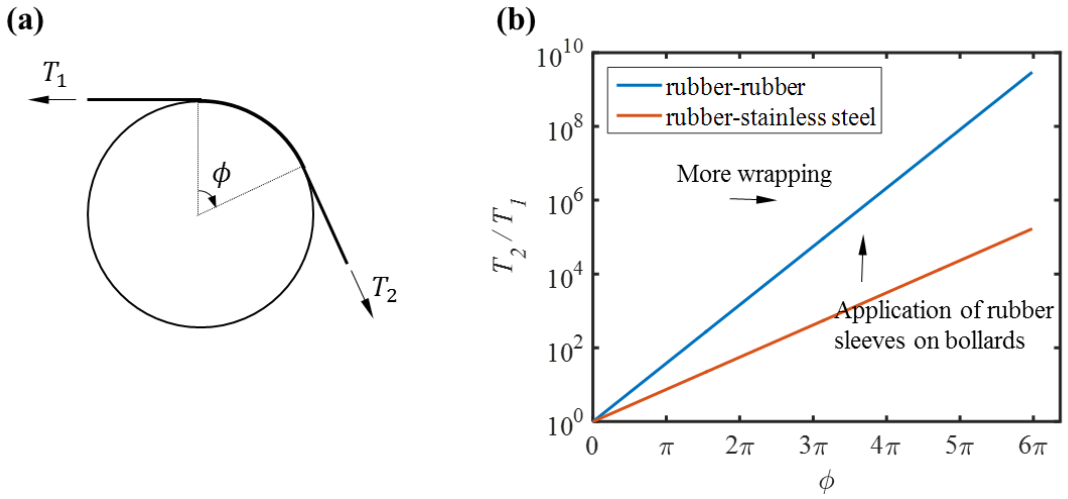

Figure 4-13. (a) Two forces T_1 and T_2on a string in contact with the capstan, showing T_2/T_1 is related to the sweeping angle ϕ, (b)T_2/T_1 as a function of sweeping angle ϕ for rubber-rubber, rubber-stainless steel contact surfaces ($\mu_{rubber-rubber}$ = 1.16, $\mu_{rubber-stainless\ steel}$ = 0.64), showing a significant increase in T_2/T_1 by either more wraps around the bollard or using a circular rubber sleeve around the bollard.

A typical bollard based fatigue test was carried out at maximum applied cyclic stress σ_{max} = 70 % UTS, R = 0.3 and f = 5 Hz. Figure 4-14a shows cord breakage in the gauge section of the specimen as recorded by thermal imaging in the form of a bright spot. This was later confirmed by nitrogen pyrolysis (Figure 4-14b). It should be noted that since the length of specimen used in bollard test setup is 240 mm, the tested bollard specimens had to be cut manually in order to fit them into the container for nitrogen pyrolysis. Compared to the conventional wedge grips based set-up, the bollard based fatigue test set-up has the advantage of avoiding the application of excessive lateral compressive forces to the specimen so as to minimise shear stress concentration in the gripping region. In this way, it avoids undesirable failure in the form of debonding whilst it facilitates a cord fracture process in the gauge section of the specimen.

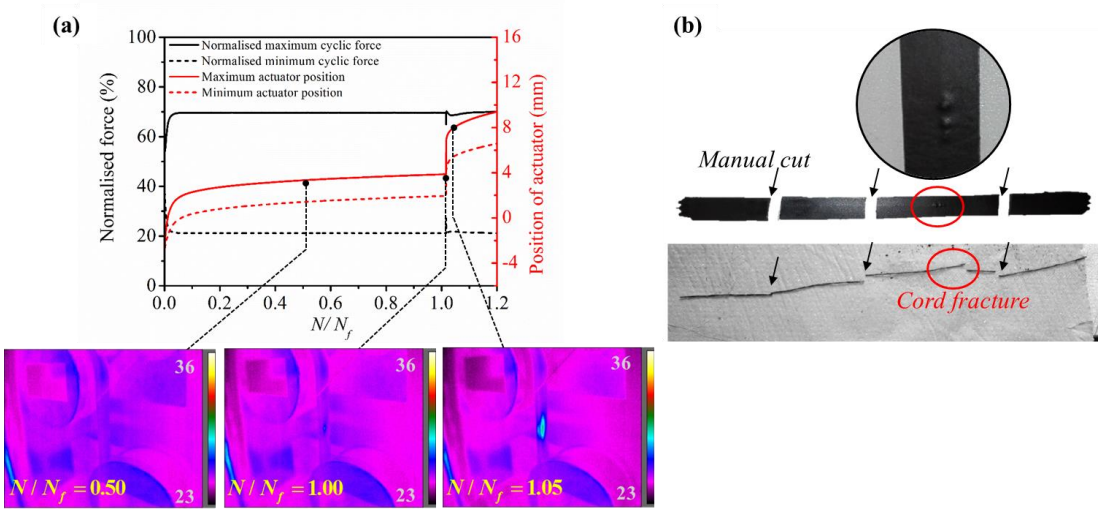

Figure 4-14. (a) A typical example of normalised maximum and minimum cyclic load together with the actuator position as a function of relative fatigue life N/N_f in a load controlled test mode (σ_{max} = 70 % UTS, R = 0.3 and f = 5 Hz), showing the cord fracture process as monitored by thermal imaging in the bollard fatigue test set-up and considerable heat build-up after cord fracture, (b) embedded cord breakage in the gauge section of the specimen as revealed after nitrogen pyrolysis, indicating a cord dominated fatigue failure mechanism.

Figure 4-15 compares the fatigue test results between bollard tests and wedge grips tests. It can be seen that the S-N data shifts significantly upwards when changing from the bollard test to the wedge grips test set-up. For instance, the specimen can withstand a normalised maximum cyclic stress level (σ_{max} / UTS) of 80 % for approximately 10^3 cycles to failure in the bollard test, as compared to just 30 % in the case of the wedge grip test, suggesting a 165% rise in fatigue stress. This implies that specimens will last much longer in bollard tests under nominally similar testing conditions. This is due to the fact that the bollard based fatigue test set-up is now actually measuring the cord dominated composite fatigue behaviour, which is dominated by the progressive breakdown of individual fibres in the reinforcing cord embedded in rubber rather than by interfacial debonding as observed in wedge grip fatigue testing. Clearly,

the ultimate tensile strength of the carbon cords is orders of magnitude higher than the IFSS, as reported earlier. Therefore, the effectiveness of the current bollard test set-up for the fatigue characterisation of cord-rubber composites has been successfully demonstrated.

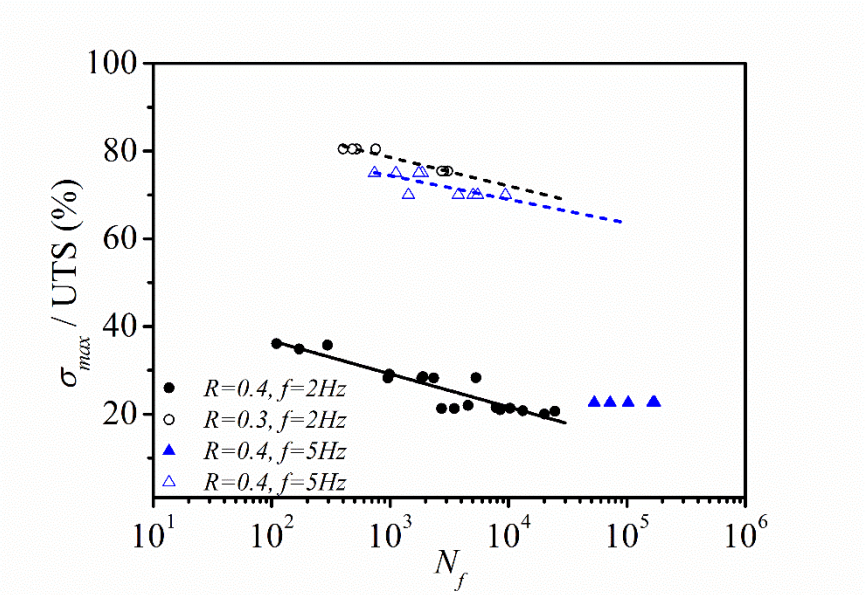

Figure 4-15. Tension-tension fatigue data obtained from the wedge grips test set-up (filled markers) and bollard test set-up (unfilled markers), indicating significantly increased fatigue stresses (165%) for the bollard based test. The lines fitted through data points are a guide for eye.

4.4 Conclusions

An experimental investigation of the interfacial damage evolution in a single carbon cord reinforced HNBR model composite was initially carried out using a conventional wedge grips based fatigue test set-up. Three stages of deformation were identified and it was concluded that specimens failed in a shear-dominated interfacial failure mode which initiated in or close to the gripping region, rather than by a failure mode that involved fracture of the cord. This was confirmed by nitrogen pyrolysis and interpreted by classic stress transfer theories as well as finite element analysis.

An alternative novel bollard test set-up was developed which avoids the unfavourable clamping effects introduced by wedge grips and allows for a true examination of fibre-dominated fatigue failure in cord-rubber composites. A comparison of wedge grips versus bollard based fatigue tests data revealed significantly increased fatigue stresses (~165%) and a greatly improved fatigue life for the bollard based test methodology. This was explained by a change in failure mode from interfacial debonding as a consequence of an artefact induced by wedge grips to actual cord fracture in the case of the bollard based test method. In short, the proposed bollard test set-up has proved itself as a reliable test method and should therefore be introduced as the method of choice for the tensile fatigue testing of the cord-rubber composite examined in our study. Having now established a reliable and reproducible fatigue test set up a detailed fatigue characterisation and life prediction of cord-rubber composites using the bollard fatigue test using this approach is reported in the following chapter.

Chapter 5 : Fatigue of carbon cord-rubber composites in tension.

5.1 Introduction

As is noted in Chapter 3, there are very few studies reported in the literature on the fatigue behaviour of flexible cord-rubber composites while most fatigue studies have focused on rigid fibre reinforced plastics (FRPs). Nevertheless, it seems appropriate to treat these studies as a guide for relevant cord-rubber composite studies, albeit these materials show significantly different viscoelastic behaviour of the polymer matrix.

However, as is discussed in Chapter 3, even on the subject of the frequency effect on the fatigue life of FRPs, the conclusions are not always consistent, depending on the type of materials tested, the loading mode and the experimental parameters employed in each study.

In terms of *R* ratio effects, improved crack resistance of pure rubber materials was observed in non-relaxing loading conditions for both strain-crystallising rubbers such as natural rubber (NR), butyl rubber (IIR), silicone rubber, and ethylene propylene diene monomer (EPDM) attributed to the presence of microcrystalline regions being created at the crack tip [166] and non-strain crystallisation rubbers such as styrene butadiene rubber (SBR) due to less strain energy in each cycle compared to those tested in fully relaxing loading conditions[12]. For cord-rubber composites, fatigue behaviours have also been studied for wire reinforced NR composites and textile-SBR/BR/NR rubber blends composites as reviewed in Chapter 3. However, no relevant work has been conducted on the cord reinforced hydrogenated nitrile butadiene rubber (HNBR) composites (to the best knowledge of the author).

Therefore, a good knowledge of how various loading parameters such as the frequency and *R* ratio affect their fatigue performance is required to validate the behaviour of products made using such cord-rubber components.

An accurate life prediction of composite materials has remained a challenging task over the years due to their complex failure modes (fibre fracture, debonding, matrix cracking and delamination). As mentioned in the Chapter 3, different from isotropic materials such as metals or rubbers whose fatigue life can be generally predicted by fracture mechanics resulting from a relatively simple failure mechanism. [167, 168] For these materials the failure initiates from a single crack and propagates until it reaches a critical size. Cumulative damage models and analytical constant life diagram (CLD) models are two commonly used methods for the life estimation ofmore complex materials such as anisotropic composites, with CLDs only being based on a mathematical analysis of limited subset of fatigue data and circumventing detailed understanding of the way fatigue damage affects the residual properties of the examined material.

Chapter 4 reported that a premature interfacial failure in the carbon cord reinforced hydrogenated nitrile butadiene rubber (CC-HNBR) composites arose when they were tested using pneumatic wedge grips. This problem was avoided when the composites were subsequently tested using bollard grips to avoid crushing the specimen in gripping region. The aim of this chapter is to evaluate the effects of testing frequency and *R* ratio on the tensile fatigue behaviour of the CC-HNBR model composite systematically again using the bollard grip test set-up. The heat build-up and the possible microstructural change of the material during fatigue loading were also analysed. Furthermore, modifications were made to the original Harris's CLD model for lifetime prediction of the CC-HNBR composite. The applicability of four other

CLD models was also investigated for comparison. This chapters shows that a modified Harris's CLD and piecewise linear CLD models give the most accurate lifetime predictions.

5.2 Experimental

5.2.1 Materials and sample preparation

The same hydrogenated nitrile butadiene rubber (HNBR) compounds and carbon cords that were used in chapter 4 were used again in this work. Details about how to prepare the CC-HNBR composite test sample are detailed in section 4.2.2

5.2.2 Fatigue characterisation of the CC-HNBR samples in tension

Tension-tension fatigue tests were performed using an Instron E10000 (UK) dynamic test machine with a 10 kN load cell in a load-controlled mode. This mode was selected to avoid buckling of the specimen which is often a major issue in a displacement-controlled test due to the cyclic strain softening of the material. The CC-HNBR composite specimen was installed in specially designed bollard clamps instead of conventional wedge grips as discussed in detail in Chapter 4 to avoid shear stress concentrations caused by the gripping, as shown in Figure 4-5. The specimens were subjected to a sinusoidal waveform. Maximum cyclic load was applied at 65 %, 67.5 %, 70 %, 72.5 %, 75 % and 80 % of maximum breaking force (F_{max}) of the CC-HNBR composite for a wide range of R ratios (*i.e.*, R=0.3, 0.4, 0.5, 0.6 and 0.7) and test frequencies (*i.e.*, f=2, 5, 10 and 20 Hz). All the tests that did not fail were stopped at a million cycles. This limit is defined as a run-out in this study. Five repeats were performed for each loading case. Additionally, the surface temperature of the specimen was monitored using a thermal camera (FLIR A35sc, USA). Test parameters encountered in a fatigue test are shown in Figure 5-1.

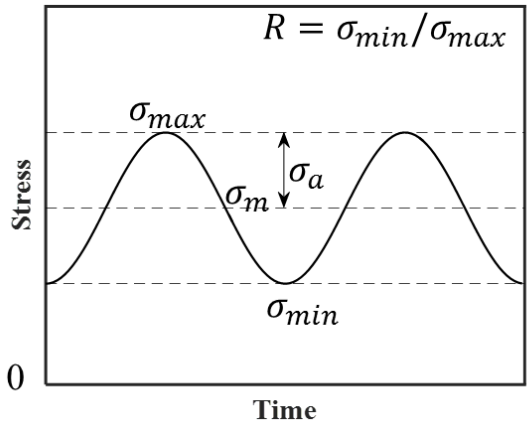

Figure 5-1. Fatigue test parameters, σ_{max}: maximum cyclic stress; σ_{min}: minimum cyclic stress; σ_m: mean stress; σ_a: alternating stress, $R = \sigma_{min}/\sigma_{max}$.

5.2.3 Differential scanning calorimetry (DSC)

A low temperature crystallisation study of the HNBR compound was carried out using a DSC 25 (TA instrument, USA). Samples with a mass of around 5 - 10 mg were sealed in aluminium pans and then cooled from 20 °C to a targeted isothermal holding temperature for a pre-defined period, as listed in

Table 5-1. After this annealing step, samples were further cooled down to - 90 °C and then heated to 90 °C at 10 °C / min. A DSC scan of a sample without the annealing step was also performed for reference. Due to partial overlapping of the glass transition region and the crystallisation peak, the crystallisation peak area was calculated by integrating the peak area between -40 °C to 10 °C for all specimens as suggested by Alcock et al [88].

Table 5-1. Summary of DSC scans under various isothermal holding temperatures and isothermal holding periods.

Isothermal holding temperature (°C)	Isothermal holding time (h)				
	1	3	6	12	24
0				×	
-10				×	
-20	×	×	×	×	×
-30				×	

5.2.4 Wide-angle X-ray diffraction (WAXD) measurements of the HNBR compound

In order to study the strain induced crystallisation (SIC) of the HNBR compound, specimens of width 2 mm × thickness 0.8 mm were pre-stretched to targeted strains (0, 100 % and 200 %) and then fixed onto a home-made rack for one-dimensional WAXD measurements (X'Pert Pro, PANalytical, Almelo, The Netherlands).

5.3 Results and discussions

5.3.1 Failure criterion and definition of N_f

Stiffness loss of the composite materials during fatigue testing is often considered as a failure criterion and the observed cycle corresponding to a sudden stiffness degradation is often defined as the fatigue failure life [67]. In this study, however, since the CC-HNBR model composite is reinforced by a single continuous carbon cord, catastrophic failure of this reinforcing cord will lead to a sudden increase in the level of extension without a major loss in stiffness. Therefore, the cycle corresponding to a sudden increase in the actuator position is here defined as fatigue life N_f in the

load-controlled fatigue test, as shown in Figure 5-2. It should be noted that the specimen was not completely torn apart at this fatigue failure point (life ratio N/N_f= 1) due to limited traveling stroke of the actuator (60 mm), but the sample was at least partially intact. Further stretching was necessary to completely rupture the specimen, which could happen at elongations comparable to the elongation at break of the pure rubber.

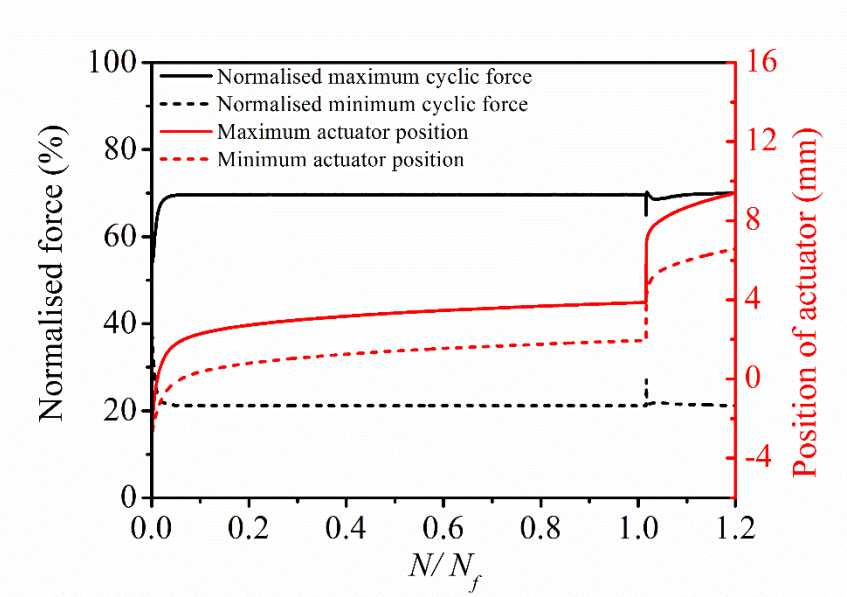

Figure 5-2. A typical example of normalised maximum and minimum cyclic force and the actuator position values as a function of fatigue life ratio N/N_f in a load controlled fatigue test at f = 5 Hz and R = 0.3. The observed cycle corresponding to a sudden increase in the position of the actuator is defined as the fatigue failure life N_f. Displacement amplitude (roughly 1 mm) experienced by the specimen can be seen from the difference of maximum and minimum cyclic value in the actuator position before failure of the specimen.

5.3.2 The effect of frequency and temperature monitoring

Since the ultimate tensile strength (UTS) of the CC-HNBR composite is commercially confidential, the level of applied maximum cyclic stress σ_{max} was indicated as the percentage of the UTS in this study. Figure 5-3 (a) presents the effect

of cyclic loading frequency on the number of cycles to failure for differentσ_{max} levels at R = 0.3. A slight increase in fatigue life was observed with increasing frequency at higher stress level (σ_{max} = 80 % UTS) while it did not appear to be affected greatly by test frequency at lower stress levels (σ_{max} = 70 % UTS and 75 % UTS) except for the loading case at σ_{max} = 70 % UTS and f = 2Hz. Overall, variations in the fatigue life were not significant in the test frequency domain except for the loading case at σ_{max} = 70 % UTS and f = 2Hz, which is discussed later in this section.

In order to further interpret the frequency effect, self-heating was investigated via thermal imaging. Figure 5-3 (c) shows the total temperature rise under different loading cases. It is worth noting that temperature measurements using thermal cameras tend to be superficial as heat can easily transmit into the environment [67]. The inability to do *in-situ* temperature monitoring might therefore underestimate the temperature inside the specimen. Regardless of this potential deficiency, no obvious temperature rise was observed for all the loading cases at a frequency up to 20 Hz. Even for the worst case, the surface temperature rose by only 2 °C at σ_{max}= 80 % UTS and f = 20 Hz. This increment was negligible compared to values reported inliterature where, for instance, up to 100 °C increment was measured for a nylon fibre reinforced elastomeric composite at 10 Hz [68] or even thermal failure that arose in the form of matrix softening, necking and melting in talc filled polypropylene at 20 Hz [64]. The temperature evolution as a function of the life ratio N/N_f for variousσ_{max} levels at 20 Hz is also shown in Figure 5-3 (d). This very small temperature increment in the range of the stress levels and frequencies evaluated in this study can be explained as a result of extremely small displacement amplitudes (roughly 1 mm) experienced by the specimen in a load controlled test, as shown in Figure 5-2, as a consequence of the high stiffness of the composite materials which is dominated by the reinforcing carbon

cord. It explains, in turn, that frequency did not significantly affect the fatigue life in our study provided that the temperature increase was minimal for all loading cases.

Upon further increasing frequency beyond 20Hz, there might be considerable heat build-up as well as a significant change of the viscoelastic properties of the materials especially the rubber matrix, leading to a lower fatigue life. However, unfortunately, the machine would gradually lose its precision on targeted minimum and maximum loads and cause severe vibrations as the testing frequency approaches to the test frame resonant frequency. It is therefore practically difficult to conduct fatigue tests beyond 20 Hz.

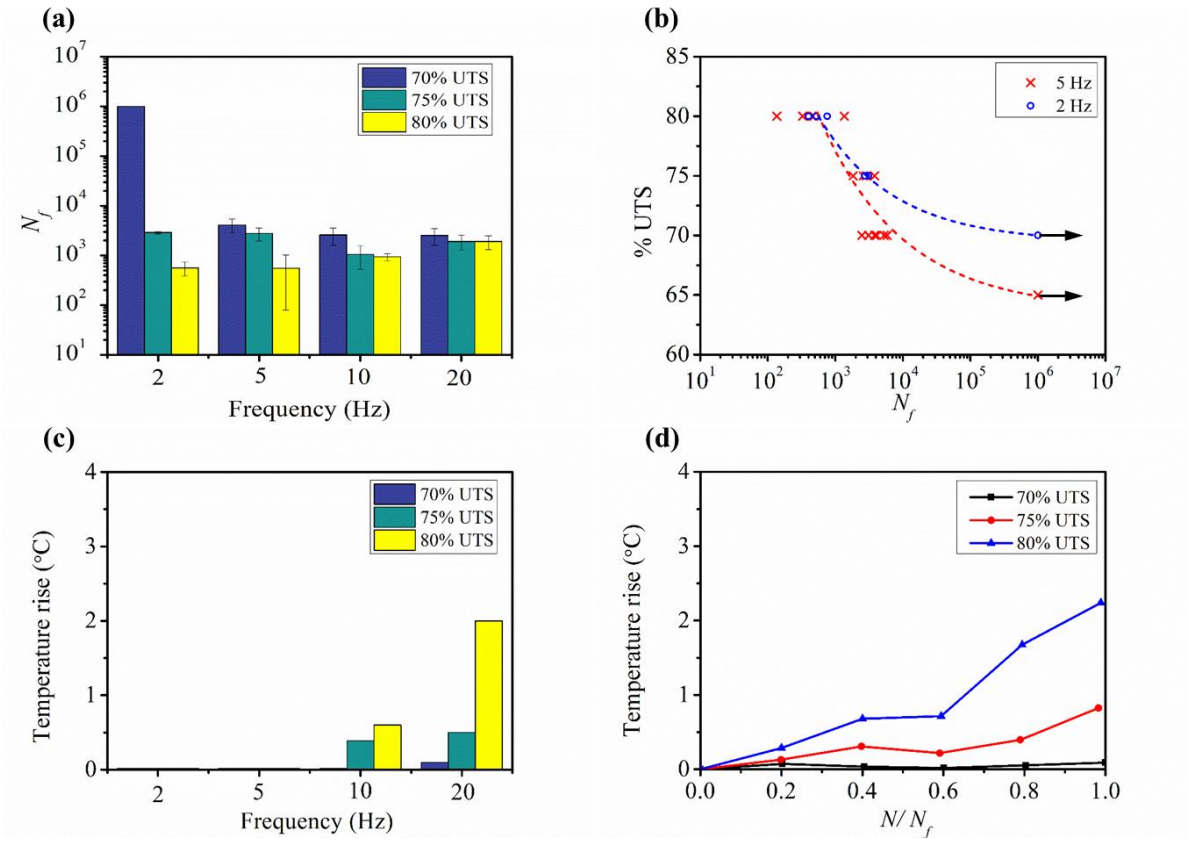

Figure 5-3. (a) Effect of frequency on the number of cycles to failure N_f at R = 0.3 and σ_{max} = 70 % UTS, 75 % UTS and 80 % UTS, showing rather similar fatigue life in terms of cycles to failure except for the loading case ofσ_{max}=70 % UTS and f = 2 Hz, (b) S-N data at R = 0.3 and f = 2 Hz and 5 Hz, indicating that lowering test frequency resulted in a rise in fatigue limit, the level of σ_{max} is normalised by the UTS,(c) temperature rise for various loading cases at R = 0.3, indicating negligible heat-build-up, (d) temperature evolution at differentσ_{max} levels at 20 Hz.

Efforts were made to calculate the theoretical temperature rise ΔT, given by

$$\Delta T = T_{sample} - T_{ambient} = \frac{f \cdot E_{diss}}{V} \cdot \frac{t^2}{8K} \qquad \text{Equation 5-1}$$

Where f is the frequency, E_{diss} is the dissipated energy which can be calculated from the hysteresis loops during fatigue testing, V is the sample volume, t is the sample thickness, K is the thermal conductivity, which is in the range of 0.2 ~ 0.3 $W/(m \cdot ℃)$ for all the rubbers [12]. The matlab code for energy calculation is shown in Appendix.

The temperature estimation for various loading cases at a frequency of 5 and 10 Hz were shown in Table 5-2. It can be seen in Figure 5-3 (b) that the theoretical temperature rise is greater than that measured experimentally. This is because the system is not adiabatic and therefore some of the dissipated energy is transmitted to the external environment away from the test piece.

Table 5-2. The temperature estimation for various loading cases at a frequency of 5 and 10 Hz.

Frequency (Hz)	$\sigma_{max}/\ UTS$	E_{diss} (mJ)	ΔT (°C)
5	70%	129.5	1.35
	75%	109.3	1.14
	80%	112.2	1.17
10	70%	114.7	2.39
	75%	104.0	2.17
	80%	96.5	2.01

Interestingly, the loading case at σ_{max} = 70 % UTS and f = 2Hz was more complicated. The fatigue life changed from a certain finite life to an infinite life when reducing frequency from 5 Hz to 2 Hz at the same stress level. Careful examinations of S-N data indicated that the use of lower frequency tended to increase the fatigue limit below which no damage accumulation occurred. Since the slope of the S-N curve often represents the strength degradation rate of materials [68], damage accumulated in a milder way at 2 Hz as shown in Figure 5-3 (b). Once it reaches a critical stress level, the specimen at lower frequency (2 Hz) did not fail at the pre-defined run-outs (10^6 cycles) while those at higher frequency (5 Hz) were still likely to fail. Similar findings were also reported previously in [68] for a nylon fibre reinforced elastomer matrix composite and a short glass fibre reinforced polyamide 6 [75].

Another indication from the frequency effect study is that increasing testing frequency can be used as an effective method to reduce testing time as long as the heat generation of the system is negligible [74]. Figure 5-4 shows the required test time decreased with the usage of higher frequency for different σ_{max} levels, respectively. By increasing the testing frequency, the total loading duration until the sample failure will become shorter at the same level of σ_{max}.

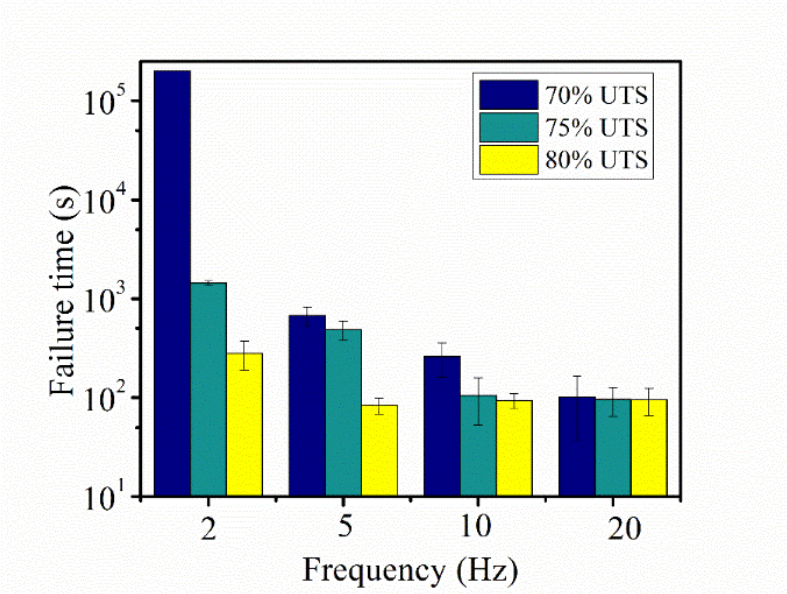

Figure 5-4. Effect of test frequency on the time to failure at R = 0.3 and σ_{max} =70 % UTS, 75 % UTS and 80 % UTS respectively, showing a time-dependent fatigue failure phenomenon of the CC-HNBR composite.

5.3.3 The effect of *R* ratio and crystallisation of HNBR compound

Figure 5-5 shows the S-N data at f = 10 Hz and at different R ratios. The data was plotted separately to avoid partial overlapping. The S-N data shifted gradually to the right when R increased from 0.3 to 0.7. Similar trend was also observed at f = 5 Hz, as shown in Figure 5-6. Unlike the findings of Lee et al. [68] that there was a critical R ratio corresponding to an optimised fatigue life resulting from the nonlinear stress-

strain behaviour of their material, the fatigue life of the CC-HNBR composite increased monotonically with increasing *R* ratio. This is due to its fairly linear static tensile behaviour controlled by a single carbon cord.

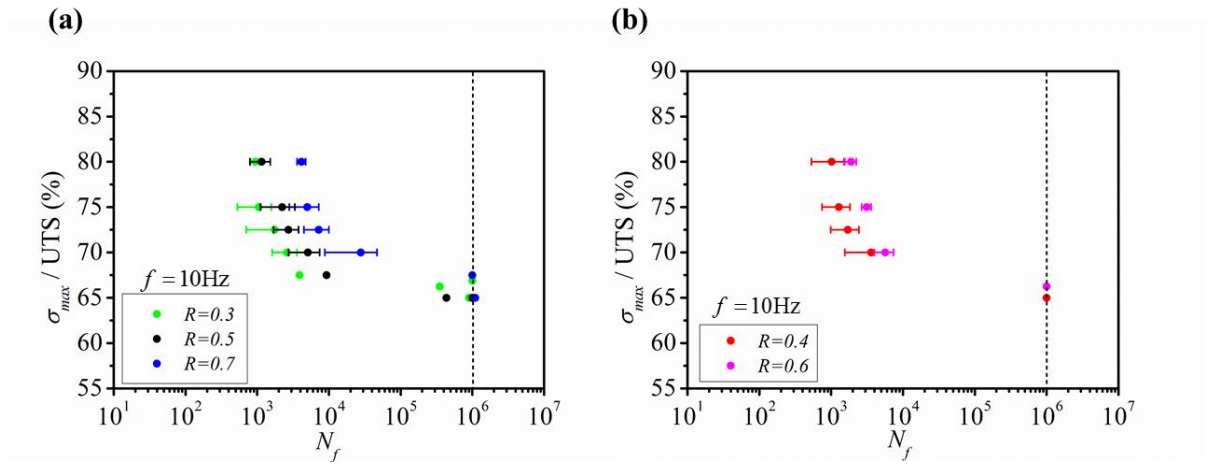

Figure 5-5. S-N data of CC-HNBR composite at f = 10 Hz for (a) R = 0.3, 0.5 and 0.7, (b) R = 0.4 and 0.6, showing higher cycles to failure at a higher R ratio.

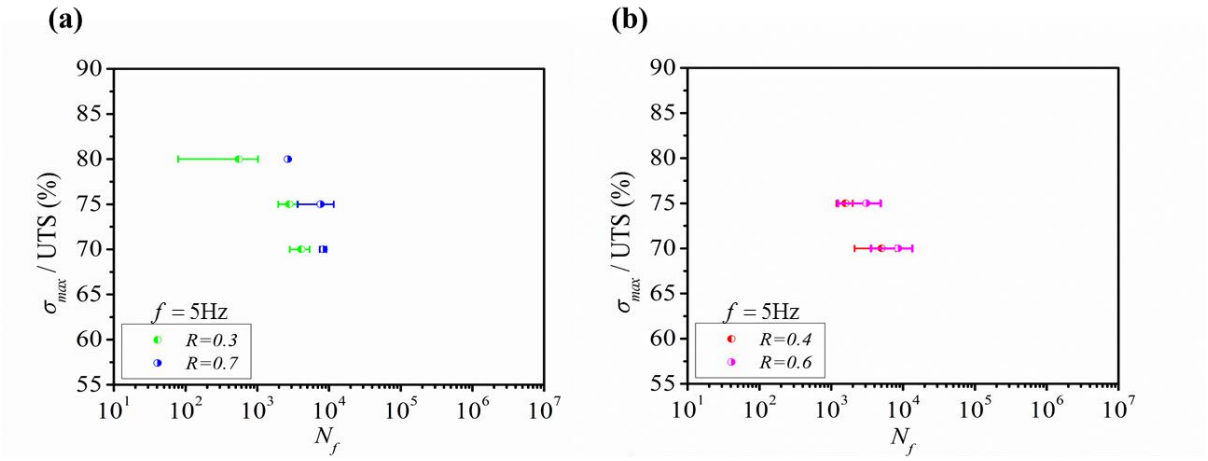

Figure 5-6. Normalised S-N data of CC-HNBR composite at f = 5 Hz for (a) R = 0.3 and 0.7, (b) R= 0.4 and 0.6, showing higher cycles to failure at a higher R ratio.

The improved fatigue life in the non-relaxing loading conditions is attributed to crack-arrest effects as a consequence of strain-induced crystallisation (SIC) of the

HNBR at a filament break. The carbon cord was fully impregnated with an HNBR latex system. Therefore, polymer chains from the HNBR matrix are present and can be thought to have migrated between carbon filaments within the cord during the cord preparation or during compression moulding. As a result, when studying the microstructural fatigue failure modes of the carbon cord-rubber composites it is appropriate to treat the carbon cord itself as a mini composite. It is an HNBR reinforced by 6000 carbon filaments. SEM image of a cross-sectional view of the carbon cord is shown in Figure 5-7 (a). The failure process of a polymer impregnated carbon cord is completely different from that of dry bundles. For a dry bundle subjected to tensile loading F_1, the weakest fibre will fail first and the surviving fibres will share the load released by the failed fibre equally and instantaneously (global load sharing). If none of fibres fail at the next stress level, the fibre bundle will not fail upon unloading and reloading to F_1 assuming there is no time-dependant failure process. However, in the case of an impregnated cord or composite subjected to a tensile load F_2 which has the equivalent influence (causing the same fibre to fail as the F_1 for dry bundles), only fibres close to the broken fibre will carry additional load released by the broken fibre (local load sharing). The broken fibre may also debond locally from the matrix whilst the matrix surrounding the fibre break will be highly strained and deform inelastically and irreversibly. Due to this irreversibility, repeated unloading and reloading causes a change of the stress state in the fibres and matrix, leading to damage accumulation until catastrophic failure [169]. In this sense, the HNBR close to a filament break might crystallise due to a significantly higher level of local strain compared to the global strain. The presence of such a microcrystalline region can cause crack blunting or deflection, which is beneficial to hinder crack propagation within the carbon cord and thus slows down the failure process, as illustrated in Figure

5-7 (b). It is proposed that a longer life at higher R ratio is related to the dynamic process of forming and melting of crystallites during loading and unloading. Considering constant σ_{max}, with higher R ratio, the HNBR shows more tendency to form crystallites during loading due to a higher mean cyclic stress σ_m whilst it shows a lower tendency to melt due to a higher level of minimum strain experienced by the specimen during unloading, leading to the accumulation of micro-crystallites at the crack tip. In addition, a fully relaxed and melted crystal at the crack will have to be reloaded to reform a new crack resisting crystal. This is not an instantaneous process and the kinetics are such that an increment of crack growth will take place before a new reinforcing crystal is developed.

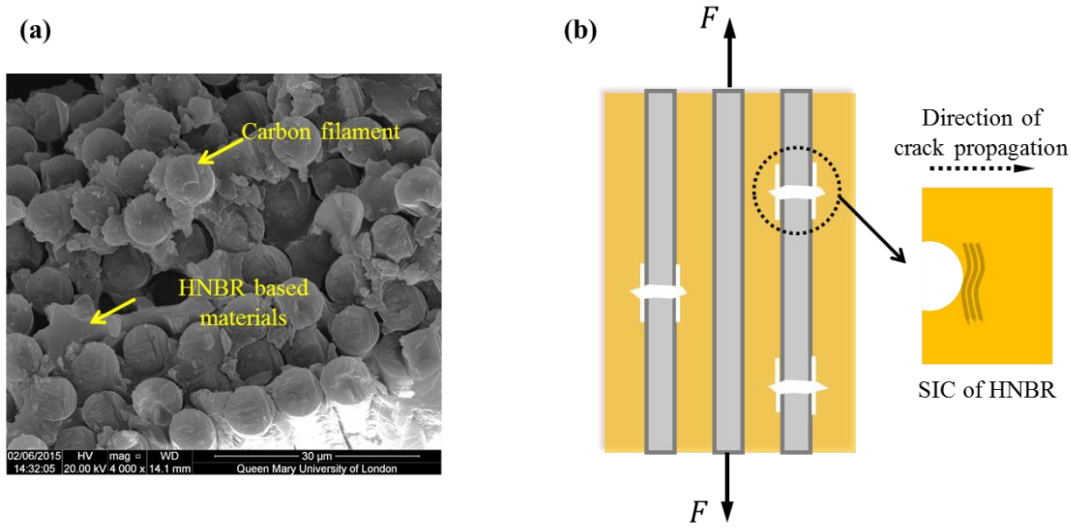

Figure 5-7. (a) SEM image of cross-sectional view of the carbon cord, showing HNBR surrounding the carbon filaments, (b) illustration of impregnated cord fracture scenario under tensile load F, showing filament breakage, debonding and crystals formation at the tip of a crack which slows down or even inhibits the crack propagation (filament scale).

The crystallinity was developed due to the alternating sequence of hydrogenated butadiene (BD) and acrylonitrile (ACN) for the HNBR with high ACN contents whilst

attributed to the tetramethylene groups at low ACN contents [84, 87]. The configurational entropies of the stretched network polymers ΔS_f decreased by orientation along the direction of the applied force. Crystallisation will occur when $T\Delta S_f < \Delta H_f$. Therefore, crystallinity may develop at an elevated temperature (like room temperature) as a result of a smaller ΔS_f compared to the unstretched state [10, 170, 171]. Low temperature crystallisation of the HNBR compound was therefore studied initially by DSC to demonstrate its crystallisation capability.

Figure 5-8 (a) shows the DSC curves with and without annealing the HNBR compound at various temperatures for 12 h. It exhibited a step change corresponding to its glass transition temperature T_g at approximately -23 °Cshortly followed by a very small hump, which denotes a very low degree of crystallinity [88] for the case of isothermal holding at 0 °C for 12 h and non-isothermal holding. In contrast, DSC curves of isothermal holding at -10 °C, -20 °C and -30 °C show crystallisation peaks, especially at an isothermal holding temperature of -20 °C with distinctive glass transition and melting transitions. Therefore, further experimental investigations with respect to the effect of isothermal holding time on crystallisation were conducted at -20 °C. The results are shown in Figure 5-8 (b). Both the onset and melting peak temperature were increased with annealing time (Figure 5-8c). Since a higher melting temperature is related to an improved crystal structure and larger crystal size [172, 173].This suggests that a longer exposure to low temperatures facilitates the perfection of crystal formation during annealing. Crystallinity developed during isothermal holding was roughly estimated by assuming it is related to the alignment of adjacent tetramethylene groups and thus the melting enthalpy value of fully crystalline linear polyethylene (ΔH_{PE}=293 J / g) was used as reference [174]. Crystallinity was then deduced from the ratio of normalised melting enthalpy during the heating scan to

ΔH_{PE}.Figure 5-8 (d) shows the effect of isothermal holding time on the resulting crystallinity. Indeed, a larger amount of microcrystallites were formed after longer low-temperature storage times.

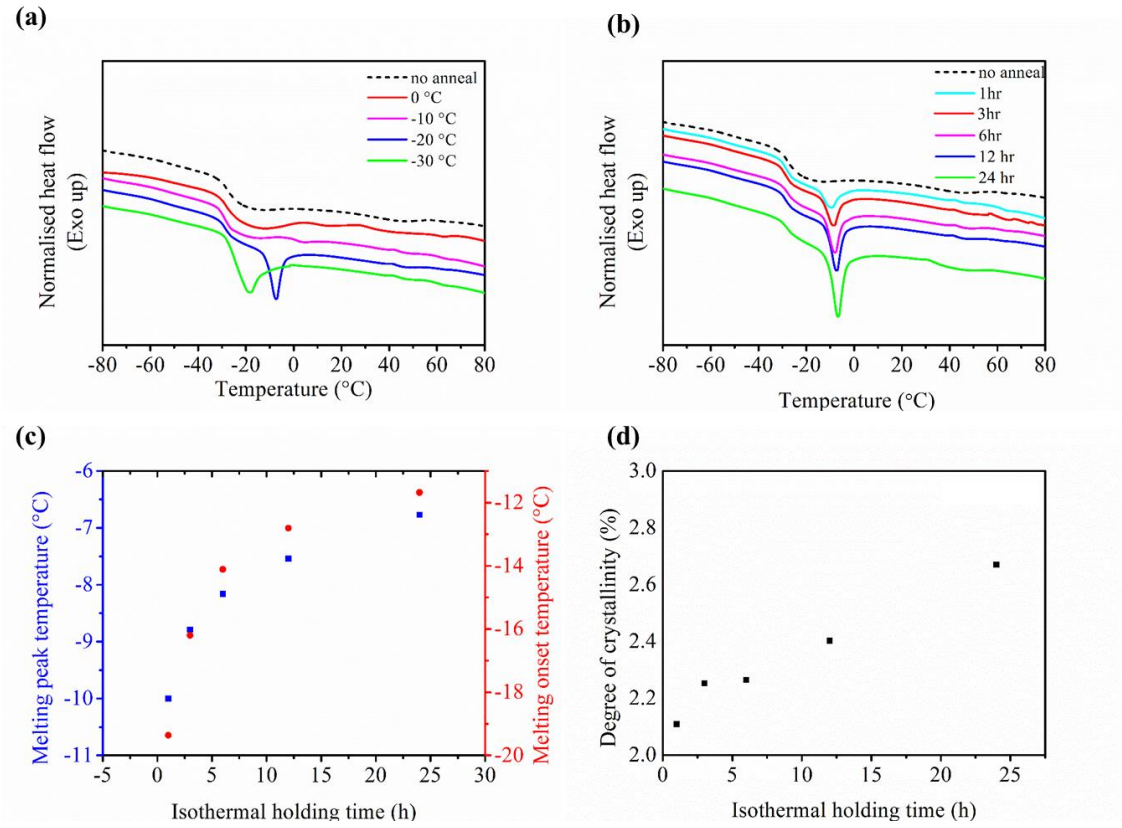

Figure 5-8. (a) DSC curves with and without annealing the HNBR at various temperatures for 12 h, (b) DSC curves with and without annealing the HNBR at -20 °C for various isothermal holding periods, (c) melting onset and peak temperatures after annealing the HNBR at -20 °C for various isothermal holding periods, showing an increase in melting temperature and suggesting more perfect crystal formation after longer isothermal holding period, (d) crystallinity after annealing the HNBR at -20 °C for various isothermal holding period, indicating large amounts of microcrystallites were formed at longer exposure times to low temperatures.

Previous wide-angle X-ray diffraction (WAXD) work has confirmed that the two characteristic diffraction angles (2θ) of stretched HNBR lie at 19 ° and 23 ° [86]. However, in this case experiments were conducted offline and it would be beneficial

to perform real-time WAXD measurements. Recently, Narynbek Ulu *et al.* detected SIC in HNBR containing 44 wt. % ACN on-line and reported that SIC initiated at 250 % strain during loading while subsequently crystallites melted completely at 140 % strain during the unloading at 20 °C[89]. In this study, WAXD experiments were conducted offline on stretched HNBR compound at 0, 100 % and 200 %strains due to the practical difficulty to accessing a synchrotron X-ray source. The results are shown in Figure 5-9. The reducing intensity is attributed to the smaller thickness as the specimen was uniaxially stretched to a higher strain. Specimens at an unstretched state and a strain level of 100 % exhibited a broad peak which was indicative of an amorphous structure [175] while specimens at a strain level of 200 % seemed to have a new sharp peak at 2θ = 23°. However, this peak was relatively hard to identify and might be questionable due to considerable noise which was related to the type of materials as materials of low crystallinity often cause high noise levels, quantity of specimens tested and the scanning programs. In addition, all of the specimens showed sharp peaks which came from inorganic additives such as Calcite (2θ = 29.41°, 39.38° and 47.53°), ZnO (2θ = 31.78°, 34.45°, 36.28°, 47.58° and 56.61°) and MgO (2θ = 43.02°) as indicated by arrows respectively [176]. Psarras *et al.*[177]reported similar WAXD pattern for an unfilled HNBR containing 21 % ACN content at an unstretched state. They calculated the degree of crystallinity as the ratio of the area under the peak at 19° against the area under the entire WAXD profile, leading to a value of crystallinity of 30 %. Their calculation method could be possibly problematic since the current samples did not show sharp and well-defined peaks belonging to the examined HNBR. The reasons why there was no obvious crystallinity detected are explained below. First, the crystallinity developed by stretching is low whilst the threshold for detection of crystallinity by regular X-ray diffraction (XRD) is

approximately 3 - 5 % [178]. The maximum crystallinity developed during low temperature exposure was less than 3 % and the crystallinity developed by stretching was anticipated to fall into a similar range. Secondly, WAXD measurements in this study are not immediate and *in-situ*. The microcrystals formed during the stretching will melt during the shelf period with HNBR molecules relaxing.

Therefore, the low temperature crystallisation behaviour of the HNBR compound has been successfully demonstrated with potential to crystallise at elevated temperature as revealed by WAXD.

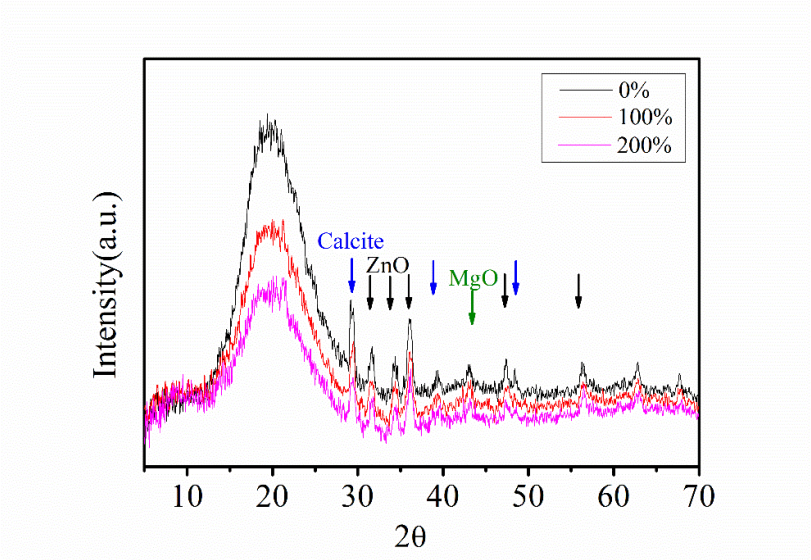

Figure 5-9. WAXD diffractograms of the HNBR compound, with arrows indicating peak positions of calcite, ZnO and MgO, respectively. Specimens at an unstretched state and at a strain level of 100 % exhibited a broad peak which is indicative of amorphous structures while specimens at a strain level of 200 % developed a sharp peak at $2\theta = 23°$.

5.3.4. Construction and analysis of a modified Harris constant life diagram (CLD)

Harris et al. [98] proposed initially a CLD model for the fatigue lifetime prediction of FRPs on the basis of a mathematical analysis of S-N data, covering an entire range

of R ratios varying from tension-tension (T-T), tension-compression (T-C) to compression-compression (C-C) loading conditions. Constant−life curves in the form of bell-shaped curves were identified and described by a relationship between normalised alternating stress a and normalised mean stress m. Additionally, the ultimate compressive strength (UCS) of the material is a compulsory parameter for construction of the model. As cord-rubber composites have a strong tendency to buckle under compressive loads, a proper determination of the UCS is practically difficult. For this reason, some modification must be made to the original Harris CLD model so as to broaden its applicability for lifetime estimation of cord-rubber composites. In this section, the procedures involved in establishing such a modified Harris CLD model will be presented in detail. The key step is to deduce a simple but appropriate mathematical formulation to describe the shape of the obtained constant life diagrams without the necessity of introducing the UCS. Later, its effectiveness was evaluated by comparing these model predictions with experimentally determined fatigue data.

The S-N data of f = 10 Hz at R = 0.3, 0.5 and 0.7 together with the UTS of the CC-HNBR composite was used for the purpose of the model construction. Similar to the construction of Harris' CLD model, first the most suitable mathematical function was selected to fit the average S-N data at three different R ratios. For instance, power [67] and linear [179] were commonly suggested forms depending on the shape of the S-N data. In this study, two-term power law fitting was employed due to the shape of S-N curve, as shown in Figure 5-10 (a), in the form of

$$\sigma_{max} = A[\log(N_f)]^B + C \qquad \text{Equation 5-2}$$

where A, B and C are fitting parameters. The data points in Figure 5-10 (a) are the average fatigue life. It should be noted here that although the sample didn't fail after 10^6 cycles, the data points corresponding to the fatigue limit are also used for fitting of S-N data. The values of A, B, C at different R ratios were determined by a least square method and tabulated together with the corresponding *coefficient of determination* r^2 in Table 5-3.

Table 5-3. Coefficients B, C and corresponding r^2 for S-N curves at R = 0.3, 0.5 and 0.7. Note*: The value of A is covered for confidentiality.

R value	A	B	C	r^2
0.3	*	-7.676	1097	0.9689
0.5	*	-5.533	1088	0.9898
0.7	*	-8.499	1138	0.9996

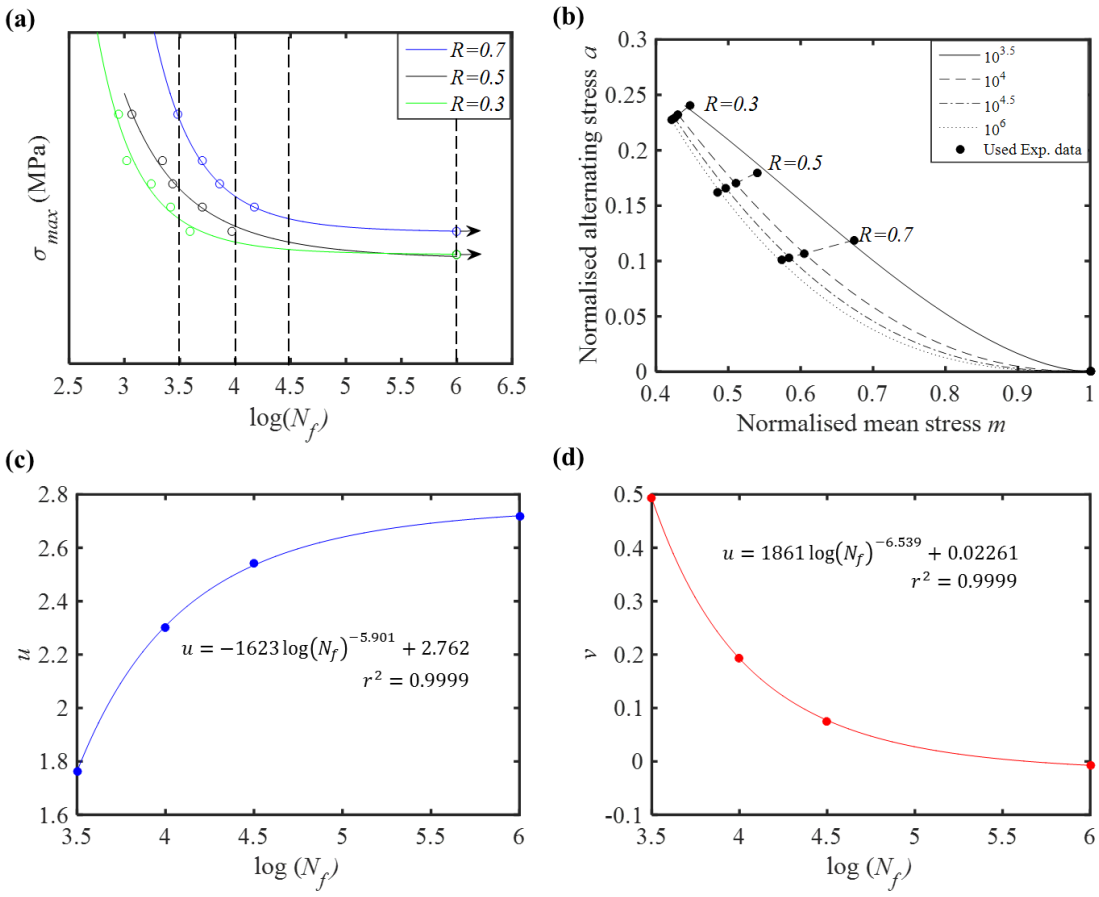

Figure 5-10. (a) Fitted curves by a two-term power law together with the average S-N data of three R ratios at various stress levels. Interpolations were made at $10^{3.5}$, 10^4, $10^{4.5}$, 10^6 cycles indicated by the dashed lines. The exact values of σ_{max} are not shown on the y axis due to confidentiality; (b) Nonlinear curve fitting in the form of $a = (1-m)^u m^v$ through (m, a) data pairs indicated by dots; (c) The values of u for four constant-life curves ($10^{3.5}$, 10^4, $10^{4.5}$ and 10^6), showing u as a function of N_f; (d) The values of v for four constant-life curves ($10^{3.5}$, 10^4, $10^{4.5}$ and 10^6), showing v as a function of N_f.

It can be seen in Figure 5-10 (a) that the S-N curves at three R ratios consisted of two parts between 10^3 and 10^6: In the first part, a continuous stress decline was observed as the fatigue life increased from 10^3 to $10^{4.5}$. In the second part, a stress plateau was found from approximately $10^{4.5}$ to and 10^6. Such a shape of the S-N curves has been reported previously for Kevlar-49 fibre reinforced epoxy composites [97]

and near-alpha titanium alloy (Ti-8Al-1Mo-1V) tested at R = 0.1 [180]. Considering the intrinsic shape of the S-N curves, interpolations were made at $10^{3.5}$, 10^4, $10^{4.5}$ and 10^6 cycles. The corresponding values of σ_{max} at three different$R$ ratios were obtained, with each σ_{max} corresponding to a unique data pair (m, a) calculated using Equation 5-3 and Equation 5-4. The values of m and $a$are listed in Table 5-4 and Table 5-4, respectively.

$$m = \frac{\sigma_m}{\text{UTS}} = \frac{(\sigma_{max}+\sigma_{min})}{2\text{UTS}} = \frac{(\sigma_{max}+\sigma_{max}\times R)}{2\text{UTS}} = \frac{\sigma_{max}(1+R)}{2\text{UTS}} \quad \text{Equation 5-3}$$

$$a = \frac{\sigma_a}{\text{UTS}} = \frac{(\sigma_{max}-\sigma_{min})}{2\text{UTS}} = \frac{(\sigma_{max}-\sigma_{max}\times R)}{2\text{UTS}} = \frac{\sigma_{max}(1-R)}{2\text{UTS}} \quad \text{Equation 5-4}$$

Subsequently, data pairs (m, a) were plotted at the $m - a$ plane together with the UTS of the materials (i.e. (1, 0) at $m - a$ plane). An initial examination of different non-linear mathematical formulations was conducted using Matlab for fitting constant-life curves through the data points. It was found that non-linear curve fitting in the form given by Equation 5-5 yielded the best results, as shown in Figure 5-10 (b).

$$a = (1 - m)^u m^v \quad \text{Equation 5-5}$$

where u and v are functions of N_f,

$$u = -1623 \log(N_f)^{-5.901} + 2.762 \quad \text{Equation 5-6}$$

$$v = 1861 \log(N_f)^{-6.539} + 0.02261 \quad \text{Equation 5-7}$$

The values u and v of each constant life curve together with its fitting functions in the form of a two-term power law were shown in Figure 5-10 (c) and (d), respectively. As a result, the fatigue life of the CC-HNBR composite at f = 10 Hz can be predicted once the test conditions are known (that is once the value of a and m are known) by solving the three simultaneous equations above.

Table 5-4. Summary of values of m at R = 0.3, 0.5 and 0.7 at selected lives $10^{3.5}$, 10^4, $10^{4.5}$ and 10^6.

	Cycles at interpolation			
m	$10^{3.5}$	10^4	$10^{4.5}$	10^6
R = 0.3	0.4467	0.4309	0.4257	0.4225
R= 0.5	0.5398	0.5100	0.4969	0.4856
R= 0.7	0.6745	0.6052	0.5844	0.5734

Table5-5. Summary of values of a at R= 0.3, 0.5 and 0.7 at selected lives $10^{3.5}$, 10^4, $10^{4.5}$ and 10^6.

	Cycles at interpolation			
a	$10^{3.5}$	10^4	$10^{4.5}$	10^6
R = 0.3	0.2405	0.2320	0.2292	0.2275
R = 0.5	0.1799	0.1700	0.1656	0.1619
R = 0.7	0.1190	0.1068	0.1031	0.1012

Further efforts were made to assess the accuracy of the modified Harris CLD model by making comparisons with actual experimental data for several representative loading conditions at R = 0.4 and 0.6. These results are shown in Figure 5-11 (a) and Table 5-6. It can be seen that predictions given by the modified Harris CLD model were in a good agreement with experimental data, with an overall error of less than 36 % and better predictive power in moderate cycle regions.

It needs to be pointed out that the modified Harris CLD model has some limitations particularly in the high-cycle region, especially from $10^{4.5}$ to 10^6 cycles. This is due to

the intrinsic appearance of an S-N curve, which typically asymptotes to a horizontal line, at the fatigue limit.

Additionally, the modified Harris CLD model revealed the combined effect of mean stress and alternating stress on the fatigue life of CC-HNBR composites, as shown in Figure 5-11 (b). It can be seen that m is required to increase twice as much as$a$ when crossing the constant-life lines, implying the failure process was dominated by alternating stress. It should be noted that scaling of the y axis is half that of the x axis.

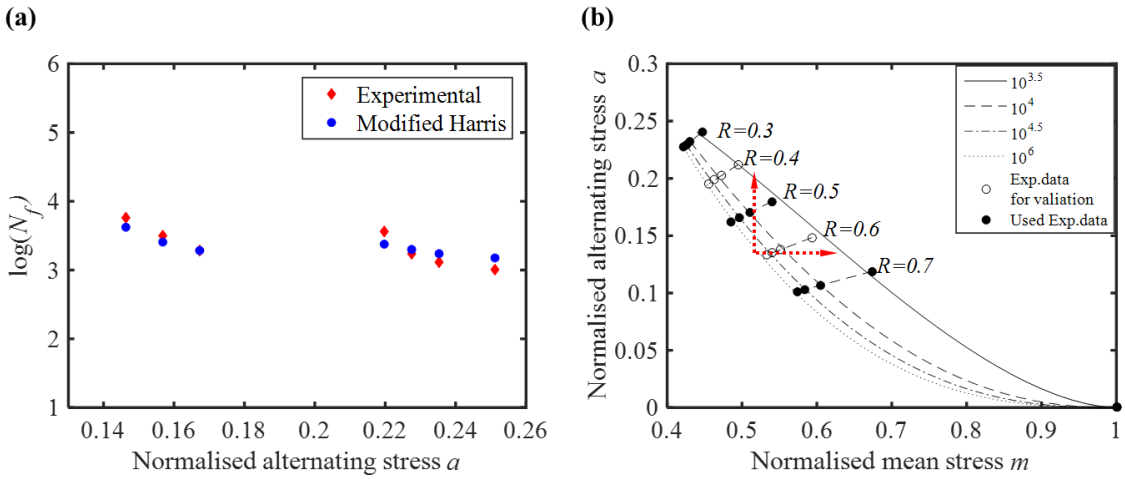

Figure 5-11. (a) Comparisons between the modified Harris CLD predictions and actual experimental data obtained for several loading cases at R = 0.4 and 0.6 at a frequency of 10 Hz, (b) the modified Harris CLD predictions, indicating that alternating stress dominates the failure process. Note that scaling of the y axis is half that of the x axis.

Table 5-6. Comparison between predictions made by the modified Harris CLD model and actual experimental data obtained for several loading cases at R = 0.4 and 0.6 at f = 10 Hz.

R	% UTS	m	a	Experimental average $N_{f,E}$	Standard deviation	Modified Harris $N_{f,H}$	Error (%)
0.4	70	0.5126	0.2197	3611	2058	2364	34.52
0.4	72.5	0.5309	0.2275	1706	722	1974	15.70
0.4	75	0.5492	0.2354	1288	543	1749	35.88
0.4	80	0.5858	0.2511	1021	489	1485	45.39
0.6	70	0.5858	0.1464	5680	1686	4169	26.61
0.6	75	0.6276	0.1569	3135	474	2575	17.86
0.6	80	0.6695	0.1674	1895	346	1898	0.14

Note: Error (%)=$\left|N_{f,H} - N_{f,E}\right|/N_{f,E} \times 100\%$

5.3.5 Evaluation of other CLD models

Attempts were also made to demonstrate the potential of four other widely used CLD models (that is, linear, piecewise linear[94], Kawai's CLD [77]and Kassapoglou's CLD[99]) for the life prediction of the CC-HNBR composite. For the construction of the linear model, the fatigue data at R = 0.3 was used while data at R = 0.3, R = 0.5 and R = 0.7 was used to create the piecewise linear model. The main feature of Kawai et al.'s model is that it can be derived from the S-N data at a critical R ratio, referred to as χ. χ is defined as the ratio of the UCS to the UTS of the examined material ($\chi < 0$) [77]. In this study, however, no fatigue data at χ was available due to the inability to conduct T-C fatigue tests on the CC-HNBR composites. Therefore, the fatigue data at R =0.3 which is closest to χ was used to

construct the Kawai CLD model. The Kassapoglou's CLD model was generated by assuming that the scale and shape parameters as those for reinforcing carbon cord of the same gauge length in a two parameter Weibull distribution. It should be noted that all the fatigue data used for the model construction was generated at a frequency of 10 Hz. The results are presented in Figure 5-12.

It can be seen that the piecewise linear model can predict sufficiently accurate actual fatigue data whilst the other three models give relatively poor results. The reason for this is explained as follows. In linear CLD, one assumes identical damage mechanism under tension and compression. While this may be genuinely correct for metallic materials, this assumption greatly oversimplifies the fatigue failure mechanisms in anisotropic cord-rubber composites. Here tensile failure is mainly governed by the reinforcing fibres while it is mostly controlled by the matrix and fibre-matrix interface in compressive loadings[93]. Therefore, predictions proved less reliable when applied to composites materials. However, by making use of additional sets of experimental fatigue data and applying linear interpolation between adjacent R ratios in the $m-a$ plane, predictions tended to become more powerful and precise, as revealed by the piecewise linear CLD model in Figure 5-12 (b) and Table 5-7. The error between experimental data and model predictions is within 40 % with a reduced accuracy for higher fatigue lives. In contrast, the modified Harris's model showed greater accuracy in the moderate cycle regime (from$10^{3.5}$ to $10^{4.5}$). With regards to the Kawai's CLD model, the inaccuracy mainly arose from improper use of the reference S-N data although it was suggested in [93] to select S-N data closest to χif S-N data at $R = \chi$is not available. Moreover, it is worth noting that the reference S-N data used in [93] was obtained from T-C test data with only slight deviations to χ, that is, reference S-N data at R_1= -1, R_2= -1 and R_3 = -0.5 was used to represent χ_1 = -0.79, χ_2= -0.77 and χ_3= -

0.63, respectively for three examined materials. However, in our case, by employing S-N data obtained in the tension-tension (T-T) regime (R = 0.3) to represent data at χ (T-C) would most likely lead to questionable predictions since T-T and T-C leads to completely different fatigue behaviour. Kassapoglou's CLD model requires no experimental data at all and uses only the scale and shape parameters derived from static tests of the examined material in order to predict the dynamic fatigue life behaviour with an assumption of a constant failure probability per cycle p. However, in real tests, the failure probability p is cycle-dependent, with larger values of $p$for later stages of fatigue tests. The failure modes under static loading and dynamic loading are also different, for instance, cord-rubber debonding and matrix cracking are two main types of fatigue damage mechanisms which do not prevail in static loading. As shown in Figure 5-12 (d), the predictions therefore deviated significantly from the experimental data.

In summary, besides the modified Harris's CLD model as proposed earlier, the piecewise linear CLD model gave also relatively good fatigue lifetime predictions especially in the low-cycle region. It is advised that the linear, Kawai's and Kassapoglou's CLD models are only used for preliminary lifetime estimations. More sophisticated models should be employed for more reliable and robust lifetime predictions.

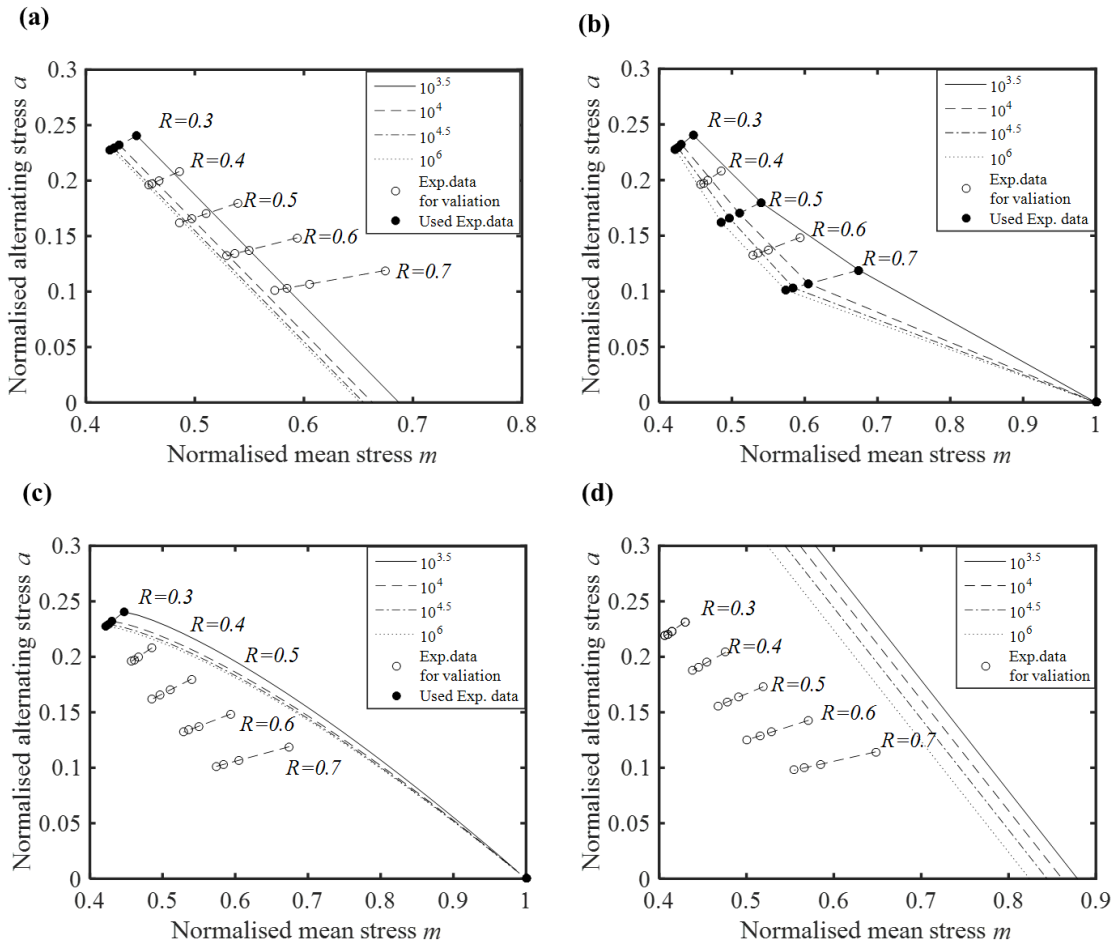

Figure 5-12. Constant life diagrams: (a) Linear, (b) Piecewise linear, (c) Kawai (d) Kassapoglou.

Table 5-7. Comparisons between piecewise linear CLD predictions and actual experimental data obtained for several loading cases at R=0.4 and 0.6 at a frequency of 10 Hz.

R	% UTS	m	a	Experimental average $N_{f,E}$	Standard deviation	Piecewise Linear $N_{f,P}$	Error (%)
0.4	70	0.5126	0.2197	3611	2058	3846	6.51
0.4	72.5	0.5309	0.2275	1706	722	2243	31.48
0.4	75	0.5492	0.2354	1288	543	1642	27.48
0.4	80	0.5858	0.2511	1021	489	1051	2.94
0.6	70	0.5858	0.1464	5680	1686	16466	189.89
0.6	75	0.6276	0.1569	3135	474	3614	15.28
0.6	80	0.6695	0.1674	1895	346	2663	40.53

Note: Error (%)=$\left|N_{f,P} - N_{f,E}\right|/N_{f,E} \times 100\%$

5.4 Conclusions

The effect of frequency and$R$ ratio on the fatigue behaviour of the carbon cord reinforced hydrogenated nitrile butadiene rubber (CF-HNBR) model composites was studied based on a comprehensive characterisation of non-relaxing tension-tension fatigue experiments. Frequency was found to have a negligible effect on fatigue life within the tested regime (2 - 20 Hz) due to limited self-heating even at the highest loading frequencies. This can be explained as a consequence of the very small strain amplitudes experienced as a result of presence of the high-modulus carbon cord in the specimens. Additionally, lower frequencies had also an impact on raising the fatigue limit.

On the other hand, fatigue life was increased with increasing R ratio because of improved crack resistance of the HNBR matrix which here is proposed to result from strain induced crystallisation in the vicinity of a carbon filament break. The ability to crystallise was demonstrated and confirmed by DSC and off-line WAXD investigations.

Efforts were made to predict the fatigue life of the cord-rubber composites by modifying the original Harris's constant life diagram (CLD) model for the lifetime prediction of CC-HNBR composites. The applicability of four other established CLD models was also examined. It was shown that predictions made by the modified Harris's CLD model and the piecewise linear CLD model agreed reasonably well with experimental data.

Chapter 6 : Fatigue of carbon cord-rubber composites in tension combined with bending

6.1 Introduction

Chapter 5 reports an investigation of the tensile fatigue of the single carbon cord reinforced hydrogenated butadiene rubber (CC-HNBR) model composite. In practice, cord-rubber composites found in components such as a timing belt often undergo a combination of complex tension and bending deformations rather than that in simple extension alone. Compared to fibre reinforced plastics (FRPs) where three-point bending, four-point bending or short beam shear test are often employed, there appears a lack of scientific literature examining this type of fatigue loading for cord-rubber composites as is discussed in Chapter 3.

In a tensile test, the stress is uniform over the entire length of the testing sample, thus the strength of the examined material is dominated by the worst flaw in the gauge section. In a flexural test, when the sample is bent upwards without tension at either end of the specimen, the bottom surface becomes compressed while the top surface becomes stretched. This creates a stress distribution across the thickness of the sample. As expected the performance of the material in this mode is typically controlled by the maximum tensile and compressive stresses at the sample surfaces. Flexural tests typically force the fracture to occur in a small region furthest from the neutral axis. Despite this disadvantage, these tests are necessary in order to estimate the fatigue behaviour in service.

In this chapter, a novel experimental set-up is described that makes use of fixed flat pulleys of different diameters to add known level of bending strain into our model composite specimens. The effects of the pulley diameter (which relates to the applied bending strain in the cord) and other test parameters such as frequency and *R* ratio were assessed on the flex fatigue of single carbon cord reinforced hydrogenated butadiene rubber (CC-HNBR) composites.

6.2 Experimental

6.2.1 Materials

The same carbon cords that were used in chapter 5 were used in this work. For the flex fatigue test, samples needed to be sufficiently long to ensure full wrapping around the bollard clamps. Therefore, long spiral single carbon cord reinforced hydrogenated butadiene rubber (CC-HNBR) composites of a width 11.1 mm × thickness 5.3 mm were supplied by Transmission Development Co Ltd (UK) using the same carbon cord as reinforcement, with one surface covered by a facing fabric, as shown in Figure 6-1 (a).

6.2.2 Bending fatigue tests

Figure 6-1 (b) shows the experimental set-up where the middle pulley can be changed in order to alter the radius of curvature and hence the extent of the bending strain in the cord. The static bending strain was calculated for different pulleys with different diameters of 20, 30, 40 and 50 mm. Bending fatigue tests were performed on the CC-HNBR composite. The specimen was wrapped around the immovable pulleys and clamped at both ends (the fabric side is always facing the middle interchangeable pulley). The gauge length is essentially zero, as illustrated in Figure 6-1 (c). The

sliding guides on the base plate were designed to adjust the position of bollard clamps to ensure the specimen wrapped the central pulley over a complete sweep angle of roughly 180° regardless of changes in pulley diameters, as shown in Figure 6-1 (d). In addition, a thermal camera (FLIR A35sc, USA) was set up to monitor the evolution of heat to help identify the onset of a fracture site. For the carbon cord, the edges of the bending region were identified using two white dots. The cycles to failure N_{fb} was recorded as a function of the wheel diameter (20, 30, 40 and 50 mm), frequency (1, 5 and 10 Hz), R ratio (0.4 and 0.7) and maximum applied cyclic force F_{max} (600~1200 N). The data is presented as a force in this chapter instead of a stress such as σ_{max} in this chapter because the stress distribution changes across the thickness of the sample.

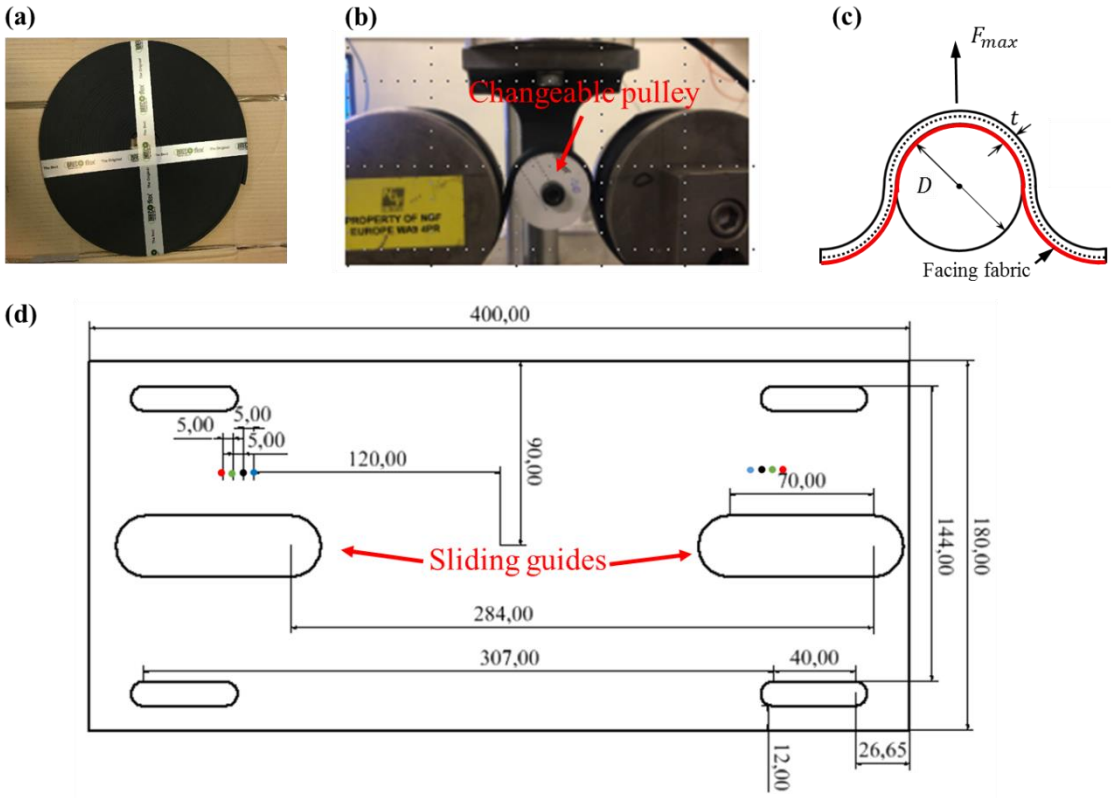

Figure 6-1. (a) The long spiral CC-HNBR composite sample with a width of 11.1 mm and a thickness of 5.3 mm, (b) bending fatigue test set-up used to replicate in a simplified way the real-pulley loading situation encountered in service, (c) illustration of the specimen wrapping around the middle immovable changeable pulleys, showing zero length in vertical direction. The dashed line and the red line indicate the central reinforcing carbon cord and fabric side of the specimen respectively, (d) the sliding guides on the base plate with fixed position marks for bollard grips corresponding to pulleys of different sizes(blue dot: 20 mm; black dot: 30 mm; green dot: 40 mm; red dot: 50 mm).

6.3 Results and discussions

6.3.1 The effect of bending strain on the fatigue life of the carbon cord and CC-HNBR composite.

Initially, a significant number of tests were made to measure the bending fatigue properties using self-made specimens with a length of 240 mm with long cord ends, similar to those used in Chapter 4 and which are shown in Figure 4-2 (c). However, it was found that specimens with this geometry always failed at the isolated cord ends where the cord extended out of the composites even when a significant effort was made to redesign the rubber cushion to avoid a kink in this area. This was because the samples were no longer long enough for the stresses to be diminished to a low enough value by being wrapped around the bollard and so even longer samples were needed to perform this type of test. . In tensile fatigue, the maximum stress in the cord can be estimated by the Rule of Mixtures (RoM) whilst the tensile stresses are reduced during the bending section of the specimen following a relationship that is described using the Euler-Eytelwein equation, as shown in Equation 4-5. The additional bending component that is introduced by the changeable pulley further complicates the stress field in the cord. Tashiro *et al.*[181] studied the stress distribution within the same CC-HNBR composite under both the simple tension and the coupled tension and bending loading situations using finite element analysis (FEA). It should be noted that the stress was normalised to a standard reference value, rather than the ultimate tensile strength (UTS) of the material, in order to retain the confidentiality of this property as required in this study. Therefore, the value of normalised stress can in this case now exceed 1. Figure 6-2 (a) shows the carbon cord FEA model of 0.7 mm diameter, where y axis represents the height of the cord with origin located at the centre of the carbon cord. A stress concentration was found in the centre of the carbon cord under uniaxial tensile

loading resulting from the twisted cord structure (Figure 6-2 (b)). Since the exterior carbon filaments are longer than those located in the middle of the cord so as to realise the twisted structure, the local stresses within the central filaments are greater due to higher level of local strain originated from an initially shorter filament length at a given global tensile force. As mentioned earlier in the introduction, a symmetrical stress field (about the neutral axis) will be expected with a similar absolute value at very low levels of applied tension at both ends of the specimen. This is observed for example when bending over the 50 mm wheel with a modest tension level of just 0.006 (Figure 6-2 (c)). With the increasing applied tension at low level of bending (50 mm), there is a critical stress level (a normalised stress level of 0.209) at which the stress fields changed from tension-compression to always being in tension (Figure 6-2 (c)). For smaller pulleys, a higher critical stress level was required to reach tension-tension stress fields, for instance, a normalised stress level of 0.348 was required for 10 mm pulley due to higher compressive stress induced on the inside of the cord by being bent around the pulley. In addition, the stress field was distorted especially for smaller pulley (Figure 6-2 (d)) due to the interactions between the embedded cord and highly compressed rubber matrix. As anticipated the level of the maximum tensile stress at the outer edge of the cord in the coupled tension and bending condition is higher than that encountered in simple tension. For instance, at a normalised stress level of 0.556, the maximum tensile stress in tension is 1.040 whilst that is increased in bending to 1.167 and 2.172 for the case of 50 mm and 10 mm pulley respectively. Due to this increase in stress resulting from extra bending, the length of the self-made specimens wrapped around the bollard which exploits the capstan effect as described by Euler-Eytelwein equation is now not long enough for the stresses to be diminished sufficiently and hence these samples fractured on the bollards. To ensure that a sample

of sufficient length was used, these self-made model composite specimens were replaced by continuously manufactured composite samples that were cut to a much longer length. Figure 6-3 shows the theoretical value of T_2/T_1 in the case of using the self-made composite samples tested at different pulley diameters and using continuous sample. Here T_2 is a fixed value which equals half of the applied force and $T_1$is the force at the isolated cord end in the case of the self-made sample or the force in the cord embedded in the continuous sample where the wrapping ends. It can be seen that using continuous sample reduces the force to 13 % T_2 whilst using the self-made composite samples remains that to 26 % T_2 and 36 % T_2 for the case of testing at 20 mm and 50 mm pulley respectively. For these longer test pieces, the matrix rubber will carry some extra load which will reduce the stress carried by the carbon cord and also provide better protection of the carbon cord by avoiding kinking of the cord. The results presented in this chapter are therefore only for the bending fatigue measurements using long composite samples as shown in Figure 6-1 (a).

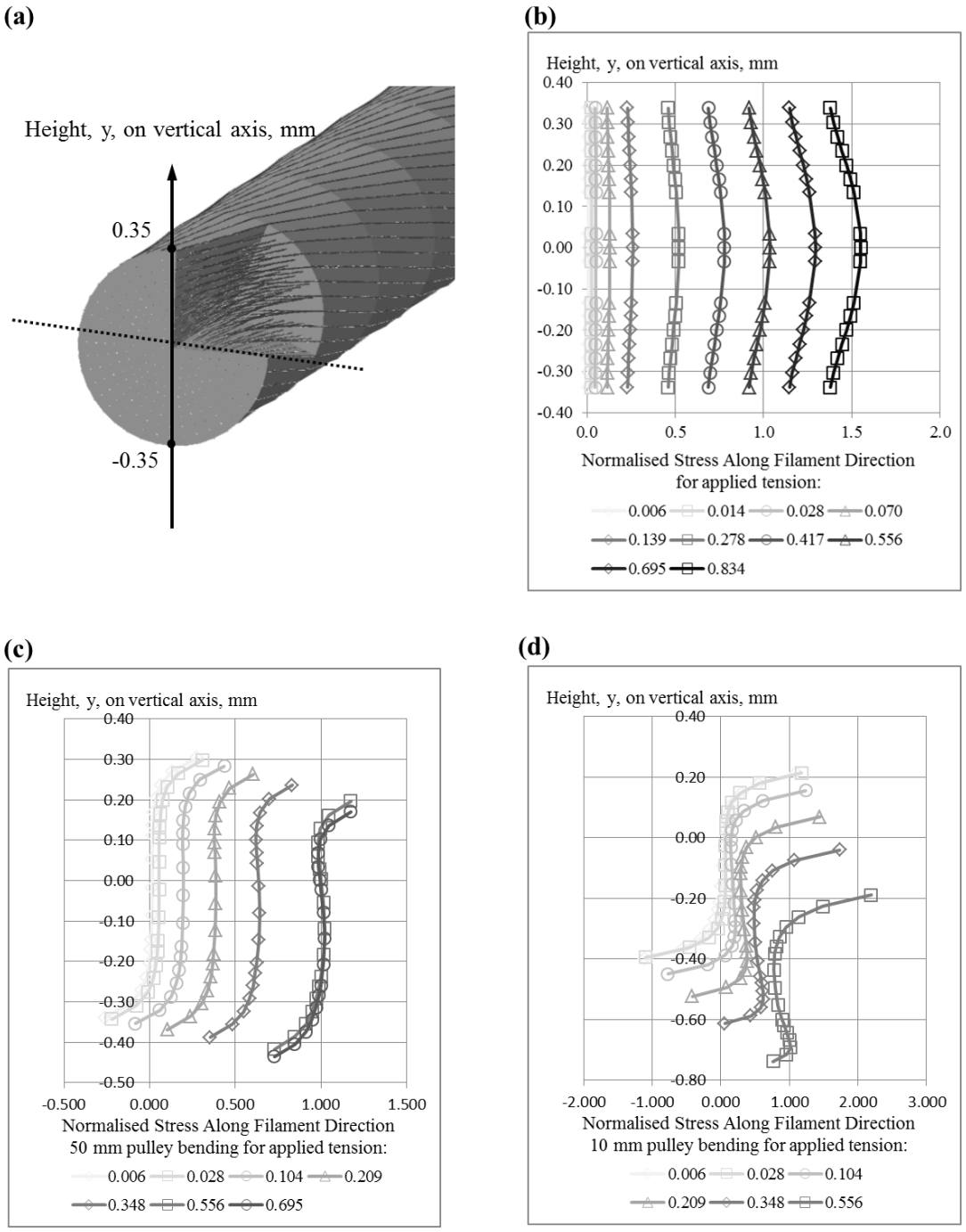

Figure 6-2. Stress variation across the height of the carbon cord with increasing tension: (a) the carbon cord FEA model of 0.7 mm diameter, indicting y axis is in the cord height direction, (b) under uniaxial tension, (c) the cord bent over a 50 mm pulley embedded in the rubber of modulus of 80 MPa, (d) the cord bent over a 10 mm pulley embedded in the rubber of modulus of 80 MPa. Note: the stress was normalised to a random reference value for confidentiality in this study. Taken from Tashiro et al [181].

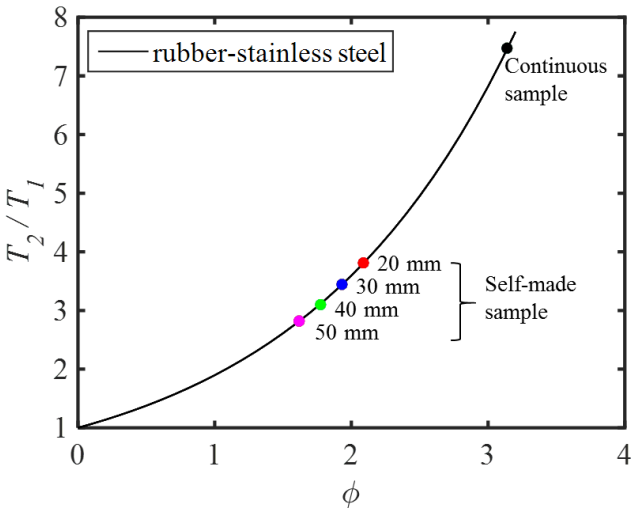

Figure 6-3: Theoretical value of T_2/T_1 in the case of using the self-made composite samples tested at different pulley diameters and using continuous sample. Note: T_2 is a fixed value which equals half of the applied force and $T_1$is the force at the isolated cord end in the case of the self-made sample or the force in the cord embedded in the continuous sample where the wrapping ends. Note: The bollard diameter is 100 mm.

Figure 6-4 shows that a cord-dominated fracture occurred close to the point where the specimen leaves the pulley as detected by the thermal imaging. This results from the combined effects of bending and maximum tension being at a maximum in this location. According to Euler-Eytelwein equation, the value of tensile force will be largest in the tensile region just before the specimen starts to wrap around any pulley. It is diminished quickly with the sweep angle required to do the wrapping, depending upon the geometry of the pulley and the friction coefficient between the composite and the pulley. Meanwhile, the bending contribution was uniform around the specimen as a consequence of the pulley having a uniform radius. Therefore, the specimen has the highest combined stress and is therefore most likely to fail at the point where the bending is introduced at a fixed additional contribution and where the tensile stress

has not yet been diminished. Additional tests were also carried out on the carbon cord. A similar fracture site was found with white arrows indicating the start of the bending region, as shown in Figure 6-7 (a). It can be seen that fracture took place fairly close to the end of the bending section. Damage developed in the form of axial splitting was observed for the carbon cord, as shown in Figure 6-7 (c) and (d), which was considered to be due to the shearing force generated between the twisted carbon filaments.

Figure 6-5 (a) shows the bending fatigue life as a function of wheel diameter at f= 5 Hz, R= 0.4 and F_{max}=1000 N. A more comprehensive characterisation was carried out at f= 10 Hz, R=0.4 and the relationship between maximum cyclic force F_{max} and the cycles to failure N_{fb} is shown in Figure 6-5 (b). There is a reduction in the bending fatigue life as the pulley diameter is reduced. This is attributed to the higher level of bending strain being introduced as the wheel diameter is reduced.

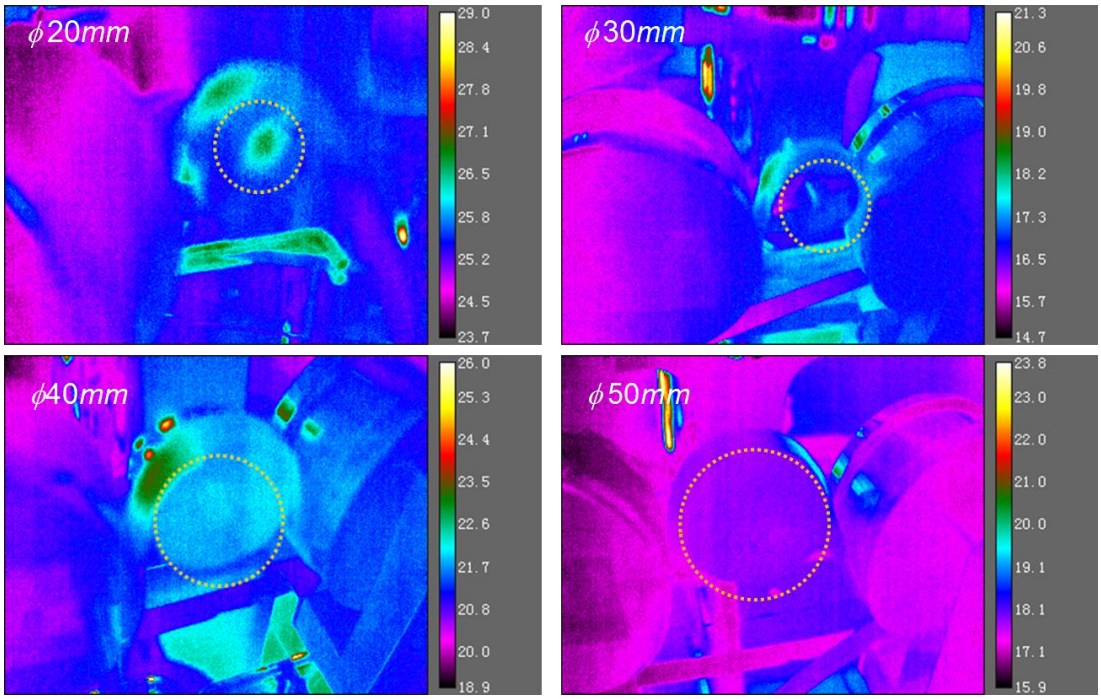

Figure 6-4. Fracture sites originating close to the point where the specimens leave the pulley.

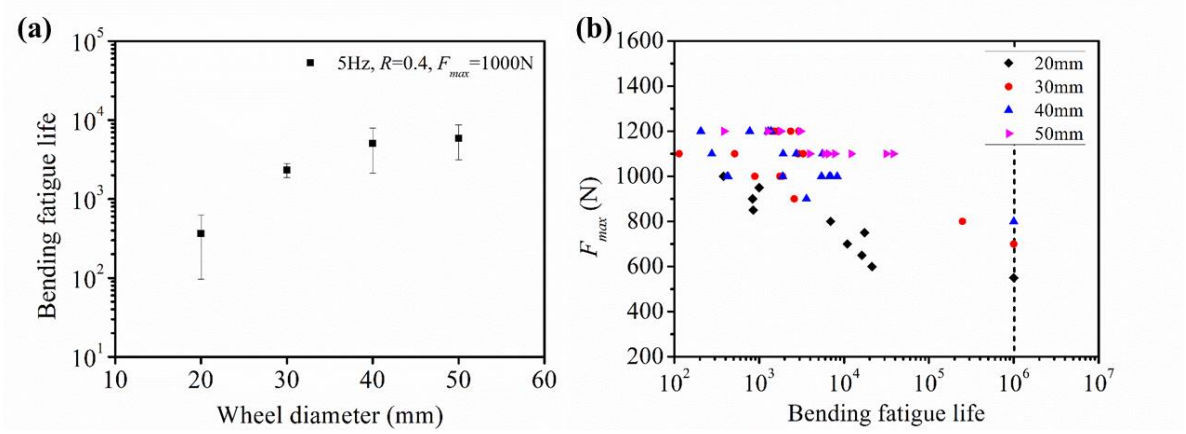

Figure 6-5. (a) bending fatigue life as a function of pulley diameter at f=5 Hz, R=0.4 and F_{max}=1000N, showing higher cycles to failure at larger pulley, (b) S-N data using pulleys of various diameters at f=10 Hz and R = 0.4, indicting longer life with larger pulley at a given load.

For simplicity, assuming the cord is a perfect uniform cylindrical body, the maximum bending strain introduced by the pulley is approximated by

$$\varepsilon_{bmax} = \frac{\theta\left(\frac{D_1}{2}+\frac{t'}{2}+\frac{d}{2}\right)-\theta\left(\frac{D_1}{2}+\frac{t'}{2}\right)}{\theta\left(\frac{D_1}{2}+\frac{t'}{2}\right)} = \frac{d}{D_1+t'} \times 100\% \qquad \text{Equation 6-1}$$

Where θ is the sweeping angle around the pulley, D_1 is the diameter of the pulley, t' is sample thickness (t'= 5.3 mm) and d is cord diameter (d = 0.7 mm), as shown in Figure 6-6 (a). Therefore, it can be written as

$$\varepsilon_{bmax} = \frac{0.7}{D_1+5.3} \times 100\% \qquad \text{Equation 6-2}$$

Figure 6-6 (b) shows the relationship between the maximum bending strain $\varepsilon_{b\,max}$ and the pulley diameter D_1. The dashed red line represents the level of tensile breaking strain of the carbon cord ε_t. Assuming the bending fracture strain of the composite equals the tensile breaking strain of the carbon cord ε_t, the usage of the smaller pulley caused a higher level of bending strain within the CC-HNBR composite, leading to

earlier failure of the material. Cai *et al.*[109] also found larger bending angle had a detrimental effect on the bending fatigue life of Kevlar 49 fibres as a consequence of the resulting increase in the amount of the bending strain. Similar dependence of pulley diameter on the bending fatigue life was also found in the fatigue testing of the pure carbon cord. (Figure 6-7 (b)). Compared to that of the CC-HNBR composite, it has a more linear relationships between the N_{fb} and pulley diameter, which is probably due to the simpler stress distribution found in the carbon cord.

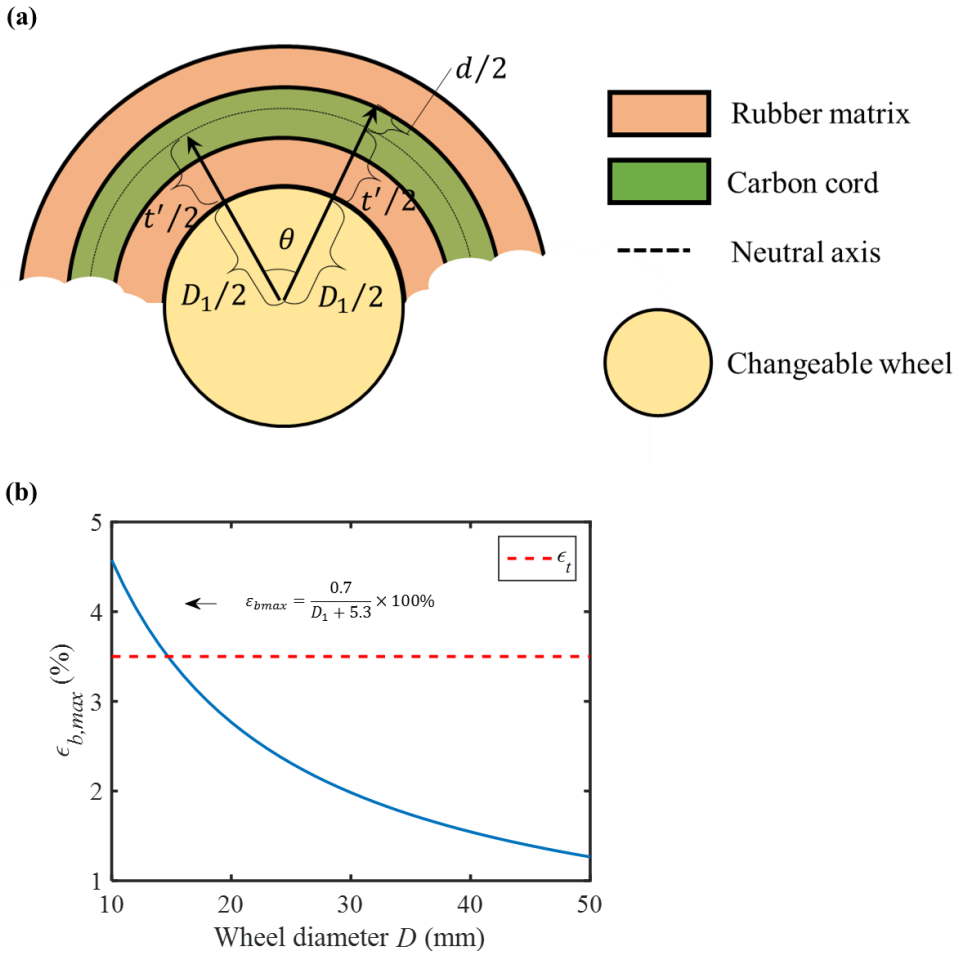

Figure 6-6. (a) Schematic showing the calculation of maximum bending strain in carbon cord (not drawn to scale). θ is the sweeping angle around the pulley, D_1 is the diameter of the pulley, t' is sample thickness (t'= 5.3 mm) and d is cord diameter (d = 0.7 mm), (b) the relationship between the maximum bending strain ε_{bmax} and the pulley diameter.

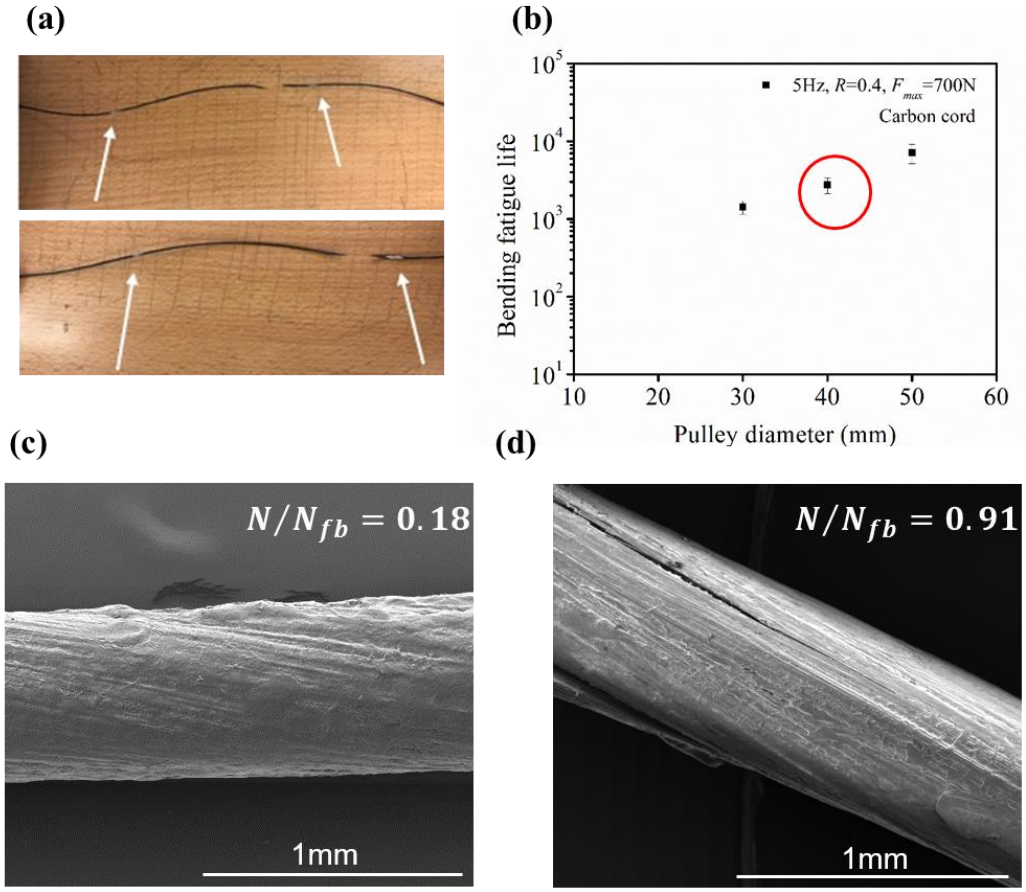

Figure 6-7. (a) Fracture site with white arrows indicating edges of the bending region on the carbon cord, showing fracture occurred near the end of the bending section,(b) the effect of pulley diameter on the bending fatigue life of the pure carbon cord, showing a reduction in fatigue life with the decreasing pulley diameter, (c)SEM image of the carbon cord at N/N_{fb} = 0.18 for the loading case highlighted in (b), showing intact surface morphology, (d) SEM image of the carbon cord at N/N_{fb} = 0.91, showing axial splitting of the cord.

6.3.2 The effect of frequency and *R* ratio on the bending fatigue life of the CC-HNBR composite

Similar frequency effect on the bending fatigue life was observed to that described previously in Chapter 5 for tensile fatigue for both the CC-HNBR composite and carbon cord. The frequency did not significantly influence the bending fatigue life,

measured as the number of cyles to failure, in our study, as shown in Figure 6-8 (a). This is due to the negligible heating as a consequence of frictional sliding between the specimen and the changeable middle pulley in this test set-up. Therefore, the internal heating was controlled by similar mechanism as it was in tensile fatigue. No obvious heating effect regardless of the loading frequency was detected due to small strain amplitude experienced by the specimen. It further validated the approach of using a higher frequency for the fatigue testing which is beneficial in terms of saving testing time provided that the heat generation during the fatigue tests is negligible, as shown in Figure 6-8 (b).

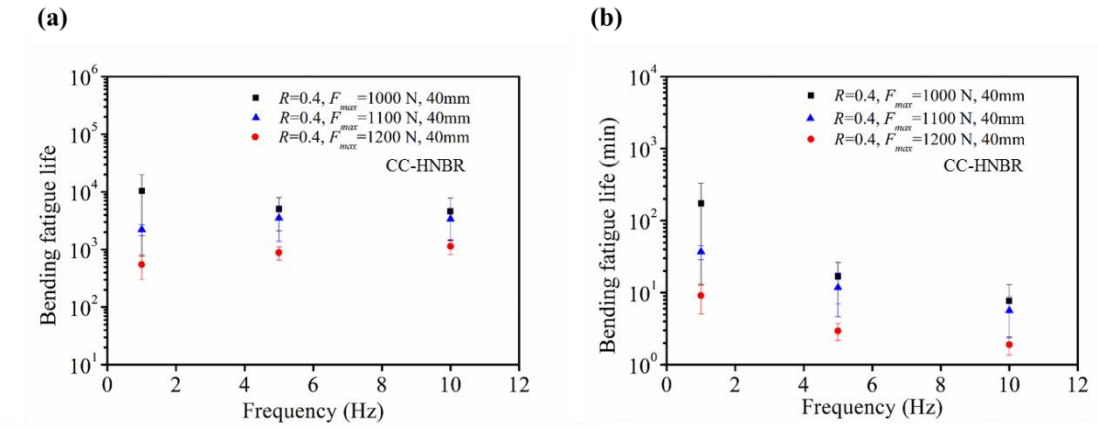

Figure 6-8. The effect of frequency on the (a) bending fatigue life in terms of cycles to failure, (b) bending fatigue failure time of the CC-HNBR composite.

It is, however, very difficult to directly compare the bending fatigue data with the tensile fatigue results of CC-HNBR composites due to different manufacturing methods being employed to make each specimen. This created a variance in both the detailed structure of the specimen geometry and as a consequence of the bending a much more complex stress distribution.

Figure 6-9 shows S-N data at R= 0.4 and 0.7 for two loading conditions. Longer bending fatigue life was observed with increasing R ratio. This is attributed again to a

similar crack blunting mechanisms in the neighbouring rubber due to a potential for strain induced crystallisation (SIC) arising in the matrix HNBR at a fibre break as was explored in Chapter 5.

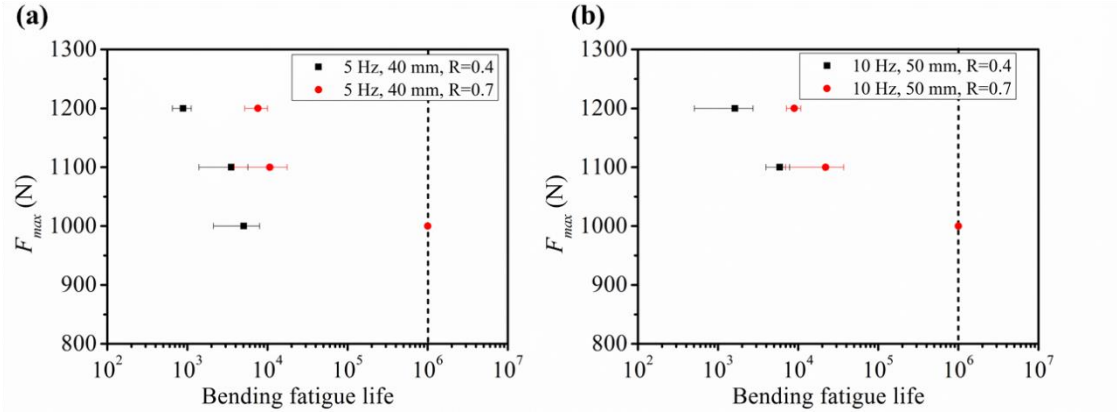

Figure 6-9. The effect of R ratio on the bending fatigue of the CC-HNBR composite. (a) S-N data at f = 5Hz, D = 40 mm and R = 0.4 and 0.7 respectively, (b) S-N data at f = 10 Hz, D = 50 mm and R = 0.4 and 0.7 respectively.

6.4 Conclusions

A novel test set-up was specifically designed to study the bending fatigue behaviour for CC-HNBR composites under the interaction of tension and bending. The effects of the bending curvature, frequency and R ratio were investigated on the fatigue life of the single carbon cord reinforced hydrogenated butadiene rubber (CC-HNBR) composite subject to coupled tension and bending conditions. There was a reduction in bending fatigue life with decreasing pulley diameter due to extra bending strain being introduced by the pulley. Similar effects of the frequency and R ratio were observed as was the case for the tensile fatigue. Compared to the tensile fatigue, the stress fields in the cord rubber composite under the combination of tension and bending were far more complicated.

Chapter 7 : Smart cord-rubber composites with integrated structural health monitoring (SHM) capabilities

7.1. Introduction

The wide applications for cord-rubber composites in critical engineering applications such as aircraft, subsea seals, naval transportation and automotive components have resulted in an interest in developing real-time structural health monitoring (SHM) systems during usage to maintain structural safety and avoid catastrophic failure.

In this chapter, inspired by the work of Coleman *et al.*[139, 140, 182] described in the Chapter 3 and taking advantage of the presence of the elastomeric coating on reinforcing cords for rubber products, carbon nanotubes (CNTs) were introduced into this coating via a simple swelling and infusion method. This resulted in CNT infused glass cords with self-sensing properties that can be utilised as interfacial strain and damage sensors for cord-rubber composites. The electrical conductivity and surface morphologies of these CNT infused glass cords swollen in different CNT dispersions have been investigated. These CNT infused glass cords exhibited good strain sensing abilities and reproducibility. For the first time, *in-situ* health monitoring of cord-rubber composites has been demonstrated, unveiling insightful interfacial health conditions such as local interface failure under both static and cyclic tensile loading. Further investigations involved single cord pull-out tests while fractographic analysis revealed no detrimental effects of the presence of the CNTs on cord-rubber adhesion. The proposed methodology is an easy and efficient process to produce smart reinforcing

Part of this chapter has been published in *Composites Science and Technology,https://doi.org/10.1016/j.compscitech.2018.07.023.*

cords with tailored sensing functionalities, which is also compatible with current cord manufacturing procedures for potential industrial scale-up. These smart cords can be used for a multitude of SHM systems embedded into cord reinforced rubber products.

7.2. Experimental

7.2.1. Materials

The multiwall carbon nanotubes (MWCNTs) (NC7000) used in this study were supplied by Nanocyl S.A. (Belgium). The E-glass cords with an average diameter of 1.1 mm were supplied by NGF Europe Limited (UK) and used as-received. The cords had been dipped through a proprietary resorcinol formaldehyde latex (RFL) bath as the strand coating and subsequently chlorosulfonated polyethylene synthetic rubber (CSM) bath as the cord adhesive overcoat prior to reception. Both strand coating and cord coating are elastomeric in behaviour. The same CSM used for the preparation of the adhesive overcoat was provided in the form of dry sheets. A commercial hydrogenated acrylonitrile butadiene rubber (HNBR) compound was used as matrix for embedding the glass cord. The solvents N-methylpyrrolidone (NMP) and Dimethylformamide (DMF) were purchased from Sigma-Aldrich Company Ltd, while toluene, methanol and chloroform were purchased from VWR Chemicals. Acetone was purchased from Honeywell International Inc. Silver paint and MG Chemicals 8481 carbon conductive grease were purchased from RS Components Ltd (UK).

7.2.2. Sample preparation

Preparation of CNT infused glass cords

The various CNT dispersions were made by dispersing MWCNTs in three different solvents (NMP, DMF, acetone) at a concentration of 50 mg/100 ml using an ultrasonic

processor (Sonics VCX500) for 20 min with a pulse of 2 s on and 2 s off at 25 % amplitude.

Afterwards, the as-received glass cords with lengths of ~80 mm were soaked into the various CNT dispersions using an ultrasonic bath (PS-60A, 360W) for 0.5 h, 1 h, 2 h, 3 h, 4 h, 5 h and 6 h, respectively. All sonication processes were performed with ice-bath to avoid temperature build-up. After this swelling and infusion step, the CNT infused glass cords were washed in ethanol without sonication for 20 s, followed by sonication in ethanol for 20 s and a final ethanol wash for 20 s to remove any CNTs that are attached loosely to the surface of the glass cords as well as residual solvent. The infused glass cords were then dried in an oven at 60 °C for 20 h. As-received glass cord and CNT-infused glass cord are illustrated in Figure 7-1 (a).

Fabrication of the glass cord-rubber pull-out sample

The preparation method used is described in Chapter 4 and illustrated in Figure 7-1(b). A cross-sectional view of the pull-out sample is shown in Figure 7-1 (c).

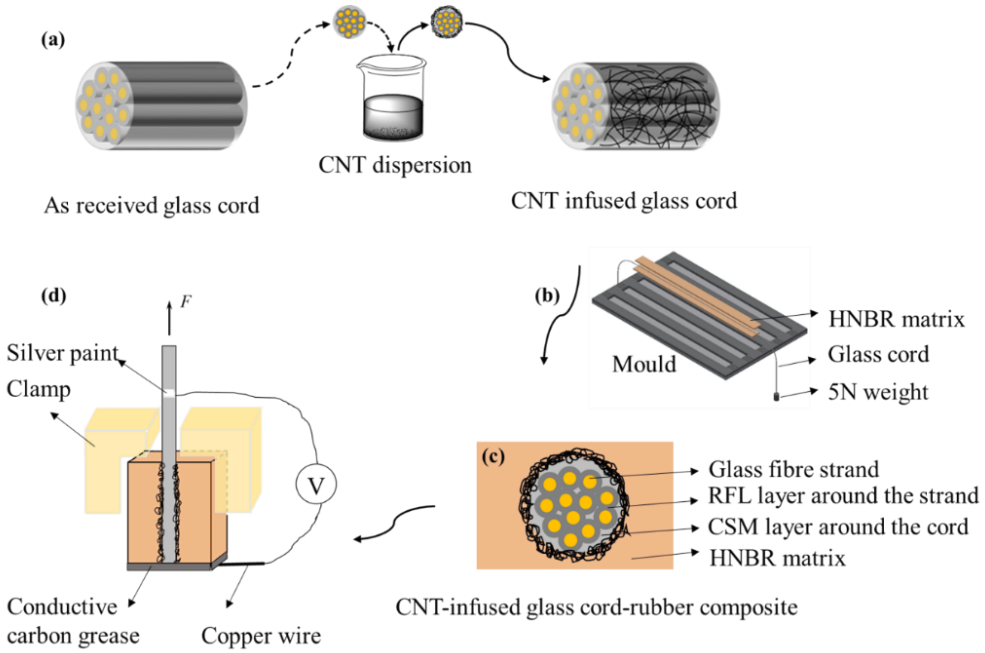

Figure 7-1. Schematic of (a) CNT infused glass cord preparation, (b) glass cord-HNBR pull-out specimen preparation, (c) cross-sectional view of pull-out specimen, (d) *in-situ* damage sensing tests of pull-out of CNT infused glass cord from HNBR matrix (not drawn to scale).

7.2.3. Characterisations

Swelling behaviour of dried adhesive overcoat chlorosulfonated polyethylene (CSM)

Swelling experiments were performed on dried adhesive overcoat chlorosulfonated polyethylene (CSM)(the same composition as the coating material on the cord)in a fumehood at ambient temperature using NMP, DMF, acetone, toluene, methanol, and chloroform. Samples with dimensions of 8mm×8mm× 1.1 mm were cut from a dried adhesive sheet and then immersed completely into 50 ml of each solvent for 24hours before the mass was measured. The swelling ratio Q was measured by dividing the mass increase after saturation against the initial dry mass [183, 184].

Thermogravimetric analysis (TGA) of CNT-infused glass cord

Thermogravimetric analysis (TGA) was performed on a TA Instrument (Q500) under air atmosphere from 20 °C to 1000 °C at 10 °C/min, with the aim of quantifying the amount of CNTs incorporated into the elastomeric coating of the CNT infused glass cord after the swelling and infusion process.

Electrical conductivity measurements

The various dried CNT infused glass cords were cured at 180 °C for 20 min in an oven before their conductivity was measured using a Keithley 2400 sourcemeter (Tektronix). Silver paint was applied to the circumference of the CNT infused glass cord at 20 mm intervals in order to reduce the surface contact resistance. Three measurements were taken at different positions of the treated cords, as shown in Figure 7-2. The conductivity σ can be calculated by

$$\sigma = \frac{l}{\rho} = \frac{l}{A \cdot R} \qquad \text{Equation 7-1}$$

Where l is the distance between two spots painted by silver, R is the resistance between two spots painted by silver which can be calculated by the slope of the voltage-current curve, A is the cross-sectional area of the CNT-infused carbon cord.

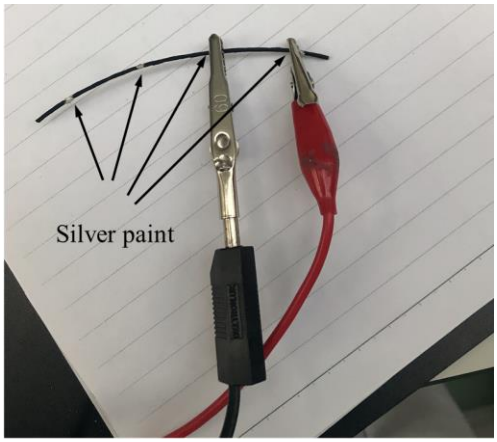

Figure 7-2. Conductivity measurement of the CNT-infused cords.

Morphology

Scanning electron microscopy (SEM) (FEI, Inspect-F) on gold coated samples was employed to assess the CNT distribution and location from both longitudinal and cross-sectional views of the CNT infused glass cord after the curing. The fracture surfaces after pull-out tests were investigated to examine the failure mode with and without CNT infusion.

Single cord in-situ strain sensing tests

Static tensile tests of the CNT-infused cords were carried out on an Instron 5566 universal mechanical tester equipped with a 1 kN load cell at a crosshead speed of 20 mm/min coupled with simultaneous electrical measurements recorded by a 34401A multimeter (Agilent). The gauge length of the cord was 200 mm, while two electrodes were attached to the middle of the cord at distances of 100 mm with silver paint applied to the contact points.

Single cord pull-out tests

Static single cord pull-out tests were carried out on an Instron 5566 universal mechanical tester equipped with a 1 kN load cell at a crosshead speed of 20 mm/min. A minimum of three measurements for each sample were recorded. The interfacial shear strength (IFSS) τ is given by Equation 4-1.

In-situ damage and strain sensing tests of cord-rubber composites

Both static and cyclic strain and damage sensing tests of the CNT infused cord-rubber composite pull-out samples were performed. To enable real-time electrical measurements, the entire bottom surface of the pull-out sample was coated with carbon grease, while a copper wire electrode was attached to the sample using a high strength flexible acrylic tape. Another electrode was directly attached to the CNT-infused glass cord at a distance of 20 mm away from the top surface of the rubber matrix with silver-

paint applied at the contact points to ensure a good electrical connection. A schematic illustration of the *in-situ* sensing test setup is shown in Figure 7-1 (d). Cyclic loading and unloading of the pull-out specimen was applied using different displacement levels with 1 min dwell in between each cycle at the same displacement level while the specimen was held for 5 min before being reloaded to a higher displacement level.

7.3. Results and discussions

7.3.1. The distribution of CNTs on the surface of various CNT-infused cords

A good swelling capacity of the elastomeric adhesive coating material induced by the organic solvent is favourable to provide enough free volume for CNT infusion. This swelling cannot be too excessive though as it is important to ensure that the dissolution of the adhesive coating material is also avoided.

Figure 7-3 presents the swelling ratios of dry CSM materials after swelling in various solvents for 24 hours. It should be noted that CSM materials became small pieces after 24 hours swelling in chloroform and toluene, which makes it impossible to weigh the mass. Therefore the swelling ratios in these two solvents were disregarded. It can be seen that dry CSM materials has the lowest swelling ratio in methanol while it reaches the highest swelling ratio at around 100 times in NMP. On the other hand, specimens swollen in DMF and acetone exhibited a relatively moderate swelling ratio.

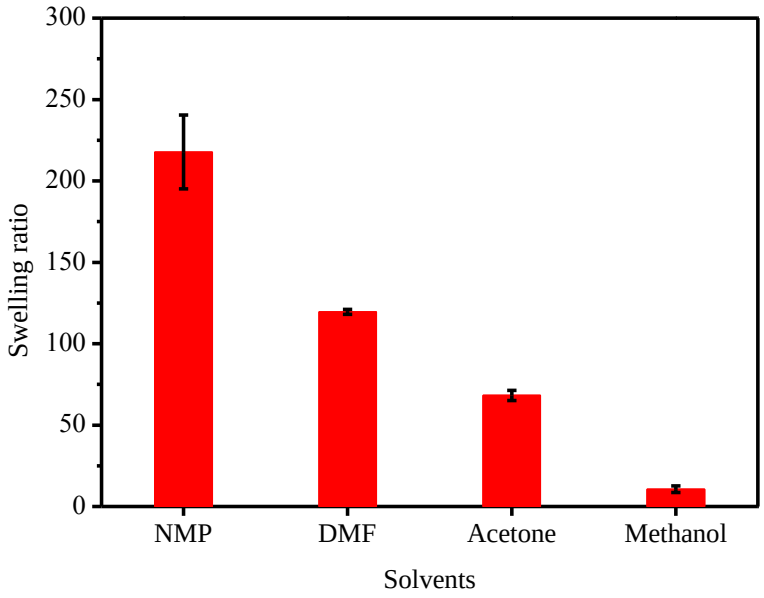

Figure 7-3. Swelling ratios of dry CSM materials in (a) NMP, (b) DMF, (c) acetone, (d) methanol after 24 h.

The Hansen solubility parameter (HSP) is widely used to provide general guidelines for the compatibility of two phases, and was used here to assess the affinity or miscibility between CNTs and various dispersion solvents[185-187].The total cohesion solubility parameter δ_t is defined as $\delta_t^2 = \delta_D^2 + \delta_P^2 + \delta_H^2$, where δ_D, δ_P and δ_H are Hansen solubility parameter components from dispersion cohesion, polar cohesion and hydrogen bonding cohesion, respectively. Good CNT dispersion requires the individual solubility parameter between solvent and CNT to be similar. Table 7-1 summarises the Hansen solubility parameters (HSPs) for CNT and solvents used in this study taken from literature. [185, 186, 188-190].The match of HSPs between CNT and NMP, CNT and DMF,CNT and acetone, sets a prerequisite for improved CNT dispersions.

Table 7-1.Comparison of Hansen solubility parameters (HSPs) of CNT and various solvents used in this study [185, 186, 188-190]

Material	δ_D(MPa$^{1/2}$)	δ_P(MPa$^{1/2}$)	δ_H(MPa$^{1/2}$)	δ_t(MPa$^{1/2}$)
MWCNT	19.7	6.2	4.2	21.1
NMP	18.0	12.3	7.2	23.0
DMF	17.4	13.7	11.3	24.8
Toluene	18.0	1.4	2.0	18.2
Acetone	15.5	10.4	7.0	19.9
Methanol	15.1	12.3	22.3	29.6
Chloroform	17.8	3.1	5.7	18.9

According to dry CSM swelling data combined with HSPs of CNT and solvents, methanol was regarded as not suitable for CNT infusion due to the limited swelling ratios. Chloroform and toluene were also not an ideal dispersion medium due to the CSM dissolution, leading to a lower free volume for CNT infusion. NMP, DMF and acetone were chosen as potential solvents due to their good swelling capacity and compatibility with MWCNTs.

To evaluate the effectiveness of the introduction of CNTs via the swelling and infusion method, a treatment time of 1 h was used initially for the fabrication of CNT-infused glass cords. This is to limit CSM dissolution, which is of particular importance considering the thin adhesive coating on the as-received glass cords. Figure 7-4 shows SEM images of the lateral surface of CNT infused glass cords and as-received glass cord prior to the swelling process. CNT networks were uniformly distributed along the entire cord surface after swelling in CNT/acetone dispersions (Figure 7-4a). A

dense and thick CNT network was observed, indicating that a considerable amount of CNTs was attached to the cord surface. In contrast, less dense CNT networks were formed after swelling in CNT/NMP (Figure 7-4b) and CNT/DMF dispersions (Figure 7-4c) owning to the partial dissolution of CSM in the strong polar NMP and DMF solvents. Moreover, in the case of CNT/DMF dispersions, a relatively inhomogeneous CNT network was observed with the presence of some CNT agglomerates at the cord surface indicated by the arrows. These images can be contrasted with the as-received glass cords which exhibited a similar elastomeric surface morphology but without the presence of fibrous CNTs. As such acetone stood out as the optimum dispersion solvent in terms of CNT infusion.

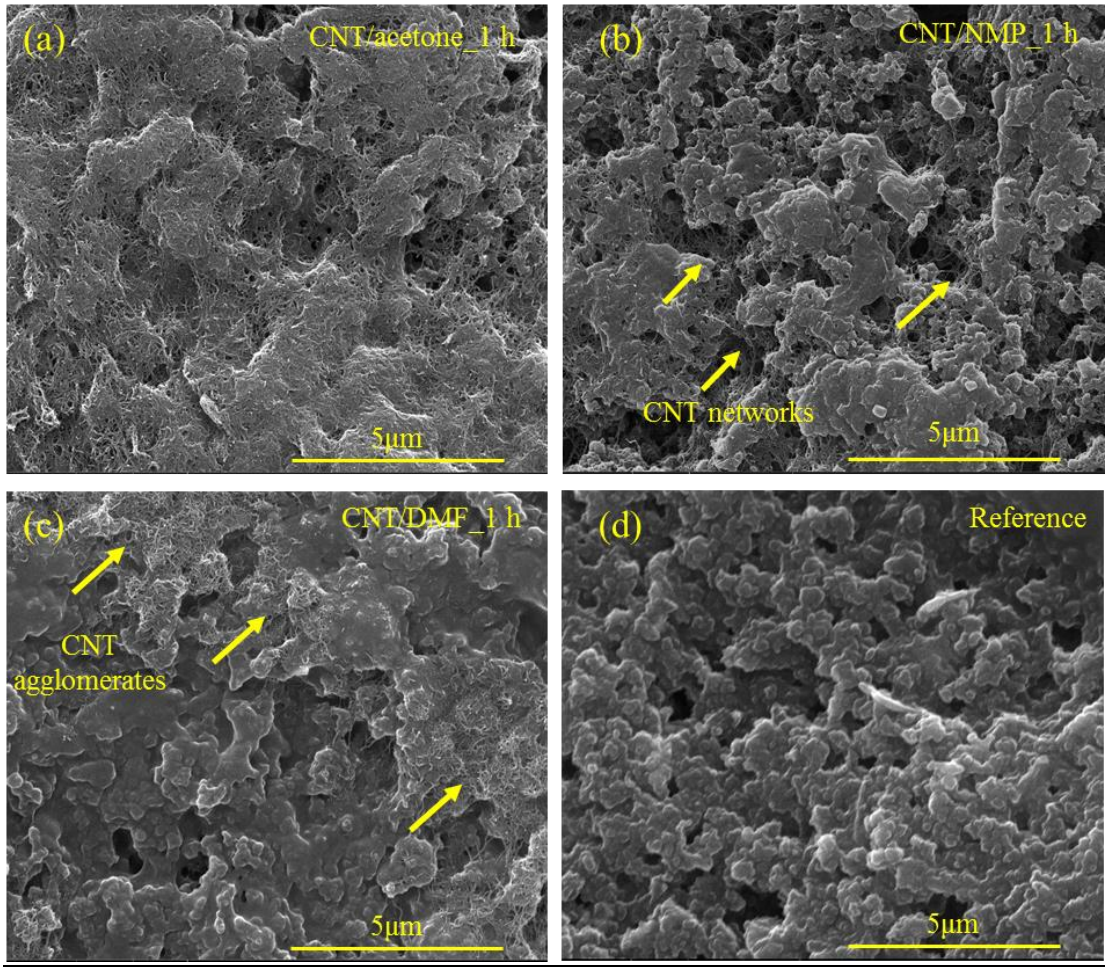

Figure 7-4. SEM images of the lateral surface of CNT-infused glass cords in (a) CNT/acetone, showing a uniform and dense CNT network covering the entire cord surface, (b) CNT/NMP, showing a less dense CNT network, (c) CNT/DMF, showing a relatively inhomogeneous CNT network with the presence of some CNT agglomerates indicted by the arrows for 1 h and (d) as-received glass cord prior to the swelling process without the presence of CNTs.

7.3.2. Morphology of CNT infused glass cords from CNT/acetone dispersions

Since acetone was selected as the most promising solvent for CNT infusion, further SEM observations of cross-sections of the cords were performed. Figure 7-5 shows the cross-sectional view of as-received glass cord and CNT infused glass cord from

CNT/acetone dispersions for 1 h. Each glass cord contains 11 twisted strands of glass fibres (Figure 7-5a). A representative strand is indicated by the dashed yellow line. A two-step coating process was involved on both strands and the outer surface of the cord during manufacturing as described in experimental section, leading to two distinctive coating layers: the RFL coating on the glass fibre strand and the CSM coating on the RFL coated glass cord. The average thickness of the CSM layer around the cord is approximately 25 μm (Figure 7-5b) which provides improved adhesion between cord and rubber matrix. It can be seen that most of the CNTs were accumulated on the coating with an infusion depth of 2-4 μm, while very few traces of CNTs were found at a penetration depth greater than 5 μm from the CSM layer (Figure 7-5d). Apparently, the current swelling and infusion process concentrates CNTs preferentially into the outer CSM coating rather than into the RFL coated glass fibre strands.

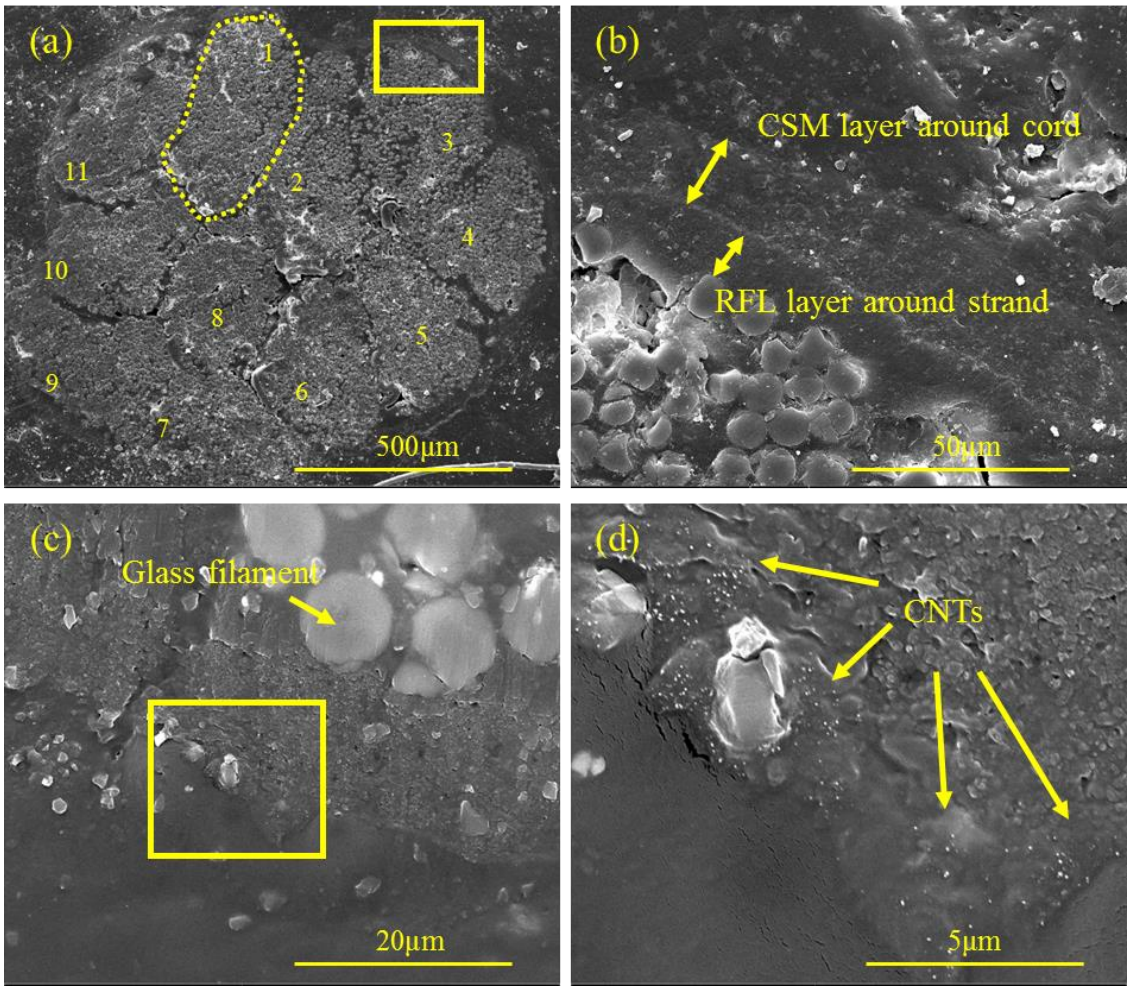

Figure 7-5. SEM cross-sectional views of glass cord embedded into an acrylic resin. (a) As-received glass cord consisting of 11 twisted strands. The dashed yellow line indicates the location of a single strand in the image, (b) Higher magnification of the region as indicated by the yellow box in (a), showing RFL layer around the strand and CSM layer around the cord, (c) CNT traces in the CSM layer after swelling in CNT/acetone dispersions, (d) Higher magnification of the infused region as indicated by the yellow box in (c), showing a CNT infusion depth of 2-4 µm.

7.3.3. Electrical conductivity of CNT infused glass cords

Since the total amount of CNTs introduced via the simple swelling and infusion process was extremely low it was difficult to quantify the exact amount of CNT from thermogravimetric analysis (TGA) data, as shown in Figure 7-6. However, a good level of electrical conductivity was successfully imparted in all the intrinsically

insulating glass cords. As such it demonstrates the efficiency of the proposed methodology to introduce a percolating network of conductive nanocarbon into glass cords with the aim of delivering additional functionality.

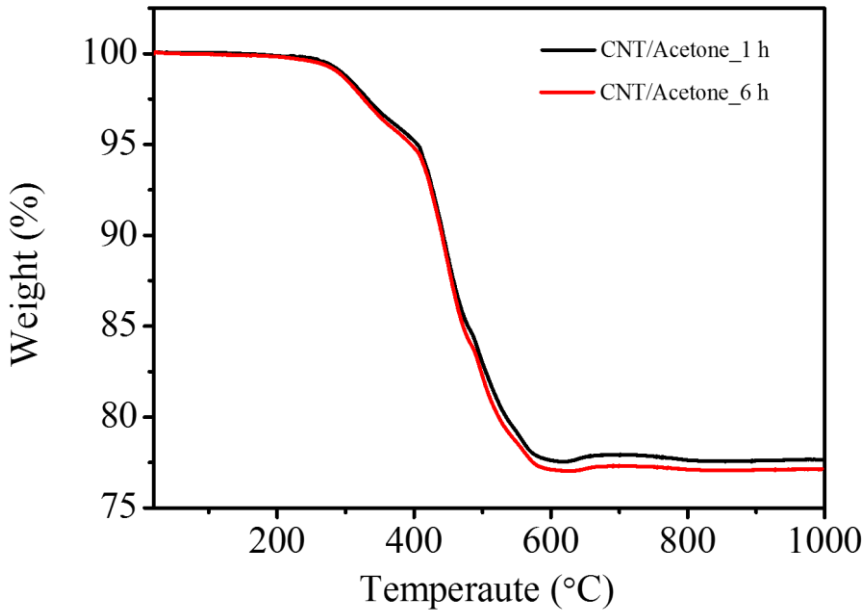

Figure 7-6. TGA results for CNT infused glass cord fabricated from CNT/Acetone dispersions.

Figure 7-7 (a) compares the electrical conductivity of CNT infused glass cords produced using various different dispersions as a function of swelling time. Not surprisingly, glass cords swollen in CNT/acetone dispersions reached the highest electrical conductivity with levels above 10^{-2} S/m after only 30 min soaking time, implying the formation of a continuous CNT network as shown in Figure 7-4a. No obvious change in electrical conductivity was observed with longer soaking times (> 30 min), suggesting that a saturated CNT network was formed in the swollen elastomeric coating within a relatively short period of time.

The electrical conductivity of the glass cords swollen in CNT/NMP and CNT/DMF dispersions were slightly lower compared to those swollen in CNT/acetone dispersions, in the range of 10^{-3} S/m after 30 min swelling. An increase in cord conductivity was observed for treatments with both dispersions, until a drop was seen after 3 h soaking. This decrease was attributed to a reduced amount of free volume for CNT infusion, resulting from a gradual dissolution of CSM after prolonged swelling in both dispersions. This effect was also indicated by the observed solvent colour change after swelling as-received glass cords for 1 h in acetone, DMF and NMP without CNTs under the same conditions, as shown in Figure 7-7 (b). Clearly, a certain amount of CSM material has been removed from the cord surface and migrated into NMP and DMF. Repeats were carried out in order to ensure batch to batch consistency on electrical performance, as shown in Figure 7-8. It was concluded that the obtained conductivity results of the CNT infused glass cords are highly consistent, confirming the reliability of the current method.

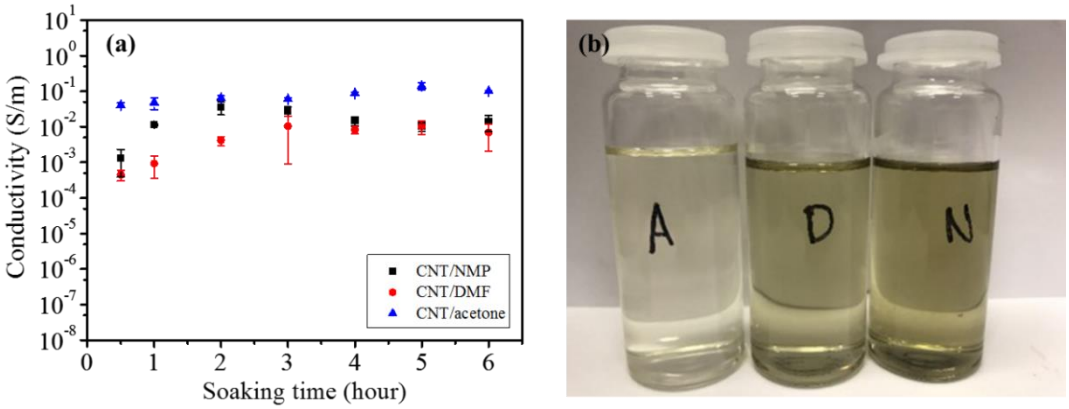

Figure 7-7. (a) Electrical conductivity of CNT infused glass cords via various CNT dispersions as a function of swelling time, (b) Solvent colour change after swelling of as-received glass cords in acetone, DMF and NMP for 1 h, confirming the partial removal of the CSM coating from the glass cords especially in the case of DMF and NMP.

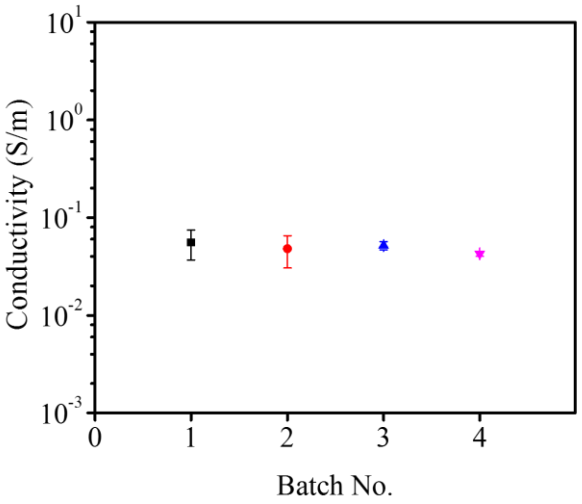

Figure 7-8. Electrical conductivity variations of glass cords swollen in CNT/acetone dispersions for 1 h.

7.3.4. *In-situ* strain and damage sensing during static and cyclic loading

Having successfully manufactured the conductive CNT infused glass cord, its strain sensing properties were first evaluated by recording its electrical resistance change $\Delta R / R_0$ simultaneously during static tensile loading. Subsequently these cords were embedded into a HNBR matrix. Both static and cyclic loading tests, coupled with real-time electrical measurements were performed to examine its potential as interfacial strain and damage sensors for cord-rubber composites. As CNT infused glass cords made from CNT/acetone dispersions reach the optimum conductivity after 1 h swelling and infusion, 1 h treatment time was also chosen for the other two systems for sensing investigations.

Strain sensing behaviour of CNT infused glass cord

Figure 7-9a shows the electrical resistance change $\Delta R / R_0$ and its relationship with load and displacement under static tensile loading of CNT infused glass cord specimens swollen in CNT/acetone dispersions for 1 h. A small drop in the value of

$\Delta R / R_0$ was initially observed due to the interlocking of glass fibre strands within the cord by straightening them along the direction of the applied force (Figure 7-9d), also known as the setting effect [191]. This was then followed by a continuous rise in $\Delta R / R_0$ as the CNT network began to deform with increasing applied extension until cord fracture.

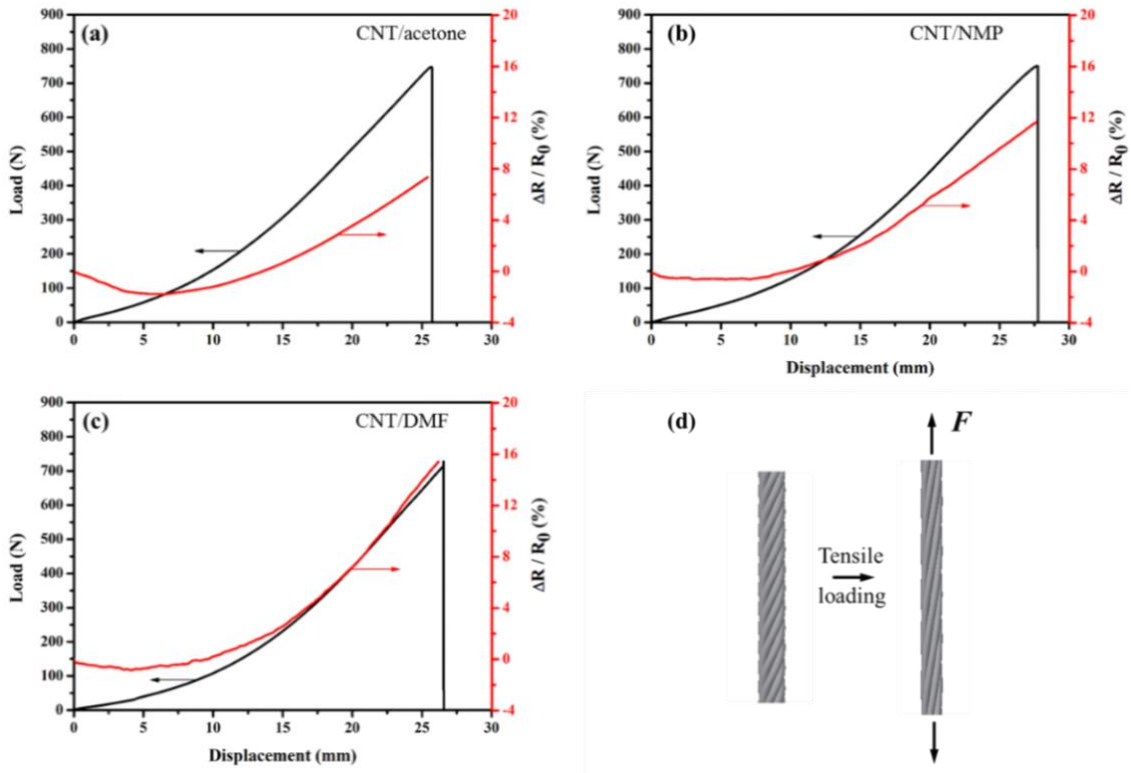

Figure 7-9. Static electro-mechanical response of CNT infused glass cord fabricated from (a) CNT/acetone, (b) CNT/NMP, (c) CNT/DMF, as dispersions for 1 h swelling and infusion time, (d) Straightening of twisted glass fibre strands along the direction of the applied force.

An approximately linear relationship exists between sensing signal and applied load when the sensing signals ($\Delta R / R_0$) are greater than zero, indicating a correlation between applied extension and sensing signal [126]. Similar findings were also observed in the other two systems (Figure 7-9b and Figure 7-9c) with less significant

setting effects and slightly larger sensitivity resulting from fewer conductive pathways arisen from a lower density of CNTs [192]. Direct comparison is shown in Figure 7-10.

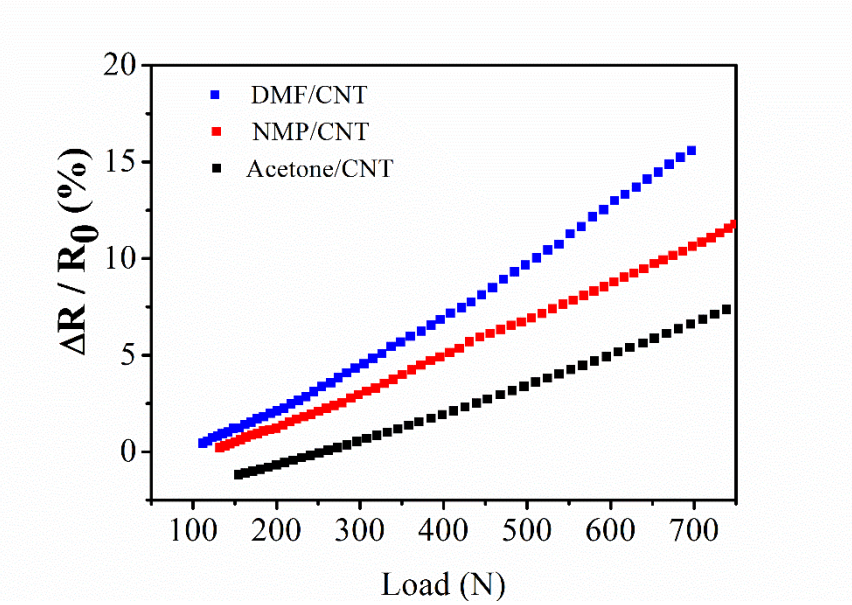

Figure 7-10. Electrical signal ($\Delta R / R_0$) – applied load relationship of CNT infused glass cord fabricated from CNT/acetone, CNT/NMP and CNT/DMF after initial 10 mm displacement, showing the linear relationship between sensing signal and applied load.

Static damage sensing of the CNT infused glass cord-rubber composites

After examining and confirming the good sensing properties of CNT infused glass cord, the sensing characterisation was applied to cord-rubber composites to demonstrate the feasibility to use these conductive cords as interfacial damage sensors.

Figure 7-11 shows a correlation between resistance change and applied load during pull-out tests for various CNT infused glass cord-rubber composites. Three well defined regions can be identified from the resistance change data, in agreement with findings reported by Mäder and Rausch on CNT-modified sizings on GF in PP matrix [193]. For the case of CNT/acetone dispersions, the value of $\Delta R / R_0$ increased

gradually for the first 7 mm of extension. This behaviour is reversible, as confirmed later in the cyclic sensing section, and is due to the elastic deformation of the interfacial region. The first reversible region is followed by a second stage characterised by an increase in the slope of the sensing signal for the following 5 mm extension. At a critical point just before catastrophic interfacial failure, the resistance suddenly increases to a value beyond the multimeter limits, followed by visible macroscopic interfacial failure at the top surface of the pull-out sample as a result of shear stress concentration, propagating along the interface (see schematic (d)-②). The cord was eventually pulled out from the HNBR matrix by a frictional sliding mechanism after interface failure was complete at the end of the test (schematic (d)-③).

Similar trends of the electro-mechanical response were observed in cord-rubber composite specimens with conductive glass cords made from CNT/NMP and CNT/DMF dispersions respectively (Figure 7-11b and Figure 7-11c). However, unlike the CNT/acetone specimen, the other conductive glass cords were only able to detect damage that occurred at the early stages of the test, which was then followed by a sharp increase in electrical resistance beyond the measurable range at a point much earlier than the onset of catastrophic interface failure. This early signal loss was attributed to the relatively high initial resistance compared to that of the glass cord infused in a CNT/acetone dispersion. It is worth pointing out that the sensing properties of these cords made from CNT/NMP and CNT/DMF dispersions could be tuned and improved by adjusting the period of swelling and infusion treatment time.

In addition, the observed $\Delta R / R_0$ change for the CNT/acetone specimen was also much higher (up to 850 %) than that of other composite pull-out specimens, demonstrating a strongly enhanced interface damage monitoring capability. The

sensing properties of different systems including displacement values corresponding to the last measurable electrical signal point ΔD_1 and maximum pull-out force ΔD_2 are summarised in Table 7-2.

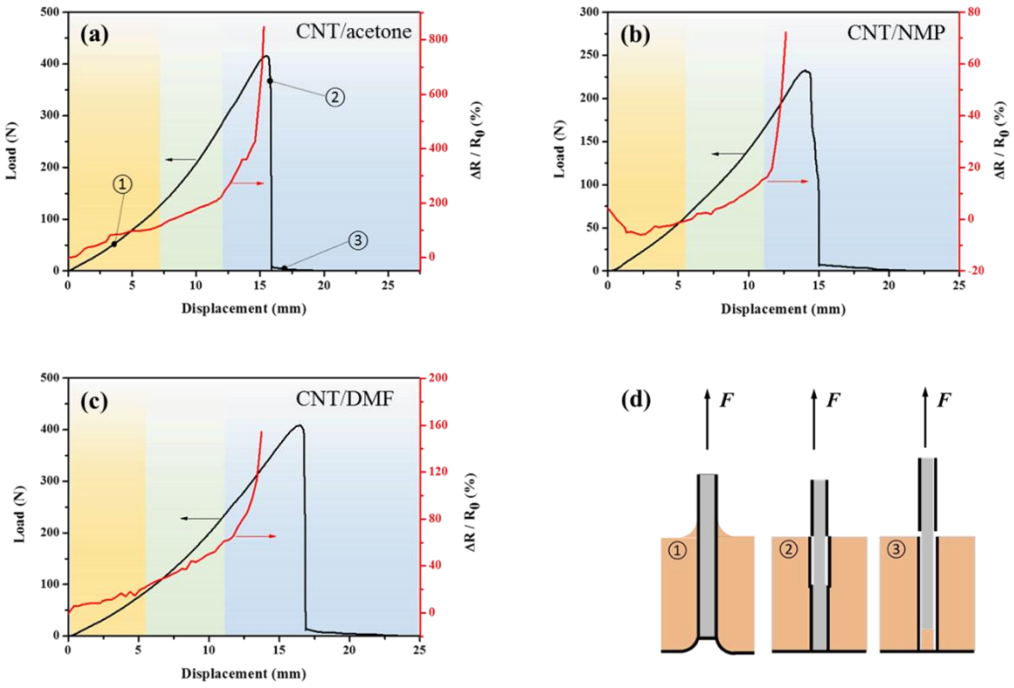

Figure 7-11.Static electro-mechanical response of the pull-out of a CNT infused glass cord from a HNBR matrix using (a) CNT/acetone, (b) CNT/NMP, (c) CNT/DMF, as dispersions for a swelling and infusion time of 1 h, (d) Illustration showing the interfacial failure process during single cord pull-out: ①perfectly bonded to matrix, ② crack initiation at the top surface, ③ completely debonded interface with the cord pulled out by frictional sliding.

Table 7-2. Summary of sensing properties of conductive glass cord-rubber composites, with a comparison between displacement values corresponding to the last measurable electrical signal point and maximum pull-out force.

Systems	R_0 (MΩ)	R_t (MΩ)	$\Delta R / R_0$ (%) at last measurable point	Displacement ΔD_1 (mm) at last measurable point	Displacement ΔD_2 (mm) at maximum pull-out force	$\Delta D_1 / \Delta D_2$ (%)
CNT/acetone	0.38	3.58	842.10	15.26	15.57	98.01
CNT/NMP	3.67	6.32	72.21	12.65	14.03	90.17
CNT/DMF	17.84	45.41	154.54	13.72	16.47	83.70

Cyclic strain and damage sensing of CNT infused glass cord-rubber composites

As the glass cord swollen in CNT/acetone dispersions had a more continuous and sensitive sensing signal among all other composite samples when applied as interfacial damage sensor under static loading, it was selected for further evaluation in cyclic *in-situ* damage sensing.

Figure 7-12 shows the cyclic electro-mechanical behaviour of the same composite pull-out specimen subjected to a series of cyclic loading conditions before the application of a static tensile load to ultimate interfacial failure. At low displacement levels (Figure 7-12a) with an applied cyclic extension from 3.5 mm to 7 mm, the sensing signals increased up to 80 % with applied load whilst the values fully recover to the initial levels upon unloading, indicating good reversibility at these extension levels. This was attributed to the reversible deformation of the elastomeric interphase without the permanent break-down of the CNT network. This is consistent with previous static sensing results of glass cord-rubber composite pull-out specimens (see Figure 7-11a) where the resistance change was roughly the same value when displaced to 7 mm.

When the applied strain increased from an extension level of 3.5 mm to 10.5 mm (Figure 7-12b), a clear change in $\Delta R / R_0$ values (about 50~80 % increment) was observed after the first loading cycle. Instead of returning to its initial level, the following sensing signals went up gradually upon unloading, which can be explained by a partial interruption of conductive paths as a result of some degree of permanent interfacial damage. Upon further static tensile loading (Figure 7-12c), the sensing signals increased continuously with a sharp and clear jump when catastrophic interface failure was achieved.

The potential of conductive glass cords made using the proposed infusion method for structural integrity monitoring of interfacial damage in cord-rubber composites has, therefore, been demonstrated. Glass cords made by swelling in CNT/acetone dispersions offered the most sensitive and continuous sensing signals just before catastrophic interfacial failure.

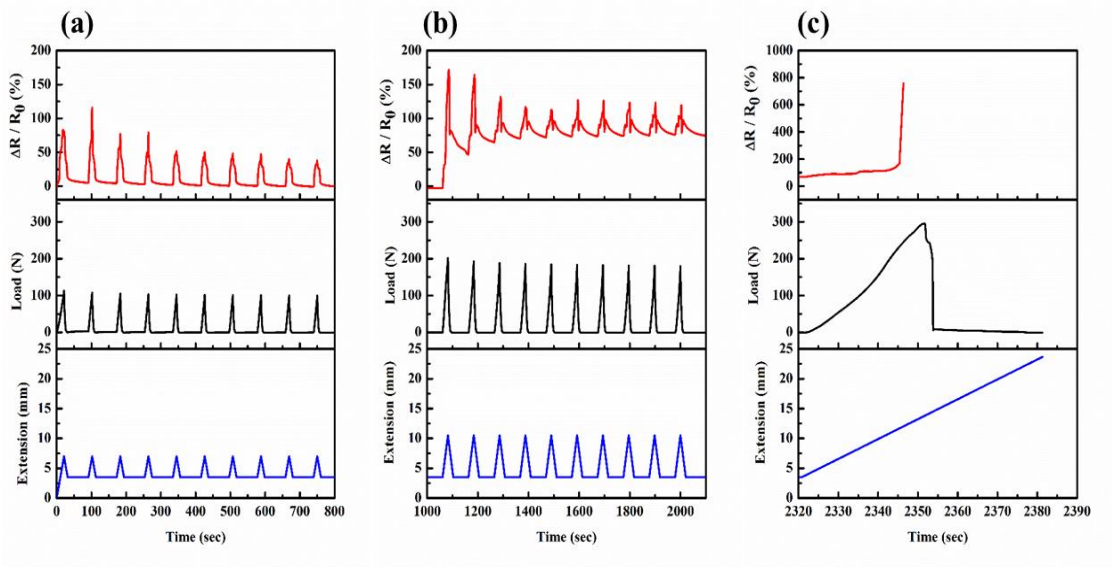

Figure 7-12.Cyclic electro-mechanical characterisation of the CNT infused glass cord-rubber composite pull-out specimen using CNT/acetone dispersions subjected to cyclic extension from (a) 3.5 mm to 7.0 mm with 1 min relaxation time between each cycle, showing reversible interfacial deformation, (b) 3.5 mm to 10.5 mm extension with 1 min relaxation time, showing some degree of permanent interfacial damage, (c) continuous increased extension until complete pull-out, with a clear sharp increment in sensing signals. Note: The specimen was held for 5 min before being reloaded to a higher displacement level.

7.3.5. Interfacial shear strength

After demonstrating the potential of the developed CNT infused glass cord as smart reinforcements for rubber products, with added interfacial damage and strain sensing capabilities, efforts were made to evaluate the effect of CNT infusion on adhesion between cord and rubber.

Several micromechanical characterisations can be used to quantitatively evaluate the interfacial shear strength (IFSS) between a reinforcing fibre and its surrounding matrix, such as the single fibre pull-out test or the fibre fragmentation test which are

discussed in Chapter 3. Figure 7-13a presents the single cord pull-out test results of various CNT infused glass cord-rubber and as-received glass cord-rubber composites swollen in various solvents without the presence of CNTs (acetone, NMP, and DMF, respectively) for 1 h under the same conditions before embedded into the HNBR matrix. It can be seen that no significant change in IFSS values was observed, within typical experimental error [132, 135, 194]. Fractographic analysis (Figure 7-13b and Figure 7-13c) of fracture surfaces after pull-out indicated a change from failure mode of the elastomeric coating/HNBR interface failure to failure at the elastomeric coating/glass fibre interface, indicating a toughening of the elastomeric coating/HNBR interphase due to the presence of CNTs.

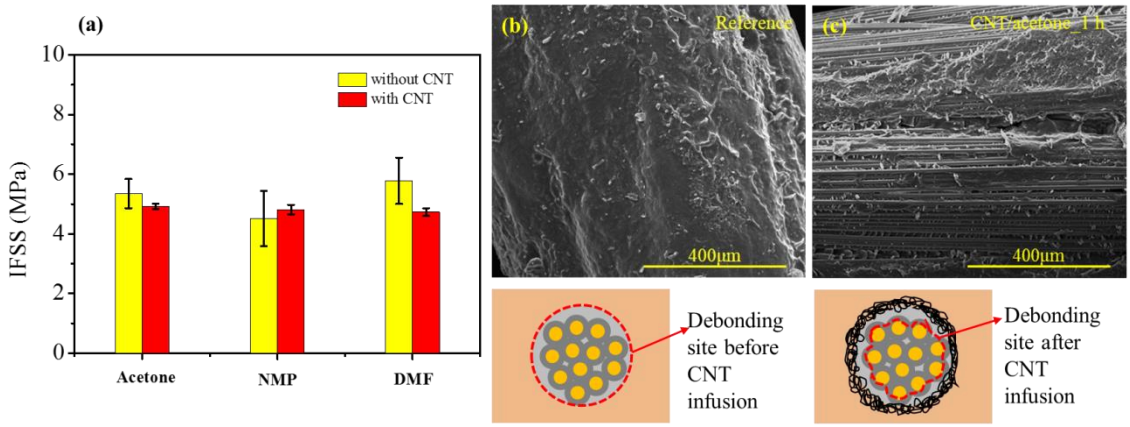

Figure 7-13. (a) Single cord pull-out test results of glass cord-rubber composites with and without CNT treatment. (b) Fracture surface of reference cord specimens after pull-out testing, showing failure at the elastomeric coating/HNBR interface with most of the elastomeric coating remaining present on the cord surface, (c) Fracture surface of cord specimens swelled in CNT/acetone dispersions showing failure at the elastomeric coating/glass fibre interface with glass fibres exposed at the fracture surface.

7.4. Conclusions

In this chapter, a simple and efficient method was developed for the fabrication of self-sensing CNT infused glass cords based on a swelling and infusion process. The percolated CNT network has been successfully localised into the existing elastomeric coating present on the reinforcing cords, acting as an integrated interfacial strain and damage sensors for cord-rubber composites. The effect of various solvents on CNT infusion has been investigated. Good electrical conductivity (10^{-2} S/m) was achieved with extremely low amounts of CNTs after only 30 min of swelling, with no detrimental effects on original mechanical performance of the composites.

Stable and repeatable sensing signals were obtained under both static and cyclic loading conditions by embedding those fabricated smart sensing cords into rubber matrix, providing insightful information of the interfacial structural integrity of the system. With such smart hierarchical cord-rubber composites, early detection of interfacial damage before catastrophic failure becomes viable.

Chapter 8 : Summary of the major findings from this work and potential future supporting investigations

8.1 Summary

In this thesis, the fatigue properties of cord-rubber composites that can be used for timing belt applications have been systematically investigated. Further to the introduction and literature sections the thesis is broken down into four major investigations.

In chapter 4, initial fatigue tests on a single carbon cord reinforced hydrogenated nitrile butadiene rubber (CC-HNBR) model composite were undertaken using conventional wedge grips which are routinely employed for fatigue testing of cord-rubber composites. Damage evolution was monitored using thermal imaging, while post-failure modes were evaluated using scanning electron microscopy (SEM). Finite element analysis (FEA) was performed to understand the stress state in the gripping region. The observed failure mode in wedge grips based testing was found to be interfacial debonding as a consequence of shear stress concentrations induced by the grips, leading to a significant underestimation of fatigue life. Consequently, an alternative bollard based test methodology was developed for cord-rubber composites. Fatigue data generated using this novel bollard test set-up was compared with data obtained by using conventional wedge grips. Bollard-based testing resulted in tensile fatigue behaviour dominated by cord failure rather than failure by interfacial debonding during accelerated laboratory fatigue testing, making the developed test methodology better suited for the characterisation of intrinsic fatigue behaviour of cord-rubber composites.

The influences of frequency and R ratio on the tensile fatigue behaviour of CC-HNBR composites was studied based upon a comprehensive laboratory accelerated testing protocol using bollard based testing in chapter 5. Frequency was found to have negligible effect on the fatigue life within the evaluated test regimes (2, 5, 10 and 20 Hz). This was due to modest amount of heat build-up in the rubber matrix even at the highest testing frequency by evaluating the specimen surface temperature rise using thermal imaging. Additionally, the use of lower test frequency tended to increase the fatigue limit. By increasing the R ratio, the fatigue life was increased under non-relaxing testing conditions. This can be explained by crack-arresting effects potentially as a consequence of strain induced crystallisation (SIC) of highly strained HNBR in the vicinity of a carbon filament break. A longer fatigue life at higher R ratios for a given maximum cyclic stress level was associated with the dynamic process of forming and melting of crystallites during loading and unloading, leading to a larger extent of net accumulation of crystallites in each cycle. Furthermore, an effort was made by modifying Harris's constant life diagrams (CLD) to predict the lifetime of the cord-rubber composites. The applicability of other established analytical CLD models was also examined. It showed that a simple modification of Harris's CLD and piecewise linear CLD gave a good agreement with the experimental fatigue data.

In chapter 6, the fatigue testing was extended to couple both tension and bending conditions using fixed pulleys of different diameters that introduced an additional bending strain into the composite specimens. The effect of the pulley diameter and other test parameters such as frequency and R ratio were assessed on the flex fatigue of single CC-HNBR composites. It was found the flex bending fatigue life was significantly influenced by the pulley diameter whilst no obvious change in bending

fatigue life was observed over the entire frequency regime used in this study. Meanwhile, there was an increase in the fatigue life of cord-rubber composites with the increasing *R* ratio. This was again thought to be related to the microstructural changes in the HNBR at the tip of a fibre break.

The wide application of cord-rubber composites in the automobile industry necessitates its structural health monitoring (SHM) to prevent the catastrophic failure. A feasible strategy to fabricate smart glass cords with integrated damage detection capabilities is introduced in chapter 7. Conductive glass cords with good self-sensing capabilities were obtained by a swelling and infusion method to incorporate CNTs into the chlorosulfonated polyethylene synthetic rubber (CSM) coating layer of the impregnated glass cord. The localised percolated CNT network enabled online health monitoring via electrical sensing methods using a variety of different mechanical loading conditions, with clear warning signal (with a change in resistance up to 850 %) before the final failure. The developed simple methodology offers an industrially feasible solution for cord rubber composites to integrate multi-functionality whilst maintaining good compatibility with current manufacturing processes.

8.2 Future works

This thesis carried out a systematic investigation on the fatigue of cord rubber composites. In addition, the structural health monitoring (SHM) of such composites was developed for the first time. However, there are still some aspects that can be further explored or improved.

In chapter 5, preliminary wide-angle X-ray diffraction (WAXD) measurement of the HNBR compound was carried out at different strains offline. However, it would be desirable to study its strain induced crystallisation (SIC) behaviour *in-situ* using

synchrotron WAXS under cyclic loading conditions. It would be very useful to understand the kinetics of the crystallisation process in order to help interpret further the fatigue dependence on *R* ratio and frequency.

In chapter 6, one outstanding issue would be to try to correlate the bending fatigue data with the tensile fatigue data. This would require the development of sophisticated models of the fibre bundles in the cord to see how the stresses develop in bending around the middle pulley. The model would have to account accurately for the fibre twisting that is present in the real cord. This would allow the stresses in the region of maximum stress in the individual fibre bundle to be examined more closely. Clearly more test data under the combination of tension and bending could be generated and this would have to be compared to the models of the stresses that are present under specific loading conditions in the fibre to allow the development of more sophisticated fatigue life model. Another issue that is broadly ignored in this work is the effect of the fabric that is moulded into the inside surface of the continuous belt used for the combined bending and tensile fatigue testing. It is not clear how this introduction of a fabric will modify the friction at this interface and then alter the stresses and the resulting measured fatigue life. This would have an impact potentially on the diminution of the tensile stress as the cord wraps around the central pulley. Could a more sophisticated FEA model be developed that considers the frictional interactions at the fabric interface be used to examine the problem. In this way, the data generated from two types of loading conditions could be compared for example under a specific maximum stress levels within the cord.

Chapter 7 examines the ability to produce a smart sensing cord. It is clear that other types of conductive nanofillers such as graphene could be introduced into the elastomeric coating of the glass cord using the proposed simple swelling method to

compare the effectiveness and the sensitivity of any proposed damage detection system. The question remains is this swelling and infusion technique the most effective way to create the smart sensing cords. So alternative processing pathways can be explored such as a simple spray coating as reported already in the literature [136]. By measuring the behaviour changes with strain of these different systems it would be possible to see if even stronger changes in the electrical conductivity with strain are possible.

References

[1] G.L. Miller, Differences in synchronous belts, Plant Engineering, (1991).
[2] C. Tiemann, J. Dohmen, C. Steffens, S. Wedowski, R. Walter, H. Schulte, T. Di Giacomo, Belt vs. Chain-Study on the potential for CO2 saving by the timing drive, in: Aachener Kolloquium Fahrzeug und Motorentechnik, 2008.
[3] D. Hull, T. Clyne, An Introduction to Composite Materials, Cambridge University Press, 1996.
[4] L.R.G. Treloar, The Physics of Rubber Elasticity, 3rd ed., Oxford University Press, Oxford, 2009.
[5] ISO, 1382:2012, Rubber-Vocabulary, 2012.
[6] N. Mathew, J. White, S. De, Rubber Technologist Handbook, Rapra Technology Limited, UK, (2003).
[7] P. Allen, K. Jones, Natural Rubber Science and Technology, Oxford University Press, Oxford, 1988.
[8] S. Toki, T. Fujimaki, M. Okuyama, Strain-induced crystallization of natural rubber as detected real-time by wide-angle X-ray diffraction technique, Polymer, 41 (2000) 5423-5429.
[9] M. Tosaka, S. Murakami, S. Poompradub, S. Kohjiya, Y. Ikeda, S. Toki, I. Sics, B.S. Hsiao, Orientation and crystallization of natural rubber network as revealed by WAXD using synchrotron radiation, Macromolecules, 37 (2004) 3299-3309.
[10] M. Tosaka, Strain-induced crystallization of crosslinked natural rubber as revealed by X-ray diffraction using synchrotron radiation, Polymer Journal, 39 (2007) 1207-1220.
[11] A. Ciesielski, An Introduction to Rubber Technology, iSmithers Rapra Publishing, 1999.
[12] A.N. Gent, Engineering with Rubber: How to Design Rubber Components, 3rd ed., Carl Hanser Verlag GmbH & Co. KG, 2012.
[13] T. Eduard, K. Erich, Rubber like masses from butadiene hydrocarbons and polymerizable nitriles, US1973000A, 1934.
[14] H. Wang, L. Yang, G.L. Rempel, Homogeneous hydrogenation art of nitrile butadiene rubber: A review, Polymer Reviews, 53 (2013) 192-239.
[15] P.R. Dluzneski, Peroxide vulcanization of elastomers, Rubber Chemistry and Technology, 74 (2001) 451-492.
[16] G. Holden, H.L. Stephens, K.C. Baranwal, Basic Elastomer Technology, Ruber Division, American Chemical Society, The University of Akron, 2001.
[17] J. Gough, A description of a property of Caoutchouc, or Indian rubber, Memories of the Literacy and Philosophical Society of Manchester, 1 (1805) 288-295.
[18] J.P. Joule, On some thermo-dynamic properties of solids, Philosophical Transactions of the Royal Society of London, 149 (1859) 91-131.
[19] R.L. Anthony, R.H. Caston, E. Guth, Equations of state for natural and synthetic rubber-like materials. I. Unaccelerated natural soft rubber, The Journal of Physical Chemistry, 46 (1942) 826-840.
[20] O. Yeoh, Some forms of the strain energy function for rubber, Rubber Chemistry & Technology, 66 (1993) 754-771.
[21] L.B. Tunnicliffe, Particulate Reinforcement of Elastomers at Small Strains, Queen Mary University of London, 2015.

[22] L. Mullins, Effect of stretching on the properties of rubber, Rubber Chemistry & Technology, 21 (1948) 281-300.
[23] J. Harwood, L. Mullins, A. Payne, Stress softening in natural rubber vulcanizates. Part II. Stress softening effects in pure gum and filler loaded rubbers, Journal of Applied Polymer Science, 9 (1965) 3011-3021.
[24] C. Davies, D.K. De, A. Thomas, Characterisation of the behaviour of rubber for engineering design purposes: Stress relaxation under repeated stressing, Progress in Rubber and Plastics Technology, 12 (1996) 208-220.
[25] A. Blanchard, D. Parkinson, Breakage of carbon-rubber networks by applied stress, Industrial & Engineering Chemistry, 44 (1952) 799-812.
[26] R. Houwink, Slipping of molecules during the deformation of reinforced rubber, Rubber Chemistry and Technology, 29 (1956) 888-893.
[27] G. Kraus, C. Childers, K. Rollmann, Stress softening in carbon black reinforced vulcanizates. Strain rate and temperature effects, Rubber Chemistry & Technology, 39 (1966) 1530-1543.
[28] D.E. Hanson, M. Hawley, R. Houlton, K. Chitanvis, P. Rae, E.B. Orler, D.A. Wrobleski, Stress softening experiments in silica-filled polydimethylsiloxane provide insight into a mechanism for the Mullins effect, Polymer, 46 (2005) 10989-10995.
[29] J. Diani, B. Fayolle, P. Gilormini, A review on the Mullins effect, European Polymer Journal, 45 (2009) 601-612.
[30] M.L. Williams, R.F. Landel, J.D. Ferry, The temperature dependence of relaxation mechanisms in amorphous polymers and other glass-forming liquids, Journal of the American Chemical Society, 77 (1955) 3701-3707.
[31] D. Dew-Hughes, J. Way, Fatigue of fibre-reinforced plastics: a review, Composites, 4 (1973) 167-173.
[32] J.G. Williams, Fracture Mechanics of Polymers, Horwood, 1984.
[33] R. Talreja, Fatigue of composite materials: damage mechanisms and fatigue-life diagrams, Proceedings of the Royal Society of London A: Mathematical, Physical and Engineering Sciences, The Royal Society, 1981, 461-475.
[34] T.J. Myers, H.K. Kytömaa, T.R. Smith, Environmental stress-corrosion cracking of fiberglass: Lessons learned from failures in the chemical industry, Journal of Hazardous Materials, 142 (2007) 695-704.
[35] A. Kelly, a.W. Tyson, Tensile properties of fibre-reinforced metals: copper/tungsten and copper/molybdenum, Journal of the Mechanics and Physics of Solids, 13 (1965) 329-350.
[36] H. Cox, The elasticity and strength of paper and other fibrous materials, British journal of applied physics, 3 (1952) 72.
[37] B.W. Rosen, Mechanics of composite strengthening: Fibre Composite Materials, American Society of Metals, Chapter 3. (1965).
[38] J.D. Eshelby, The determination of the elastic field of an ellipsoidal inclusion, and related problems, Proceedings of the Royal Society of London A: Mathematical, Physical and Engineering Sciences, The Royal Society, 1957, pp. 376-396.
[39] J. Eshelby, The elastic field outside an ellipsoidal inclusion, Proceedings of the Royal Society of London A: Mathematical, Physical and Engineering Sciences, The Royal Society, 1959, pp. 561-569.
[40] C.M. Landis, R.M. McMeeking, A shear-lag model for a broken fiber embedded in a composite with a ductile matrix, Composites Science and Technology, 59 (1999) 447-457.

[41] P.W.J. van den Heuvel, B. Hogeweg, T. Peijs, An experimental and numerical investigation into the single-fibre fragmentation test: stress transfer by a locally yielding matrix, Composites Part A: Applied Science and Manufacturing, 28 (1997) 237-249.
[42] J. Bowling, G. Groves, The debonding and pull-out of ductile wires from a brittle matrix, Journal of Materials Science, 14 (1979) 431-442.
[43] C. DiFrancia, T.C. Ward, R.O. Claus, The single-fibre pull-out test. 1: Review and interpretation, Composites Part A: Applied Science and Manufacturing, 27 (1996) 597-612.
[44] D.B. Marshall, An Indentation method for measuring matrix-fibre frictional stresses in ceramic composites, Journal of the American Ceramic Society, 67 (1984) C259-C260.
[45] Y. Dai, J.-K. Kim, J. Park, Numerical study of the single fibre push-out test: Part III. Singularity of interface stresses, Composite Interfaces, 10 (2003) 17-39.
[46] A.F. Kalton, C.M. Ward-Close, T.W. Clyne, Development of the tensioned push-out test for study of fibre/matrix interfaces, Composites, 25 (1994) 637-644.
[47] W.M. Mueller, J. Moosburger-Will, M.G.R. Sause, S. Horn, Microscopic analysis of single-fiber push-out tests on ceramic matrix composites performed with Berkovich and flat-end indenter and evaluation of interfacial fracture toughness, Journal of the European Ceramic Society, 33 (2013) 441-451.
[48] P.W.J. van den Heuvel, Y.J.W. van der Bruggen, T. Peijs, Failure phenomena in multi-fibre model composites: Part 1. An experimental investigation into the influence of fibre spacing and fibre—matrix adhesion, Composites Part A: Applied Science and Manufacturing, 27 (1996) 855-859.
[49] X. Wang, B. Zhang, S. Du, Y. Wu, X. Sun, Numerical simulation of the fiber fragmentation process in single-fiber composites, Materials & Design (1980-2015), 31 (2010) 2464-2470.
[50] R.B. Durairaj, Resorcinol formaldehyde latex (RFL) adhesives and applications, Resorcinol: Chemistry, Technology and Applications, (2005) 263-339.
[51] M. Jamshidi, F.A. Taromi, Estimation of dynamic adhesion from static test results in the model cord-RFL-rubber system, Journal of Adhesion Science and Technology, 20 (2006) 1693-1703.
[52] C. Valantin, F. Lacroix, M.P. Deffarges, J. Morcel, N. Aït Hocine, Interfacial damage on fatigue-loaded textile-rubber composites, Journal of Applied Polymer Science, 132 (2015).
[53] W.B. Wennekes, R.N. Datta, J.W.M. Noordermeer, Mechanistic Investigations into the Adhesion between RFL-Treated Cords and Rubber. Part II: The Influence of the Vinyl-Pyridine Content of the RFL-Latex, Rubber Chemistry and Technology, 80 (2007) 565-579.
[54] M. Razavizadeh, M. Jamshidi, Adhesion of nitrile rubber to UV-assisted surface chemical modified PET fabric, part II: Interfacial characterization of MDI grafted PET, Applied Surface Science, 379 (2016) 114-123.
[55] Z. Li, T.L. Xiao, S.G. Zhao, Effects of surface treatments on mechanical properties of continuous basalt fibre cords and their adhesion with rubber matrix, Fibers and Polymers, 17 (2016) 910-916.
[56] W.B. Wennekes, Adhesion of RFL-Treated Cords to Rubber: New Insights into Interfacial Phenomena, University of Twente, The Netherlands, 2008.

[57] D.B. Wootton, R.T.L. Staff, The Application of Textiles in Rubber, Rapra Technology Shawbury, 2001.

[58] P. Langevin, R. Payne, C. Shephard, A Dynamic Rubber-Cord Composite Adhesion and Fatigue Test, Rubber Chemistry and Technology, 47 (1974) 171-187.
[59] X. Shi, C. Lian, Y. Shang, H. Zhang, Evolution of the dynamic fatigue failure of the adhesion between rubber and polymer cords, Polymer Testing, 48 (2015) 175-182.
[60] X.Y. Shi, M.Q. Ma, C.B. Lian, D.W. Zhu, Investigation of the effects of adhesion promoters on the adhesion properties of rubber/steel cord by a new testing technique, Journal of Applied Polymer Science, 131 (2014) 1145–1153.
[61] X. Shi, M. Ma, C. Lian, D. Zhu, Investigation on effects of dynamic fatigue frequency, temperature and number of cycles on the adhesion of rubber to steel cord by a new testing technique, Polymer Testing, 32 (2013) 1145-1153.
[62] C. Valantin, R. Benoit, M.P. D, F. Lacroix, E. Gomez, P. Phalip, J. Morcel, D. Tricoche, N.A. Hocine, SEM-EDX analysis and TOF-SIMS 3D imaging of a textile/rubber interface undergoing fatigue loading, Applied Surface Science, 360, Part B (2016) 623-633.
[63] C. Manjunatha, S. Sprenger, A. Taylor, A. Kinloch, The tensile fatigue behavior of a glass-fiber reinforced plastic composite using a hybrid-toughened epoxy matrix, Journal of Composite Materials, 44 (2010) 2095-2109.
[64] Y. Zhou, P. Mallick, Fatigue performance of an injection molded talc-filled polypropylene, Polymer Engineering and Science, 45 (2005) 510.
[65] B. Harris, H. Reiter, T. Adam, R. Dickson, G. Fernando, Fatigue behaviour of carbon fibre reinforced plastics, Composites, 21 (1990) 232-242.
[66] E.K. Gamstedt, L.A. Berglund, T. Peijs, Fatigue mechanisms in unidirectional glass-fibre-reinforced polypropylene, Composites Science and Technology, 59 (1999) 759-768.
[67] H. Kotik, J. Perez Ipiña, Frequency effect in short-beam shear fatigue of a glass fiber reinforced polyester composite, International Journal of Fatigue, 90 (2016) 116-124.
[68] B. Lee, D. Liu, M. Chawla, P. Ulrich, Fatigue of cord-rubber composites, Rubber Chemistry and Technology, 67 (1994) 761-774.
[69] J.H. Song, F. Costanzo, B.L. Lee, Fatigue of cord-rubber composites: V. cord reinforcement effect, Rubber Chemistry and Technology, 77 (2004) 593-610.
[70] J.D. Walter, Cord-Rubber Tire Composites: Theory and Applications, Rubber Chemistry and Technology, 51 (1978) 524-576.
[71] J. Kawamoto, Fatigue of rubber composites, Massachusetts Institute of Technology, 1988.
[72] S. Mortazavian, A. Fatemi, Fatigue behavior and modeling of short fiber reinforced polymer composites: A literature review, International Journal of Fatigue, 70 (2015) 297-321.
[73] R.P.L. Nijssen, 2. Phenomenological fatigue analysis and life modeling, in: Fatigue Life Prediction of Composites and Composite Structures, Woodhead Publishing, 2010, pp. 47-78.
[74] M. Eftekhari, A. Fatemi, On the strengthening effect of increasing cycling frequency on fatigue behavior of some polymers and their composites: Experiments and modeling, International Journal of Fatigue, 87 (2016) 153-166.
[75] A. Bernasconi, R.M. Kulin, Effect of frequency upon fatigue strength of a short glass fiber reinforced polyamide 6: A superposition method based on cyclic creep parameters, Polymer Composites, 30 (2009) 154-161.

[76] F.M. Xu, S.J. Zhu, J. Zhao, M. Qi, F.G. Wang, S.X. Li, Z.G. Wang, Effect of stress ratio on fatigue crack propagation in a functionally graded metal matrix composite, Composites Science and Technology, 64 (2004) 1795-1803.
[77] M. Kawai, M. Koizumi, Nonlinear constant fatigue life diagrams for carbon/epoxy laminates at room temperature, Composites Part A: Applied Science and Manufacturing, 38 (2007) 2342-2353.
[78] N. Gathercole, H. Reiter, T. Adam, B. Harris, Life prediction for fatigue of T800/5245 carbon-fibre composites: I. Constant-amplitude loading, International Journal of Fatigue, 16 (1994) 523-532.
[79] B. Ku, D. Liu, B. Lee, Fatigue of cord-rubber composites: III. Minimum stress effect, Rubber Chemistry and Technology, 71 (1998) 889-905.
[80] S. Seichter, V.-M. Archodoulaki, T. Koch, A. Holzner, A. Wondracek, Investigation of different influences on the fatigue behaviour of industrial rubbers, Polymer Testing, 59 (2017) 99-106.
[81] S. Seichter, Rubber Blends and Rubber-Textile Composites: Considering Application-Relevant Aspects, Technische Universitat of Wien, 2017.
[82] K. Bruning, K. Schneider, S.V. Roth, G. Heinrich, Kinetics of strain-induced crystallization in natural rubber studied by WAXD: dynamic and impact tensile experiments, Macromolecules, 45 (2012) 7914-7919.
[83] J.B. Le Cam, Energy storage due to strain-induced crystallization in natural rubber: The physical origin of the mechanical hysteresis, Polymer, 127 (2017) 166-173.
[84] D. Braun, A. Haufe, D. Leiss, G.P. Hellmann, Strain-induced crystallisation and miscibility behaviour of hydrogenated nitrile rubbers, Angewandte Makromolekulare Chemie, 202 (1992) 143-158.
[85] T. Kobatake, K. Kodama, S. Hayashi, A. Yoshioka, Improvement of low-temperature flexibility of hydrogenated nitrile-butadiene rubber, Rubber Chemistry and Technology, 70 (1997) 839-854.
[86] D.M. Bieliński, L. Ślusarski, A. Włochowicz, C. Ślusarczyk, Structure and mechanical properties of nitrile rubbers modified with iodine, Journal of Applied Polymer Science, 67 (1998) 501-512.
[87] G. Severe, J.L. White, Physical properties and blend miscibility of hydrogenated acrylonitrile-butadiene rubber, Journal of Applied Polymer Science, 78 (2000) 1521-1529.
[88] B. Alcock, K. Olafsen, J. Huse, F. Grytten, The low temperature crystallization of hydrogenated nitrile butadiene rubber (HNBR), Polymer Testing, 66 (2018) 228-234.
[89] K. Narynbek Ulu, Dragicevic, M., Albouy, P. A., Huneau, B., Beranger, A. S., Heuillet, P., Strain-induced crystallization ability of hydrogenated nitrile butadiene rubber, in: M.J. Alexander Lion (Ed.) Constitutive Models for Rubber X, CRC Press, 2017, pp. 279–282.
[90] D. Socie, J. Morrow, Review of contemporary approaches to fatigue damage analysis, in: Risk and Failure Analysis for Improved Performance and Reliability, Springer, 1980, pp. 141-194.
[91] W. Hwang, K. Han, Cumulative damage models and multi-stress fatigue life prediction, Journal of Composite Materials, 20 (1986) 125-153.
[92] N.L. Post, S.W. Case, J.J. Lesko, Modeling the variable amplitude fatigue of composite materials: A review and evaluation of the state of the art for spectrum loading, International Journal of Fatigue, 30 (2008) 2064-2086.

[93] A.P. Vassilopoulos, B.D. Manshadi, T. Keller, Influence of the constant life diagram formulation on the fatigue life prediction of composite materials, International Journal of Fatigue, 32 (2010) 659-669.
[94] T.P. Philippidis, A.P. Vassilopoulos, Life prediction methodology for GFRP laminates under spectrum loading, Composites Part A: Applied Science and Manufacturing, 35 (2004) 657-666.
[95] S. Ramani, D. Williams, Notched and unnotched fatigue behavior of angle-ply graphite/epoxy composites, in: Fatigue of Filamentary Composite Materials, ASTM International, 1977.
[96] M.H. Beheshty, B. Harris, T. Adam, An empirical fatigue-life model for high-performance fibre composites with and without impact damage, Composites Part A: Applied Science and Manufacturing, 30 (1999) 971-987.
[97] T. Adam, G. Fernando, R. Dickson, H. Reiter, B. Harris, Fatigue life prediction for hybrid composites, International Journal of Fatigue, 11 (1989) 233-237.
[98] B. Harris, A parametric constant-life model for prediction of the fatigue lives of fibre-reinforced plastics, Fatigue in Composites, (2003) 546-568.
[99] C. Kassapoglou, Fatigue life prediction of composite structures under constant amplitude loading, Journal of Composite Materials, 41 (2007) 2737-2754.
[100] T.K. O'Brien, M. Rigamonti, C. Zanotti, Tension fatigue analysis and life prediction for composite laminates, International Journal of Fatigue, 11 (1989) 379-393.
[101] S. Amijima, T. Fujii, M. Hamaguchi, Static and fatigue tests of a woven glass fabric composite under biaxial tension-torsion loading, Composites, 22 (1991) 281-289.
[102] M.K. Cvitkovich, T.K. O'brien, P.J. Minguet, Fatigue debonding characterization in composite skin/stringer configurations, in: Composite Materials: Fatigue and Fracture: 7th Volume, ASTM International, 1998.
[103] A.N. Anoshkin, V.Y. Zuiko, 3. Experimental methods and standards for fatigue of fiber-reinforced composites, in: V. Carvelli, S.V. Lomov (Eds.) Fatigue of Textile Composites, Woodhead Publishing, 2015, pp. 57-73.
[104] R. Sakin, İ. Ay, R. Yaman, An investigation of bending fatigue behavior for glass-fiber reinforced polyester composite materials, Materials & Design, 29 (2008) 212-217.
[105] Y. Yamada, K. Iwata, T. Kadowaki, T. Sumiya, Method of reduced variables for stiffness degradation process of unidirectional CFRP composites subjected to alternating bending, Composites Science and Technology, 138 (2017) 117-123.
[106] Craig.Hayes, Manufacture of glass / rubber cord with improved durability, The University of Sheffield, 2012.
[107] L. Nkiwane, S.K. Mukhopadhyay, A study of flex fatigue characteristics of nylon 6.6 tire yarns and cords, Journal of Applied Polymer Science, 75 (2000) 1045-1053.
[108] M. Furusawa, Y. Tsukada, T. Morimoto, H. Iizuka, Asme, IMPROVEMENT OF BENDING FATIGUE STRENGTH FOR HYBRID CORDS WITH CARBON AND GLASS FIBERS, 2010.
[109] G. Cai, D. Li, D. Fang, W. Yu, A new apparatus to measure the effect of temperature and light on the bending fatigue properties of Kevlar 49 and PBO fibers, Polymer Testing, 40 (2014) 143-148.

[110] G.M. Cai, X.J. Shi, W.D. Yu, Apparatus for Measuring the Bending Fatigue Properties of High Performance Polyethylene Fibre, Fibres & Textiles in Eastern Europe, 20 (2012) 37-40.
[111] X.Y. Liu, Z.S. Zhang, X.X. Xu, Bending Fatigue Numerical Simulation of Single Kevlar Fiber, in: Y. Li, J.H. Xin, K.J. Yoon, J.S. Li (Eds.) Textile Bioengineering and Informatics Symposium Proceedings, 2014, Vols 1 and 2, 2014, pp. 633-637.
[112] R. Hobbs, S. Nabijou, Changes in wire curvature as a wire rope is bent over a sheave, The Journal of Strain Analysis for Engineering Design, 30 (1995) 271-281.
[113] S. Nabijou, R. Hobbs, Relative movements within wire ropes bent over sheaves, The Journal of Strain Analysis for Engineering Design, 30 (1995) 155-165.
[114] T.M. Mower, Sheave-bending and tensile fatigue of aramid-fiber strength members for communications cables, International Journal of Fatigue, 22 (2000) 121-135.
[115] S.B. Abilash Kumar Nair, Wei Li, Andrew Turner, Fatigue and damage resistant materials in next-generation aircraft tyres, RIEG Conference 2016, London (UK), 2016.
[116] I. Ridge, C. Chaplin, J. Zheng, Effect of degradation and impaired quality on wire rope bending over sheave fatigue endurance, Engineering Failure Analysis, 8 (2001) 173-187.
[117] F. Sloan, R. Nye, T. Liggett, Improving bend-over-sheave fatigue in fiber ropes, in: OCEANS 2003. Proceedings, IEEE, 2003, pp. 1054-1057.
[118] K. Schulte, C. Baron, Load and failure analyses of CFRP laminates by means of electrical resistivity measurements, Composites Science and Technology, 36 (1989) 63-76.
[119] N. Alexopoulos, C. Bartholome, P. Poulin, Z. Marioli-Riga, Structural health monitoring of glass fiber reinforced composites using embedded carbon nanotube (CNT) fibers, Composites Science and Technology, 70 (2010) 260-271.
[120] J.-M. Park, P.-G. Kim, J.-H. Jang, Z. Wang, J.-W. Kim, W.-I. Lee, J.-G. Park, K.L. DeVries, Self-sensing and dispersive evaluation of single carbon fiber/carbon nanotube (CNT)-epoxy composites using electro-micromechanical technique and nondestructive acoustic emission, Composites Part B: Engineering, 39 (2008) 1170-1182.
[121] L. Böger, M.H. Wichmann, L.O. Meyer, K. Schulte, Load and health monitoring in glass fibre reinforced composites with an electrically conductive nanocomposite epoxy matrix, Composites Science and Technology, 68 (2008) 1886-1894.
[122] L. Gao, E.T. Thostenson, Z. Zhang, T.W. Chou, Sensing of damage mechanisms in fiber-reinforced composites under cyclic loading using carbon nanotubes, Advanced Functional Materials, 19 (2009) 123-130.
[123] E.T. Thostenson, T.W. Chou, Carbon nanotube networks: sensing of distributed strain and damage for life prediction and self healing, Advanced Materials, 18 (2006) 2837-2841.
[124] J. Rausch, E. Mäder, Health monitoring in continuous glass fibre reinforced thermoplastics: Manufacturing and application of interphase sensors based on carbon nanotubes, Composites Science and Technology, 70 (2010) 1589-1596.
[125] H. Zhang, Y. Liu, S. Huo, J. Briscoe, W. Tu, O.T. Picot, A. Rezai, E. Bilotti, T. Peijs, Filtration effects of graphene nanoplatelets in resin infusion processes: Problems and possible solutions, Composites Science and Technology, 139 (2017) 138-145.

[126] R. Zhang, H. Deng, R. Valenca, J. Jin, Q. Fu, E. Bilotti, T. Peijs, Carbon nanotube polymer coatings for textile yarns with good strain sensing capability, Sensors and Actuators A: Physical, 179 (2012) 83-91.
[127] D.L. He, B.H. Fan, H. Zhao, X.X. Lu, M.H. Yang, Y. Liu, J.B. Bai, Design of electrically conductive structural composites by modulating aligned CVD-grown carbon nanotube length on glass fibers, ACS Applied Materials & Interfaces, 9 (2017) 2948-2958.
[128] S.L. Gao, R.C. Zhuang, J. Zhang, J.W. Liu, E. Mader, Glass Fibers with Carbon Nanotube Networks as Multifunctional Sensors, Advanced Functional Materials, 20 (2010) 1885-1893.
[129] E. Bilotti, R. Zhang, H. Deng, M. Baxendale, T. Peijs, Fabrication and property prediction of conductive and strain sensing TPU/CNT nanocomposite fibres, Journal of Materials Chemistry A, 20 (2010) 9449-9455.
[130] R. Zhang, H. Deng, R. Valenca, J. Jin, Q. Fu, E. Bilotti, T. Peijs, Strain sensing behaviour of elastomeric composite films containing carbon nanotubes under cyclic loading, Composites Science and Technology, 74 (2013) 1-5.
[131] J. Zhang, R. Zhuang, J. Liu, E. Mäder, G. Heinrich, S. Gao, Functional interphases with multi-walled carbon nanotubes in glass fibre/epoxy composites, Carbon, 48 (2010) 2273-2281.
[132] S. Tamrakar, Q. An, E.T. Thostenson, A.N. Rider, B.Z. Haque, J.W. Gillespie, Tailoring interfacial properties by controlling carbon nanotube coating thickness on glass fibers using electrophoretic deposition, ACS Applied Materials & Interfaces, 8 (2016) 1501-1510.
[133] H. Qian, A. Bismarck, E.S. Greenhalgh, G. Kalinka, M.S. Shaffer, Hierarchical composites reinforced with carbon nanotube grafted fibers: the potential assessed at the single fiber level, Chemistry of Materials, 20 (2008) 1862-1869.
[134] J. Sebastian, N. Schehl, M. Bouchard, M. Boehle, L. Li, A. Lagounov, K. Lafdi, Health monitoring of structural composites with embedded carbon nanotube coated glass fiber sensors, Carbon, 66 (2014) 191-200.
[135] Q.X. Li, J.S. Church, M. Naebe, B.L. Fox, Interfacial characterization and reinforcing mechanism of novel carbon nanotube - Carbon fibre hybrid composites, Carbon, 109 (2016) 74-86.
[136] H. Zhang, Y. Liu, M. Kuwata, E. Bilotti, T. Peijs, Improved fracture toughness and integrated damage sensing capability by spray coated CNTs on carbon fibre prepreg, Composites Part A: Applied Science and Manufacturing, 70 (2015) 102-110.
[137] H. Zhang, M. Kuwata, E. Bilotti, T. Peijs, Integrated damage sensing in fibre-reinforced composites with extremely low carbon nanotube loadings, Journal of Nanomaterials, (2015), Article 785834.
[138] W.B. Wennekes, J.W.M. Noordermeer, R.N. Datta, Mechanistic investigations into the adhesion between RFL-treated cords and rubber. Part I: The influence of rubber curatives, Rubber Chemistry and Technology, 80 (2007) 545-564.
[139] C.S. Boland, U. Khan, C. Backes, A. O'Neill, J. McCauley, S. Duane, R. Shanker, Y. Liu, I. Jurewicz, A.B. Dalton, J.N. Coleman, Sensitive, high-strain, high-rate bodily motion sensors based on graphene-rubber composites, ACS Nano, 8 (2014) 8819-8830.
[140] I. O'Connor, S. De, J.N. Coleman, Y.K. Gun'ko, Development of transparent, conducting composites by surface infiltration of nanotubes into commercial polymer films, Carbon, 47 (2009) 1983-1988.

[141] ASTM D412-16, Standard test methods for vulcanized rubber and thermoplastic elastomers - Tension, ASTM International, West Conshohocken, PA, 2016, www.astm.org.
[142] ISO 37: Rubber, vulcanized or thermoplastic - Determination of tensile stress-strain properties, 2017.
[143] ISO 13003, Fibre-reinforced plastics - Determination of fatigue properties under cyclic loading conditions, 20033.
[144] ASTM D3479 / D3479M-12, Standard test method for tension-tension fatigue of polymer matrix composite materials, ASTM International, West Conshohocken, PA, 2012, www.astm.org.
[145] P.B.S. Bailey, A.D. Lafferty, Specimen gripping effects in composites fatigue testing - Concerns from initial investigation, Express Polymer Letters, 9 (2015) 480-488.
[146] I. De Baere, W. Van Paepegem, J. Degrieck, On the design of end tabs for quasi-static and fatigue testing of fibre-reinforced composites, Polymer Composites, 30 (2009) 381-390.
[147] G. Portnov, V. Kulakov, A. Arnautov, A refined stress-strain analysis in the load transfer zone of flat specimens of high-strength unidirectional composites in uniaxial tension 1. Theoretical analysis, Mechanics of Composite Materials, 42 (2006) 547-554.
[148] G. Portnov, V. Kulakov, A. Arnautov, A refined stress-strain analysis in the load transfer zone of flat specimens of high-strength unidirectional composites in uniaxial tension 2. Finite-element parametric analysis, Mechanics of Composite Materials, 43 (2007) 29-40.
[149] A.A.J.M. Peijs, J.M.M. de Kok, Hybrid composites based on polyethylene and carbon fibres. Part 6: Tensile and fatigue behaviour, Composites, 24 (1993) 19-32.
[150] Z. Tian, H. Tan, X. Du, Fatigue damage accumulation of steel/rubber composite, Journal of Materials Science & Technology, 22 (2006) 647-650.
[151] Z. Tian, H. Song, Z. Wan, X. Du, Fatigue properties of steel cord-rubber composite, Journal of Elastomers and Plastics, 33 (2001) 283-296.
[152] S. Rao, I.M. Daniel, E.E. Gdoutos, Mechanical properties and failure behavior of cord/rubber composites, Applied Composite Materials, 11 (2004) 353-375.
[153] J. Llobet, P. Maimi, J.A. Mayugo, Y. Essa, F.M. de la Escalera, A fatigue damage and residual strength model for unidirectional carbon/epoxy composites under on-axis tension-tension loadings, International Journal of Fatigue, 103 (2017) 508-515.
[154] MR Mitchell, RW Landgraf, Advances in Fatigue Lifetime Predictive Techniques, American Society for Testing and Materials, 1996.
[155] B. Lee, B. Ku, D. Liu, P. Hippo, Fatigue of cord-rubber composites: II. Strain-based failure criteria, Rubber Chemistry and Technology, 71 (1998) 866-888.
[156] H. Anmin, W. Xiaoping, J. Demin, L. Yanmei, Thermal stability and aging characteristics of HNBR/clay nanocomposites in air, water and oil at elevated temperature, e-Polymers, 7 (2007) 588-598.
[157] S. Chen, Y. Zhang, R. Wang, H. Yu, M. Hoch, S. Guo, Mechanical properties, flame retardancy, hot-air ageing, and hot-oil ageing resistance of ethylene-vinyl acetate rubber/hydrogenated nitrile-butadiene rubber/magnesium hydroxide composites, Journal of Applied Polymer Science, 114 (2009) 3310-3318.

[158] T. Lacroix, B. Tilmans, R. Keunings, M. Desaeger, I. Verpoest, Modelling of critical fibre length and interfacial debonding in the fragmentation testing of polymer composites, Composites Science and Technology, 43 (1992) 379-387.
[159] Z. Chen, W. Yan, A shear-lag model with a cohesive fibre–matrix interface for analysis of fibre pull-out, Mechanics of Materials, 91 (2015) 119-135.
[160] P. Van den Heuvel, M. Wubbolts, R. Young, T. Peijs, A finite element analysis of a planar carbon fibre/epoxy model composite: 2D versus 3D, Advanced Composites Letters, 6 (1997) 155-160.
[161] P. Van Den Heuvel, T. Peijs, R. Young, Analysis of stress concentrations in multi-fibre microcomposites by means of Raman spectroscopy, Journal of Materials Science Letters, 15 (1996) 1908-1911.
[162] J. Andersons, E. Spārniņš, R. Joffe, L. Wallström, Strength distribution of elementary flax fibres, Composites Science and Technology, 65 (2005) 693-702.
[163] J. Song, W.D. Wen, H.T. Cui, S.B. Zhao, Study on static and fatigue behaviors of carbon fiber bundle and the statistical distribution by experiments, Journal of Composite Materials, 49 (2015) 3157-3168.
[164] M.L. Euler, Remarques sur l'effect du frottement dans l'equilibre, Mem. Acad. Sci, 18 (1762) 265-278.
[165] S.D. Sheppard, B.H. Tongue, Statics: Analysis and Design of Systems in Equilibrium, John Wiley & Sons Incorporated, 2005.
[166] S. Cadwell, R. Merrill, C. Sloman, F. Yost, Dynamic fatigue life of rubber, Industrial & Engineering Chemistry Analytical Edition, 12 (1940) 19-23.
[167] S. Asare, J.J.C. Busfield, Fatigue life prediction of bonded rubber components at elevated temperature, Plastics, Rubber and Composites, 40 (2011) 194-200.
[168] J.J.C. Busfield, V. Jha, H. Liang, I.C. Papadopoulos, A.G. Thomas, Prediction of fatigue crack growth using finite element analysis techniques applied to three-dimensional elastomeric components, Plastics, Rubber and Composites, 34 (2005) 349-356.
[169] R. Talreja, 1 - A conceptual framework for studies of durability in composite materials, in: V. Carvelli, S.V. Lomov (Eds.) Fatigue of Textile Composites, Woodhead Publishing, 2015, pp. 3-27.
[170] M. Yamamoto, J.L. White, Theory of deformation and strain-induced crystallization of an elastomeric network polymer, Journal of Polymer Science Part a-2-Polymer Physics, 9 (1971) 1399-1415.
[171] P.J. Flory, Thermodynamics of crystallization in high polymers. I. Crystallization induced by stretching, The Journal of Chemical Physics, 15 (1947) 397-408.
[172] K. Fuller, J. Gough, A. Thomas, The effect of low-temperature crystallization on the mechanical behavior of rubber, Journal of Polymer Science Part B: Polymer Physics, 42 (2004) 2181-2190.
[173] J.-M. Chenal, L. Chazeau, Y. Bomal, C. Gauthier, New insights into the cold crystallization of filled natural rubber, Journal of Polymer Science Part B: Polymer Physics, 45 (2007) 955-962.
[174] L. Mandelkern, A. Allou Jr, M. Gopalan, Enthalpy of fusion of linear polyethylene, The Journal of Physical Chemistry, 72 (1968) 309-318.
[175] H.P. Klug, L.E. Alexander, X-ray diffraction procedures: for polycrystalline and amorphous materials, X-Ray Diffraction Procedures: For Polycrystalline and Amorphous Materials, 2nd Edition, by Harold P. Klug, Leroy E. Alexander, pp. 992.(1974) 992.

[176] R.T. Downs, M. Hall-Wallace, The American Mineralogist Crystal Structure Database, American Mineralogist, 88 (2003) 247-250.
[177] G.C. Psarras, G.A. Sofos, A. Vradis, D.L. Anastassopoulos, S.N. Georga, C.A. Krontiras, J. Karger-Kocsis, HNBR and its MWCNT reinforced nanocomposites: Crystalline morphology and electrical response, European Polymer Journal, 54 (2014) 190-199.
[178] M.F. Bukhina, M.a.F. Bukhina, S.K. Kurlyand, Low-Temperature Behaviour of Elastomers, Brill, 2007.
[179] B. Harris, Engineering composite materials, Institute of metals London, 1986.
[180] K. Yang, B. Zhong, Q. Huang, C. He, Z.Y. Huang, Q. Wang, Y.J. Liu, Stress ratio effect on notched fatigue behavior of a Ti-8Al-1Mo-1V alloy in the very high cycle fatigue regime, International Journal of Fatigue, 116 (2018) 80-89.
[181] S.Y. R. Tashiro, C.A. Stevens, Rubber reinforcing carbon fibre cord under tension and bending, Part 1: stress analysis, in: M.J. Alexander Lion (Ed.) ECCMR X, CRC Press, Taylor & Francis Group, 2017.
[182] I. O'Connor, H. Hayden, J.N. Coleman, Y.K. Gun'ko, High-strength, high-toughness composite fibers by swelling Kevlar in nanotube suspensions, Small, 5 (2009) 466-469.
[183] B. Alcock, J.K. Jørgensen, The mechanical properties of a model hydrogenated nitrile butadiene rubber (HNBR) following simulated sweet oil exposure at elevated temperature and pressure, Polymer Testing, 46 (2015) 50-58.
[184] B. Alcock, N.O. Cabrera, N.M. Barkoula, J. Loos, T. Peijs, The mechanical properties of unidirectional all-polypropylene composites, Composites Part A: Applied Science and Manufacturing, 37 (2006) 716-726.
[185] M. Larsen, Hansen solubility parameters and SWCNT composites, Procedings of the 17th International Conference on Composite Materials, ICCM-17, Edinburg, 2009.
[186] C.M. Hansen, Hansen Solubility Parameters: A User's Handbook, CRC press, 2007.
[187] Y. Li, H. Zhang, M. Crespo, H. Porwal, O. Picot, G. Santagiuliana, Z.H. Huang, E. Barbieri, N.M. Pugno, T. Peijs, E. Bilotti, In situ exfoliation of graphene in epoxy resins: A facile strategy to efficient and large scale graphene nanocomposites, ACS Applied Materials & Interfaces, 8 (2016) 24112-24122..
[188] H. Launay, C.M. Hansen, K. Almdal, Hansen solubility parameters for a carbon fiber/epoxy composite, Carbon, 45 (2007) 2859-2865.
[189] S. Detriche, J. Nagy, Z. Mekhalif, J. Delhalle, Surface state of carbon nanotubes and Hansen solubility parameters, Journal of Nanoscience and Nanotechnology, 9 (2009) 6015-6025.
[190] S.W. Kim, T. Kim, Y.S. Kim, H.S. Choi, H.J. Lim, S.J. Yang, C.R. Park, Surface modifications for the effective dispersion of carbon nanotubes in solvents and polymers, Carbon, 50 (2012) 3-33.
[191] J.W.S. Hearle, L.W.C. Miles, The Setting of Fibres and Fabrics, Merrow Publishing Company Limited, 1971.
[192] J. Lee, M. Lim, J. Yoon, M.S. Kim, B. Choi, D.M. Kim, D.H. Kim, I. Park, S.-J. Choi, Transparent, flexible strain sensor based on a solution-processed carbon nanotube network, ACS Applied Materials & Interfaces, 9 (2017) 26279-26285.
[193] J. Rausch, E. Mäder, Health monitoring in continuous glass fibre reinforced thermoplastics: Tailored sensitivity and cyclic loading of CNT-based interphase sensors, Composites Science and Technology, 70 (2010) 2023-2030.

[194] S. Aziz, S.A. Rashid, S. Rahmanian, M.A. Salleh, Experimental evaluation of the interfacial properties of carbon nanotube coated carbon fiber reinforced hybrid composites, Polymer Composites, 36 (2015) 1941-1950.

Appendix

Matlab code for hysteresis calculation

```
clear all;
close all;
ShowPlot='On';
CSVnames = dir('*tracking.CSV');

fig1=figure(1);

for i=1:length(CSVnames)
    CSVnames(i).name
    RawData = csvread(CSVnames(i).name, 1, 0);  %%i is field variable

    CycleList=unique(RawData(:,4));
    sort(CycleList);
    CycleList([1 2 3])=[];
    DeltaArea=zeros(length(CycleList),1)
    ElasticEnergy=zeros(length(CycleList),1)
    for j=1:length(CycleList)
        CycleInAnalysis=RawData(find(RawData(:,4)==CycleList(j)),[8
9]);


        [~,I]=min(CycleInAnalysis(:,1));
        Xmin=CycleInAnalysis(I,1);
        Ymin=CycleInAnalysis(I,2);
        [~,I]=max(CycleInAnalysis(:,1));
        Xmax=CycleInAnalysis(I,1);
        Ymax=CycleInAnalysis(I,2);
        k=(Ymax-Ymin)/(Xmax-Xmin);
        b=Ymax-k*Xmax;
        %         CycleInAnalysis(:,2)-CycleInAnalysis(:,1)*k-b;
        IncreaseData=CycleInAnalysis(find((CycleInAnalysis(:,2)-
CycleInAnalysis(:,1)*k-b)>=0),:);
        IncreaseData=sortrows(IncreaseData,1);
        DecreaseData=CycleInAnalysis(find((CycleInAnalysis(:,2)-
CycleInAnalysis(:,1)*k-b)<=0),:);
        DecreaseData=sortrows(DecreaseData,1);

        Delta=0.01;
        FitX=Xmin:Delta:Xmax;

FitY=interp1(IncreaseData(:,1),IncreaseData(:,2),FitX,'linear');
        AreaIncrease=sum(FitY)*Delta;

FitY2=interp1(DecreaseData(:,1),DecreaseData(:,2),FitX,'linear');
        AreaDecrease=sum(FitY2)*Delta;
        DeltaArea(j)=AreaIncrease-AreaDecrease;
        ElasticEnergy(j)=AreaDecrease
        % Hysteresis loop
        if strcmp('Off',ShowPlot)
            figure(j)
            plot(CycleInAnalysis(:,1),CycleInAnalysis(:,2),['o'
'k'])
            hold on
```

```
            plot(IncreaseData(:,1),IncreaseData(:,2),['*' 'g'])
            plot(DecreaseData(:,1),DecreaseData(:,2),['*' 'y'])
            plot(FitX,FitY,['.' 'g'])
            plot(FitX,FitY2,['.' 'y'])
            hold on
             xlabel('Position [mm]');
             ylabel('Force [N]');
        end
    end
    Result{i,1}=CycleList;
    Result{i,2}=DeltaArea;
    K2=10;
    [~,I2]=min(abs(CycleList-K2));

    set(0, 'currentfigure', fig1);
    colour='rgbk'

semilogx(CycleList(I2:length(CycleList)),ElasticEnergy(I2:length(Cyc
leList)),['-' 'o' colour(i)]);
    xlabel('Cycle number');
    ylabel('ElasticEnergy [mJ]');
```